Downloaded from orbit.dtu.dk on: May 05, 2023

DTU Library

Attitude Fusion Techniques for Spacecraft

Bjarnø, Jonas Bækby

Publication date:
2011

Link back to DTU Orbit

Citation (APA):
Bjarnø, J. B. (2011). *Attitude Fusion Techniques for Spacecraft*. DTU Space.

General rights
Copyright and moral rights for the publications made accessible in the public portal are retained by the authors and/or other copyright owners and it is a condition of accessing publications that users recognise and abide by the legal requirements associated with these rights.

- Users may download and print one copy of any publication from the public portal for the purpose of private study or research.
- You may not further distribute the material or use it for any profit-making activity or commercial gain
- You may freely distribute the URL identifying the publication in the public portal

If you believe that this document breaches copyright please contact us providing details, and we will remove access to the work immediately and investigate your claim.

DTU Space
National Space Institute

Department of Measurement & Instrumentation Systems
DTU Space - National Space Institute
Technical University of Denmark
2800 Lyngby
Denmark

Attitude Fusion Techniques for Spacecraft

PhD Dissertation

Jonas B. Bjarnø

August 31st 2010

Colophon

This dissertation has been typeset with LaTeX2e using the *memoir* documentclass and compiled by means of the MiKTeX Version 2.8.3761 TeX implementation. Graphs, figures and diagrams have been produced using MatLab^{TM} R2008a from Math Works Inc., CorelDRAW(R) by the Corel Corporation, AutoCAD(R) by autodesk(R) and the Dia 0.97.1 open source software package. Schematics and PCB layouts have been prepared using the Altium Designer toolset from Altium Limited.

The manuscript has been prepared for a 100% A4 format with two-side openright printing.

- If I have seen further it is by standing on the shoulders of giants -

Sir Isaac Newton
(1643 – 1727)

Abstract

Spacecraft platform instability constitutes one of the most significant limiting factors in hyperacuity pointing and tracking applications, yet the demand for accurate, timely and reliable attitude information is ever increasing. The PhD research project described within this dissertation has served to investigate the solution space for augmenting the DTU μASC stellar reference sensor with a miniature Inertial Reference Unit (IRU), thereby obtaining improved bandwidth, accuracy and overall operational robustness of the fused instrument. Present day attitude determination requirements are met and surpassed by the μASC in the low frequency domain. However, the intrinsic limitation in the photon flux available from starlight necessitates relatively long sensor exposure periods for the μASCs unparalleled performance to be realized, thus introducing an inherently limited time resolution of the instrument, and affecting operations during agile and complex spacecraft attitude maneuvers.

As such, there exists a theoretical foundation for augmenting the high frequency performance of the μASC instrument, by harnessing the complementary nature of optical stellar reference and inertial sensor technology. With both sensor types providing measurements of the spacecraft attitude in space, harnessing the extreme accuracy of the μASC throughout the low frequency range and the inherent fidelity of miniature accelerometers in the high frequency domain allows the combined instrument to provide unsurpassed accuracy over the entire span of frequencies applicable to spacecraft attitude control systems.

Completing the first steps from theoretical possibility towards a proven concept constitutes the primary focus of the project, having necessitated extensive research and development within several diverse technical areas such as highly miniaturized analog and digital electronics, instrument space qualification, test and validation procedures, sensor fusion techniques and optimized software implementations to reach a successful conclusion. The content of the project thus represents cutting edge aerospace technology due to the extreme performance that must be ascertained on all fronts whilst harnessing only a minimum of resources. Considering the physical limitations imposed by the μASC instrument as well as the next generation of smaller and more agile satellites, the main design drivers of the IRU implementation become critical parameters such as power consumption, volume and mass in addition to system level robustness and operational safety. The nature of the Ph.D. project requires not only cross disciplinary research, but also the application of emerging technologies never before employed in High-Rel space instrumentation systems.

Project supervisor:
Head of Department, Professor John Leif Jørgensen,
Measurement and Instrumentation Systems, DTU-Space

Resumé

Generel mekanisk ustabilitet ombord på satellitter udgør en af de største begrænsende faktorer for præcisionsudmålinger af fartøjets absolutte attitude, og det til trods for et stadigt stigende behov for præcis og pålidelig data. Ph.D.-forskningsprojektet, som denne afhandling beskriver, har haft til formål at kortlægge løsningsrummet for at for at forbedre det DTU-udviklede μASC stjernekamera ved tilføjelse af en inertiel referenceenhed for derigennem at opnå bedre egenskaber af det samlede instrument. For indeværende kan de grundlæggende krav til attitudebestemmelse tilfredsstilles og endog overgås i det lavfrekvente område af observationsbaserede stjernereferencesystemer, som eksempelvis μASC stjernekameraet. Det begrænsede antal fotoner, der kan opfanges fra stjernelys, nødvendiggør dog relativt lange eksponeringstider for at opnå fuld ydelse. Deraf følger, at stjerne-baserede referencesensorer er naturligt begrænsede, når det kommer til hurtige og komplekse satellitmanøvrer.

Der eksisterer således det teoretiske grundlag for at forbedre μASC stjernekameraets egenskaber ved højere frekvenser, gennem udnyttelse det komplementære forhold imellem optiske og inertielle sensorer. Da begge instrumenttyper foretager udmåling af satellittens orientering i rummet, er det således muligt at udnytte stjernekameraets ekstreme nøjagtighed ved lave frekvenser og den tilsvarende målekvalitet produceret af miniatureaccelerometre i højfrekvensdomænet. Principielt vil der derved kunne opnås en nær ideel attitudesensor, der spænder fra de laveste til de højeste mekaniske frekvenser, man kan komme ud for i moderne satellitsystemer.

Projektets primære fokus har været at gennemgå de nødvendige skridt for at kunne demonstrere konceptets viabilitet, hvilket har krævet gennemgribende forskning og udvikling indenfor talrige tekniske områder - herunder, miniature analog- og digitalelektronik, kvalifikationsmetoder til rumfart, test og valideringsprocedurer, optimal sensor co-integration og optimerede softwareimplementationer. Projektets indhold repræsenterer således det fremmeste niveau af rumfartsteknologi med tanke på det niveau af ydelse, der har måttet opnås på disse områder indenfor de stærkt afgrænsede ressourcer, som typisk er tilgængelige ombord på satellitter. Dette kombineret med de høje ydelseskrav introduceret af μASC stjernekameraet har gjort effektforbrug, størrelse og masse til kritiske parametre for den inertielle referenceenhed på niveau med kravene til operationel robusthed og sikkerhed. Interdisciplinær forskning samt introduktionen af nye teknologier til rumfartsbrug er således nøglebegreber i den forhåndenværende afhandling.

Projektvejleder:
Sektionsleder, Professor John Leif Jørgensen,
Måling og Instrumenting, DTU-Space

Preface

This dissertation is submitted in partial fulfillment of the requirements for obtaining the PhD degree at the Danish Technical University - DTU. The work described herein has been conducted in cooperation with the Space Instrumentation Group (SIG) at the National Space Institute - DTU Space, under the framework of the Danish Doctoral School of Space Science and Technology.

The project has been structured as a development effort towards introducing novel inertial sensing techniques to high fidelity spacecraft attitude determination sensors. The ultimate manifestation of these efforts has been the realization of a new type of Inertial Reference Unit (IRU), particularly designed to enhance high frequency performance of the μASC stellar reference sensor as developed and produced by Space Instrumentation Group at Measurement & Instrumentation System (MIS), DTU Space.

Acknowledgements

I remain deeply grateful to my supervisor Professor John L. Jørgensen for his enduring support and guidance throughout the project effort. Likewise, I should like to extend my gratitude to the members of the Space Instrumentation Group and personnel at Measurement & Instrumentation Systems, DTU Space, without whom none of these activities would have been possible. Their dedication, skill and professionalism is truly admirable. Furthermore, I thank José M.G. Merayo and Peter S. Jørgensen of DTU Space for numerous stimulating conversations regarding high fidelity calibration theory and application.

Similarly, I also thank my fellow Ph.D. student Mathias Benn, with whom I have had the pleasure of sharing three incredibly exiting years and countless discussions regarding technical and non-technical matters. Finally, I would also like to extend my most heartfelt gratitude to family and friends for their enduring support throughout this endeavor.

Contents

List of Figures

List of Tables

Nomenclature

Typographical Conventions

Applicable bibliographic entries are collected at the end of each chapter. Bibliographic references are structured as squared brackets containing primary author surname and year of publication e.g. [Bjarnoe-2007]. For publications prepared by organizations or non-personalized authorships references will be provided in the same format, but with the surname of the primary author replaced by a capital letter version of the organizational acronym e.g. [IEEE-2000]. For publications within the same authorship and year of publication an additional alphabetic designator will follow the year of publication e.g. [IEEE-2000a]. For multiple citations in the same reference, each citation will be separated by a comma e.g. [Bjarnoe-2007,IEEE-2000a]. References within the dissertation are structured as Chapter and Section references only, using a standardized notation e.g. (see Section 1.1). When used in the dissertation footnotes are implemented using the LaTeX2e standard[1]. Figures, Tables and equations are numbered with incremental numbers in reference to the chapter number. Moreover, the introduction of new variables by the declaration of an equation will be implemented as exemplified by equation 0.1:

$$F = m \cdot a \tag{0.1}$$

where:
F: signifies force [N].
m: mass [kg].
a: acceleration $[\frac{\mathrm{m}}{\mathrm{s}^2}]$.

In equations, letters with *italic* notation will be representing variables, e.g. x, $\overrightarrow{u_i}$ and $\underline{\underline{R}}_{\phi}$, whereas roman letters will be representing units, e.g. $\frac{\mathrm{m}}{\mathrm{s}^2}$ and $\frac{^{\circ}}{\mathrm{s}}$. In number notifications all commas(,) and periods(.) symbolize decimal separators throughout the thesis, i.e. no 1000 separators are used.

[1] Footnote example.

Acronyms and Abbreviations

The following list contains acronyms and abbreviations used throughout the thesis:

ADC Analog to Digital Converter

ADEV Allen Deviation

AVAR Allen Variance

CAD Computer-Aided Design

CCD Charge Coupled Device

CDM Charged Device Model

CDS Correlated Double Sampling

CHU Camera Head Unit

CNC Computed Numerically Controlled

COI Centre of Integration

CoM Centre of Mass

COTS Commercial Off The Shelf

CPLD Complex Programmable Logic Device

CW ClockWise

CCW Counter-ClockWise

DAC Digital to Analog Converter

DCL Declared Components List

DCM Data Conversion Module

DNR Dynamic Range

DOF Degree Of Freedom

DPA Destructive Physical Analysis

DPU Data Processing Unit

DSMC Direct Simulation Monte Carlo

DTU Technical University of Denmark

ECSS European Cooperation for Space Standardization

EEPROM Electrically Erasable Programmable Read-Only-Memory

EM Engineering Model

EMI Electromagnetic Interference

ESA European Space Agency

ESD Electrostatic Discharge

FIR Finite Impulse Response

FPGA Field Programmable Gate Array

GUI Graphical User Interface

GSE Ground Support Equipment

HBM Human Body Model

ICBM Intercontinental Ballistic Missile

IFOG Interferometric Fiber Optic Gyroscope

IIR Infinite Impulse Response

IMU Inertial Measurement Unit

IR Infrared

IRU Inertial Reference Unit

ISA Inertial Sensor Assembly

LDO Low Dropout Regulator

LSB Least Significant Bit

MEMS Micro Electro Mechanical System

MOS Metal Oxide Semiconductor

MM Machine Model

uASC micro Advanced Stellar Compass

Opamp Operational Amplifier

PAL Programmable Logic Array

PCB Printed Circuit Board

PSD Power Spectral Density

PPS Pulse Per Second

RLG Ring Laser Gyroscope

RMS Root Mean Square

SAR Successive Approximation Register

SEE Single Event Effects

SIG Space Instrumentation Group

STS Space Transportation System

TID Total Ionizing Dose

TTL Transistor-Transistor Logic

UART Universal Asynchronous Receiver Transmitter

VR Vertical Reset

WBS Work Breakdown Structure

WC Worst Case

Terminology and Definitions

The following terms will be used throughout the dissertation with provisos as outlined in the following.

AC: Used to indicate short term activity of a system or short term assessment of the parametric evolution of a specific parameter.

Arcseconds: is a unit of angular measurement, defined as $\frac{1}{3600}$ of a degree, or $\frac{\pi}{648000} \simeq 4.848\mu$rad radians. In this context the arcsecond will be represented with the unit ["].

Attitude: Signifies object or coordinate system orientation. Relative attitude used to express orientation with respect to another variable object or coordinate system, absolute attitude to specify orientation with respect to a given reference frame e.g. J2000.

Centre Of Integration: or COI, describes the time of which a μASC image is referred to, stamped in the centre of integration during image capture. Moreover, this term is used to established a mutual time reference between the μASC and the μIRU.

DC: Used to indicate long term activity of a system or long term assessment of the parametric evolution of a specific parameter.

Gravitational acceleration *g*: In the context of this dissertation the gravitational acceleration is defined by the 1967 Geodetic Reference System Formula yielding g_ϕ for sea level operations. As such, the gravitational acceleration used throughout this work equals:

$$\begin{aligned} g_\phi &= 9.780327 \cdot (1 + 0.0053024 \sin^2 \phi - 0.0000058 \sin^2 \phi) \\ &= 9.8157 \frac{m}{s^2} \end{aligned}$$

where:
g_ϕ: signifies the acceleration in [m/s^2] at the latitude ϕ.
ϕ: DTU laboratory latitude N55°46'59.48".

Inter-calibration: Term used to encompass the procedures associated with determining the relative orientation of separate attitude sensors.

N/A: Notation used to signify "Not Available" in data or parametric context and "Not Applicable" in textual context.

Rotation: Expresses frame transformations with coinciding origins.

Spacecraft: The terms Spacecraft, Satellite and S/C will be used interchangeably throughout the text.

Transformation: Signifies the changing of coordinate system. Used in reference to changes including rotation, translation and scaling.

Translation: Term used to express object or coordinate system movement along the principle axes of a reference coordinate system.

Chapter 1

Introduction

This chapter introduces the concept of the μIRU augmented μASC stellar reference sensor and the perspectives for wide-band fused attitude determining instrumentation. Further, it details the proviso for the treatise, before outlining the overall scope and structure of the dissertation.

1.1 Background

Contrary to common perception, the steady state flight regime for a vehicle operating in space is not characterized by being a perfect force free environment. Indeed the quality of the microgravity environment commonly encountered onboard an orbiting spacecraft far exceeds the levels that can be generated by other means (eg. parabolic flights, drop towers etc.), yet instances can be identified where substandard microgravity levels have affected operations. From a scientific perspective not only microgravity research requires high fidelity force free environments. The extreme pointing requirements of space-based telescopes make the quality of scientific observations highly dependent upon ensuring amenable levels of vibration and commonly spacecraft designers will go to great lengths to mitigate adverse effects from excessive vibration. One example hereof is the extensive vibration isolation mechanism developed for the NASA James Webb Space Telescope as reported upon by [Bronowicki-2006].

One of the few characterizations of the in-flight microvibrational environment on a spacecraft was performed in 1989, when the ESA Olympus communication satellite was deployed into geostationary orbit. Using the PAX triaxial accelerometer package, wide-band (0.5Hz-1000Hz) acceleration measurements where performed and confirmed the presence of substantial mechanical vibration correlated with the operation of platform subsystems.

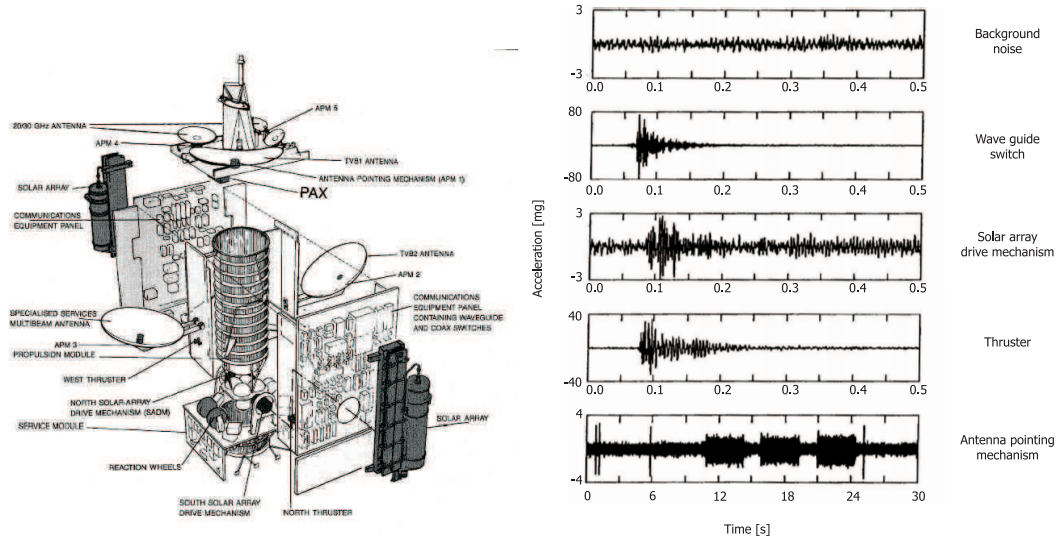

Figure 1.1. *ESA Olympus satellite and typical output data from the PAX triaxial accelerometer package. (Sources [Tunbridge-1990, Dyne-1993])*

What was found on-board Olympus was a highly diverse selection of vibration sources, most of which featured unanticipated scale and frequency content. Figure 1.1 presents a selection of typical events as recorded by PAX. Interestingly the largest transient accelerations detected exceeded 100 mg and where generated by the wave guide switches in the communication system, not as anticipated by the station keeping thrusters. Similarly, disturbances from the different hardware drive mechanisms for the solar panels, antennas and reaction wheels where clearly discernable in the acquired data as providing lengthy intervals with moderately increased disturbance levels as well as short term shock-like disturbance signatures.

The influence on spacecraft attitude estimation due to platform vibration should not be underestimated either. The ensuing motion can manifest itself as increased pointing jitter leading to significant reductions in delivered attitude data accuracy, and could in extreme cases force a reduction data availability. To exemplify these issues, inflight attitude data covering approximately one orbit from the DTU Advanced Stellar Compass (ASC) included on the JAXA ADEOS-II mission is reflected in Figure 1.2.

As indicated by the blue circles in Figure 1.2 the platform experiences a series of disturbances around sample number 6550. The acquired attitude data indicates that the event is uncorrelated with known noise sources such as thermal transitions and straylight intrusions. However, as the matching misfit clearly shows, the disturbances are associated with real motion, thus leading to the conclusion that the platform encountered transient vibrations giving rise to a temporary, albeit significant, degradation of the accuracy. It is specifically this type of behavior the μIRU augmentation concept seeks to address.

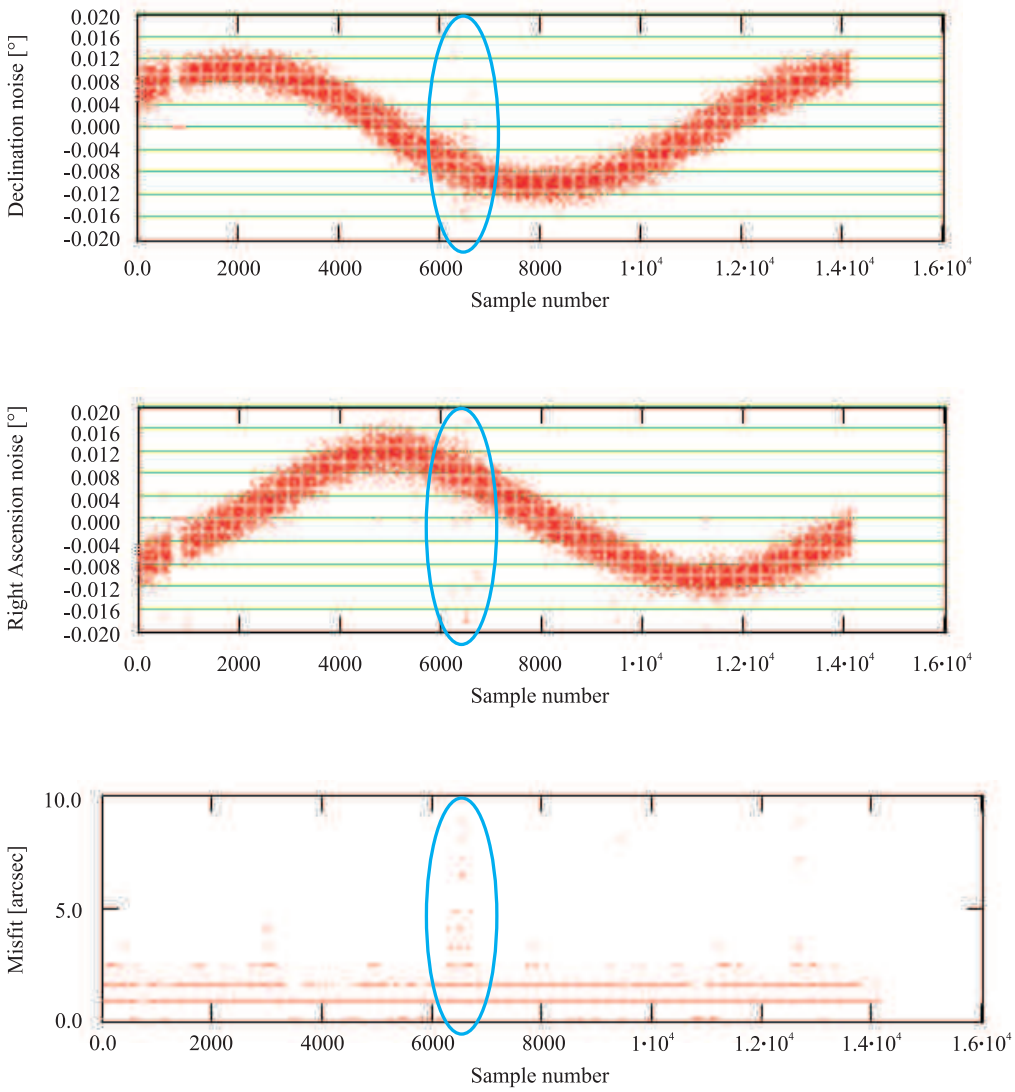

Figure 1.2. *On-orbit vibrations encountered during the ADEOS-II mission. (Source [SIG-2003])*

1.2 μIRU Augmentation Concept

The μASC represents the 4^{th} generation development of the Advanced Stellar Compass (ASC) instrument originally designed as a high fidelity 3DOF attitude sensor for the Danish geomagnetic research satellite Ørsted successfully launched in February 1999.
The ASC was developed as a fully autonomous star tracker capable of incorporating all brighter stars within the camera Field Of View (FOV) in the spacecraft attitude solution. This approach has yielded an extremely flexible system capable of providing attitude data with unsurpassed accuracy and high availability. The μASC has inherited the majority of the ASC technol-

ogy, methodology and software structure whilst making significant advances in terms of reducing the physical outline and optimizing the electronics design.

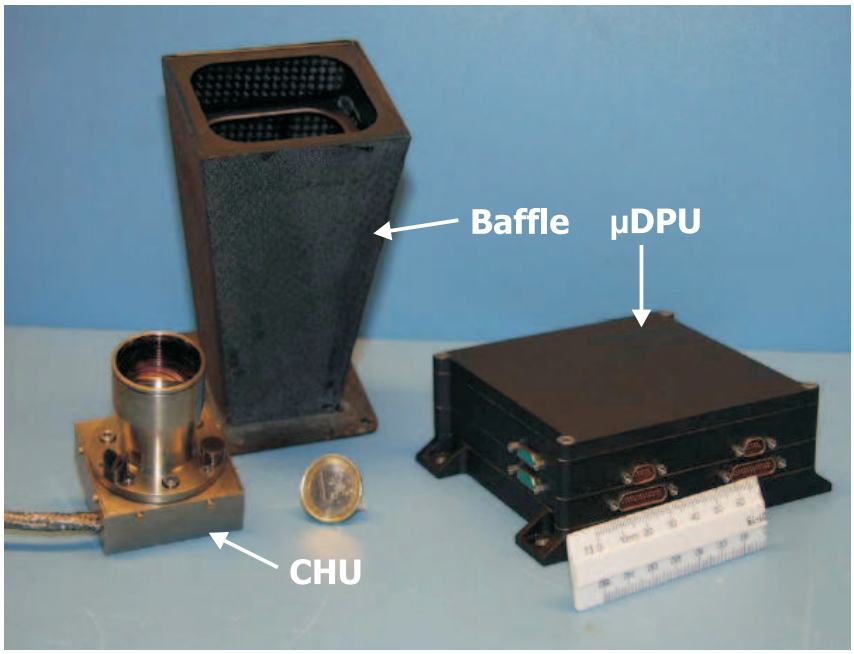

Figure 1.3. *μASC system level elements. (Source [SIG-2006a])*

The μIRU augmentation concept as developed over the course of the project introduces an additional 3 degree of freedom (3DOF) attitude sensor to the μASC stellar reference framework. Targeting a frequency domain which overlaps that of the stellar reference sensor while extending into the high frequency domain, facilitates intercalibration of the two sensor systems while improving both performance, robustness and data availability through complementary sensor fusion techniques. During a 2006 conceptual study [Bjarnoe-2007], the notion of the all-accelerometer μIRU augmentation was derived. As illustrated by Figure 1.4, a configuration (hereinafter denoted the GEO3 configuration) of four dual axis linear accelerometers where found to provide the highest achievable performance of any compatible inertial sensing solution. As such, the GEO3 physical arrangement constitutes the first vantage point for the Ph.D. project.

The second vantage point was also among the most significant results of the 2006 study. An extensive survey of the limited in-flight experience with high frequency vibration monitoring was conducted and based upon the results a set of average power spectral density profiles was derived. As depicted in Figure 1.5, the commonality derived from these profiles was a coarse determination of the required bandwidth to encompass the majority of vibration power for a given spacecraft. It was proven that for all surveyed spacecraft $\sim$99% of the RMS signal would be contained for a 200Hz bandwidth, hence this value was selected as the upper 3dB frequency bound for the conceptual design.

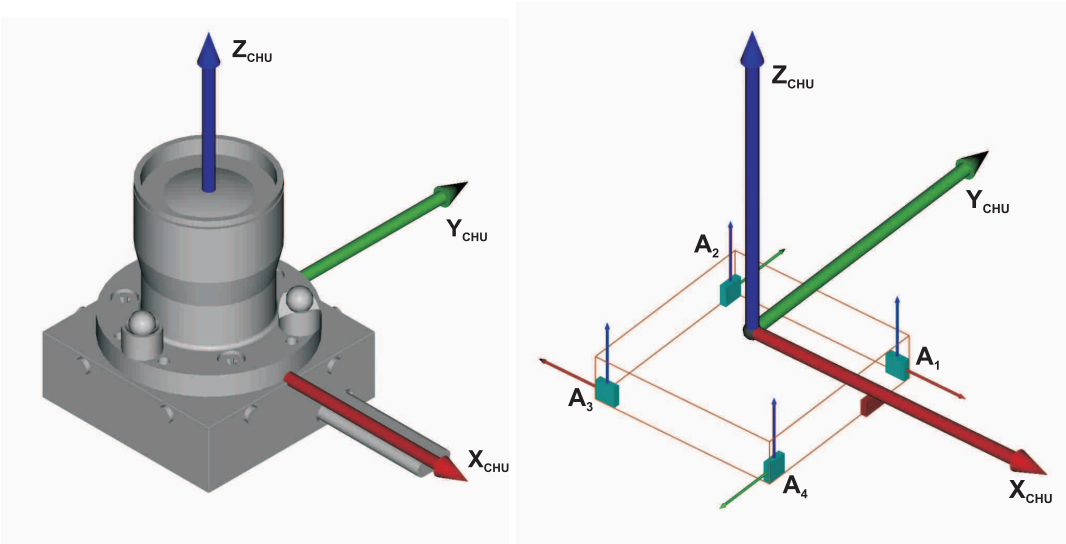

Figure 1.4. *The GEO3 μIRU sensor configuration in relation to the native μASC coordinate system convention.*

Moreover it should be noted that a lower bound of $f_{-3dB} = 1$Hz was selected to ensure overlap between the frequency response of the μIRU and the μASC to facilitate intercalibration.

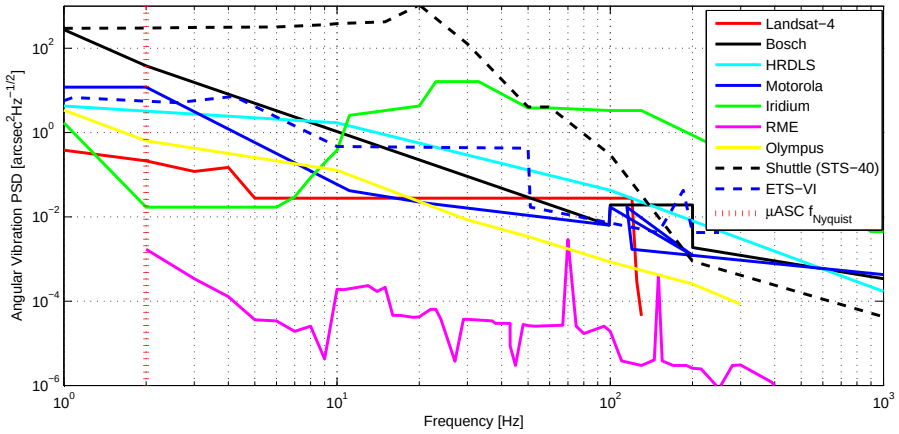

Figure 1.5. *Vibration power spectral density plots for surveyed spacecraft.*

The third and final vantage point for the Ph.D. project is of an even more pertinent nature than the preceding ones. Stated as the minimum impact requirement, it infers that however the μIRU augmentation is implemented it should strive to have a minimum impact upon existing aspects of the heritage μASC design. As such, no measure of performance on behalf of the μASC will be unduly sacrificed to accommodate the μIRU augmentation.

1.3 Future Perspectives

The outlook for an μIRU augmented μASC with the previously outlined characteristics is extremely positive in terms of viable flight opportunities. As is the case for all platform critical systems for use in space, obtaining flight heritage for a previously unflown system constitutes the single largest hurdle to be surmounted. The μIRU augmented μASC can, however, benefit from extensive flight heritage pertaining to elements of the μASC design, as these characteristics will be retained in their entirety.

Several high-end missions being planned by both ESA and CNES for the coming decade and currently in their early phases will involve advanced formation flying concepts, where, for instance, several satellites move through space in a fixed constellation to perform interferometry based measurements. One such proposed mission is the highly ambitious ESA Darwin Space Telescope designed to study extrasolar planets. The Darwin concept as depicted in Figure 1.6 is based upon a number of individual telescopes flying in a $\sim$100m circular formation with a hub satellite at the constellation centre and a relay satellite to transmit data to Earth. The scientific potential inherent in such a mission is extremely large, whereas the attitude control technology needed still remains fledgling.

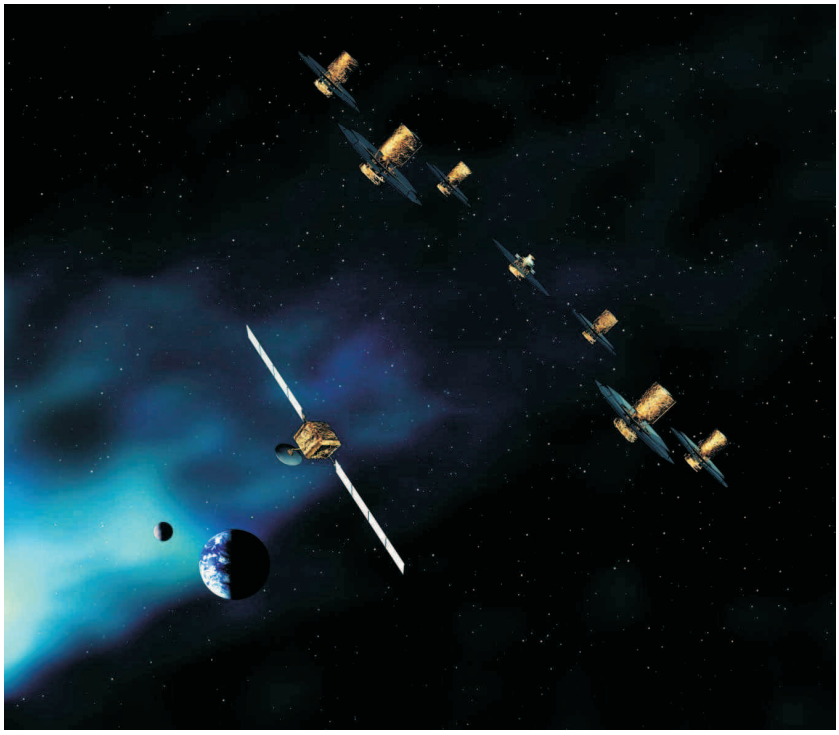

Figure 1.6. *Darwin Space Telescope Constellation.(Images courtesy of ESA).*

Similarly, advances are being made in inter-satellite laser communication tech-

nology, where information is beamed through the void of space from one satellite to another. In such cases the main experiment is entirely dependent upon the quality and frequency with which satellite attitude data is generated, in order to efficiently reduce attitude control limit cycles.

When successfully demonstrated the μIRU augmented μASC will be capable of providing such missions with extremely accurate, high bandwidth attitude data, which in turn will further the quality of the scientific observations. Near term development should, as such, involve a demonstration mission to acquire the crucial flight heritage for the μIRU augmented design, whereas the long term perspectives will serve to consolidate DTU-developed stellar reference units at the forefront of spacecraft attitude determination technology.

1.4 Objectives and Methodology

This dissertation and the project work it describes constitute only a first step towards enhancing the μASC instrument through sensory augmentation by an inertial reference unit. The development process from inception to final flight qualified product comprises a task of significant proportions - certainly beyond the reach of a single person Ph.D project. As such, this project focuses on formulating the initial system level design requirements and from there deriving a viable design, optimized towards functional integration with the μASC instrument. Working from the 2006 sensor head optimality study [Bjarnoe-2007], a design baseline is established from the co-integration requirements pertaining to the μASC. From here a physical prototype implementation is realized as a proof-of-concept entity.

The primary objectives for the project work described in this dissertation can thus be summarized as follows:

1: To determine requirements and establish prerequisites for co-integration between the μASC and the μIRU augmentation.

2: To develop a viable design for a μIRU capable of interfacing with the μASC instrument, whilst adhering to the outlined requirements.

3: To establish a functional proof-of-concept μIRU sensor that will facilitate co-integration testing with the μASC.

4: To establish and apply procedures and methodologies for testing, calibrating and characterizing a μIRU.

What is clear from the listing is the fact that the objectives only encompass a subset of the development tasks required to establish a fully augmented

μASC. Key aspects, such as the development of a suitable sensor fusion algorithm for optimally combining the attitude data from the μASC and its μIRU augmentation, as well as the development of the software and firmware interface segments on the μASC DPU end, have all been deferred to future project work. This descoping has been introduced to ensure the remaining objectives can be met in a diligent and exhaustive fashion.

1.5 Scope of Dissertation

The overall scope of this dissertation is to formally summarize the work conducted throughout the project period extending from March 2007 to August 2010 at the department for Measurement & Instrumentation Systems, DTU Space in developing an inertial reference unit augmentation for the μASC stellar reference sensor. The work breakdown structure has been organized as follows:

- Revisit of the μIRU conceptual design/configuration baseline as developed by [Bjarnoe-2007] to assess applicability.
- Adaptation of the existing physical and electronics configuration of the μASC CHU to accommodate the μIRU augmentation.
- Primary inertial sensor candidate selection, environmental test and characterization.
- Baseline μIRU design development, including parts selection, test and characterization.
- μIRU prototype design and development, including both electronic, mechanical, software and GSE entities.
- Calibration strategy and platform development.
- Prototype calibration experimentation and performance assessment.

This structure is also evident in the project timeline, included in coarse form as Figure 1.7. The project plan has been continuously updated throughout the course of the project with its current form reflecting the timehistory of the entire project.

The dissertation at hand is comprised of six main chapters which treat the different aspects of the development project. Chapters 3 and 2 serve to introduce the basic principles of the μIRU augmentation and the MEMS inertial sensors that comprise it, with the latter chapter emphasizing the characterization of the primary sensor candidate to assess its applicability to space-based

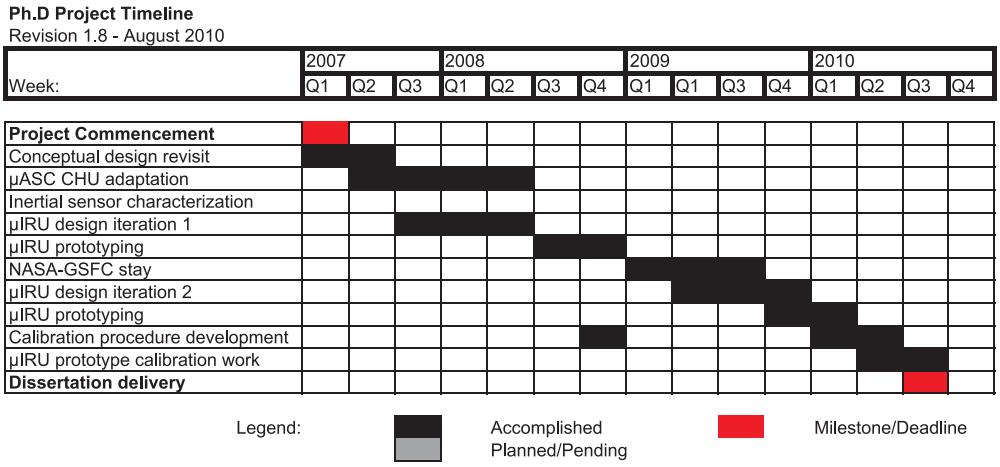

Figure 1.7. *Coarse form Ph.D project timeline.*

operations. Chapter 4 provides a very detailed outline of the methodology applied in the development of the μIRU baseline design. This encompasses all parts selection and characterization evaluations as well as overall topological considerations regarding specific aspects of the sampling system configuration. Chapter 5 uses the outlined design baseline to derive and implement a full prototype of the μIRU, while Chapter 6 deals with the development and application of calibration procedures. Chapter 7 finalizes the treatise by providing an assessment of the performance level achieved by the μIRU prototype.

1.6 Summary

This chapter has presented the project background and the problems encountered when applying band-limited attitude determination instrumentation in environments marred by wide-band mechanical noise. The objectives of the project and the methodologies applied in reaching them have been introduced, as has some perspectives on future use of the augmented μASC. Finally, the scope and structure of the dissertation have outlined.

1.7 Bibliography

[Bjarnoe-2007] Jonas Bjarnoe. *Inertial Sensor Augmentation of Stellar Reference Units in the High Frequency Domain.* DTU Space, 2007.

[Bronowicki-2006] A.J. Bronowicki. Vibration isolator for large space telescopes. *Journal of Spacecraft and Rockets*, 2006.

[Dyne-1993] S.J.C. Dyne, D.E.L. Tunbridge, and P.P. Collins. The vibration environment on a satellite in orbit. IEE Colloquium, 1993.

[SIG-2003] Space Instrumentation Group. Assessment of the adeos2 asc performace. Technical report, Measurement and Instrumentation Systems, Ørsted•DTU, 2003.

[SIG-2006a] Space Instrumentation Group. micro advanced stellar compass user's manual. Technical Report ASC-DTU-MA-3001, Measurement and Instrumentation Systems, Ørsted•DTU, May 2006.

[SIG-2006b] Space Instrumentation Group. micro advanced stellar compass general information. Technical Report ASC-DTU-PRP-3000, Measurement and Instrumentation Systems, Ørsted•DTU, May 2006.

[Tunbridge-1990] D. Tunbridge. The "pax" instrument on olympus. *ESA Bulletin*, No.64:84–91, 1990.

Chapter 2

Spacecraft Inertial Attitude Determination

The ultimate goal of the generic inertial navigation system is to establish full 6-DOF attitude and positional knowledge for the carrier vehicle. However, for space-based applications, translational movement will be bound by the vehicle trajectory and only subject to significant change in correlation with maneuvering of the spacecraft by impulsive measures. As such, spacecraft inertial navigation systems will often be relegated to providing attitude data only. The following chapter presents the basic principles of attitude determination by inertial means, and extends the application to spacecraft navigation. This leads to the fundamental concepts of the μIRU being derived.

2.1 The Principles of Inertial Navigation

The fundamental principles behind inertial sensing where originally established by the Newtonian laws of motion, effectively stating that it is possible to discern the motion of an object with a known inertial mass within an inertial reference frame by merely assessing the net sum of forces acting upon it. To quantify these forces in the case at hand consider the situation depicted in Figure 2.1.

The vehicle body reference frame has been deployed in inertial space (J2000 frame), and the acceleration a experienced by a particle at the point P in relation to the body frame B can thus be expressed as a vector sum of acceleratory contributions:

$$a = a_B^I + a_g^I + a_P^B + a_T^B + a_{CT}^B + a_{Cor}^B \tag{2.1}$$

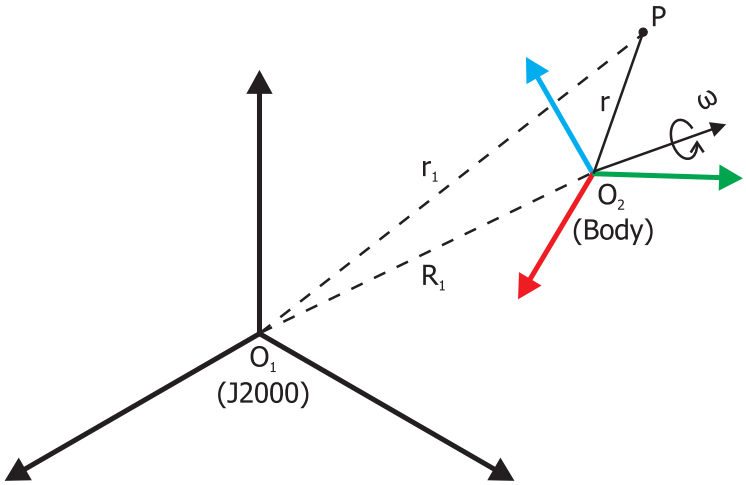

Figure 2.1. *The CHU frame moving in the J2000 inertial reference frame.*

where:
a_B^I: represents linear acceleration of O_2 (Body) in relation to O_1 (J2000).
a_g^I: represents Body linear acceleration due to gravity.
a_P^B: represents linear acceleration of the point P in relation to the Body frame.
a_T^B: represents tangential acceleration due to Body reference frame rotation.
a_{CT}^B: represents centripetal acceleration due to Body reference frame rotation.
a_{Cor}^B: represents the Coriolis acceleration of P.

Normally a spacecraft body will be operating beyond large scale gravitational influence of other attracting bodies, and as such the gravitational acceleration can be ignored in this context without loss of generality. Moreover, assuming that P retains a stationary position within the Body reference frame (as would be the case for an inertial sensor fastened within the μASC CHU) allows the Coriolis acceleration and point linear acceleration to be negated, thus simplifying equation 2.1 in relation to Figure 2.1 to the following expression:

$$a = a_B^I + a_T^B + a_{CT}^B = \ddot{\vec{R}}_B + \dot{\vec{\omega}}_B \times \vec{r} + \vec{\omega}_B \times (\vec{\omega}_B \times \vec{r}) \tag{2.2}$$

where:
$\ddot{\vec{R}}_B$: describes the linear acceleration of the body.
$\vec{\omega}_B$: describes the angular velocity of the body.
$\dot{\vec{\omega}}_B$: describes the angular acceleration of the body.
r: the point position vector with respect to the body frame.

Equation 2.2 constitutes the fundamental relationship which governs the use of inertial navigation technology in space. When adapting it to a directly mea-

surable quantity, consider the situation where a physical linear accelerometer S has been firmly attached to the body B with its axis of sensitivity along the $\vec{d}$ axis, producing the output A_S.

$$A_S = \left(\ddot{\vec{R}}_B + (\dot{\vec{\omega}}_B \times \vec{r}) + [\vec{\omega}_B \times (\vec{\omega}_B \times \vec{r})]\right) \cdot \vec{d} + a_o \tag{2.3}$$

where:
a_o: describes the offset of the linear acceleration sensor.

Equation 2.3 simply states the fundamental fact that an accelerometer fixed within the body B will experience acceleration contributions from rotational and translational components. The exact scale of the individual contributions will in turn depend upon the location $\vec{r}$ and orientation vectors $\vec{d}$ of the sensor, and it is as such necessary to determine these time invariant parameters to correctly estimate the total acceleration incurred. By expanding the cross product terms equation 2.3 takes on the form depicted in equation 2.4 which reveals both linear, non-linear, quadratic and cross-coupling terms along each of the principle axes.

$$\begin{aligned}
A_S &= d_x\left(\ddot{R}_{B,x} + \omega_{\dot{B},y} r_z - \omega_{\dot{B},z} r_y + \omega_{B,y}\left(\omega_{B,x} r_y - \omega_{B,y} r_x\right) - \omega_{B,z}\left(\omega_{B,z} r_x - \omega_{B,x} r_z\right)\right) \\
&+ d_y\left(\ddot{R}_{B,y} + \omega_{\dot{B},z} r_x - \omega_{\dot{B},x} r_z + \omega_{B,z}\left(\omega_{B,y} r_z - \omega_{B,z} r_y\right) - \omega_{B,x}\left(\omega_{B,x} r_y - \omega_{B,y} r_x\right)\right) \\
&+ d_z\left(\ddot{R}_{B,z} + \omega_{\dot{B},x} r_y - \omega_{\dot{B},y} r_x + \omega_{B,x}\left(\omega_{B,z} r_x - \omega_{B,x} r_z\right) - \omega_{B,y}\left(\omega_{B,y} r_z - \omega_{B,z} r_y\right)\right) \\
&\Rightarrow d_x\left(\ddot{R}_{B,x} + \omega_{\dot{B},y} r_z - \omega_{\dot{B},z} r_y - \omega_{B,y}^2 r_x - \omega_{B,z}^2 r_x + \omega_{B,y}\omega_{B,x} r_y + \omega_{B,z}\omega_{B,x} r_z\right) \\
&+ d_y\left(\ddot{R}_{B,y} + \omega_{\dot{B},z} r_x - \omega_{\dot{B},x} r_z - \omega_{B,z}^2 r_y - \omega_{B,x}^2 r_y + \omega_{B,z}\omega_{B,y} r_z + \omega_{B,x}\omega_{B,y} r_x\right) \\
&+ d_z\left(\ddot{R}_{B,z} + \omega_{\dot{B},x} r_y - \omega_{\dot{B},y} r_x - \omega_{B,x}^2 r_z - \omega_{B,y}^2 r_z + \omega_{B,x}\omega_{B,z} r_x + \omega_{B,y}\omega_{B,z} r_y\right)
\end{aligned} \tag{2.4}$$

The time invariant parameters of equation 2.4 thus become the sensitive axis **d**, the position **r** and for a physical accelerometer also a bias a_o. Extracting individual fundamental terms of acceleration or angular rate from equation 2.4 is the goal of an inertial navigation system. To obtain full 6DOF knowledge the inertial sensor complement of the navigation system must necessarily resolve the six basic parameters $\ddot{R}_{B,x}$,$\ddot{R}_{B,y}$,$\ddot{R}_{B,z}$,$\omega_{B,x}$,$\omega_{B,y}$,$\omega_{B,z}$, the integration of which will result in position and attitude being determined. Formally, the system must also provide a seventh inertial parameter without which integration would be impossible, and that parameter is time.

What is often recognized as the "classical" solution to the 6DOF problem, is the functional combination of three orthogonal gyroscopes and three orthogonal accelerometers to resolve both rotation and translation in all three principle axes. Combining these six sensors into a single entity exemplifies a

system capable of 6DOF determination, yet the limitations of the early instruments versus the advances having been made later years have lead to two separate implementation strategies, namely the Platform and the Strapdown inertial navigation systems.

2.1.1 Platform Systems

Adhering to the terminology proposed by the IEEE in [IEEE-2001, IEEE-2004] and [Curey-2004], the generic inertial platform system may be illustrated as seen in Figure 2.2.

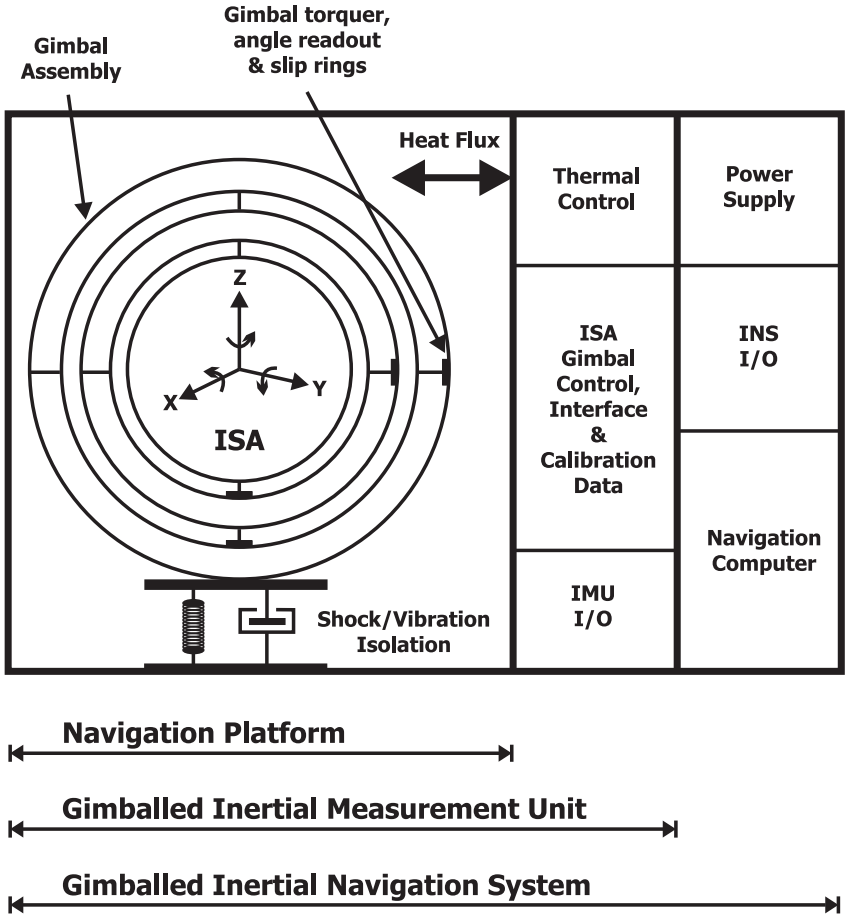

Figure 2.2. *Platform Inertial Navigation System.*

The inertial platform uses gyroscopes to maintain the Inertial Sensor Assembly (ISA) accelerometers at a fixed attitude in space, thus allowing the platform to define the directions of the acceleration measurements. The gyroscopes operate in a null-loop measuring the platform rotation with respect to inertial space and feeding corrective signals to the gimbal torquers to maintain attitude [Walchko-2002]. As such, the gyroscopes will never experience large scale

rotation rates, but merely small deviations from null positions during nominal operations. However, under more extreme maneuvers the gimbal planes may become aligned causing loss of attitude. This condition is termed "Gimbal Lock" and clearly illustrates a deficiency associated with reading spacecraft attitude directly from the gimbal angles. Often Gimbal Lock is mitigated by adding a fourth gimbal to the ISA, but at the expense of added system cost and complexity.
The ISA of inertial platform systems are complex mechanical entities subject to degradation from local environment and wear. They do, however, provide excellent accuracy and allow vehicle rotation rates above 1000°/s which is the prime reason for their use today. Applications include rocket launch vehicles, combat aircrafts etc.

2.1.2 Strapdown Systems

The strapdown inertial navigation system has benefited from the advances in electronics made since the 1960s to allow the removal of the gimballed platform from the ISA. Again adhering to IEEE terminology, the generic strapdown system may be illustrated as seen in Figure 2.3.

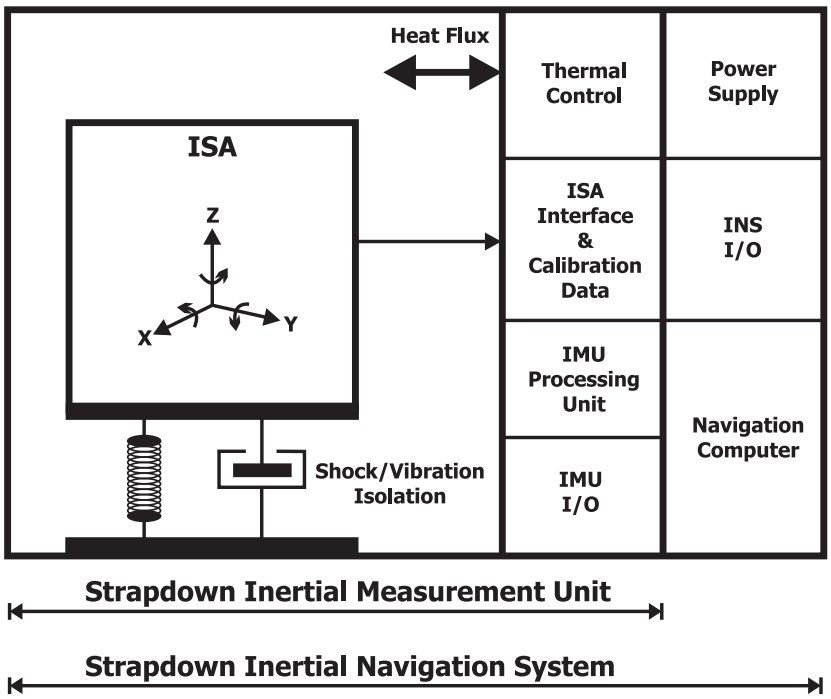

Figure 2.3. *Strapdown Inertial Navigation System.*

The strapdown system attaches both accelerometers and gyroscopes to the vehicle body, allowing rotation angles and translation components to be measured directly in the body frame. For highly dynamic vehicles such as airplanes,

this approach imposes strict requirements upon the gyroscopes capability to handle high rotation rates - often exceeding 400°/s. As such, the gyroscope quality needed for strapdown systems is generally much larger, with the dynamic range requirement commonly exceeding that of the platform inertial system by two orders of magnitude [Lawrence-2001].

As illustrated by Figures 2.2 and 2.3 the inertial navigation systems contain several elements in addition to the sensor assembly. Generally, when referring to an inertial navigation system most will relate to the Inertial Measurement Unit (IMU) structure, which combines the sensor assembly with basic corrective calibration and data processing. The IMU thus provides a conditioned version of the raw ISA outputs properly corrected for sensor non-orthogonality, thermal variations etc. The full Inertial Navigation System (INS) compounds the IMU outputs to a unified solution expressed in the vehicle reference frame (or any other reference frame for that matter), providing directly usable data to the onboard attitude control system. However, it should be noted that modern microprocessing capabilities are gradually removing the need to distinguish between the IMU and the INS, as all computational tasks can be undertaken by a single processor.

2.1.3 The Inertial Reference Unit

In addition to the generic navigation systems previously described, scaled down versions have been realized for application specific purposes. One such implementation is the Inertial Reference Unit (IRU), which is a terminology used to describe a navigation system only operating in 3DOF determining roll, pitch and yaw rotational motion. Such systems are commonly used as heading and attitude references in smaller aircraft as a reasonably cheap substitute for a full scale navigation system, but the terminology also applies well in spacecraft pointing applications where translational knowledge has little or no merit. Through inertial sensing, three basic techniques exist that allow for recovery of angular motion, namely the application of gyroscopes, angular accelerometers or differential linear accelerometers. Of those three, gyroscopes are by far the most used technology for this purpose, due to their inherently lower long term error accumulation rate when compared to accelerometer based solutions. The angular accelerometer does not see widespread use as its primary area of operation is also serviced by gyroscopes, again offering better long term accuracy when estimating angular position. Similarly the differential accelerometers offer only limited long term performance as integration errors compound faster than for a comparable gyroscope. Even so, a number of specialized applications requiring high bandwidth attitude determination have successfully applied differential accelerometer techniques, the results of which are reported by [Chen-1994, Lee-2001, Tan-2001, Lee-2003].

2.1.4 The Differential Accelerometer Pair

During the course of the 2006 study, as reported upon in [Bjarnoe-2007], it was unequivocally determined that the optimal realization of an augmentation of the μASC capability in the high frequency domain, would be a 3-DOF IRU type inertial sensor based upon differential accelerometer sensing. Considering the sensor technology available at that time, physically compatible gyroscopes simply failed to deliver performance comparable to that achievable by a differential accelerometer pair. In particular, short term angular error accumulation and sensor bandwidth specification, where areas where miniature gyroscopes simply did not meet requirements of the envisioned μIRU augmentation.

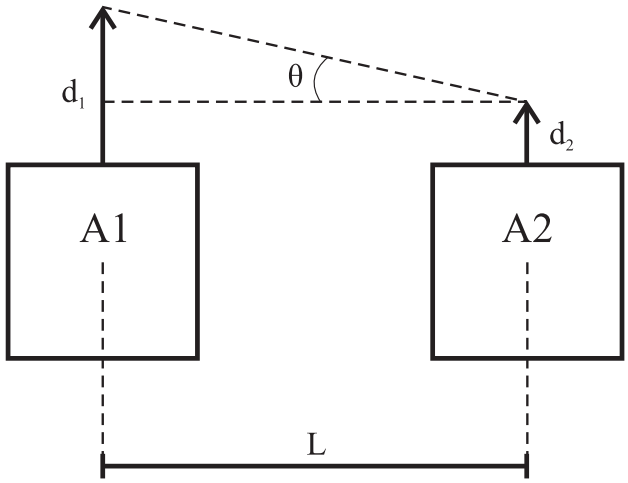

Figure 2.4. *Differentially coupled linear accelerometers.*

The operating principle of the differential linear accelerometer pair illustrated in Figure 2.4 is extremely simple. By aligning the sensitive axes of two linear accelerometers and separating them along a physical baseline L, any in-plane angular motion θ will be perceivable as a difference in the sensed linear quantities d_1 and d_2. Using the small angle approximation the expression may be formalized as:

$$\theta = \tan^{-1}\frac{d_1 - d_2}{L} \simeq \frac{d_1 - d_2}{L} \tag{2.5}$$

Assuming the linear displacements are derived by double integration of the accelerometer outputs and constitute identically distributed, uncorrelated random variables with RMS error contributions σ_{dA}, the angular error σ_θ may be expressed as:

$$\sigma_\theta^2 = \frac{var(d_1) + var(d_2)}{L^2} = \frac{2\sigma_{dA}^2}{L^2} \quad \Longrightarrow \quad \sigma_\theta = \frac{\sqrt{2}\sigma_{dA}}{L} \tag{2.6}$$

thereby having made the assumptions of L being a known invariant quantity and the noise distributions pertaining to the two accelerometers being identical. The latter assumption is justifiable when utilizing identical accelerometers.

Critical to the performance of the differential pair, the dependence of the sensed linear quantities d_1 upon the sensor noise is evaluated using the methodology derived by [Thong-2002]. The standard deviation of the measured position σ_{dA} due to accelerometer white noise can thus be expressed as:

$$\sigma_{dA}(T) = \frac{1}{2}T^2\frac{\sigma_A}{\sqrt{N}} = \frac{1}{2}T^2\frac{\sigma_A}{\sqrt{Tf_s}} = \frac{1}{2}\frac{\sigma_A}{\sqrt{f_s}}T^{1/2} \tag{2.7}$$

where:
N: signifies the number of samples over the integration period T [samples].
f_s: denotes the sample frequency [Hz].

Equation 2.7 serves to constrain the angular estimation error of the differential pair over time by two parameters critical to the design of the μIRU augmentation, namely sensor noise and sample rate. Using the relationship between these two parameters to establish a scoring function it is possible to compare the error accumulation of differential pairs using different accelerometer devices and baselines. Moreover, this method facilitates direct comparison with similar angular error growth models for gyroscopes.

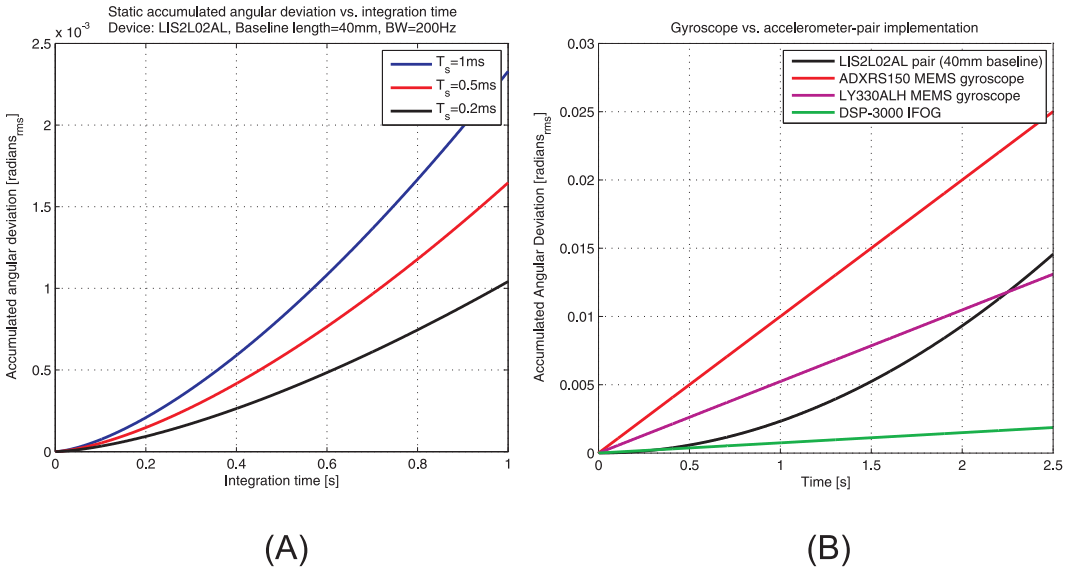

Figure 2.5. *1σ formalized error accumulation for sample rate and device noise characteristic dependencies. Sample rate 1kHz.*

Figure 2.5(B) provides a 1σ angular error growth model for different sensors. The LIS2L02AL MEMS acceleromenter was in 2006 identified as the primary candidate for the implementation of differential linear acceleration sensing in

the μIRU augmentation[1]. Similarly, the ADXRS150 was found to be the lowest noise COTS MEMS gyroscope available in 2006, producing an output noise density of $0.05°/s/\sqrt{Hz}$. The revisited survey in 2010 showed the LIS330ALH as having significantly improved this specification by reaching $0.014°/s/\sqrt{Hz}$. The performance of these three COTS devices arranged for angular sensing when compared to the DSP-3000 navigation grade interferometric fiber optic gyroscope, do however illustrate a distinct qualitative difference. While the LIS2L02AL differential pair still provide a better constrained error accumulation envelope than the best COTS gyroscopes on shorter timescales, it is evident that advances in MEMS gyroscope technology has narrowed the performance gap. This is, however, not that case when comparing sensor bandwidth, where the linear accelerometers typically retain about a factor of 10 higher f_{-3dB} frequencies. Figure 2.5(A) also provides a simulation of the dependence of 1σ angular error growth upon sample rate in accordance with equation 2.7, clearly illustrating the incentive towards adopting the highest possible sample rate for the μIRU.

To provide a more realistic performance model for the differential pair than the 1σ integration envelope, the Simulink model describing the differential pair sampling system depicted in Figure 2.6 has been established. For static initial conditions ($d_A = 0, \dot{d_A} = 0$) a Monte Carlo simulation based upon this model is conducted for the time evolution of θ.

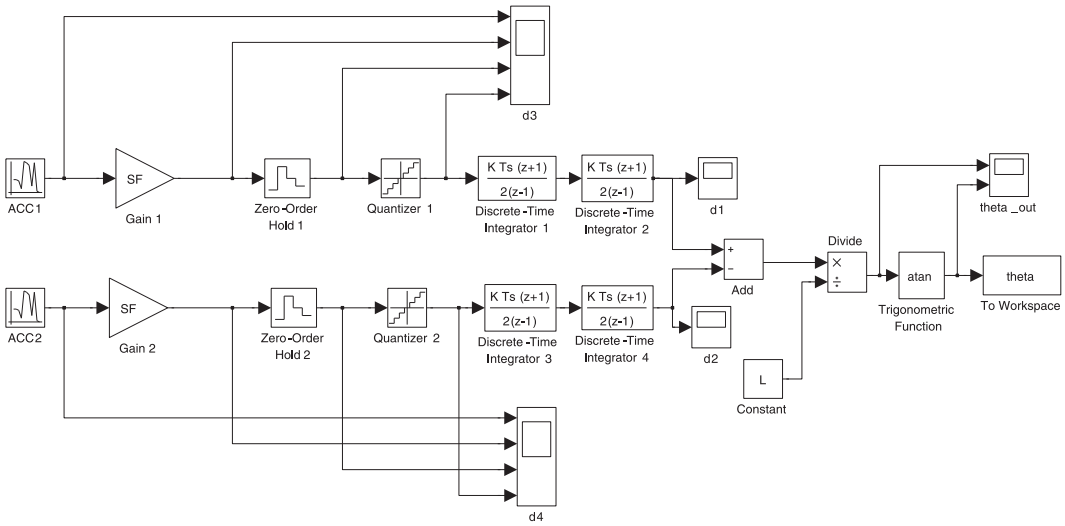

Figure 2.6. *Simulink model of LIS2L02AL differential pair.*

The simulation is based upon an accelerometer output white noise distribution adhering to the specifications provided by ST Microelectronics, the manufacturer of the LIS2L02AL accelerometer, for a nominal bandwidth of 200Hz delimited by a single-pole roll-off. The results depicted in Figure 2.7 show the

[1]Chapter 3 discusses the present day applicability of that classification.

accumulation of angular error at 200Hz, 1kHz and 2kHz sample rate, respectively.

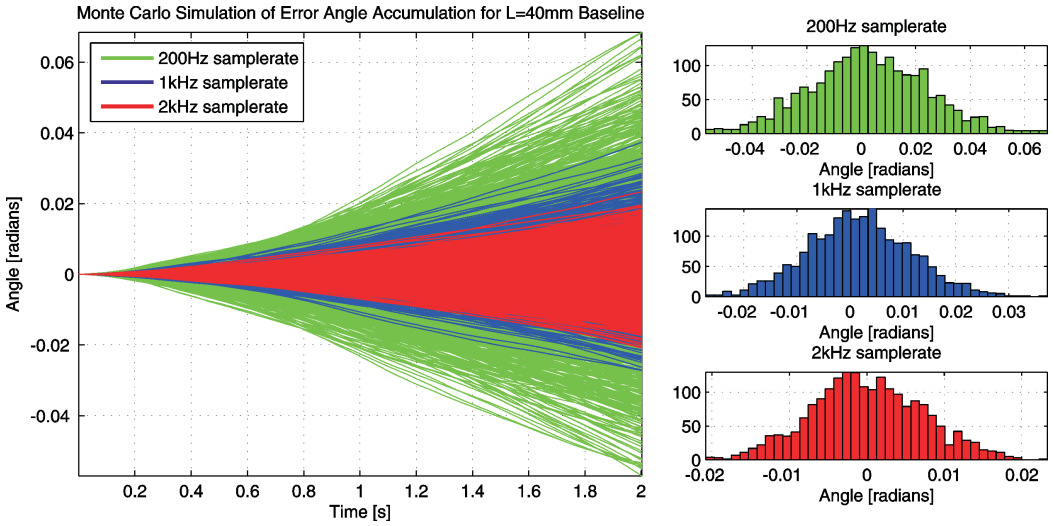

Figure 2.7. *Angular error growth Monte Carlo simulation for LIS2L02AL differential pair at 200Hz (green), 1kHz (blue) and 2kHz (red) samplerates.*

With the simulation input being artificially generated zero-mean Gaussian distributed white noise, the derived angular distribution will mimic what can be obtained by a well conditioned pair of AC coupled accelerometers. When considering DC coupled accelerometer, any presence of bias drift will effectuate further deviations in the angular error mean.

2.2 The μIRU Augmentation

Compared to conventional inertial navigation systems, the μIRU concept differs in four significant areas, namely

- The collection of DC attitude data is unnecessary.
- The willingness to trade DC stability for AC performance.
- Spacecraft translational data unnecessary to fulfill objectives.
- Hard physical restrictions on volume, mass and power consumption dictated by the μASC.

The fact that DC attitude data is provided with the most extreme fidelity by the μASC essentially precludes any inertially based augmentation from significantly improving the DC attitude knowledge through fused operations. Moreover, with the μASC being a native 3DOF sensor, no direct means of bounding

the translational errors would exist if cooperatively fused with a 6DOF inertial sensor. As such, the μIRU baseline configuration seeks to emphasize AC angular motion resolution only.

Traditional approaches to gyroscope-free IMU implementations feature a minimal number of linear sensors specifically oriented so as to allow full 6DOF recovery. Several such configurations exist, and in particular the minimum 6 sensor implementation by [Chen-1994] has been subject to extensive study [Tan-2001, Ang-2003]. Common among these gyroscope-free IMU implementations is however the ambition to recover full 6DOF motion, and for the configurations to incur no direct restrictions upon sensor geometry, volume or resource consumption.

Functionally fusing the μASC CHU with a μIRU augmentation does in this regard introduce a substantial drawback. When considering an all-accelerometer IRU implementation within the confines of the CHU envelope, only minimal physical separation can be generated between individual accelerometers placed along the Z-axis (CHU boresight) if the original mechanical envelope of the μASC CHU is to be preserved. If the differential sensing principle is to be employed, analysis has shown the GEO3 sensor configuration to provide optimal resolution within the physical constraints of the existing envelope [Bjarnoe-2007].

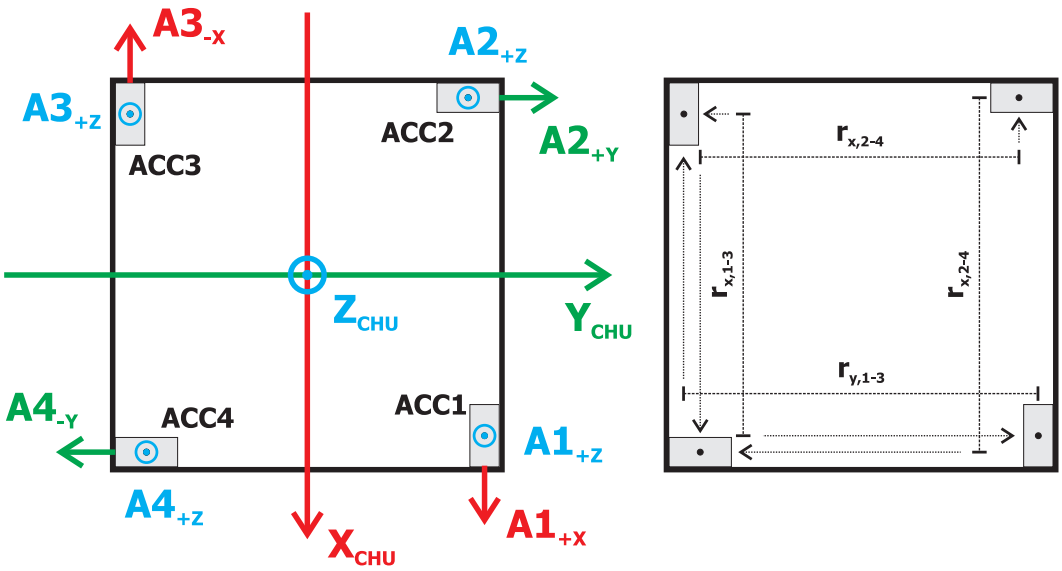

Figure 2.8. *μIRU accelerometer GEO3 sensor configuration and naming conventions. Top view.*

The GEO3 sensor configuration allows angular motion to be recovered for all three principle axes of the CHU, even though it incorporates no physical sensor separation along the Z-axis. As such, with all sensors mounted in the same Z-axis plane, X-axis and Y-axis rotation can be recovered using direct

combination of the sensor displacements derived from the differential pairs as outlined in Equation 2.8 through 2.11.

$$\theta_{X_{CHU}} = \frac{d_{A1_{+Z}} - d_{A3_{+Z}}}{r_{Y_{1-3}}} \tag{2.8}$$

$$\theta_{X_{CHU}} = \frac{d_{A2_{+Z}} - d_{A4_{+Z}}}{r_{Y_{2-4}}} \tag{2.9}$$

$$\theta_{Y_{CHU}} = \frac{d_{A1_{+Z}} - d_{A3_{+Z}}}{r_{X_{1-3}}} \tag{2.10}$$

$$\theta_{Y_{CHU}} = \frac{d_{A2_{+Z}} - d_{A4_{+Z}}}{r_{X_{2-4}}} \tag{2.11}$$

Deriving Z-axis rotation is complicated by the applicable differential pairs ($A2_{+Y}$,$A4_{-Y}$ and $A1_{+X}$,$A3_{-X}$) not being co-planar. As such, rotation about Z must be recovered by a more rigorous treatment of the angular terms in equation 2.4 pertaining to each sensor. However, the GEO3 configuration has been judiciously designed so as to ameliorate the issue by positioning the accelerometers symmetrically with respect to the CHU boresight Z-axis. This aspect is also clearly visible in the GEO3 configuration matrices in equation 2.13 and 2.14, which references the idealized accelerometer positions (in units of [mm]) and orientations to the CHU reference frame origo.

$$\mathbf{R_{GEO3_{CHU}}} = \begin{bmatrix} r_{A1_y}, r_{A1_z}, r_{A2_x}, r_{A2_z}, r_{A3_x}, r_{A3_z}, r_{A4_y}, r_{A4_z} \end{bmatrix} \tag{2.12}$$

$$= \begin{bmatrix} 22.2 & 22.2 & -20.5 & -20.5 & 20.5 & 20.5 & -22.2 & -22.2 \\ -20.5 & -20.5 & -22.2 & -22.2 & 22.2 & 22.2 & 20.5 & 20.5 \\ -12.5 & -12.5 & -12.5 & -12.5 & -12.5 & -12.5 & -12.5 & -12.5 \end{bmatrix}$$

$$\mathbf{D_{GEO3_{CHU}}} = \begin{bmatrix} d_{A1_y}, d_{A1_z}, d_{A2_x}, d_{A2_z}, d_{A3_x}, d_{A3_z}, d_{A4_y}, d_{A4_z} \end{bmatrix} \tag{2.13}$$

$$= \begin{bmatrix} 0 & 0 & 1 & 0 & 1 & 0 & 0 & 0 \\ -1 & 0 & 0 & 0 & 0 & 0 & -1 & 0 \\ 0 & 1 & 0 & 1 & 0 & 1 & 0 & 1 \end{bmatrix}$$

This feature of the design facilitates cancellation of the centripetal acceleration terms when tabulating the differences $A2 - A4$ and $A1 - A3$, hence leaving only tangential acceleration terms from which $\omega_{CHU,z}$ can be found through integration. When negating the offset voltage of the physical sensors, this relation for the A2,A4 accelerometer pair can formally be expressed as:

$$\begin{aligned} A2-A4 &= \left(\ddot{\vec{R}}_{CHU} + (\dot{\vec{\omega}}_{CHU} \times \vec{r}_{A2}) + [\vec{\omega}_{CHU} \times (\vec{\omega}_{CHU} \times \vec{r}_{A2})]\right) \cdot \vec{d}_{A2_Y} \\ &- \left(\ddot{\vec{R}}_{CHU} + (\dot{\vec{\omega}}_{CHU} \times \vec{r}_{A4}) + [\vec{\omega}_{CHU} \times (\vec{\omega}_{CHU} \times \vec{r}_{A4})]\right) \cdot \vec{d}_{A4_Y} \\ &= (\dot{\vec{\omega}}_{CHU} \times \vec{r}_{A2}) - (\dot{\vec{\omega}}_{CHU} \times \vec{r}_{A4}) \\ &= \dot{\omega}_{CHU,z} r_{A2x} - \dot{\omega}_{CHU,x} r_{A2z} - \dot{\omega}_{CHU,z} r_{A4x} - \dot{\omega}_{CHU,x} r_{A4z} \\ &= \dot{\omega}_{CHU,z} r_{A2x} + \dot{\omega}_{CHU,z} r_{A4x} = \dot{\omega}_{CHU,z} \cdot r_{x,2-4} \end{aligned} \tag{2.14}$$

where the last relations hold true if $r_{A2z} = r_{A4z}$ as is the case for the baseline design. Note that this expression extends directly to the A1,A3 accelerometer pair as well.

It should though be stressed that the positioning of each accelerometer sensor is only to within machining, mounting and calibration tolerances, and consequently cross couplings can occur which will compromise the accuracy of equation 2.8 through 2.11 as well as 2.14. In this case a more rigorous method can be applied to derive the angular rates with respect to the principle axes.

By compounding the total eight sensitive axes in the GEO3 configuration a linear set of equations can be constructed in the form of equation 2.15, where the 8x12 parameter matrix $\mathbf{A}$ as illustrated by equation 2.16 only contains information about the positions $\mathbf{r}$ and sensitive axes $\mathbf{d}$ of the sensors.

$$\mathbf{y} = \mathbf{A}\mathbf{z} + \mathbf{a_o} \tag{2.15}$$

$$\begin{bmatrix} a_{S1} \\ a_{S2} \\ a_{S3} \\ a_{S4} \\ a_{S5} \\ a_{S6} \\ a_{S7} \\ a_{S8} \end{bmatrix} = \mathbf{A} \begin{bmatrix} \ddot{R}_{B,x} \\ \ddot{R}_{B,y} \\ \ddot{R}_{B,z} \\ \dot{\omega}_{B,x} \\ \dot{\omega}_{B,y} \\ \dot{\omega}_{B,z} \\ \omega^2_{B,x} \\ \omega^2_{B,y} \\ \omega^2_{B,z} \\ \omega_{B,x}\omega_{B,y} \\ \omega_{B,x}\omega_{B,z} \\ \omega_{B,y}\omega_{B,z} \end{bmatrix} + \begin{bmatrix} a_{oS1} \\ a_{oS2} \\ a_{oS3} \\ a_{oS4} \\ a_{oS5} \\ a_{oS6} \\ a_{oS7} \\ a_{oS8} \end{bmatrix}$$

$$\mathbf{A} = \begin{bmatrix}
d_{x1} & d_{y1} & d_{z1} & d_{z1}r_{y1} - d_{y1}r_{z1} & d_{x1}r_{z1} - d_{z1}r_{x1} & d_{y1}r_{x1} - d_{x1}r_{y1} & -d_{y1}r_{y1} - d_{z1}r_{z1} & -d_{x1}r_{x1} - d_{z1}r_{z1} & -d_{x1}r_{x1} - d_{y1}r_{y1} & d_{x1}r_{y1} + d_{y1}r_{x1} & d_{x1}r_{z1} + d_{z1}r_{x1} & d_{y1}r_{z1} + d_{z1}r_{y1} \\
d_{x2} & d_{y2} & d_{z2} & d_{z2}r_{y2} - d_{y2}r_{z2} & d_{x2}r_{z2} - d_{z2}r_{x2} & d_{y2}r_{x2} - d_{x2}r_{y2} & -d_{y2}r_{y2} - d_{z2}r_{z2} & -d_{x2}r_{x2} - d_{z2}r_{z2} & -d_{x2}r_{x2} - d_{y2}r_{y2} & d_{x2}r_{y2} + d_{y2}r_{x2} & d_{x2}r_{z2} + d_{z2}r_{x2} & d_{y2}r_{z2} + d_{z2}r_{y2} \\
d_{x3} & d_{y3} & d_{z3} & d_{z3}r_{y3} - d_{y3}r_{z3} & d_{x3}r_{z3} - d_{z3}r_{x3} & d_{y3}r_{x3} - d_{x3}r_{y3} & -d_{y3}r_{y3} - d_{z3}r_{z3} & -d_{x3}r_{x3} - d_{z3}r_{z3} & -d_{x3}r_{x3} - d_{y3}r_{y3} & d_{x3}r_{y3} + d_{y3}r_{x3^v} & d_{x3}r_{z3} + d_{z3}r_{x3} & d_{y3}r_{z3} + d_{z3}r_{y3} \\
d_{x4} & d_{y4} & d_{z4} & d_{z4}r_{y4} - d_{y4}r_{z4} & d_{x4}r_{z4} - d_{z4}r_{x4} & d_{y4}r_{x4} - d_{x4}r_{y4} & -d_{y4}r_{y4} - d_{z4}r_{z4} & -d_{x4}r_{x4} - d_{z4}r_{z4} & -d_{x4}r_{x4} - d_{y4}r_{y4} & d_{x4}r_{y4} + d_{y4}r_{x4^v} & d_{x4}r_{z4} + d_{z4}r_{x4} & d_{y4}r_{z4} + d_{z4}r_{y4} \\
d_{x5} & d_{y5} & d_{z5} & d_{z5}r_{y5} - d_{y5}r_{z5} & d_{x5}r_{z5} - d_{z5}r_{x5} & d_{y5}r_{x5} - d_{x5}r_{y5} & -d_{y5}r_{y5} - d_{z5}r_{z5} & -d_{x5}r_{x5} - d_{z5}r_{z5} & -d_{x5}r_{x5} - d_{y5}r_{y5} & d_{x5}r_{y5} + d_{y5}r_{x5} & d_{x5}r_{z5} + d_{z5}r_{x5} & d_{y5}r_{z5} + d_{z5}r_{y5} \\
d_{x6} & d_{y6} & d_{z6} & d_{z6}r_{y6} - d_{y6}r_{z6} & d_{x6}r_{z6} - d_{z6}r_{x6} & d_{y6}r_{x6} - d_{x6}r_{y6} & -d_{y6}r_{y6} - d_{z6}r_{z6} & -d_{x6}r_{x6} - d_{z6}r_{z6} & -d_{x6}r_{x6} - d_{y6}r_{y6} & d_{x6}r_{y6} + d_{y6}r_{x6} & d_{x6}r_{z6} + d_{z6}r_{x6} & d_{y6}r_{z6} + d_{z6}r_{y6} \\
d_{x7} & d_{y7} & d_{z7} & d_{z7}r_{y7} - d_{y7}r_{z7} & d_{x7}r_{z7} - d_{z7}r_{x7} & d_{y7}r_{x7} - d_{x7}r_{y7} & -d_{y7}r_{y7} - d_{z7}r_{z7} & -d_{x7}r_{x7} - d_{z7}r_{z7} & -d_{x7}r_{x7} - d_{y7}r_{y7} & d_{x7}r_{y7} + d_{y7}r_{x7^v} & d_{x7}r_{z7} + d_{z7}r_{x7} & d_{y7}r_{z7} + d_{z7}r_{y7} \\
d_{x8} & d_{y8} & d_{z8} & d_{z8}r_{y8} - d_{y8}r_{z8} & d_{x8}r_{z8} - d_{z8}r_{x8} & d_{y8}r_{x8} - d_{x8}r_{y8} & -d_{y8}r_{y8} - d_{z8}r_{z8} & -d_{x8}r_{x8} - d_{z8}r_{z8} & -d_{x8}r_{x8} - d_{y8}r_{y8} & d_{x8}r_{y8} + d_{y8}r_{x8^v} & d_{x8}r_{z8} + d_{z8}r_{x8} & d_{y8}r_{z8} + d_{z8}r_{y8}
\end{bmatrix} \tag{2.16}$$

With all information about the relative body pose and position given by vector $\mathbf{z}$, the body pose and position can be approximated for a given measurement $\mathbf{y}$ by determining the left inverse of A:

$$\mathbf{z} = \mathbf{A}^{-1}(\mathbf{y} - \mathbf{a_o}) \tag{2.17}$$

As a final remark, equation 2.15 has an interesting implication regarding the design of gyroscope-free inertial reference units. Extending the parameter matrix $\mathbf{A}$ to 12x12 and ensuring its invertability, would allow the twelve individual parameters of vector $\mathbf{z}$ to be determined directly. The implication hereof is that 12 linear accelerometer arranged completely arbitrarily can realize a full 6DOF IMU, provided the sensitive axes are linearly independent and not coplanar.

2.3 Summary

The purpose of this chapter has been to introduce the fundamental principles of inertial attitude determination and its extension to space-based applications. Subsequently, the concept of the all-accelerometer IRU has been presented as has the concept of the differential accelerometer pair. The latter topic extends directly to μIRU augmentation, which has led to the derivation of the mechanization equations for the envisioned instrument.

2.4 Bibliography

[Ang-2003] Cameron N. Riviere Wei T. Ang, Pradeep K. Khosla. Design of all-accelerometer inertial measurement unit for tremor sensing. *Proc. International Conference on Robotics and Automation*, 2003.

[Bjarnoe-2007] Jonas Bjarnoe. *Inertial Sensor Augmentation of Stellar Reference Units in the High Frequency Domain.* DTU Space, 2007.

[Chen-1994] Jeng-Heng Chen, Sou-Chen Lee, and Daniel B. DeBra. Gyroscope free strapdown inertial measurement unit by six linear accelerometers. *Journal of Guidance, Control and Dynamics*, Vol.17, No.2:286–290, 1994.

[Curey-2004] Randall K. Curey, Michael E. Ash, Leroy O. Thielman, and Cleon H. Barker. Proposed ieee inertial systems terminology standard and other inertial sensor standards. *IEEE*, 7803(8416-4), 2004.

[IEEE-2001] IEEE. Ieee standard for inertial sensor terminology (ieee std. 528-2001). Technical report, The Institute of Electrical and Electronics Engineering, November 2001.

[IEEE-2004] IEEE. Proposed ieee inertial systems terminology standard and other inertial sensor standards (proposed ieee std. 1559). Technical report, The Institute of Electrical and Electronics Engineering, 2004.

[Lawrence-2001] Anthony Lawrence. *Modern Inertial Technology*. Springer-Verlag, second edition edition, 2001.

[Lee-2001] Shinhak Lee, Gerry G. Ortiz, James W. Alexander, Angel Portillo, and Christian Jeppesen. Accelerometer-assisted tracking and pointing for deep space optical communications: Concept, analysis, and implementations. In *IEEE Aerospace Conference*, 2001.

[Lee-2003] S. Lee, G.G. Ortiz, W. Liu, and V. Garkanian. Increasing tracking bandwidth for deep-space optical communications using linear accelerometers. Technical report, Jet Propulsion Laboratory, November 2003.

[Tan-2001] Chin-Woo Tan, Sungsu Park, Kirill Mostov, and Pravin Varaiya. Design of gyroscope-free navigation systems. In *IEEE Intelligent Transportation System*, 2001.

[Thong-2002] J.A. Crowe B.R. Hayes-Gill R.E. Challis Y.K. Thong, M.S. Woolfson. Dependence of inertial measurements of distance on accelerometer noise. *Measurement Science and Technology*, 2002.

[Walchko-2002] Kevin J. Walchko. Inertial navigation. In *Florida Conference on Recent Advances in Robotics*, 2002.

Chapter 3

Micro-Electro-Mechanical Systems Based Inertial Sensors

Since work on the μIRU augmentation for the μASC stellar reference sensor commenced in 2006, the field of inertial sensor technology has seen substantial development. This is particularly true for MEMS-based inertial sensors, which are currently experiencing extreme levels of proliferation driven by the automotive, medical and communications industry. The chapter at hand thus includes an analysis of MEMS inertial sensor technology development over the course of the last four years to determine the state of the art, and to assess whether the sensor selection prerequisites for the μIRU augmentation remain optimal. Finally, a performance assessment of the selected sensor and its applicability to operations in space will be discussed.

3.1 State of The Art

One of the significant outcomes of the 2006 project effort, was an extensive in-depth survey of inertial sensor technologies, their availability and applicability to the μIRU augmentation. The primary conclusion derived from that survey was the fact that at that time no non-MEMS based sensor would meet the stringent requirements to mass, volume and power consumption that the application inferred. Presently, the results of this survey have been revisited, and another survey encompassing both obsoleted, currently in production and white papers on soon to be released devices has been conducted.

As previously established a primary hindrance to the proliferation of MEMS inertial technology has been achieving the long term stability required for navigation or even tactical grade applications, thus relegating their primary use so far to the commercial/industrial sector. However, the recent growth observed in the MEMS inertial commercial market [Yole-2007] spurred on by the

inclusion of gravitational and angular rate sensing in a number of products, has sparked both added sensor development, increased device miniaturization and an overall reduction in pricing levels. These recent developments has though had two significant consequences on the type and quality of commercially available MEMS inertial sensors. One illustration of this point can be given by comparing portfolios of the two largest COTS MEMS inertial sensor manufacturers as it was in 2006 in relation to present day (2010).

2006	
Device Feature	**Value**
Total accelerometers	13
• Analog output	11
• Digital output	2
Number of 1-axis devices	0
Number of 2-axis devices	11
Number of 3-axis devices	2
Total gyroscopes	0
• Analog output	-
• Digital output	-
Number of 1-axis devices	-
Number of 2-axis devices	-
Number of 3-axis devices	-
Smallest accelerometer	5×5×1.6mm
Smallest gyroscope	-
Best accelerometer noise density	$30\mu g/\sqrt{Hz}$
Best gyroscope noise density	-

2010	
Device Feature	**Value**
Total accelerometers	18
• Analog output	7
• Digital output	11
Number of 1-axis devices	0
Number of 2-axis devices	3
Number of 3-axis devices	15
Total gyroscopes	33
• Analog output	30
• Digital output	3
Number of 1-axis devices	8
Number of 2-axis devices	20
Number of 3-axis devices	5
Smallest accelerometer	3×3×1mm
Smallest gyroscope	3×5×1mm
Best accelerometer noise density	$50\mu g/\sqrt{Hz}$
Best gyroscope noise density	$0.014^\circ/s/\sqrt{Hz}$

Table 3.1. *Overview of ST Microelectronics MEMS inertial sensor portfolio 2006 vs. 2010.*

For ST Microelectronics the development trend illustrated in Table 3.1 has been towards significantly expanding the MEMS sensor portfolio, particularly by including a considerable complement of gyroscopes. For linear accelerometers though, development has been more towards increased miniaturization, higher levels of feature integration and digitalization. The cost of this has been a reduction in performance, as the lowest noise accelerometer available has gone from $30\mu g/\sqrt{Hz}$ (LIS2L02AL) in 2006 to $50\mu g/\sqrt{Hz}$ (LIS244ALH), with the higher performance devices having been gradually obsoleted.

For Analog Devices, the development trend has also been one of added feature integration. Additionally a number of single axis gyroscopes have been added and achievable noise performance level for these devices significantly improved. Similar to the ST Microelectronics portfolio, the number of digital output devices has increased substantially, yet from a performance perspective the analog output solutions continue to provide superior resolution and signal to noise ratio. Also note that the best accelerometer noise specification remains the same for 2006 and 2010 (and does in fact pertain to the same device, as the ADXL103/ADXL203 continues to be available), clearly indicating that even though a number of new accelerometers have been introduced, there is no sales incentive or technical merit for improving this specification. Finally it should

2006	
Device Feature	**Value**
Total accelerometers	10
• Analog output	8
• Digital output	2
Number of 1-axis devices	4
Number of 2-axis devices	6
Number of 3-axis devices	0
Total gyroscopes	4
• Analog output	4
• Digital output	0
Number of 1-axis devices	4
Number of 2-axis devices	0
Number of 3-axis devices	0
Smallest accelerometer	5×5×2mm
Smallest gyroscope	7×7×3.7mm
Best accelerometer noise density	$110\mu g/\sqrt{Hz}$
Best gyroscope noise density	$0.05^\circ/s/\sqrt{Hz}$

2010	
Device Feature	**Value**
Total accelerometers	21
• Analog output	10
• Digital output	11
Number of 1-axis devices	5
Number of 2-axis devices	9
Number of 3-axis devices	7
Total gyroscopes	15
• Analog output	7
• Digital output	8
Number of 1-axis devices	14
Number of 2-axis devices	1
Number of 3-axis devices	0
Smallest accelerometer	3×3×0.95mm
Smallest gyroscope	7×7×2.5mm
Best accelerometer noise density	$110\mu g/\sqrt{Hz}$
Best gyroscope noise density	$0.015^\circ/s/\sqrt{Hz}$

Table 3.2. *Overview of Analog Devices MEMS inertial sensor portfolio 2006 vs. 2010.*

be noted that Analog Devices have put significant effort into developing fully integrated MEMS IMU systems [ADI-2008]. This development is not reflected in Table 3.2, as the presently available IMUs are non-compliant with the mass, volume, power consumption and noise performance requirements of the μIRU augmentation.

What Tables 3.1 and 3.2 seek to illustrate is a trend within the commercial MEMS inertial sector indicating that for linear accelerometers, development emphasis has shifted from performance to physical scale and feature integration. Likely this development is driven by the strive towards achieving even further miniaturization of commercial electronic devices. At the same time MEMS gyroscopes, being a considerably less mature technology type (first commercially available MEMS gyroscope developed in 1996 [Lawrence-2001]), are still in the early stages of being introduced to commercialization, and advances in feature integration as well as performance is an ongoing process.

The result of this development is that the application of more novel inertial sensor concepts, as well as the MEMS scientific market end, having to an increasingly large degree been left to more specialized developers (eg. Colibrys, Crossbow). Within the linear accelerometer segment these manufacturers have achieved significant advances in both sensor performance and physical scale, specifically breaking into the $<1\mu g/\sqrt{Hz}$ range through the use of bulk micromachining techniques and differential capacitive transduction principles. However, these performance levels still come at a penalty with respect to device physical characteristics and power consumption as illustrated by the comparison to the LIS2L02AL μIRU augmentation baseline sensor in Table 3.3.

Device	Manufacturer	Axes	Range [g]	Supply Range [V]	Consumption [mW@V]	Sensitivity [mV/g]	Cross Axis Sensitivity [%]	3dB Bandwidth [Hz]	Output Noise Density [$\frac{\mu g}{\sqrt{Hz}}$]	Dimensions (W,B,H) [mm]	Operating Temperature [°C]	Thermal Sensitivity [ppm/°C]	Mass [g]
LIS2L02AL	ST	XY	±2.0	2.4-5.25	2.8@3.3	660	±4	2000	30	5,5,1.6	-40 to 85	±100	0.08
LIS244ALH	ST	XY	±2.0	2.4-3.6	2.2@3.3	660	±2	2000	50	4,4,1.6	-40 to 85	±100	0.04
ADXL203	ADI	XY	±1.7	3.0-6.0	5.5@5.0	1000	±3	2500	110	5,5,2	-40 to 125	±18	0.16
KXM52-1050	Kionix	XYZ	±2.0	2.7-5.5	5.9@3.3	660	±3	1500	65	5,5,1.8	-40 to 125	±180	0.12
VS9002.D	Colibrys	Z	±2.0	2.5-5.5	2.0@5.0	1000±8	N/A	250	25	8.9,8.9,3.2	-55 to 125	±100	1.5
MS9001.D	Colibrys	Z	±1.0	2.5-5.5	2.0@5.0	2000±8	N/A	100	18	8.9,8.9,3.2	-55 to 125	±100	1.5
SF1500	SiFlex	Z	±3.5	±6-±15	110@±6	1200	±0.5	1500	0.5	17.8,17.8,8.5	-40 to 125	±75	6
1221J-002	SDI	Z	±2.0	4.75-5.25	50@5.0	2000	±3	400	5	9.1,9.1,2.9	-55 to 125	±250	0.62

Table 3.3. *Parametric comparison of high end MEMS accelerometer devices.*

As Table 3.3 illustrates the only strong competitors to the ST LIS2L02AL which offer an improvement in terms of sensor noise at a comparable physical scale would be either the Colibrys MS9001.D or the SDI 1221J-002, yet adopting either of those devices would entail incurring a significant disadvantage from the fact that they are only single axis devices. Moreover, the SDI 1221J-002 brings an added difficulty in accommodating its significant power consumption.

Within the MEMS research sector, continuing efforts are being made towards improving the performance and resolution of MEMS linear accelerometers beyond what is possible with the contemporary differentially capacitive transduction principles. Presently the transduction principle which holds the most promise with regards to noise levels and resolution is based upon the tunneling tip. Rather than using differential capacitance to detect the spatial difference between electrodes, the distance is estimated by measuring the tunneling current between two electrodes, which adheres to the exponential relationship of equation 3.1 as presented by [Hartwell-1998].

$$I_t = V_B \cdot e^{-\alpha_I d_{tg} \sqrt{\Phi}} \tag{3.1}$$

where:
V_B: signifies tunneling bias over the electrode gap $[V]$.
α_I: signifies the tunneling constant defined as $\alpha = 1.025 \frac{1}{\text{Å} \cdot \sqrt{eV}}$.
d_{tg}: indicates electrode separation [Å].
Φ: indicates tunneling barrier height $[eV]$.

Utilizing the tunneling principle reliably necessitates electrode separations of $\leq$10Å, thus requiring closed loop operations if any significant acceleration range is to be tolerated. Recent developments combine electrostatic force feedback with the tunneling tip principle, and the resultant devices exhibit excellent acceleration resolution while still maintaining noise characteristics comparable to those of the high end differential capacitive devices [Titterton-2004, Ramos-2008, Chaudhuri-2009]. For low bandwidth applications the tunneling MEMS accelerometer does as such hold great promise, however the necessary steps beyond experimental demonstration towards reliable commercialization of devices using this technology has yet to be taken.

Despite the much higher sensitivity of the tunneling transduction principle as compared to differential capacitive sensing, the fundamental noise limit for both types remain identical. With both principles relying on the displacement of a rigid body proof mass as the means of detecting acceleration, both suspend their respective proof masses in a sealed non-evacuated cavity, utilizing the local cavity atmosphere to introduce squeezed film damping of mechanical oscillations pertaining to the proof mass. However, even though the atmosphere is usually comprised of a monoatomic inert gas, the Brownian motion

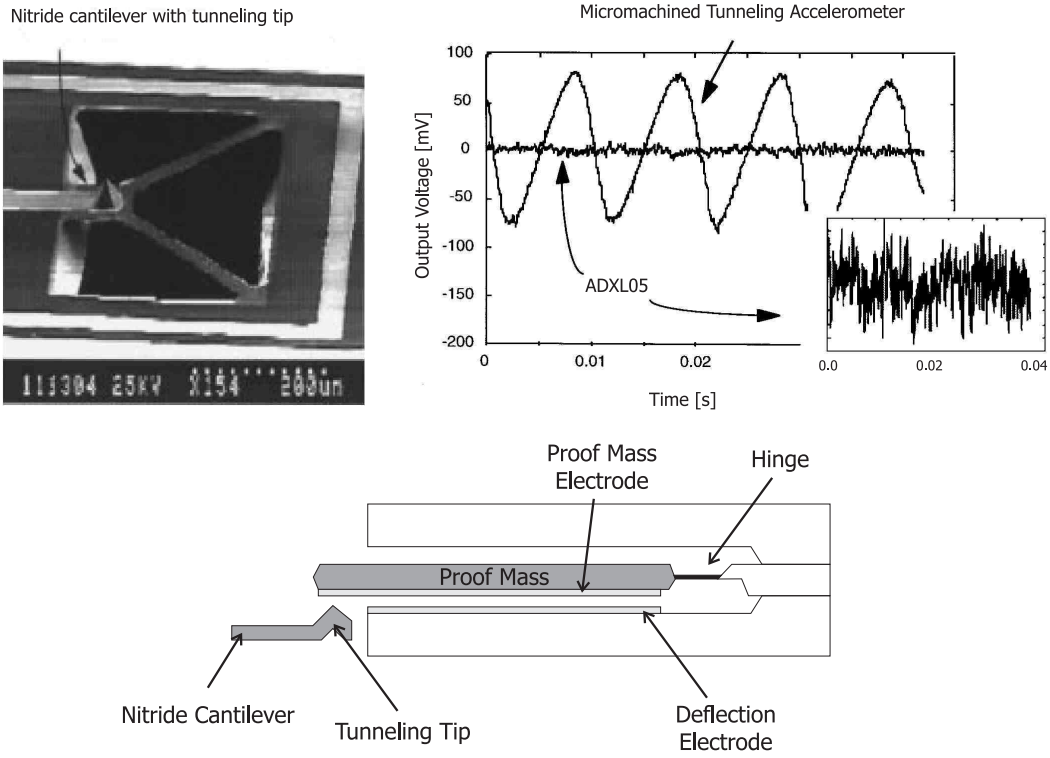

Figure 3.1. *Tunneling MEMS device overview and physical implementation. Adapted from [Liu-1998].*

of its constituents cause repeated random molecular impacts upon the MEMS proof mass, thus giving rise to an equivalent RMS acceleration noise a_b formulated as:

$$a_b = \sqrt{\frac{4k_bT\omega_0}{mQ}} \tag{3.2}$$

where:
k_b: indicates the proof mass retainer spring constant [N/m].
T: indicates absolute temperature [K].
ω_0: indicates MEMS element undamped resonance frequency [Hz].
m: signifies proof mass scale [kg].
Q: signifies mechanical quality factor of the MEMS element.

This fundamental expression clearly illustrates the possibility of controlling the sensor noise level by increasing the proof mass size and lowering the resonance frequency, provided the noise contribution from the on-chip conditioning circuitry remains negligible. Similarly the damping coefficient can be controlled by ventilating the proof mass or operating at reduced ambient pressures. Essentially, equation 3.2 constitutes a primary design driver for any

MEMS accelerometer, as a design compromise must always be negotiated between sensitivity, bandwidth and noise floor. Shown previously through the market analysis, it is clear that for MEMS linear accelerometers the market has segregated into two segments. The first emphasizes development towards the commercial segment trading device performance for physical size and mass, whereas the second targets achievable performance for precision applications and scientific observations (eg. seismic monitoring) at the expense of device physical envelope, bandwidth and power consumption. These observations are corroborated by a number of market analyses conducted over the last three years [Dixon-2006, Heeren-2007, Yole-2007, Chun-long-2009, Yole-2010], all of which also point to the likelihood of MEMS gyroscope technology maturing sufficiently over a five year period to reach tactical grade performance in accordance with the IEEE classification outlined in Table 3.4 on a broad scale.

	Performance Grades		
Parameter	**Inertial/Navigation**	**Tactical**	**Rate**
Input range [°/s]	>400	>500	50-1000
Scale factor accuracy [%]	$<10^{-3}$	0.01-0.1	0.1-1
Shock tolerance [g]	10^3	10^3-10^4	10^3
Angular random walk [$°/\sqrt{hr}$]	$<10^{-3}$	0.5-0.05	>0.5
Bias drift [°/hr]	$<10^{-2}$	0.1-10	10-1000

Table 3.4. *Gyroscope performance grade classification. (Sources [IEEE-2001] and [Wise-2006])*

3.1.1 Non-MEMS Inertial Sensors and Full Miniature IMUs

As in 2006, the present state of the non-MEMS segment of the inertial sensor market has also been assessed for the availability of sensors applicable to the μIRU augmentation. Performance-wise several technologies, including Dynamically Tuned Gyroscopes, Hemispherical Resonator Gyroscopes, Ring Laser Gyroscopes and Interferometric Fiber Optic Gyroscopes, are all known to deliver attitude resolution capabilities and short term stability levels on par with those of the μASC stellar reference sensor, and as was identified in the case of the KVH DSP-3000 IFOG, even with the required bandwidth. Market trends indicate some improvements primarily in terms of miniaturization of IFOGs [Buret-2006, Jerebets-2007], yet the relatively small number of applications requiring high performance gyroscopes as well as the prohibitively high unit pricing levels means development remains slow.

With regards to full IMU implementations, classical high performance units typically employ a combination of non-MEMS inertial sensors, thus render-

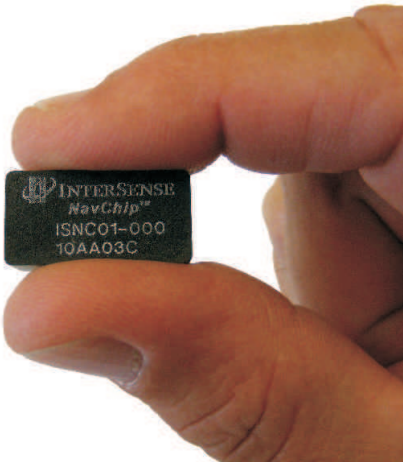

Navchip Specifications

Device Feature	Value
Acceleration Range	±11g
Angular Rate Range	$\pm 480^\circ/s$
Temperature Range	-40°C-85°C
Accelerometer noise density	$70\mu g/\sqrt{Hz}$
Gyroscope noise density	$0.004^\circ/s/\sqrt{Hz}$
Interface	SPI/UART
Max. Datarate	1000Hz
Bandwidth	200Hz
Supply voltage	3.25V - 5.5V
Power Consumption	120mW
Dimensions	24×12.8×8.3mm
Mass	6g

Figure 3.2. *InterSense NavChip integrated MEMS-based IMU. Image courtesy of [ISN-2010]*

ing them bulky and power consuming. However, recent advances in MEMS-technology have also had an impact on IMU design. Most recently this has been emphasized by InterSense commercializing the first fully integrated MEMS IMU with performance levels approaching tactical grade. From a μIRU augmentation perspective, however, the stand-alone chipscale IMU remains unapplicable due to physical size, power consumption and ITAR issues. Nevertheless it constitutes a promising harbinger on future developments in the MEMS inertial sector. Consequently, even though a number of non-MEMS inertial sensors and full IMUs meet the μIRU augmentation performance requirements, they fail on three key points, namely mass, volume and power consumption.

3.2 Sensor Candidate Selection

Despite four years of technological development having passed since the ST Microelectronics LIS2L02AL MEMS accelerometer was first made commercially available, and despite the fact that the device was discontinued as of January 2009, no miniature commercially available device has as of yet managed to surpass its combination of size, power consumption, environmental tolerance specification and performance with regards to output noise density. In particular the last parameter is vital for the μIRU augmentation, as it is directly determining for the achievable performance and angular resolving capability of the instrument.
Having successfully procured a full 400 piece batch of the LIS2L02AL accelerometers in mid-2008, the decision was made to continue development of the μIRU prototype baseline founded on this sensor pending completion of

device characterization testing.

LIS2L02AL MEMS Accelerometer Main Specifications					
Parameter	**Condition**	**Min Value**	**Nom. Value**	**Max Value**	**Unit**
Acceleration Range		±1.8	±2.0	min.	g
Scale Factor		V_{dd}/5-10%	V_{dd}/5	V_{dd}/5+10%	V/g
Scale Factor vs. Temperature	Δ from +25°C		±0.01		%/°C
Zero-g Level	@25°C	V_{dd}/2-6%	V_{dd}/2	V_{dd}/2+6%	V
Zero-g Level vs. Temperature	Δ from +25°C		±0.2		mg/°C
Non-Linearity	Best fit, ±2g		±0.3	±1.5	%
Cross-Axis Sensitivity			±2	±4	%
Noise Density	V_{dd}=3.3V		30		$\mu g/\sqrt{Hz}$
Supply Voltage		2.4	3.3	5.25	V
Supply Current	Mean value		0.85	1.5	mA
Output Impedance		80	110	140	kΩ
Operating Temperature Range		-40		85	°C
Shock Loading	for 0.5ms for 0.1ms			3000 10000	g g
ESD Protection	HBM MM CDM			2000 200 1500	V V V

Table 3.5. *LIS2L02AL main specifications as derived from [ST-2006]. Values specified at a supply voltage of V_{dd}=3.3V.*

The overall manufacturer specifications pertaining to the LIS2L02AL accelerometer are provided in Table 3.5 for reference. Full specifications are available from [ST-2006].

3.3 LIS2L02AL Sensor Candidate Characterization

Operations in space entail exposure to a number of environmentally conditioned stresses not normally included in the manufacturers characterization and qualification program for a newly developed COTS component. MEMS accelerometers are no exception to this paradigm, although the fact that they feature movable parts tends to warrant additional rigorous testing, particularly from a mechanical standpoint. As such, shock and vibration tolerances are extensively tested by the manufacturer, and most sensors are designed to provide nominal performance even after exposure to severe overload levels.
In all, however, considering COTS MEMS accelerometers for space applications necessitate a number of parametric characterizations beyond those provided by the manufacturer. In the context of this project, characterization tests of the LIS2L02AL MEMS accelerometer have been performed with respect to total ionizing dose tolerance, thermal scale factor sensitivity and long term bias stability. Moreover, destructive physical analysis (DPA) and X-ray

imaging has been employed to analyze the physical configuration of the sensor. These tests and evaluations are reported upon the in the subsequent sections.

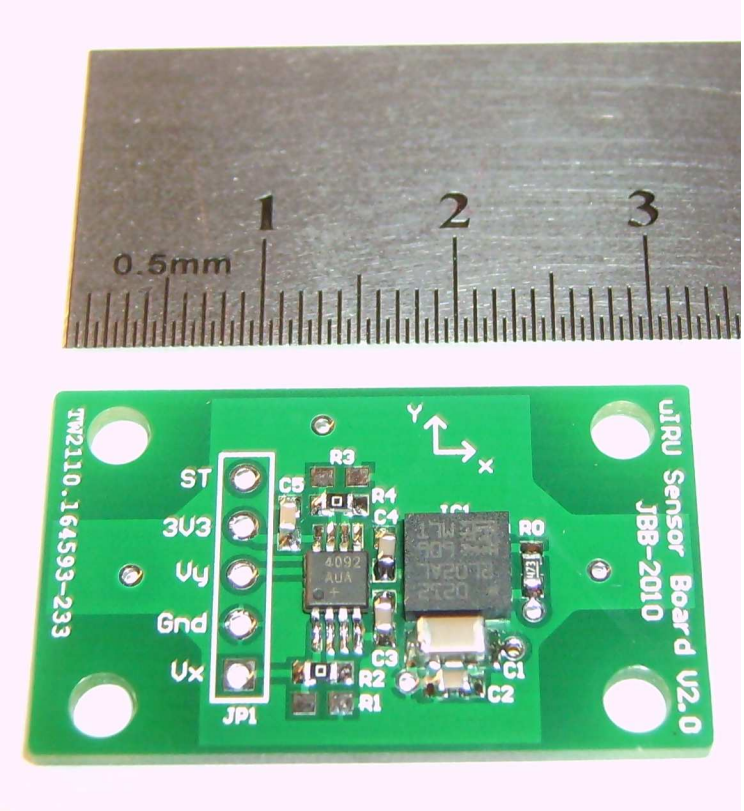

Figure 3.3. *LIS2L02AL sensor board for part characterization testing.*

The physical basis for the planned tests is an adaptation of the minimalistic sensor implementation depicted in Figure 3.3. Containing only the LIS2L02AL and the generic RC single pole anti-aliasing filter based upon the native output impedance of the sensor, the board is designed to provide a direct representation of the sensor outputs for testing purposes. The test results of the following sections shall as such be interpreted with the following proviso:

- All measurements are conducted for a nominal f_{3dB} bandwidth of $212Hz$ corresponding to each of the accelerometer outputs having been decoupled to ground using a 6.8nF NP0 ceramic capacitor
- All measurements are conducted with only the simple low pass filter formed by the accelerometer output impedance and the decoupling capacitor, thus retaining full integrity of the signal DC content.
- When powered, the accelerometer is supplied at 3.3V generated by an external high stability power supply.

- Decoupling is implemented at the sensor level by a 10uF capacitor in parallel with a 100nF capacitor. Both capacitors are ceramic of dielectrica X7R.
- The self-test pin of the LIS2L02AL is pulled to ground at the sensor level through a 47kΩ resistor

A full schematic of the LIS2L02AL sensor board and associated PCB layout is included as Appendix F.1, with the significant difference that the MAX4092AUA buffer stage is not mounted for the characterization tests.

3.3.1 Physical Inspection

Upon procurement of the first batch of LIS2L02AL MEMS accelerometers from ST Microelectronics in 2008, a physical inspection was conducted to determine the exact mechanical configuration of the sensor. The inspection was conducted on a single sensor in a staggered manner with the least invasive procedure applied first, namely the outer envelope inspection.

As Figure 3.4 depicts the sensor is designed as a fully monolithic device with a housing comprised of a hard epoxy resin compound measuring 5mm $\times$ 5mm $\times$ 1.6mm and weighing a total of $80{\cdot}10^{-3}$g. It features eight electrical interconnect pads on the bottom face which are not accessible from the sides of the device, thus it can be deduced that only reflow soldering will provide for proper mounting.

Through a series of X-ray images, some of which are depicted in Figure 3.5, the internal configuration of the device has been established. As view number two clearly illustrates, the LIS2L02AL accelerometer comprises two separate die structures within its packaging. The lower die structure (as measured along the Z-axis) actually consists of two stacked wafer segments, between which the surface micro machined MEMS element attached to the lower wafer is held in a sealed cavity. Presumably this arrangement is adopted to allow the device to operate in a monoatomic atmosphere for better noise performance and to provide mechanical isolation when the device housing is cast. The metallic seal between the two wafer segments is clearly visible as the denser rectangular feature in view number three. The upper die structure riding on top of the MEMS cavity is seen to connect with all bonding wires to the pads on the bottom of the device, hence indicating that all the signal processing and interface electronics are associated with this die. As indicated by the specifications of the part datasheet [ST-2006], both dies are implemented using conventional silicon processing techniques (bulk CMOS).

The final stage of the physical inspection procedure saw the component subjected to DPA and microscopy imaging. The CMOS signal processing die was destroyed in the process, but the particular point of interest for this procedure

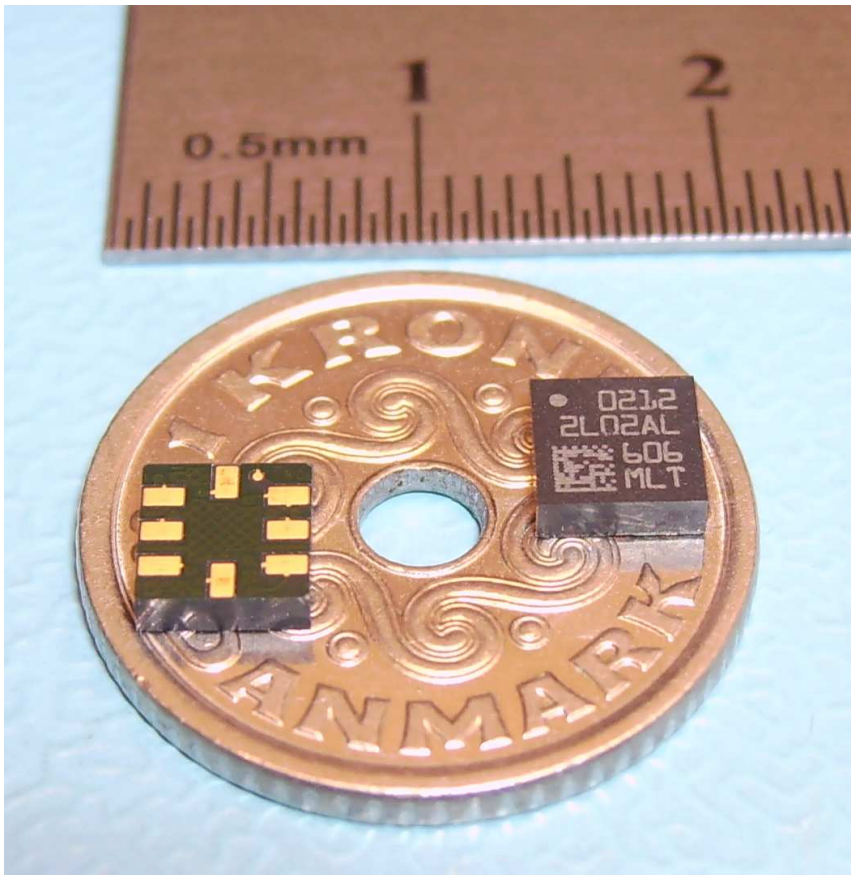

Figure 3.4. *The LIS2L02AL MEMS Accelerometer depicted in scale comparison with a danish "1-krone" coin.*

was to ascertain the configuration of the MEMS sensor element and its transduction principle, all of which can be derived from microscopy imaging of the cavity content. In the end the cavity was successfully dismantled and one of the acquired images has been included as Figure 3.6.
What can be inferred from the microscopy imaging are at least two significant points. Firstly, the two sensitive axis have their origins collocated to within the micromachining tolerances of the MEMS sensor element. This places the origo of the accelerometer at the exact center of MEMS sensor element, and constitutes an extremely important point, as it offers a significant simplification with regards to calibration of the μIRU implementation.
Secondly, the sensor element structure clearly reveals the transduction principle as being differential capacitive (the present de facto market standard for surface micromachined accelerometers found in more than 80% of COTS sensors [Bjarnoe-2007]), however with the significant difference of the sensor element and the capacitive pickoff electrodes being substantially larger than what is seen in other commercial devices [Bjarnoe-2007], which in turn serves to increase signal to noise ratio and reduce Brownian motion noise in accordance with equation 3.2.

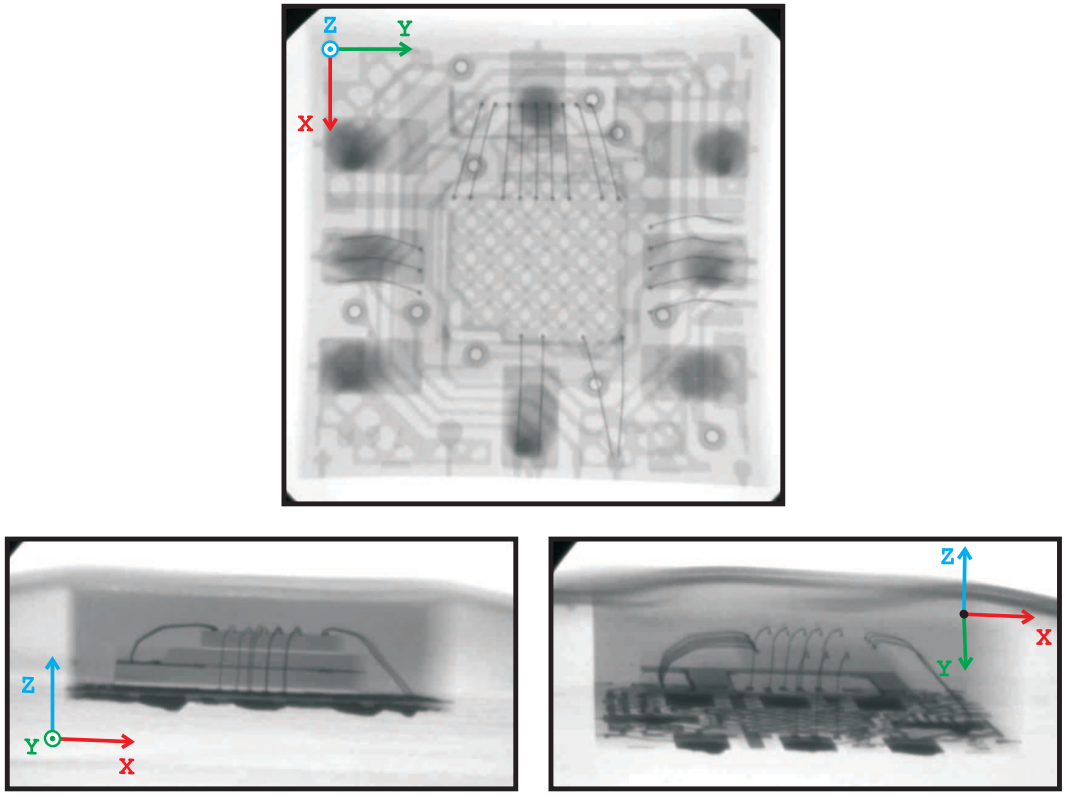

Figure 3.5. *LIS2L02AL X-ray imagery.*

The application technique of the differentially capacitive transduction principle in the LIS2L02AL sensor is illustrated by Figure 3.7. In addition to allowing both positive and negative accelerations to be measured, the differential capacitive structure accomplishes linearization about the balance point with the proof mass electrode equidistant from the sense electrodes [Senturia-2004]. When applying a voltage $\pm V_S$ across the capacitive bridge the output voltage V_O of the differential coupling becomes expressible as equation 3.3 when neglecting fringe effects:

$$V_O = \frac{C_1 - C_2}{C_1 + C_2} V_S \quad [V] \tag{3.3}$$

As the parallel plate capacitance is proportional to the spacing and assuming the electrode areas are equivalent this expression translates directly into:

$$V_O = \frac{d_1 - d_2}{d_1 + d_2} V_S \quad [V] \tag{3.4}$$

where:
d_1,d_2: signifies the spacing in the equivalent parallel plate capacitor [m].

With each capacitance $C1$ and $C2$ comprised of the parallel coupling between the individual differential pairs, values on the order of 10^{-14}-10^{-13}F can be

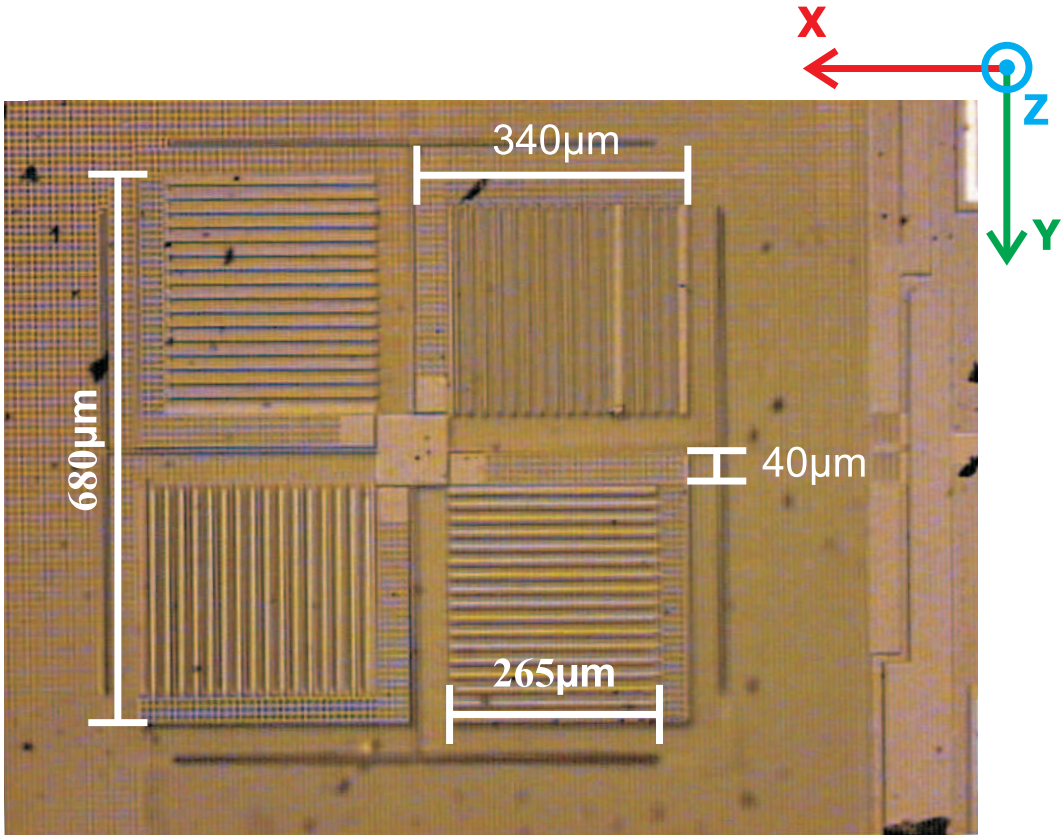

Figure 3.6. *LIS2L02AL MEMS sensor element microscopy image. Black specks seen on the image are debris from the cavity dismantling procedure.*

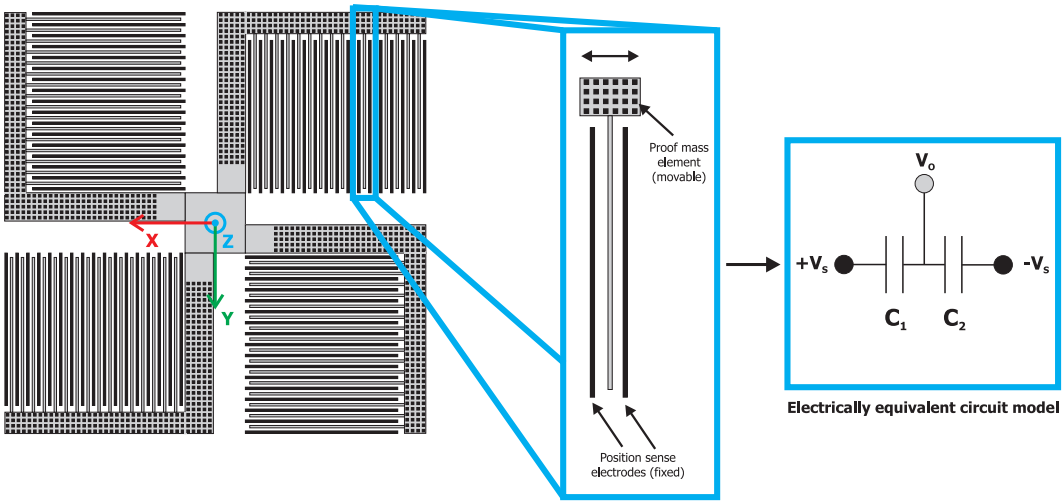

Figure 3.7. *LIS2L02AL MEMS element overview and electrical equivalent model.*

achieved [Bjarnoe-2007]. Equation 3.3 also indicates V_O scales linearly with V_S, yet achieving higher output voltages by increasing the capacitive bridge supply

voltage is usually not recommended as increased supply voltage also implies increased electrostatic disturbance of the proof mass. Naturally working with such small capacitance levels requires device level low noise signal conditioning techniques, and the commonplace solution is to implement correlated double sampling to reduce offsets and mitigate 1/f noise contributions, which is also the case in the LIS2L02AL as indicated by [ST-2006].

3.3.2 Sensor Linearity

A basic linear calibration model for the LIS2L02AL MEMS accelerometer is proposed by the manufacturer, where two measurements are performed with the accelerometer sensitive axis aligned with the gravity vector (V_{+g}) and in opposition to the gravity vector (V_{-g}). From these measurements the output bias B and scale factor S_f may be determined as:

$$B = \frac{V_{+g} + V_{-g}}{2} \quad [V] \tag{3.5}$$

$$S_f = \frac{V_{+g} - V_{-g}}{2g} \quad [V/g] \tag{3.6}$$

Which in turn allows the linear relationship between the accelerometer output voltage V_{out} and true gravity A to be expressed as equation 3.7.

$$V_{out} = S_f \cdot A + B \quad [V] \tag{3.7}$$

For these relations to be valid, perfect sensor linearity is implied. To investigate the validity of this simple linear model as proposed by the manufacturer, a linearity assessment is made through a series of rotations on a precision dividing head. The head employed constitutes the rotating base of a CNC milling machine capable of producing full 360° continuous rotations, or staggered positions with <18" absolute positional accuracy. The full rotations allow a single accelerometer axis to be exposed to the full ±1g of the Earths gravitational field and thus the linearity of nearly half its dynamic range of ±1.8g can be evaluated.

A number of minor uncertainties are associated with the linearity test setup, most of which relate directly to the operating tolerances of the CNC dividing head. Using precision instrumentation the latent misalignment of the X,Y plane of the CNC dividing head has been measured, and a total of 0.0126° in the -X axis and 0.0092° in the -Y direction corresponding to ±220μg and ±160μg error contributions for a full rotation, respectively, has been detected.

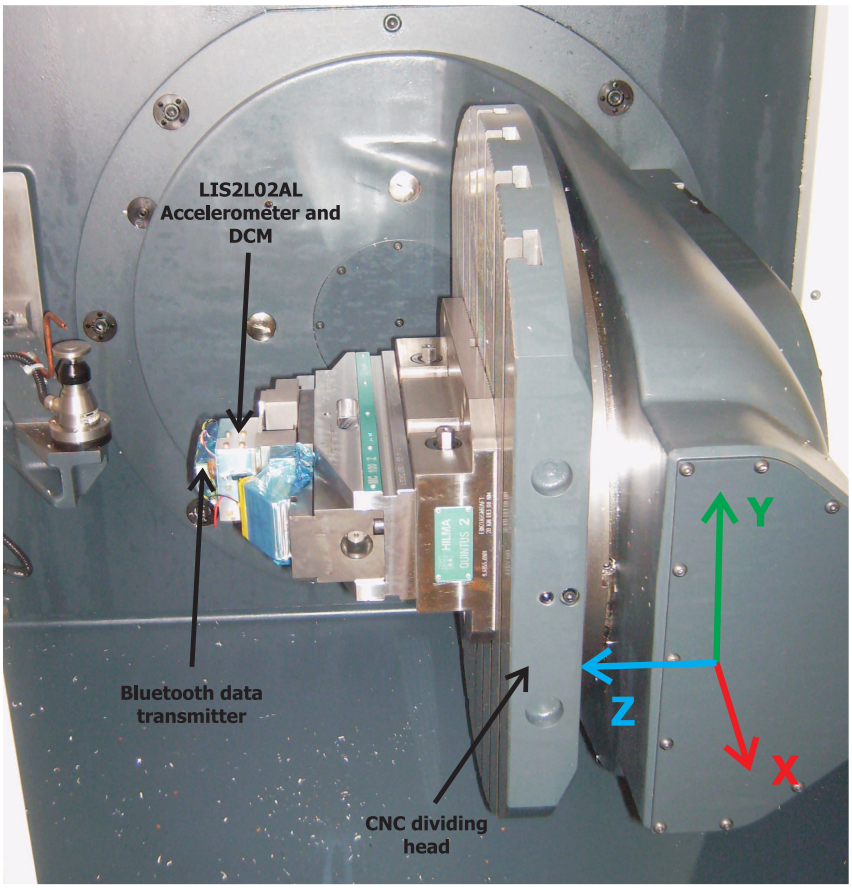

Figure 3.8. *LIS2L02AL MEMS Accelerometer linearity test setup.*

$$\begin{aligned} N_{1\sigma} &= N_d \cdot \sqrt{\frac{\pi}{2} f_{3dB}} \\ &= 30 \frac{\mu g}{Hz^{1/2}} \sqrt{\frac{\pi}{2} \cdot 212 Hz} \simeq 547 \mu g \end{aligned} \tag{3.8}$$

where:
N_d: signifies device output noise density [g/Hz$^{1/2}$].
f_{3dB}: signifies the anti-aliasing single pole filter 3dB cutoff frequency [Hz].

As these values are more than a factor of 2.4 less than the 1σ noise floor $N_{1\sigma}$ of the LIS2L02AL sensor as determined by equation 3.8 for a $212Hz$ nominal bandwidth, the precision of the CNC dividing head is considered sufficient to resolve all details of the sensor static acceleration response.

Using staggered operations at constant room temperature, a LIS2L02AL accelerometer with sensitive axes X and Y respectively aligned with the X and Z coordinate axes of the CNC dividing head (in reference to the coordinate

system introduced in Figure 3.8) is subjected to full 360° rotations in 20° steps. The accelerometer output data is digitized at 14bit resolution, 2.5V reference and the data transferred to a computer using the wireless ground support equipment (GSE) described in Section 5.7. At each rotation step roughly 2000 samples are acquired and the linearity assessment made based upon the mean and variance of the entire sample base at each rotational position step.

As Figure 3.9 illustrates the sensor response does indeed retain a degree of linearity consistent with the manufacturers nominal specification of ±0.3% over a full scale range of ±2g corresponding to $12mg$ or $7.92mV$ for a nominal device scale factor of $660mV/g$. Moreover, it is clear that the Y axis of the accelerometer is not perfectly aligned with the rotational axis Z of the CNC dividing head, thus giving rise to a residual acceleration along sensor Y, as sensor X goes through the full motion. This misalignment is a product of misalignment of the sensor die as well as misalignment of the PCB mounting. However, upon closer inspection of the residuals between a rotation from +1g to -1g and one from -1g to +1g of sensor X, it is clear that there is in fact measurable hysteresis in the sensor output.

Furthermore, it is interesting to note that the same hysteresis magnitude is present in both sensor X and sensor Y with similar distribution, thus indicating that the hysteresis phenomena does not exhibit input signal amplitude proportionality between X and Y, but rather between X and Z as well as Y and Z, with sensor Z being the inert non-sensitive axis of the accelerometer. Considering again the physical structure of the sensor MEMS element as depicted in Figure 3.6, the notion of a Z axis cross coupling with X and Y could have merit, as Z-axis acceleration will torque the capacitive sensing fingers of the MEMS element out of the plane thus potentially giving rise to a response non-linearity or at least a contribution to the device composite error. In all, the observed hysteresis is likely a composite error including contributions from material non-linearity, cross-axis sensitivity and anisotropic elasticity, yet distinguishing these effects will not be possible without specialized instrumentation and detailed fabrication specifications.
From literature it is known that in experience MEMS accelerometers, and in particular multi-axis devices, show hysteretic behavior. [Lawrence-2001] quantifies the phenomena and [Ang-2003, Ang-2004] reports on using phenomenological modeling to derive a non-linear equivalent to equation 3.7 for an Analog Devices ADXL203 two-axis accelerometer, where scale factor and bias for the X-axis are modeled as functions of Y and Z output voltages. To succeed in this approach a second orthogonally oriented accelerometer is included to provide the Z-axis measurement. It should, however, be noted that even though the ADXL203 specifications are very similar to those of the LIS2L02AL, hysteresis error reported by [Ang-2003, Ang-2004] for the former exceeds $60mV$.

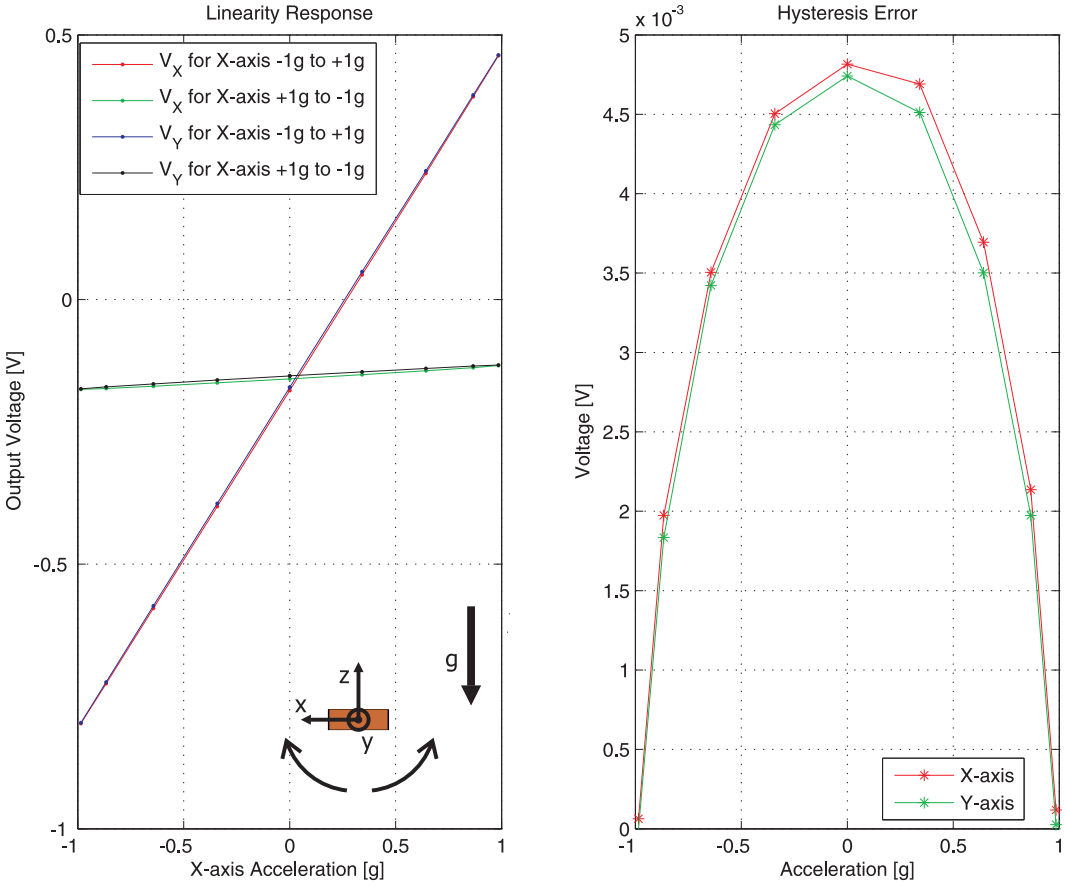

Figure 3.9. *LIS2L02AL output test. Device rotated about Y-axis in 20? steps. Note that the hysteresis error magnitude is calculated as the absolute difference between readings at identical rotation angles, but with different rotation directions.*

3.3.3 Sensor Thermal Stability

Trusting the LIS2L02AL to provide accurate measurements over a large temperature span, necessitates knowledge of the output scale factor and bias drift as a function of temperature. Outlined in Table 3.5, ST Microelectronics specifies a $\pm 0.01\%/°C$ variation of the scale factor, as well as a $\pm 0.2mg/°C$ variation of the bias, both tabulated as deltas from $+25°C$ operation. However, considering the extensive temperature span that can covered by a spacecraft under operation, dedicated temperature testing has been attempted to derive a device thermal sensitivity model, which will allow signal compensation as part of the data processing.

To determine the output scale factor the introduction of calibrated force is a necessity. However, doing so while significantly varying the device temperature precludes performing this test using an ordinary thermal chamber as the vibration levels from associated fans and compressor pumping systems intro-

duce far to much noise in the measurement for the thermal influence to be clearly discernible. As such, a method has been devised where a purpose built passive thermal chamber provides for testing to occur within the span from $\sim 0°C$ to $\sim 60°C$.

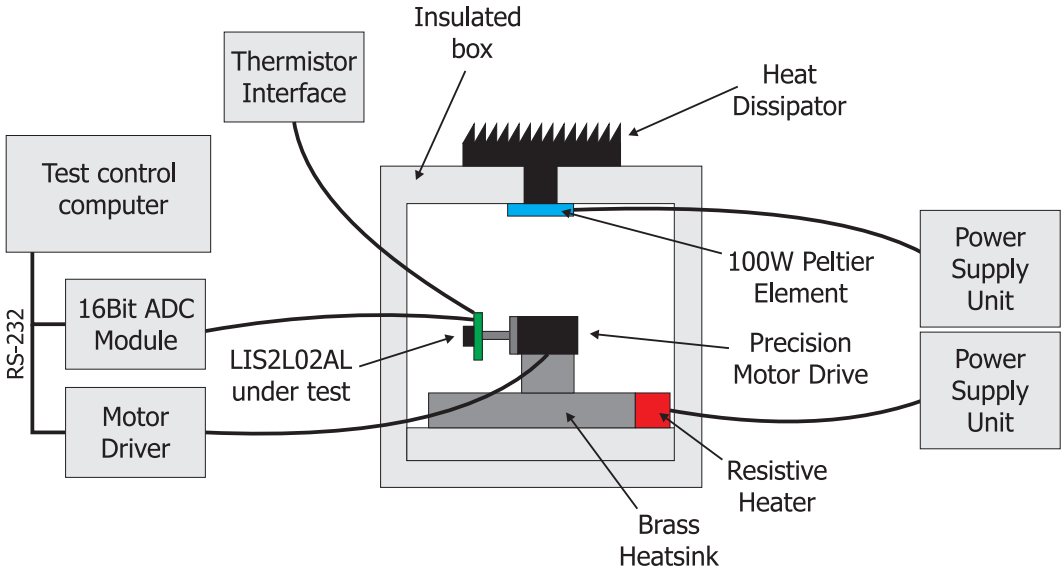

Figure 3.10. *LIS2L02AL scale factor vs. temperature characterization setup.*

Schematized in Figure 3.10 the setup uses a combination of resistive heating and passive Peltier cooling to establish a steady temperature gradient within the isolated box. At the height at which the accelerometer is suspended, testing has shown the gradient to be stable to within 0.3°C for the duration of a test run. The accelerometer board is mounted to a purpose built precision dividing head actuated by a high resolution stepper motor. In all the dividing head assembly offers 25600 steps for a full rotation corresponding to an angular resolution of 0.01406°/step or 50.625"/step.

The accelerometer output scale factor response to temperature is then derived by performing a series of >360° stepwise rotations at different ambient temperatures. To ensure thermalization of the sensor prior to conducting the test, the accelerometer is allowed to soak for ∼6 hours prior to test commencement once a new equilibrium temperature has been ascertained. In all a full rotation is conducted in 28 equally sized steps, first in a clockwise (CW) direction and secondly in a counter-clockwise (CCW) direction. This profile has been adopted in lieu of the linearity performance derived in Section 3.3.2. Subsequently the acquired test data is segmented into clockwise and counterclockwise rotations, each of which are treated individually.

Figures 3.11 and 3.12 show clockwise rotation responses for X and Y for eight individual rotations conducted at different temperatures as outlined in Table

Rotation #	Direction	Temp. [°C]	Rotation #	Direction	Temp. [°C]
1	CW	20.6	15	CW	31.1
2	CCW	20.7	16	CCW	31.4
5	CW	5.7	17	CW	55.2
6	CCW	6.0	18	CCW	56.0
9	CW	41.4	19	CW	1.7
10	CCW	42.4	20	CCW	1.9
13	CW	1.4	21	CW	8.4
14	CCW	1.7	22	CCW	9.0

Table 3.6. *Measured temperatures for test rotation segments.*

3.6. Note that counter-clockwise rotation responses have been omitted from the graphs (but not from the calculations) to enhance visibility.

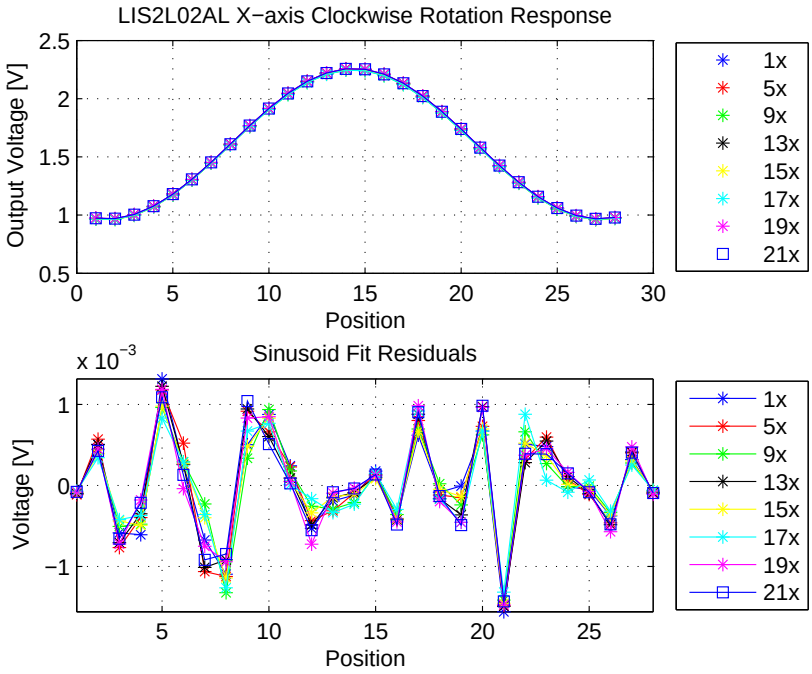

Figure 3.11. *LIS2L02AL scale factor vs. temperature characterization, X-axis clockwise rotation response.*

To assess the output scale factor and bias at each discrete temperature level a sinusoid fit is imposed upon the discrete data points pertaining to each rotation series with the residuals shown. In an effort to study the susceptibility of this analysis to the hysteresis issue previously identified, the analysis has been conducted differentially by separating CW and CCW data.
Under the assumption that mechanical invariability has been ascertained under

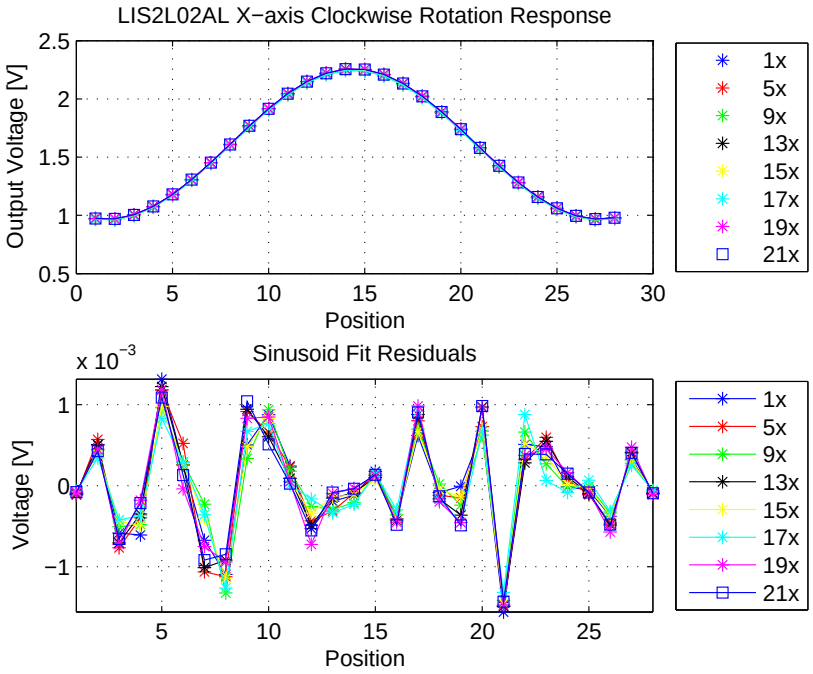

Figure 3.12. *LIS2L02AL scale factor vs. temperature characterization, Y-axis clockwise rotation response.*

all applied rotations, the one remaining limitation of the test setup is the inability to verify perfect alignment with the gravity vector, and thus to deduce the exact gravitational acceleration the sensor sees at a given rotation angle. As such, misalignments within the sensor and of the mechanical actuator platform fails to ensure that the accelerometer is exposed to the full scale $\pm 1g$ when subjected to a full rotation. Had this been the case, the extraction of bias and scale factor could have been optimized using a direct linear least squares solution incorporating the entire acquired dataset. This approach would entail formulating equation 3.7 in matrix form for N measurements:

$$\begin{aligned} & V_{out} = S_f \cdot A + B \\ \Rightarrow \quad & \mathbf{V} = M\mathbf{x} \\ \Rightarrow \quad & \begin{bmatrix} V_{out,1} \\ \vdots \\ V_{out,N} \end{bmatrix} = \begin{bmatrix} A_1 & 1 \\ \vdots & \vdots \\ A_N & 1 \end{bmatrix} \begin{bmatrix} S_f \\ B \end{bmatrix} \\ & Nx1 \quad = \quad Nx2 \quad 2x1 \end{aligned} \tag{3.9}$$

the solution of which may be approximated by

$$\begin{bmatrix} S_f \\ B \end{bmatrix} = (M^T M)^{-1} M^T \mathbf{V} \tag{3.10}$$

However, in the absence of perfect alignment, the thermal effects on bias and scale factor can still be assessed in a relative rather than absolute manner. As such, using the manufacturer linear model which expresses scale factor S_f and bias B magnitudes as previously introduced in equations 3.6 and 3.5 the relative thermal responses may be derived. The results hereof are included as Figures 3.13 and 3.14, where the data has been normalized as percentage deviations from a nominal operating temperature of $+25°C$.

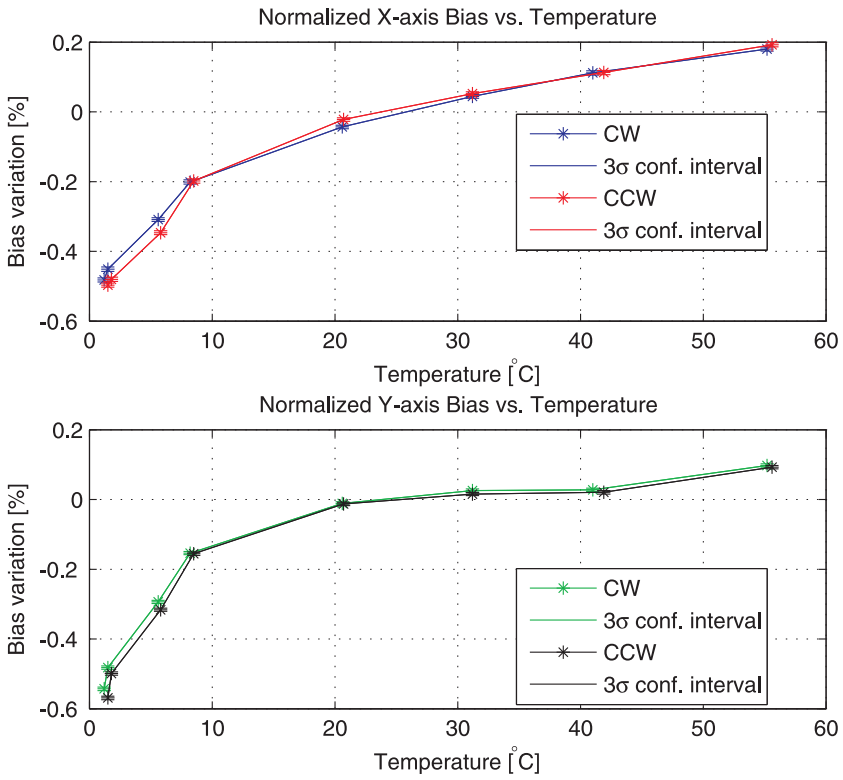

Figure 3.13. *LIS2L02AL bias response over temperature. Scale is normalized percentage deviation from 25°C value.*

It is clear that this method represents a viable means of modeling bias and scale factor thermal drifts, and could be directly applied to extract a similar model for the μIRU instrument. However, if applied to the calibrated μIRU, the availability of orthogonalized sensor triads should be harness to obtain an optimal solution in the least squares sense for the entire dataset.

3.3.4 Output Stability and Noise Performance

Long term stability is one of the key parametrization factors when comparing precision inertial instrumentation for use in navigation applications. For instance one such application could be submarine navigation where inertial

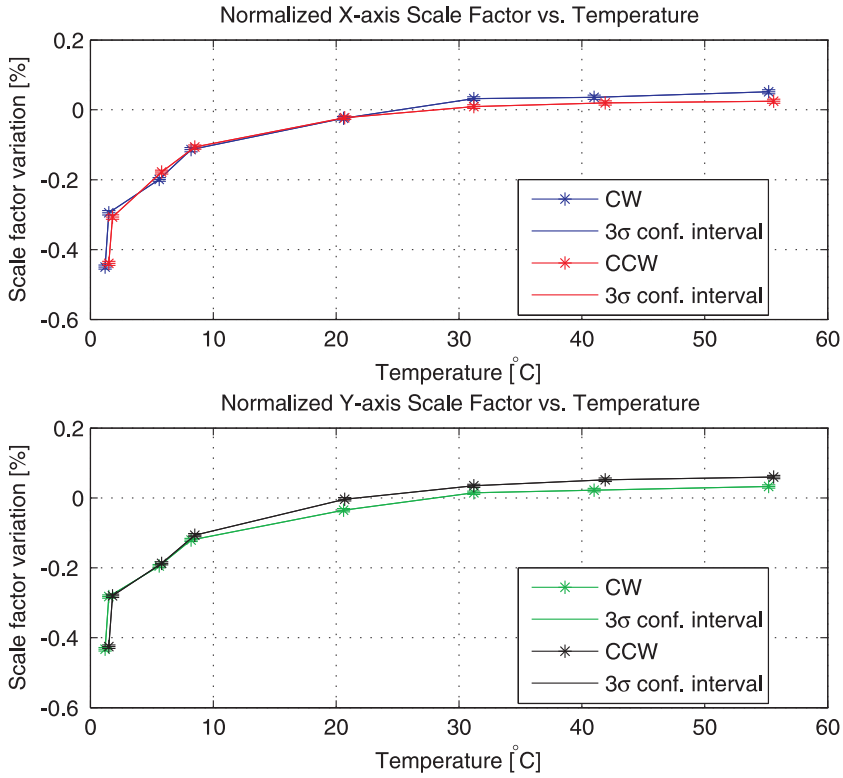

Figure 3.14. *LIS2L02AL scale factor response over temperature. Scale is normalized percentage deviation from 25°C value.*

navigation often remains the only means of attitude determination for submerged operations. In this environment the DC response and bias stability of the inertial sensors are of absolute criticality, as any parametric drift will severely impact the navigation solution when the position and attitude is derived by integration. To accurately characterize these performance aspects for the LIS2L02AL accelerometer a long term static test has been conducted. By acquiring continuous measurements from the accelerometer over a period of several hours at full sampling rate allows not only long term output stability but also noise DC and AC noise characteristics to be analyzed.

Figure 3.15 depicts a compounding of >35.5 million data points (decimated by a factor of 10^4 to enhance visibility) collected at 1096Hz for each of the two accelerometer axes. Note that the data has been detrended and converted to acceleration in units of g using a the nominal device scale factor of $660mV/g$, thus allowing for direct comparison of both axes. The data is acquired directly from powerup of the accelerometer, and both clearly exhibit a long term non-stationary tendency with the Y-axis mean increasing and the X-axis mean decreasing slightly over time. Possible explanations for this trend could be long term settling behavior, self-heating, bias drift or a combination hereof.

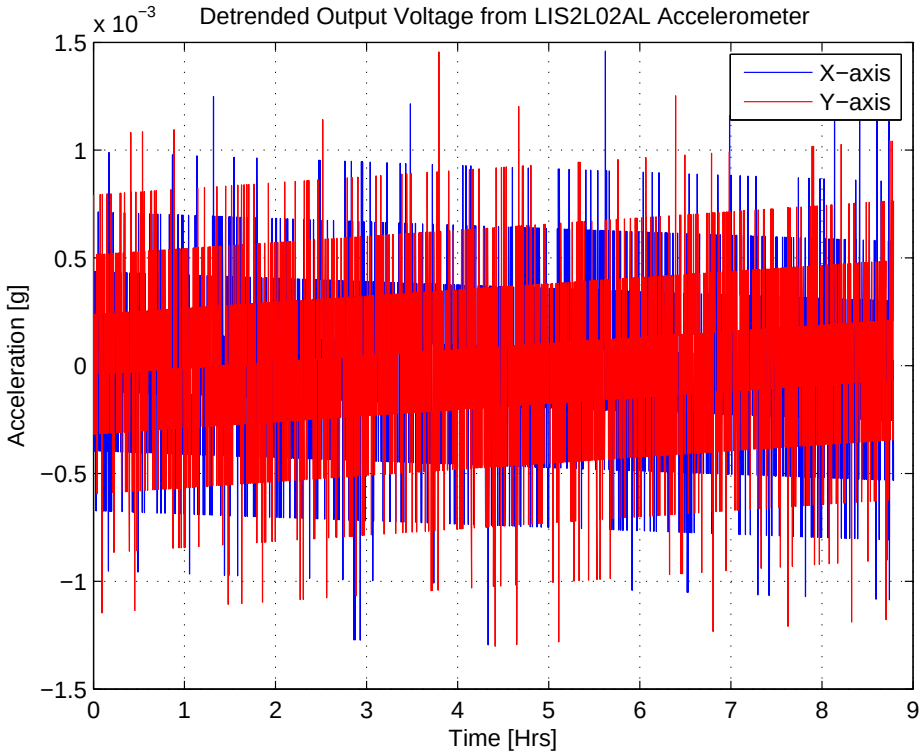

Figure 3.15. *Detrended long duration time series from LIS2L02AL MEMS accelerometer. Data acquired from a static device oriented with its Y axis aligned in opposition to the gravity vector. Data converted at* $1096Hz$ *in* $14Bit$ *resolution with a* $3.0V$ *reference, and represented with a decimation factor of* 10^4 *to enhance visibility. Nominal scale factor of* $660mV/g$ *used for unit conversion. The accelerometer outputs are fitted with the standard* $f_{3dB} = 212Hz$ *single-pole anti-aliasing filter for the test.*

The standard approach to characterizing the distribution of sensor noise over frequency would be the calculation of the power spectral density (PSD) of the time series. Figure 3.16 provides that particular calculation for each of the sensor output time series included in Figure 3.15. The PSD profiles clearly show the efficiency with which the CDS sampling system of the sensor suppresses 1/f noise present in the output, as the noise floor from $\sim 1Hz$ to the Nyquist frequency retains a reasonably flat white noise character. Below $\sim 1Hz$ the PSD profile for both axes show a distinct 1/f characteristic extending into the DC range.

Using the PSD estimates it is also possible to estimate the total output RMS noise over the time series frequency span, which in turn may be compared directly with the manufacturers noise density specification. Through integration of the PSD data presented in Figure 3.16 over the acquisition frequency bandwidth, the RMS noise pertaining to each axis is determined to be:

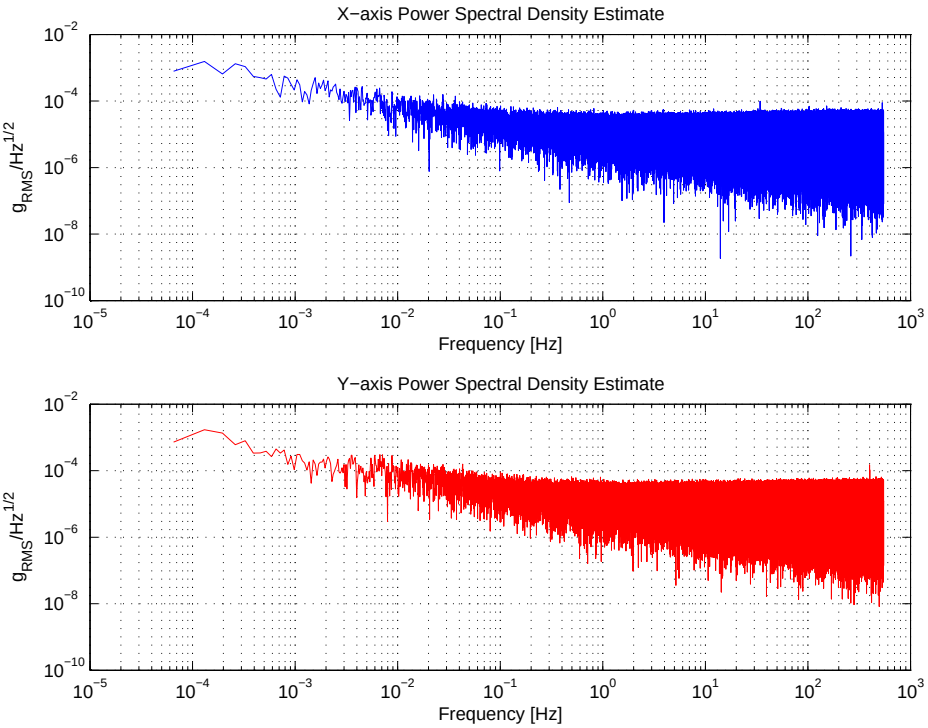

Figure 3.16. *LIS2L02AL power spectral density estimates for X- and Y-axis outputs sampled at 1096Hz.*

$$N_{X,RMS} = 396.1 \cdot 10^{-6}\, g \tag{3.11}$$
$$N_{Y,RMS} = 411.4 \cdot 10^{-6}\, g \tag{3.12}$$

It is worth noting that these experimentally acquired values constitute marked improvements over the theoretical expectation value of 547μg as previously determined from the manufacturer specifications by equation 3.8 for the same bandwidth. It is clear however, that the PSD alone does not provide sufficient information to fully account for the physical nature of the noise improvements with respect to the manufacturer performance specification, as well as the longer term variations seen in the raw data. To gain an understanding of these sensor idiosyncrasies beyond what can be gathered from the detrended raw data and the associated PSDs, the concept of Allen variance is employed. For the reader unfamiliar with Allen variance computation and its extension to inertial sensor time-series stability analysis, a short review of the method is provided in Appendix A.

Through Allen variance analysis, it is possible to distinguish the character of the latent random processes that give rise to the noise present in a measurement

time series. By calculating the overlapping Allen deviation pertaining to each of the sensor outputs the graphs of Figure 3.17 have been formed for the first 0.5 million samples of the data set acquired at 1096Hz.

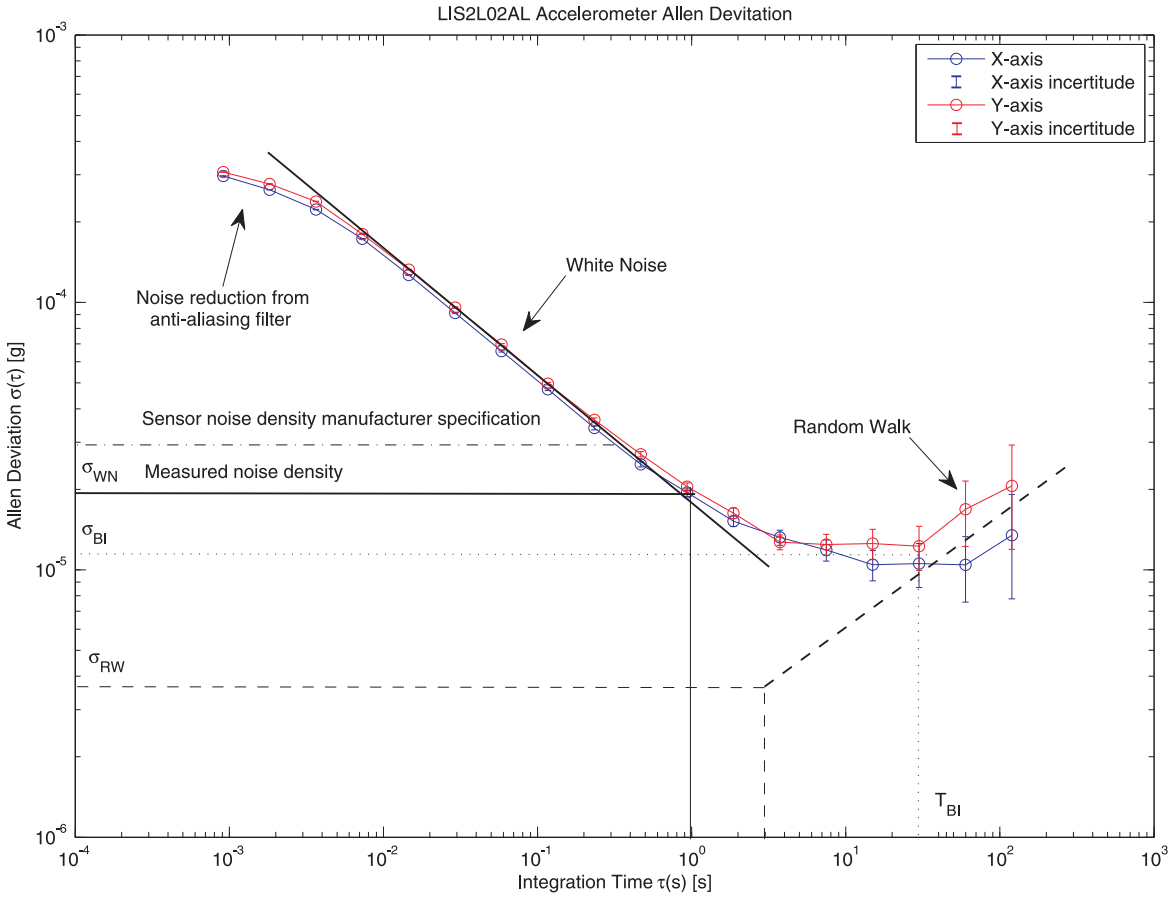

Figure 3.17. *Allen deviation calculated for LIS2L02AL X and Y axis outputs.*

The asymptotic behavior that can be derived from the Allen deviation data indicate the presence of two major noise contributers for both accelerometer axes, namely white noise and random walk as identified by the -1/2 and +1/2 slopes in the Allen deviation chart. Specifically the absence of a quantization noise contribution indicates that the sampling resolution has been sufficient, and it is as such evident that the characterization setup is adequate in assessing device performance. Equally significant, the sensor noise density may be read directly from the curve at $\tau = 1s$ as $n_d \simeq 20\mu g/\sqrt{Hz}$ which constitutes a significant 33% reduction over the manufacturer specification. Similarly, the optimal integration time T_{BI} in terms of bias instability may be estimated from the segment of the deviation plot with a slope of 0. From here an optimal integration time of $T_{BI} \simeq 30s$ and the corresponding optimal noise performance of $18.5\mu g/\sqrt{Hz}$ for the Y-axis, indicate that averaging the static data over longer intervals than T_{BI} will result in suboptimal performance due to bias drift/random walk of the sensor. Finally another interesting detail that can

be derived from the Allen deviation chart is the noise shaping influence of the anti-aliasing filter at higher frequencies (shorter integration times). The noise performance estimates for the LIS2L02AL accelerometer as derived from the Allen deviation chart in Figure 3.17 have been tabulated in Table 3.7.

Accelerometer	White Noise	Bias Instability		Random Walk
$[\mu g/\sqrt{Hz}]$	σ_{WN}	T_{BI}[s]	σ_{BI}	σ_{RW}
X-axis	18.98±0.66	60	15.70±4.30	3.0±1.1
Y-axis	20.46±0.66	30	18.46±3.45	4.3±1.6
STM Spec.	30	-	-	-

Table 3.7. *Noise parameter estimation for the dual channel LIS2L02AL accelerometer using Allen variance analysis.*

The Allen variance is used as a primary figure of merit for both the LIS2L02AL sensor and the μIRU prototype instrument, as it provides direct insight into the achieved quality of the sampling system and the noise processes present in the data. Obtaining the detailed noise parametric representation pertaining to the μIRU system also has added benefits. For instance if applied to Kalman filter design, the amplitudes of random walk/white noise terms as determined by the Allen variance analysis can be utilized directly in forming the elements of the process noise covariance matrix pertaining to the sensors.

3.3.5 Irradiation Screening

Final ratification of the selection of the LIS2L02AL MEMS accelerometer as the primary sensor for the μIRU augmentation is pending successful completion of irradiation testing for the procured batch. Being a COTS component, the accelerometers have not been designed for operations in irradiating environments, and no specific steps have been taken by the manufacturer to emphasize radiation hardening in the design process. For co-integration with the μASC CHU, however, stringent irradiation tolerance requirements are imposed. The CHU will often be situated near or on the outer surface of the spacecraft as it needs to maintain a clear view of the firmament. As such, the structure of the spacecraft does not necessarily provide much shielding in addition to what is already provided by the CHU titanium structure and gold inserts, thus potentially exposing the electronics housed inside to significant amounts of ionizing radiation. To ensure functional and performance compliance over instrument lifetime, the electronic circuits of the CHU have been designed using mainly up-screened COTS parts with significant Total Ionizing Dose (TID) tolerance levels, all adhering to a 30krad minimum requirement [SIG-2006b].

Part	Function	Numbers used	TID Test Level [krad]
CXD1261AR	Timing gen.	1	>40
CXD1267AN	Vert. driver	1	>40
MAX4452	Opamp	2	>50
CXA1439M	CDS	1	>40
CD74HC04M	Hex inverter	1	>40
ICX039DLA-6	CCD sensor	1	10
BAT54S	Schottky diode	1	>40
BFT92	PNP transistor	1	>170
BFR92	NPN transistor	2	>40
BAV99W	Silicon diode	1	>40

Table 3.8. *μASC CHU parts TID tolerance levels [Joergensen-2009].*

As outlined by Table 3.8 only the CCD sensor features a TID tolerance below 40krad[1], and the selected μIRU parts are expected to show similar performance so as to not impose additional restrictions upon the environmental tolerances of the μASC instrument. Verifying that the primary accelerometer sensor candidate for the μIRU is in fact compliant with these specifications thus become a primary design driver and a necessary prerequisite for its selection. As such, a TID screening test using energetic electrons has been conducted as a go/no go evaluation of employing the LIS2L02AL MEMS accelerometer in the μIRU augmentation prototype design.

3.3.5.1 Test Setup

The test is based upon operating the LIS2L02AL in a static setup under irradiation from a Strontium-90 isotope source with a half life of 28.90 years. The specific source used for this test is designated as SR-0 and is the weakest of the four β sources located at the DTU Space radiation test facility, producing a dose rate of 0.1 rad/s in a circular swath with radius 30mm at a calibrated target distance from the source.

The dose depth characteristic associated with the source has been previously calibrated and allows the level of attenuation/shielding offered by the component packaging to be determined, thus providing a better estimate of the actual TID delivered to the device die. As illustrated by Figure 3.18 the LIS2L02AL epoxy housing provides an attentuation ratio of approximately 24%[2]

[1] Consequently the CHU mechanical design features additional spot shielding around the CCD to achieve an effective TID tolerance level comparable to those of the other CHU parts.

[2] Determined by using $\rho_{epoxy} = 1.85 g/cm^3$ for the package material and $d_{epoxy} = 0.85 mm$ for the package thickness. The latter is derived from the X-ray images of Figure 3.5.

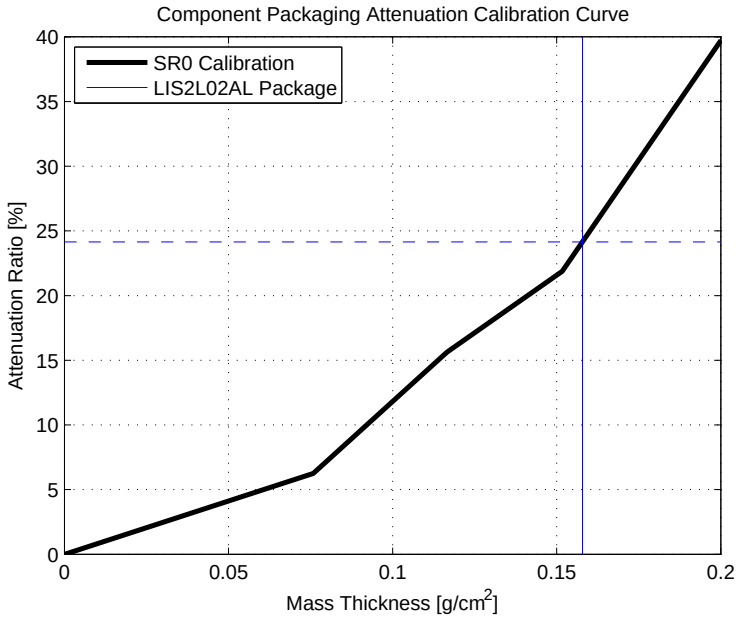

Figure 3.18. *Epoxy component packaging attenuation profile for SR-0 source.*

The test setup used for the irradiation screening procedure of the LIS2L02AL accelerometer is schematized in Figure 3.19. A single computer is used to control the sampling process and collect voltage, current and temperature level measurements via a GPIB bus as well as accelerometer output voltage data via a RS-232 interface. The latter data points are initially sampled by a PIC18 microcontroller through two identical 16Bit SAR A/D converters, and each data point delivered to the control computer is obtained as the average of 50 samples.

As the irradiation test fixture precludes any possibility of introducing calibrated force to the accelerometer under test, no assessment of the accelerometer output scale factor versus accumulated dose can be made directly. Instead a methodology has been devised which allows the self-test excitation feature of the LIS2L02AL accelerometer to be used as a means of realizing a crude Correlated Double Sampling (CDS) system, thus emulating stepwise mechanical excitation of the accelerometer along both sensitive axes.

Using the PIC18 microcontroller to operate the self test feature of the accelerometer in the manner indicated by Figure 3.20, induces a physical displacement of the sensor proof mass by electrostatic forcing, thus effectuating a change in output voltage similar to that encountered through external force stimuli. For the DC measurements, having both the reference and excitation level measurements allows the product of the excitation magnitude a_{exite} and the device sensitivity s_a (hereinafter denoted as the SE-product) to be determined independently of any bias shift in the reference level. This relationship is illustrated by equations 3.13 and 3.14.

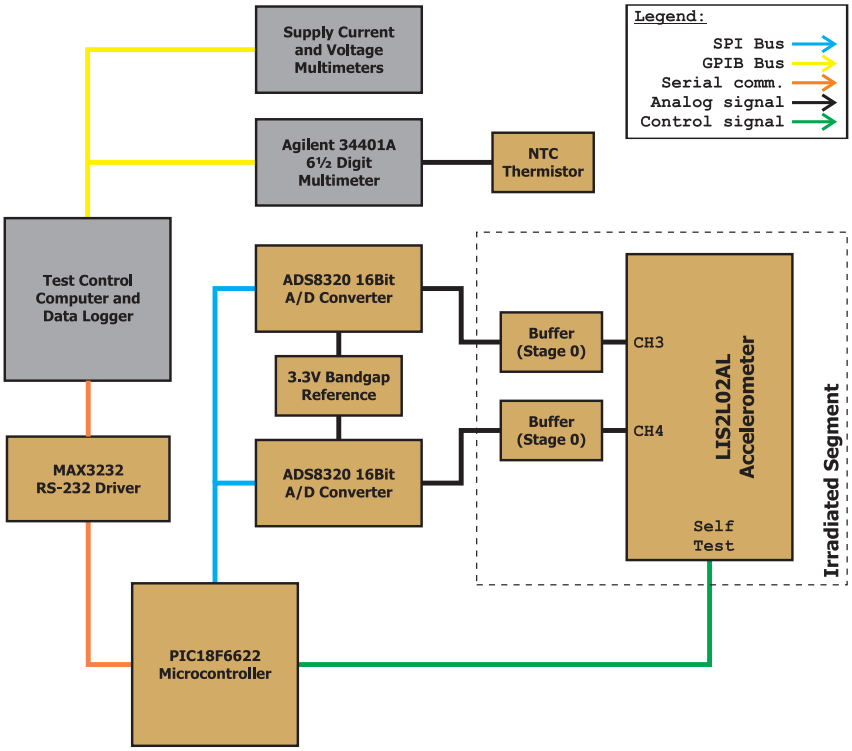

Figure 3.19. *LIS2L02AL MEMS accelerometer irradiation test setup configuration.*

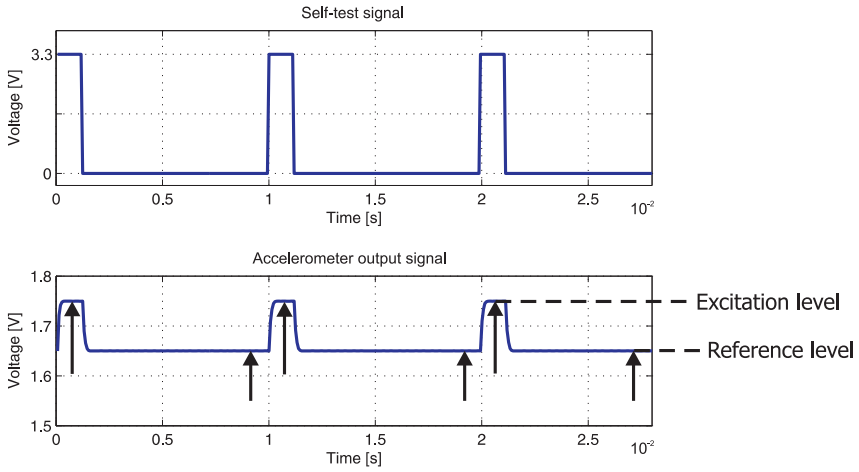

Figure 3.20. *Accelerometer CDS sampling concept. Sample instances are indicated by black arrows.*

$$V_{ref} = s_a g + V_{bias} \tag{3.13}$$

$$V_{exite} = s_a(g + a_{exite}(t)) + V_{bias} \tag{3.14}$$

$$\Rightarrow V_{DCexite} - V_{DCref} = s_a a_{exite}(t)$$

where:
g: signifies residual gravitational acceleration [m/s^2].
s_a: signifies device output sensitivity [mV/g].
V_{bias}: signifies device output bias voltage [V].
$a_{exite}(t)$: signifies the timevarying excitation equivalent acceleration [m/s^2].

It should be noted that the method allows no separation of the excitation amplitude and the device output scale factor and as such, the SE-product is used as the primary figure of merit for the accelerometer over the TID exposure. Also the temporal dispersion between the reference and excitation sample instances may allow short term vibrations to affect the signal levels, hence every attempt should be made to ensure that the test environment is as quiet as possible.

3.3.5.2 Results

Overall the irradiation test of the LIS2L02AL MEMS accelerometer progressed nominally with a total dose of 42.9krad delivered to the device die. As the test was conducted during the holiday season, external disturbances incurred by the regular use of the irradiation facilities where limited to two occurrences of other people working in the room. The mechanical disturbances associated with this remain largely undiscernable in the accelerometer data, but are visible in the temperature data, as the short term ambient room temperature has been slightly affected. Each of these occurrences have been highlighted by black arrows in Figure 3.21.

What the primary data illustrates is minimal variations in supply voltage level and device temperature over the course of the test. Moreover, the current consumption and accelerometer output data profiles show little correlation with either of the external parameters, hence the variations seen in both accelerometer outputs must be attributed to either long term bias variations or TID effects. Using the CDS technique, the exact nature of these variations may be understood.

The excitation levels and derived SE-product for accelerometer axes X and Y are presented as Figures 3.22 and 3.23, respectively. The data clearly illustrates how the SE-product remains nearly constant throughout the test. Only the Y-axis SE-product exhibits what appears to be settling behavior for the first $\sim$10% of the exposure, yet this is not reflected in the variance levels where the X-axis SE-product ($\sigma_{SE,X} = 8.8 \cdot 10^{-8} V$) remains slightly higher than that pertaining to the Y-axis ($\sigma_{SE,Y} = 6.3 \cdot 10^{-8} V$).

By means of linear regression analysis, the linear fit residuals for the SE-products of the two axes are also provided. In both instances their values are

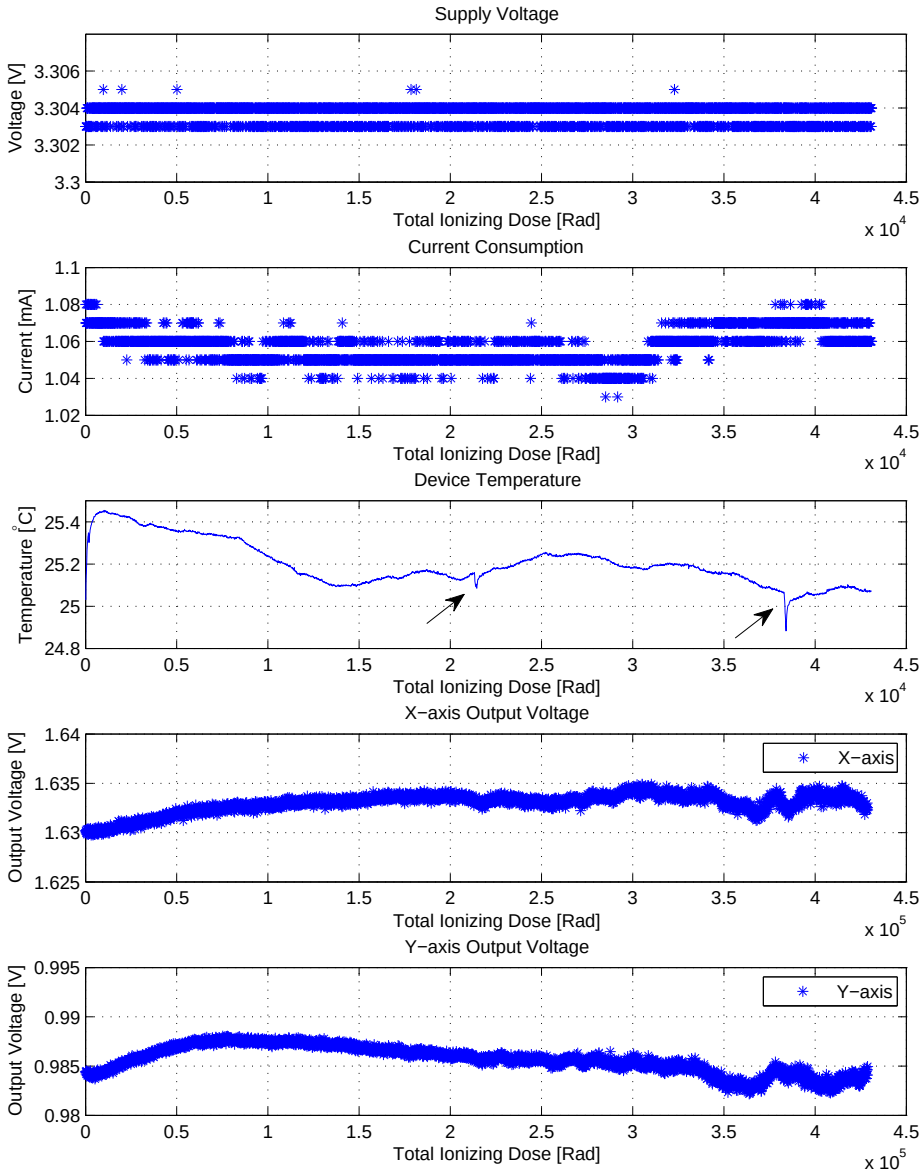

Figure 3.21. *LIS2L02AL irradiation test results - primary data.*

all found to be below ±1mV, which is consistent with the device noise floor in the tested configuration. For this test the accelerometer outputs are fitted with single pole stage 0 filters (described in greater detail in Section 4.7.1) providing a nominal 3dB bandwidth of ∼212Hz and a 1σ noise floor equivalent to that

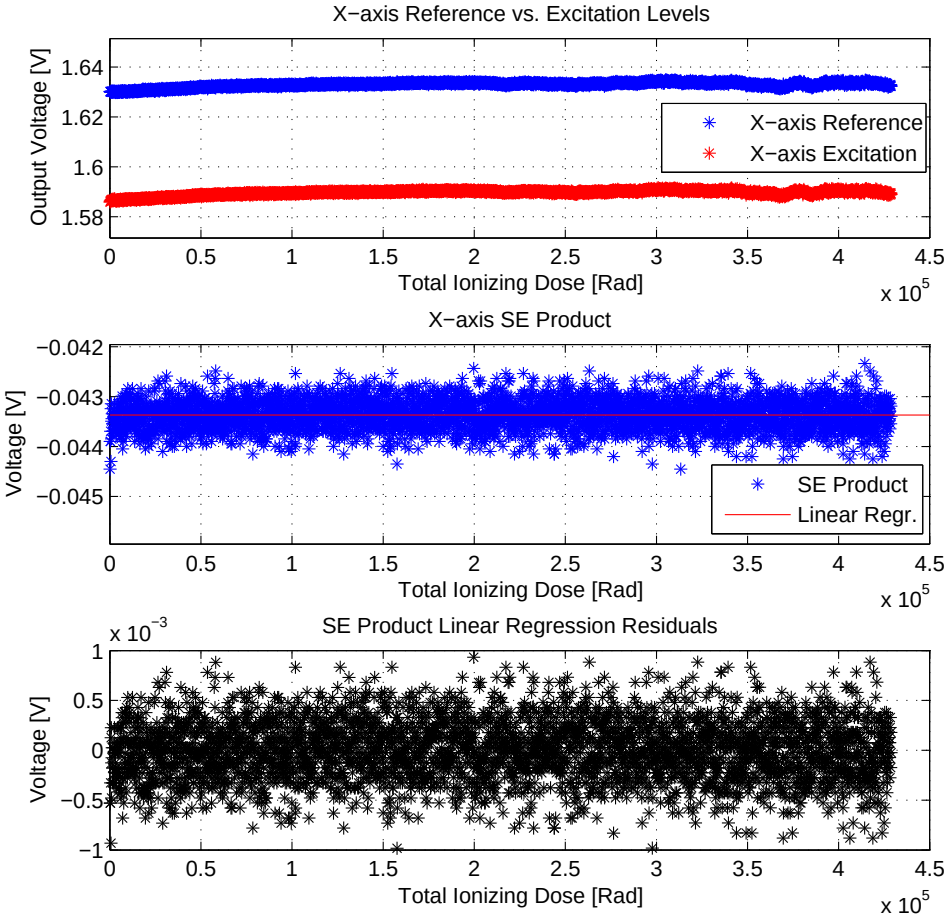

Figure 3.22. *LIS2L02AL X-axis output integrity analysis.*

outlined by equation 3.15:

$$\begin{aligned} N_{1\sigma} &= s_a \cdot N_d \cdot \sqrt{\frac{\pi}{2} f_{3dB}} \\ &= 660\frac{mV}{g} \cdot 30\frac{\mu g}{Hz^{1/2}}\sqrt{\frac{\pi}{2} \cdot 212Hz} \simeq 361\mu V_{RMS} \end{aligned} \tag{3.15}$$

where:
s_a: signifies device output sensitivity [V/g].
N_d: signifies device output noise density [g/Hz$^{1/2}$].
f_{3dB}: signifies the anti-aliasing filter 3dB cutoff frequency [Hz].

As such, the residual magnitude is clearly consistent with expected performance for a Gaussian distributed output signal, thus indicating that the accelerometer signal integrity has not been adversely affected by the sustained

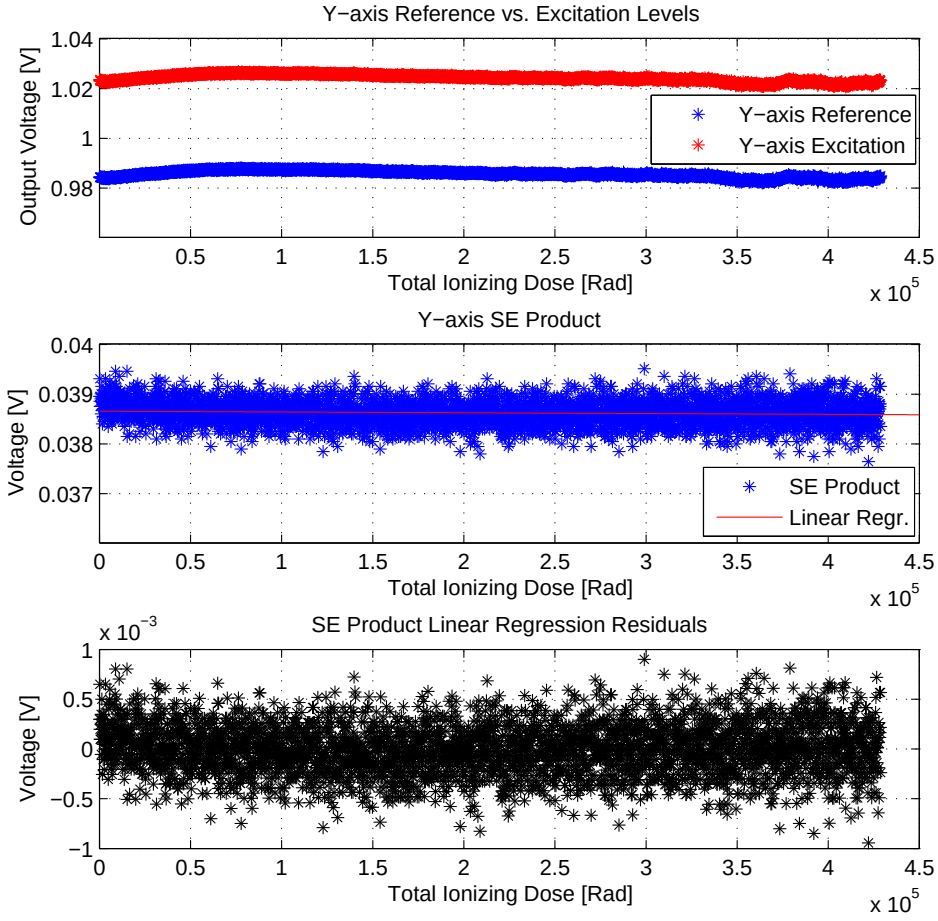

Figure 3.23. *LIS2L02AL Y-axis output integrity analysis.*

TID. Considering relative invariability of the acquired test data over the delivered dose, the LIS2L02AL MEMS accelerometer seemingly mets all applicable TID requirements for use in the μIRU augmentation.

3.3.6 Remaining Device Characterization Activities

In addition to the characterization testing already performed and reported upon in the previous sections, a few planned tests are still pending completion at the time of writing. The details of these are briefly outlined in the following sections.

3.3.6.1 Low Dose Rates Testing and SEE Susceptibility

With regards to low dose rate testing and Single Event Effects (SEE) susceptibility evaluation of MEMS accelerometers, little empirical data exists. [Gaillard-2007] reports on SEE screening standards applicable to MEMS inertial sensors and [Man-1999] details both low dose rate and heavy ion testing on two CMOS- and BiCMOS-based MEMS accelerometers, with the former giving rise to no change in TID failure level. For both accelerometers TID induced failure of the output conditioning circuitry was the primary source of impairment. With regards to SEE susceptibility one device incurred a significant output voltage change due to trapped charge affecting the differential capacitor coupling, whereas the conducting polysilicon structure of the MEMS element pertaining to the other device negated the same effect.
Similar testing was conducted on a relatively broad selection of COTS accelerometers by [Coumar-2004, Shea-2009] with a wide disparity in acquired results, though in general the MEMS devices showed little or no susceptibility to SEE. The literature consensus on the radiation sensitivity of MEMS accelerometer technology thus emphasizes the susceptibility of the embedded processing electronics rather than the MEMS sensing element itself.

Within the context of this project no low dose rate or SEE testing has been conducted, primarily for lack of facility access. Considering however the positive results of the conducted irradiation screening tests, little adverse effects from low dose rate testing would be expected. In terms of SEE susceptibility, appropriate design guidelines will be followed to mitigate effects on the device signal processing circuitry.

3.3.7 Vacuum exposure

At this time a vacuum exposure test of the LIS2L02AL has yet to be conducted. With the device MEMS proof mass being intrinsically hermetically sealed and the entire device cast into an epoxy monolithic structure, no adverse effects beyond a certain measure of outgassing are expected. As such, an outgassing constituent characterization test is planned for execution pending availability of the necessary test facilities.

3.3.8 Electromagnetic Interference

For the LIS2L02AL accelerometer electromagnetic interference (EMI) remains an issue yet to be addressed. The structure of the accelerometers internal signal processing chain is such that a low-noise capacitive charge amplifier using correlated double sampling (CDS) techniques is used to sample the differential signals from the MEMS element. This amplifier stage operates at a frequency of 200kHz. Secondly, the CDS outputs are de-multiplexed and transferred to

two individual sample/hold circuits the output of which are connected to the respective output pins of the device. Both sample holds operate at a frequency of 66kHz.

As such, the LIS2L02AL is expected to feature a radiated EMI signature at 66kHz, 200kHz and associated harmonics hereof. Considering, however, that these are internal to the device and that the device total power consumption is less than 3mW, the radiated energy at these frequencies will be small. Nevertheless, it must be emphasized that any radiance at these frequencies will occur in an uncorrelated manner with respect to the CCD main clock once co-integration of the μASC CHU and the μIRU augmentation occurs, and considering the supreme sensitivity of the CCD to electric fields this could potentially affect performance. Completing the EMI characterization test on the stand-alone accelerometer combined with the tier two co-integration experimentation as outlined in Chapter 5 does as such constitute priority tasks.

3.4 Summary

This Chapter has summarized an extensive review of the current state of COTS inertial sensors, particularly focusing on recent developments in the MEMS sector. Having investigated both gyroscope and linear acceleration sensors, it has been determined that the ST Microelectronics LIS2L02AL linear accelerometer found to be the prime candidate for the μIRU augmentation, remains so today. Developments in the gyroscope segment over the last four year period do however suggest, that the ascertainable performance level and design maturity is approaching a point where a gyroscope solution will yield performance comparable to that of the differential accelerometer concept for the same design baseline. For the present, the LIS2L02AL remains the sensor of choice, and the latter half of the chapter has emphasized characterization testing of this device, with certain idiosyncrasies such as output hysteresis and scale factor/ bias thermal drift being derived.

3.5 Bibliography

[ADI-2008] Analog Devices Incorporated. Analog devices inertial sensor reduces cost and complexity of industrial motion control designs. Press Release, 2008.

[Ang-2003] Cameron N. Riviere Wei T. Ang, Pradeep K. Khosla. Design of all-accelerometer inertial measurement unit for tremor sensing. *Proc. International Conference on Robotics and Automation*, 2003.

[Ang-2004] Pradeep K. Khosla Cameron N. Riviere Wei T. Ang, Si Yi Khoo. Physical model of a mems accelerometer for low-g motion tracking

applications. *Proceedings of the 2004 IEEE International Conference on Robotics and Automation*, 2004.

[Bjarnoe-2007] Jonas Bjarnoe. *Inertial Sensor Augmentation of Stellar Reference Units in the High Frequency Domain*. DTU Space, 2007.

[Buret-2006] Thomas Buret. Fiber optic gyroscopes for space applications. Technical report, iXSpace, 2010.

[Chaudhuri-2009] Pijus Kundu T.K. Bhattacharyya Ashesh R. Chaudhuri, Subha Chakraborty. Performance comparison and fabrication of micro machined electron tunneling accelerometers having cantilever and proof-mass structures. *International Conference on Advances in Computing, Control and Telecommunication Technologies*, 2009.

[Chun-long-2009] Liu Yi-wei Cai Chun-long. Status quo and trend of inertial integrated navigation systems based on mems. *Journal of Chinese Inertial Technology*, 2009.

[Coumar-2004] Rémi Gaillard Florent Miller Nadine Buard Laurent Marchand Oudea Coumar, Patric Poirot. Total dose effects and see screening on mems cots accelerometers. *IEEE Radiation Effects Data Workshop*, 2004.

[Dixon-2006] Richard Dixon. Prospects for mst sensors in automotive applications. Technical report, WTC Consultancy, 2006.

[Gaillard-2007] Laurent Marchand Rémir Gaillard, Courmar Oudea. Mems radiation testing guidelines. *Space Transportation*, 2007.

[Hartwell-1998] S.A. Miller K.L. Turner N.C. MacDonald P.G. Hartwell, F.M. Bertsch. Single mask lateral tunneling accelerometer. Technical report, University of California Santa Barbara, 1998.

[Heeren-2007] Henne V. Heeren. Evolution and trends in high volume production of mems. Technical report, Enabling MNT, 2007.

[IEEE-2001] IEEE. Proposed ieee intertial systems terminology standard and other intertial sensor standards (proposed ieee std. 1559). Technical report, The Institute of Electrical and Electronics Engineering, 2001.

[ISN-2010] InterSense. Navchip whitepaper. Technical report, Intersense Inc., 2010.

[Jerebets-2007] Sergei A. Jerebets. Gyro evaluation for the mission to jupiter. *IEEE Aerospace Conference*, 2007.

[Joergensen-2009] John L. Jørgensen. Juno mag critical design review - 19.0 design and implementation chu, 2009.

[Lawrence-2001] Anthony Lawrence. *Modern Inertial Technology*. Springer-Verlag, 2001.

[Liu-1998] J.K. Reynolds A. Partridge T.W. Kenny J.D. Grade Cheng-Hsien Liu, A.M. Barzali. Characterization of a high-sensitivity micromachined tunneling accelerometer with micro-g resolution. *Journal of Microelectromechanical Systems*, 1998.

[Man-1999] Kin F. Man. Mems reliability for space applications by elimination of potential failure modes through testing and analysis. Technical report, Jet Propulsion Laboratory, 1999.

[Ramos-2008] C.B. Burgner K.J. Åström F. Brewer K.L. Turner L.A. Oropeza-Ramos, N. Kataria. Noise analysis of a tunneling accelerometer based on state space stochastic theory. *Solid-State Sensors, Actuators and Microsystems*, 2008.

[SIG-2006b] Space Instrumentation Group. micro advanced stellar compass general information, asc-dtu-prp-3000. Technical report, DTU Space, 2006.

[ST-2006] ST Microelectronics. *LIS2L02AL Datasheet*. ST Microelectronics, 2006.

[Senturia-2004] Stephen D. Senturia. *Microsystem Design*. Kluwer Academic Publishers, second edition edition, 2001.

[Shea-2009] Herbert R. Shea. Radiation sensitivity of microelectromechanical system devices. *Journal of Micro/Nanolithography, MEMS, and MOEMS*, 2009.

[Titterton-2004] John Weston David Titterton. *Strapdown Inertial Navigation Technology*. The Institution of Electrical Engineers, 2nd edition edition, 2004.

[Wise-2006] Kensall D. Wise. Mems sensors for automotive applications. In *3rd Ibero American MEMS Congress*, 2006.

[Yole-2007] Yole Development. Inertial mems for consumer electronics report. Technical report, SARL, 2007.

[Yole-2010] Yole Development. Mems trends - magazine on mems technologies and markets (july 2010). Technical report, SARL, 2007.

Chapter 4

Micro Inertial Reference Unit Prototype Design

This chapter aims to convey the numerous considerations, trade studies, design iterations and tests that have gone into establishing a viable design for a gyro-free inertial reference unit in-line with proposed μIRU augmentation. The chapter first provides an analysis of the main requirements to the instrument physical and functional envelope derived from the μASC co-integration specifications, and subsequently proceeds to describe design considerations towards optimizing μIRU performance and functionality within that framework. The chapter also focuses on establishing criteria for identifying key electronic components and the tests conducted to ratify their selection.

4.1 μASC Derived Constraints and Requirements

As was determined through the 2006 study documented in [Bjarnoe-2007], the optimal configuration for an all accelerometer IRU to be integrated with the μASC system would be a collocation of sensors within the confines of the existing CHU envelope. From an angular resolution perspective, the sensors could be arranged in a manner which not only optimized the ability of the differential accelerometer pairs to resolve angular dynamics but also did so in a manner which imposed a minimum impact on the existing CHU design and performance. However, the optimality analysis also showed a number of discrepancies that would necessarily have to be resolved for the proposed configuration of the μIRU to be realized. Principal among these discrepancies was the volumetric conflict between the existing CHU electronics board and the proposed location of the accelerometer sensors as illustrated by the CAD model on the left in Figure 4.1.

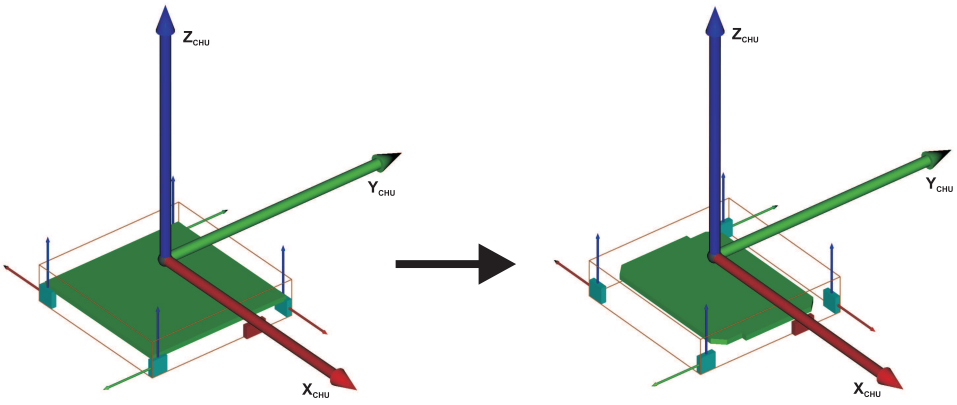

Figure 4.1. *Resolution of volumetric conflict between accelerometer placement and CHU electronics board in the GEO3 μIRU sensor configuration.*

The clearance issue was resolved during the first part of the project effort, by redesigning the form factor of the CHU electronics board to the CAD representation on the right in Figure 4.1. This was done while also taking steps towards further reducing the boards dynamic magnetic signature through employment of the principles outlined in Section 4.11. As a result, the size of the CHU board was reduced from $2070mm^2$ to $1500mm^2$, and the form factor altered so as to provide accommodation volume for the accelerometers. Figure 4.2 illustrates the physical differences in form factor introduced by revising the CHU board design.

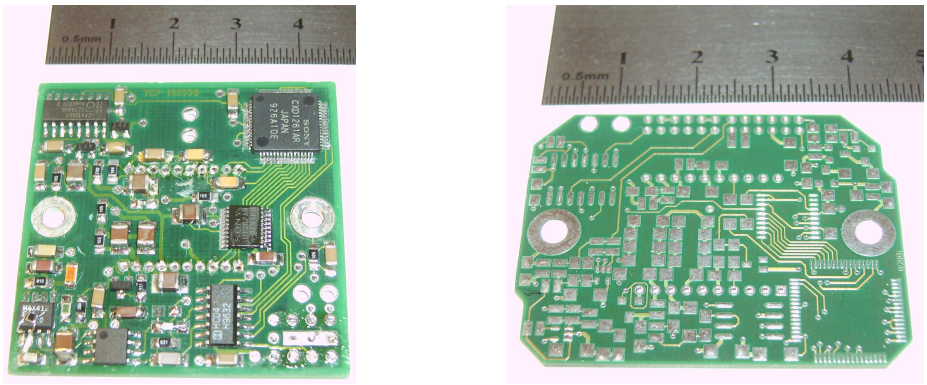

Figure 4.2. *Old CHU PCB design (Left) and revised design (Right).*

In addition to the form factor, the existing design of the CHU electronics imposed yet another constriction upon the μIRU design, as the existing harness between the μASC CHU and DPU provided no means of transporting the signals from the accelerometers to the DPU computer. In lieu of the minimum impact requirement, the μIRU data processing is to be undertaken by the DPU main processor, hence a datapath between the systems had to be established. Revisions in the electronics configuration of the CHU board succeeded in free-

ing one line between the CHU and DPU for μIRU purposes, thus imposing a key design driver requirement upon the augmentation being developed. To ensure minimum impact upon the existing μASC configuration beyond the revision of the CHU electronics board, the μIRU must as such support all necessary operations with a single dedicated line between the accelerometer sensor head and the data processing capabilities pertaining to the DPU.
With these physical envelope prerequisites established, collocation with the μASC CHU further extends a number of resource allocation and functionality requirements to the μIRU augmentation. The μIRU design baseline is thus inferred from the ambition to limit imposed loads to 10% of the corresponding μASC CHU values, leading to the following baseline requirements [SIG-2006b]:

Mass: The μASC CHU mass for flight configuration nominally accounts for 230±10g. As such the μIRU will strive for a maximum mass contribution of 23±1g.

Consumption/Thermal Loads: The CHU contains a minimum of electronics mainly to minimize thermal loads as well as the magnetic signature. Nominal CHU power consumption is 350mW for non-blinded operations, hence the μIRU augmentation will strive to limit nominal consumption to ≃35mW. As this added thermal load also affects thermo-mechanical stability of the CHU, every effort shall be made to distribute thermal loads evenly with respect to CHU boresight.

Volume: CHU volume provides a delimiting envelope for the μIRU augmentation design. Efforts shall be made to ensure all augmentation necessities can be housed within the existing envelope.

Asynchronous Behavior: The μASC extends a strict requirement that no electronics within the CHU envelope can operate in an asynchronous manner with respect to the main CCD drive frequency. The μIRU augmentation must adhere to this rule.

Operating Frequency: Capable of supporting a number of different update rates and associated CCD drive frequencies, the μASC primary update rate, and μIRU design baseline within in the context of this project, shall be 4Hz operation, corresponding to an image integration time of ∼250ms.

Operating Temperature: Nominal CHU operating temperature range extends from $-60°C$ to $+35°C$ [SIG-2006b]. μIRU parts shall be up-screened to ensure compliance.

TID Irradiation Tolerance: All integrated components of the CHU have been tested to accept a lifetime dose of 30krad 4πSi [SIG-2006b]. μIRU components shall be screened to meet similar requirements.

Magnetic Cleanliness: The μASC CHU maintains a residual dipole of <0.05 mAm^2 to allow integration close to sensitive instrumentation e.g. magnetometers. The μIRU augmentation must be designed so as to not dilute this performance specification.

Moreover, the μASC design adheres to and surpasses all EMC requirements

as defined by MIL-STD-461C, MIL-STD-461D and MIL-STD-462D, as well as derating specifications in accordance with ECSS-Q-30-11A. Naturally, the μIRU augmentation can afflict no significant performance degradation of the combined instrument in these respects, and the practicalities of the augmentation must as such allow appropriately mitigating measures to be brought into effect.

4.2 μIRU Sampling System Topological Considerations

From the requirements introduced by the μASC baseline platform in Section 4.1, a number of key aspects pertaining to the topology of the μIRU augmentation design can be derived.
Firstly, the electrical interface limitation of having only a single dedicated line (hereinafter denoted IDAT) between the CHU and the DPU precludes any design topology not involving analog to digital conversion of the accelerometer signals directly in the CHU. From a signal integrity standpoint, attempting to multiplex eight individual analog precision signals onto a single line is impractical, and moreover, the possibility of implementing simultaneous sampling would be severely impeded. The decision to proceed with the IDAT line as purely digital, thus places the μIRU A/D conversion capability squarely in the CHU.

Secondly, the synchronous operations requirement infers a frequency locked μIRU implementation which utilizes the primary CCD drive frequency as input, and does so in a manner which optimizes the accelerometer sample rate.

Thirdly, frequency locked operation entails an accelerometer sample rate which varies with applied CCD master clock frequency. As this is in fact an user selectable entity within the μASC framework, it has consequences for the decision to implement signal filtering as hardware IIR or digital FIR entities. To reduce processing loads, software implementation complexity and ensure consistent behavior regardless of μASC user interaction, hardware IIR filtering has been emphasized in the μIRU, although the prototype implementation allows some FIR experimentation to be undertaken.

These considerations has lead to the topological design of the μIRU augmentation illustrated in Figure 4.3. As the figure shows, the output data and subsequently the IDAT line constitutes the only direct communication path between the μIRU systems and the DPU signal processing facility. Moreover, the μIRU Data Processing software block in the DPU is emphasized as it is the only part of the augmentation which is not implemented within the CHU physical envelope. The remainder of the μIRU-DPU hardware/software interface makes use of existing implementations, in adherence to the minimum

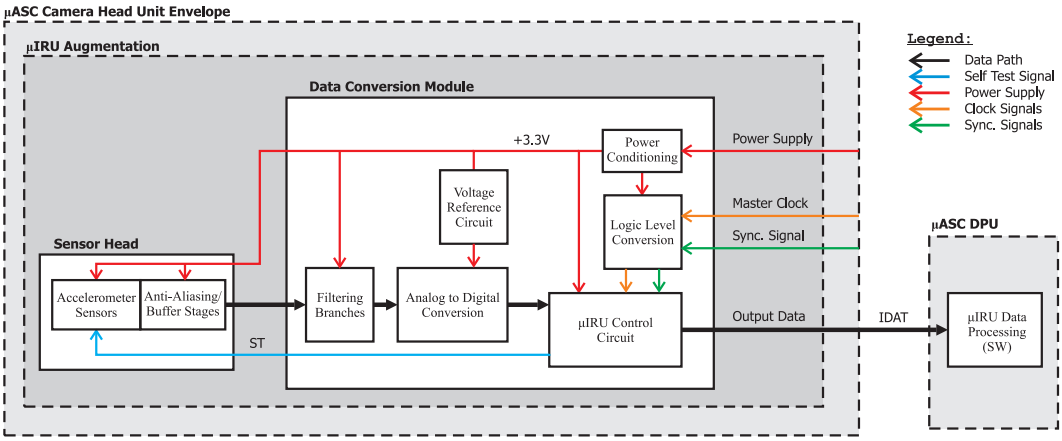

Figure 4.3. *µIRU topological design overview.*

impact requirement. Also it should be noted that the three remaining input signal entities to the μIRU all interface with the CHU. The notion behind this part of the topology is to achieve synchronous minimum impact behavior by deriving all necessary μIRU control inputs from existing signals. Finally, Figure 4.3 also conveys the ambition to operate the entire μIRU augmentation of a +3.3V rail. This voltage has been selected even though the CHU systems primarily operate of +5V and +15V, as it provides optimal performance of the LIS2L02AL accelerometers as well as an overall reduction in μIRU power consumption. Additional details on the design of the augmentation power supply chain is provided in Section 4.8.

4.3 μASC-μIRU Synchronization Analysis

A vital prerequisite for the μIRU design has been the synchronization analysis which served to establish an optimal integration strategy for the accelerometer sampling system within the confines of the μASC CHU. From a timing perspective the primary concern is to establish a common time reference between the two systems, so as to obtain correct temporal correlation of the attitude measurements. However, this reference must be established under strict adherence to the main design driver of the entire μIRU augmentation project effort, namely introducing no performance degradation of the primary functions of μASC instrument.

As such, a non-invasive strategy has been adopted which derives all μIRU control signals from signals normally used when operating the CHU, and thus available as buffered signals within the CHU envelope. Critical to understanding the nature of the timing issue, is to first understand the complex timing scheme associated with nominal operations of the CCD image sensor used in the μASC CHU.

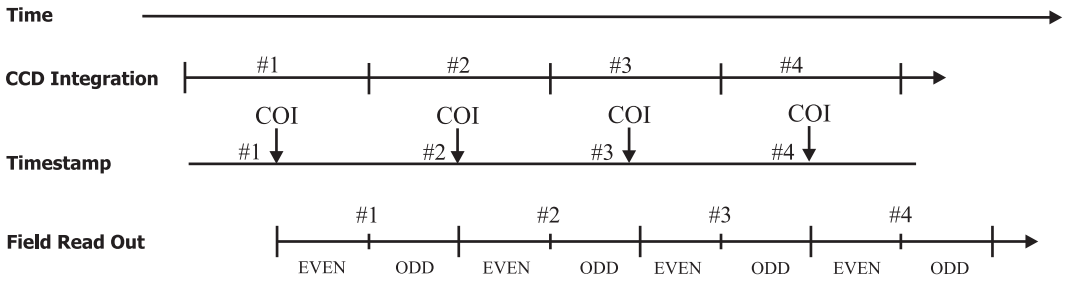

Figure 4.4. *μASC top level timing diagram.*

As shown in the μASC top level timing diagram depicted in Figure 4.4, the instrument performs continuous interlaced readout of the CCD image sensor. A single image frame is thus comprised of an even and an odd field, with the centre of integration (COI) timestamp providing the physical designation used to signify sample age. In terms of readout synchronization, the COI of the current frame is positioned at the transition from the odd field readout pertaining to the previous frame, and the even field readout of the current frame. Increasing the level of abstraction to include CCD hardware signals, the exact position of the COI can now be referenced to the CCD Vertical Reset (VR) drive signal and CHU master clock frequency (CLK) as illustrated by Figure 4.5. The VR signal initiates the transfer between field readouts and its trailing edge constitutes a time invariant entity with a fixed repetition rate of 567500 master clock pulses. The COI is located at 26707 clock pulses from the falling edge of the Even field VR pulse, and full hardware synchronization with respect to the μASC can thus be ascertained by monitoring VR and CLK only[1].

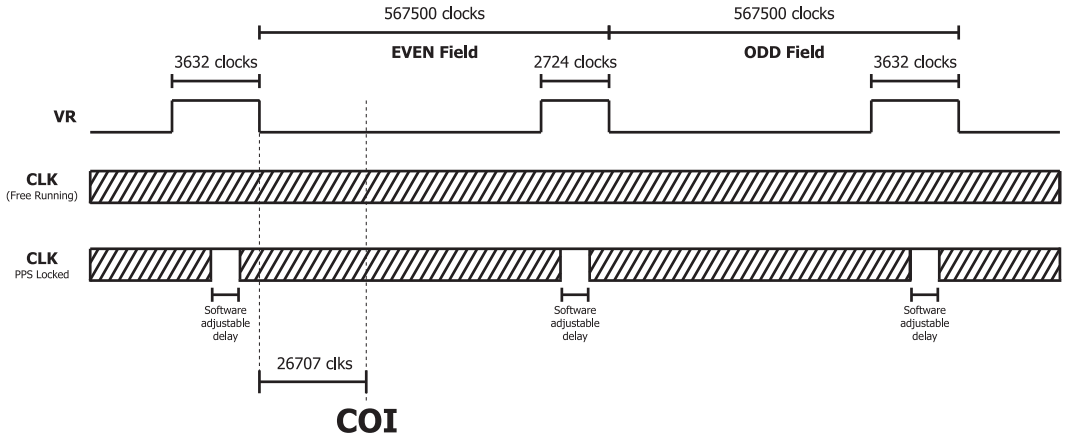

Figure 4.5. *μASC signal level timing diagram.*

Two separate CLK signals are introduced in Figure 4.5, one pertaining to

[1] An in depth timing diagram establishing the exact centre of integration in relation to the falling edge of VR is provided in Appendix B.

free-running operation of the μASC, and one for PPS-locked operations. The latter introduces a temporary cessation of the CHU master clock to synchronize μASC operations with an externally applied signal. Moreover, it should be noted that VR and CLK constitute physical signals generated in the μASC DPU and transferred to the CHU through dedicated wires in the harness, hence rendering them as viable options for implementing μASC-μIRU synchronization by allowing the μIRU augmentation timing base to relate directly to the μASC COI timestamp.
The μIRU augmentation will as such derive its primary clock signal from the CHU master clock CLK and synchronize its timebase from the falling edge of the CHU odd field VR pulse. This approach has the added benefit of ensuring fully synchronous operations with the CHU electronic systems, in adherence to the synchronicity requirement imposed in Section 4.1.

4.4 μIRU Augmentation Electronics Configuration

The GEO3 sensor configuration features four independent dual axis LIS2L02AL accelerometers, for a total of eight sensitive axes. From a signal integrity perspective the decentralized nature of the accelerometer placement in the GEO3 sensor arrangement presents an added problem, as the sensors themselves have limited output drive capability, thus rendering the signals prone to noise and interference degradation if carried over significant distances. To mitigate this behavior it was deemed prudent to implement a buffer stage directly at the sensor, as well as include basic anti-aliasing filtering directly at the signal source. In all this approach entailed developing a miniaturized PCB for each individual accelerometer to accommodate no only the sensor, but also the minimally required conditioning electronics.

Moreover, as illustrated by the topological study introduced in Section 4.2, the notion of achieving the highest degree of physical flexibility with regards to the sensor arrangement emerged early in the development process. It was as such decided to introduce a physical separation between the data conversion module (DCM) and the individual sensor modules. The centralized data conversion module would thereby handle all A/D conversion, processing, power distribution and interfacing with the μASC CHU/DPU, whereas the accelerometer sensor modules would be physically and functionally minimized so as to achieve their largest possible spatial separation while still maintaining signal integrity.

Although added system mass and board space penalties would naturally be incurred by the necessity of including wire interfaces between the DCM and the sensor boards, the added flexibility made the physical tolerances of the entire augmentation assembly much more amenable. In the end the adopted electronics configuration of the μIRU augmentation can be schematized as a

top-down evolution of the topological design from Figure 4.3 leading to the overview model depicted in Figure 4.6.

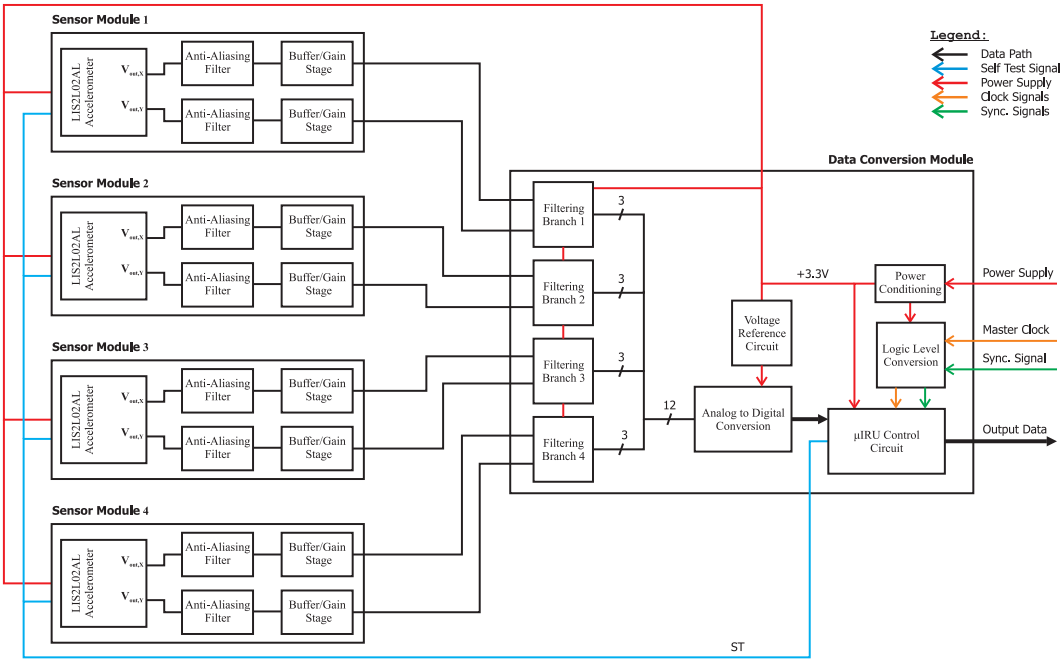

Figure 4.6. *μIRU augmentation electronics configuration overview.*

An important concept derived from [Bjarnoe-2007] was the separation of DC and AC signal content from the accelerometer outputs. When considering fused operations with the μASC, the μIRU inertial sensors will never be capable of reaching DC accuracy levels comparable of those of the μASC, nor is it the intention. Conceptually, the μIRU augmented μASC would require only AC signals from the μIRU to extend the operational bandwidth, provided the frequency responses of the individual instruments overlap so as to facilitate intercalibration. With the μASC Nyquist frequency for 4Hz operation at 2Hz, the proposed 1Hz-200Hz -3dB bandwidth for the μIRU would ensure exactly that. However, having only the AC outputs available introduces added complexity to the calibration routines described in Chapter 6, as the lack of DC signals preclude using static positioning in the gravitational field for scale factor, misalignment angles and bias level calibration. Moreover, removing DC content also removes the possibility of monitoring the health of the accelerometer devices inflight, and the possibility of inflight calibration of the AC filter constants. The gravity of these deficiencies lead to an adaptation of the originally envisioned μIRU topology, to the prototype including both AC and DC response from all accelerometers. As the DC response is only to be used for calibration purposes, the applicable sample rate requirement has though been relaxed as compared to the AC signals.

4.5 Data Conversion Module Control Circuit

Fulfilling the requirement of fully synchronous operations necessitates the control unit of the μIRU to support operations locked to an externally supplied clock signal. This clock, being a directly buffered version of the one supplied to the CHU, naturally exhibits all the idiosyncrasies required for optimally operating the CHU, including clock stops and user selectable frequencies. As such, it is vital that μIRU control unit is designed to obtain consistent behavior and to optimize throughput with a potentially discontinuous master clock. Physically the control unit is required to perform the following functions:

- Provide control/data interfaces with the μIRU ADCs.
- Provide control of the sampling system and sensor self-test functionality.
- Facilitate external sampling synchronization.
- Facilitate external transfer of accelerometer measurements to the DPU.

Moreover, control circuit form factor and power consumption constitute performance critical parameters, hence controller selection reflects their influence as well. Presently, at least three separate suitable technologies can be identified, namely generic microprocessors/microcontrollers, Complex Programmable Logic Devices (CPLD) or Field Programmable Gate Arrays (FPGA). Considerations concerning the selection criteria for each of these technologies are provided in the following.

Microcontroller Implementation

When assessing the perspectives of a microcontroller based implementation of the μIRU prototype, a number of definitive pros and cons can be identified as follows:

Microcontroller Pros

- Full stand-alone operation support.
- Facilitate platform development.
- Low power consumption, and power down features.
- Compact form factor, and few external components.

Microcontroller Cons

- Non-unity instruction cycle length.
- Commonly limited irradiation tolerance.
- External clock discontinuity tolerance.
- No parallel instruction execution.

A μIRU prototype implementation with the control circuit based upon a microcontroller solution would thus facilitate extensive stand-alone experimentation, a trait which would be highly beneficial throughout the development process. The main drawbacks associated with this approach would though entail having to contend with the inability to conduct parallel operations which in turn results in a sample rate reduction for the instrument.

CPLD Implementation

Often considered an intermediate step between the smaller programmable logic arrays (PAL) and FPGAs, CPLD technology distinguishes itself from both by being comprised of non-volatile (EEPROM) memory and numerous logic gates (typically in the range of 100-10000 gates). As such, a commonplace usage of these devices will be in boot-loader configurations for FPGA-based hardware, although recent developments in the FPGA sector trend towards the development of FPGA devices with embedded configuration memory.

CPLD Pros

- Supports fully parallel I/O processes for higher sample rates.
- Native clock discontinuity tolerance.
- Minimum of external parts required.
- High intrinsic SEE and TID tolerance levels [Fabula-2005].

CPLD Cons

- Limited configuration complexity and reconfigurability.
- Limited gate count.
- Medium device form factor.

In the context of the μIRU, the CPLD would be well suited for implementing the envisioned state-machine mode of operation with full parallel support, and the functionality of its gated logic would remain unaffected by discontinuities in the master clock signal. Similarly, prudent device selection and configuration would allow form factor and power consumption levels to be on par with the microcontroller-based solution, albeit at the expense of reduced implementation capabilities.

FPGA Implementation

A fully fledged FPGA implementation offers many of the same design and development flexibilities as delivered by the microcontroller solution. Normally being comprised of volatile-memory and necessitating an external non-volatile storage for booting, the FPGA features a very high number of logic gates and embedded features.

FPGA Pros

- Supports fully parallel I/O processes for higher sample rates.
- Native clock discontinuity tolerance.
- Extensive chip-scale feature implementation.
- Very high gate count supports high configuration complexity.

FPGA Cons

- External parts required, boot device for SRAM FPGA.
- Significant power and form factor penalties.
- Potential irradiation susceptibility of SRAM-based devices.

Implementing the μIRU prototype with an FPGA essentially offers a lot of the advantages that would also be gained with the microcontroller in terms of implementation flexibility. However, the number of external parts required and the power consumption/form factor does in several regards render the FPGA solution somewhat excessive.

With regards to the μIRU prototype DCM control circuit it has, as such, been decided to introduce a design disparity between the Tier One and the tier two implementations, favoring the microcontroller over the CPLD. The primary reason for this choice has been to promote stand-alone operations of the μIRU in the development phase, as any reliability upon external control signal generation would impose further requirements upon the discretionary availability of dedicated μASC EM hardware. The tier two implementation of the DCM will be implemented using a CPLD, and to this end the market survey has shown the Xilinx XC9500L or Coolrunner II series as well as the Altera MAX II series will meet sizing requirements. The final choice will be pending irradiation and thermal performance screening.

As for the Tier One implementation, a number of microcontrollers from Atmel, Microchip and Texas Instruments have been surveyed. In the end the part chosen was the Atmel ATmega168-Automotive 8 bit microcontroller, which is a SIG heritage part. Having previously been qualified and flown on the Prisma satellite mission (and thus readily available in-house for prototyping), the microcontroller is well characterized in terms of irradiation and thermal tolerances and furthermore, testing has verified its ability to operate with a discontinuous clock. Most importantly, the employment of the ATmega168 microcontroller retains the possibility of directly communicating with a PC through the device UART (using a level converter externally connected to the μIRU prototype), thus greatly simplifying the GSE necessary to operate the prototype instrument in stand-alone configuration.

4.6 Analog to Digital Conversion

Its performance impact perhaps second only to the MEMS accelerometer itself, the analog to Digital Converter (ADC) stage of the μIRU augmentation constitutes a component of critical importance. The selection of an ADC is driven by a number of factors. Most vital among those are found:

- Resolution, Bandwidth and Noise specifications.
- Simultaneous vs. successive sampling.
- Sample synchronization for multiple channels.
- Environmental tolerance levels.
- Power consumption.
- Feature integration.

Addressing each of these factors individually provides a means of ranking their relative importance, thus leading to a set of unified selection criteria which can be applied to the final part selection. Details of the considerations given to individual points are provided in the following:

4.6.1 Resolution, Bandwidth and Noise Specifications

The determining factor for establishing the absolute minimally sufficient performance specifications for the μIRU augmentation ADC, is the achievable signal to noise ratio (SNR) pertaining to the LIS2L02AL accelerometer. As established in Chapter 3 the manufacturer specification of an output noise density of $n_d = 30\mu g/\sqrt{Hz}$ and a scale factor of $S_f = 660mV/g$ for the LIS2L02AL accelerometer allows the SNR for a $B = 200Hz$ single pole bandwidth to be evaluated as:

$$\begin{aligned} SNR &= 20 \cdot \log\left(\frac{DNR}{n_d \cdot S_f\sqrt{B}}\right) \qquad (4.1) \\ &= 20 \cdot \log\left(\frac{2g \cdot 660mV/g}{30\mu g/\sqrt{Hz} \cdot 660mV/g \cdot \sqrt{\pi/2 \cdot 200Hz}}\right) = 71.5dB \end{aligned}$$

For the 212Hz single pole bandwidth and experimentally determined $20\mu g/\sqrt{Hz}$ noise density from Chapter 3, the SNR increases further to 74.8dB, with the noise floor at $240\mu V_{RMS}$. This specification combined with the goal of resolving the entire dynamic range of the accelerometer to enable full range calibration, thus imposes a required minimum ADC resolution. Considering the SNR expression for an ideal N-bit converter as derived by [Kester-2004]:

$$SNR_{ideal} = 20\log\left(\frac{q \cdot 2^N/2\sqrt{2}}{q/\sqrt{12}}\right) = 20\log 2^N + 20\log\sqrt{\frac{3}{2}} \qquad (4.2)$$

It is evident that an ideal 12-Bit ADC providing a maximum SNR of 74dB, would barely suffice in accommodating the sensor dynamic range in accordance with the manufacturer specification, and fail to do the same for the experimentally defined case. Moreover, considering that physical ADCs introduce a number of errors from distortion phenomena that renders them unable to ascertain the theoretically achievable SNR, it is clear that the μIRU design must provide operational margin at this point. Adopting a minimum resolution of 14-Bit would as such provide an ideal SNR of 86dB to accommodate the entire output range of the accelerometer whilst simultaneously being able to resolve the noise floor of the sensor. Considering the case where the ADC input voltage range is appropriately matched to the LIS2L02AL sensor output voltage range ($V_{ref} = 2S_f \cdot a_{max}$) the least significant bit (LSB) size for an ideal 14-Bit ADC solution may be determined as:

$$LSB = \frac{V_{ref}}{2^{14}Bit} = \frac{2 \cdot S_f \cdot a_{max}}{2^{14}Bit} = \frac{2.64V}{2^{14}Bit} = 161.1\mu V/Bit \tag{4.3}$$

Even though this value suffices in resolving the sensor noise floor (by about a factor of 1.5 for the experimentally defined case), physically obtaining a stable voltage reference of exactly 2.64V over temperature and irradiation would likely prove difficult. Standard reference values in the vicinity are 2.5V and 3.0V, which would effectuate 14-Bit resolution LSB sizes of 152.6μV/Bit and 183.1μV/Bit while accommodating a peak-to-peak acceleration range of 3.78g ($\pm$1.89g) and 4.54g ($\pm$2.27g), respectively. This tradeoff between resolution and range is summarized in Figure 4.7 for 12, 14 and 16-Bit conversion, as compared to the specification and experimentally determined noise floor of the LIS2L02AL accelerometer when considering a bandwidth with a single-pole roll-off at $f_{3dB} = 200Hz$.

As indicated by Figure 4.7, the 12-Bit solution will only resolve the accelerometer specification noise floor for reference voltages below $\sim$1.4V and the experimentally determined noise floor below 1V. As such, utilizing a 12-Bit ADC would unnecessarily degrade performance and range, while the latent $\pm 1/2$LSB quantization noise of the ADC constitutes yet another incentive towards adopting a higher resolution ADC. From this perspective the μIRU augmentation with the LIS2L02AL sensor should implement ADC capability with a resolution of no less than 14-Bit and a reference voltage of no more than 3.0V. At 3.0V reference and 14-Bit resolution the sum of the LSB and the associated quantization noise approaches the $1\sigma_{RMS}$ value of the LIS2L02AL output signal, thus resulting in near optimal conditions for the application of oversampling techniques.

With regards to sample bandwidth, the μIRU augmentation baseline design warrants the ability to resolve attitude dynamics with content of up to 200Hz, hence imposing a Nyquist frequency requirement of no less than 400Hz on the instrument sample rate. From a traditional signal conditioning perspective,

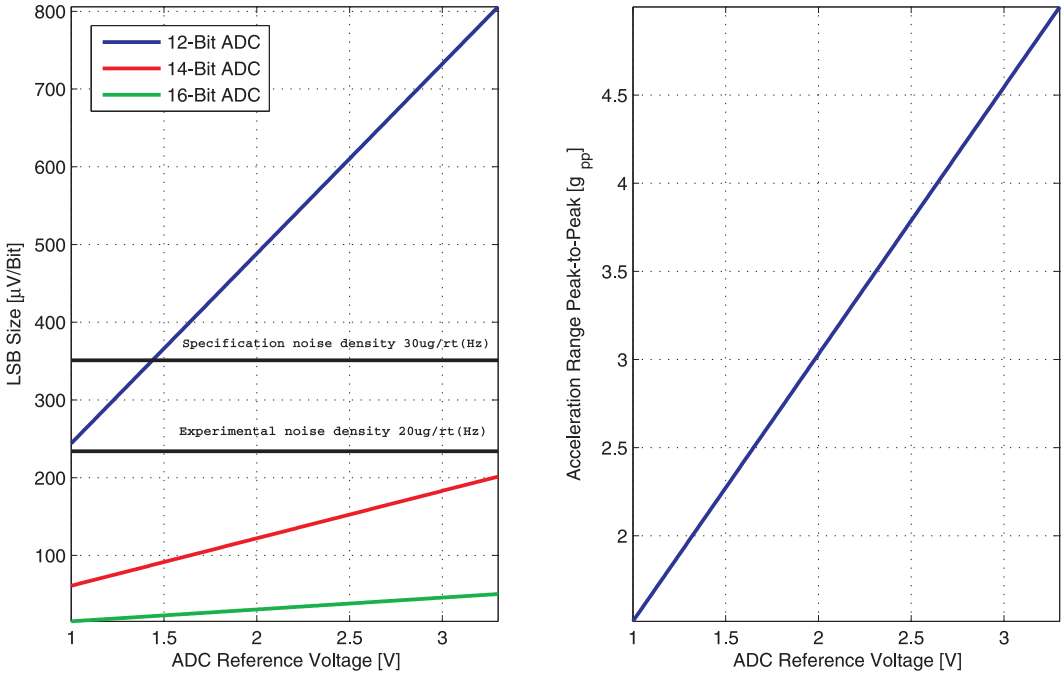

Figure 4.7. *ADC noise floor versus LIS2L02AL accelerometer output noise.*

the necessary sample rate is heavily influenced by the anti-aliasing filter design. Achieving the full dynamic range of the ADC would require the sample rate to be set beyond the point where the anti-aliasing filter achieves signal suppression equal to the ADC DNR, which in turn imposes a rather daunting requirement upon the suppression capability and necessary order of the anti-aliasing filter.
Fortunately, the application at hand does not warrant -80dB per octave anti-alias filtering. As previously illustrated by Figure 1.5 and reported by [Chubb-1975, Parvez-1990, Tunbridge-1990, Dyne-1993, Rogers-1993, Butterfield-1996, Ingham-1998, Bushnell-1999, Rice-1999, Lee-2000, Whorton-2000, Toyoshima-2001, Tryggvason-2001, Jono-2002, Ortiz-2003, Babkin-2004, Storey-2004], the vibrational energy present beyond 200Hz is extremely limited for all the surveyed spacecraft platforms. Similarly, maximum typical accelerations as reported by [Tunbridge-1990, Sutliff-1999] remain on the order of $\pm 100mg$ for a detection bandwidth of 1kHz. As such, the reasonable assumption can be made that the signal content beyond the 200Hz limit remains fairly inconsequential for the spacecraft attitude, and well within the capability of more conservative anti-aliasing filter requirements.
With the synchronization requirement imposed upon the μIRU augmentation by the μASC, the sample rate of the instrument is naturally limited by the frequency of the main clock signal delivered by the CHU. For the μIRU prototype implementation it was decided to aim for the largest possible sample rate, in an effort to reach the first oversampling criterion for the full 200Hz bandwidth in accordance with equation 4.4.

$$f_{oversampling} = 4^n \cdot f_{Nyquist} \tag{4.4}$$

where:
$f_{oversampling}$: signifies the necessary sample frequency to gain n additional resolution bits.

As such, the design target for μIRU has been a 1600Hz sample rate for synchronized operations with the μASC operating in 4Hz mode. Regarding the sample rate a final point should be made. As explained in Chapter 2 the RMS error on the estimation of position for a given time interval as derived from double integration of N measurements from a linear accelerometer is proportional to $1/\sqrt{N}$ when considering a Gaussian distributed noise model. As such, minimizing position estimate errors (and thereby angular evolution errors for the μIRU), constitute a strong incentive towards adopting the highest feasible sample rate.

4.6.2 Simultaneous vs. Successive Sampling

Deciding between a simultaneous or a successive sampling strategy has profound implications not only for the way in which the instrument is operated, but also for the hardware implementation of the sampling system. Figure 4.8 provides a simplified overview of the two sampling strategies when applied to the μIRU application.

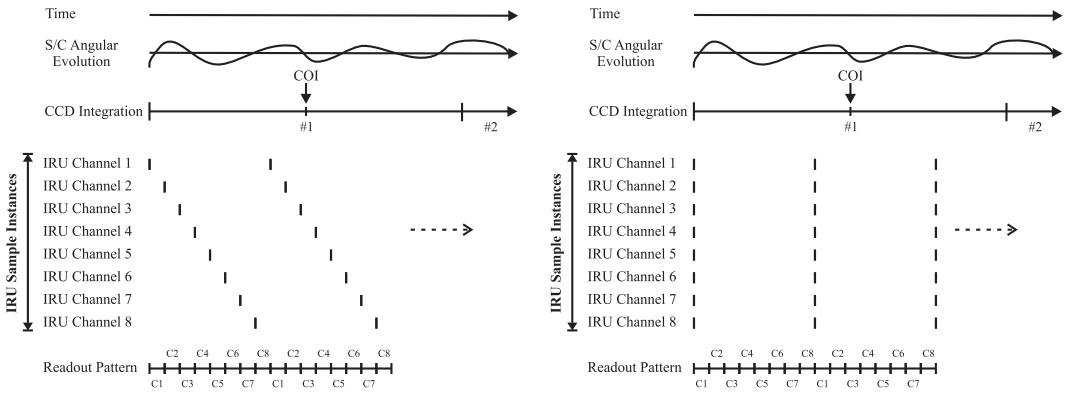

Figure 4.8. *Successive vs simultaneous sampling in the μIRU application.*

Successive sampling as depicted on the left, introduces a temporal disparity between individual samples of the accelerometer channels. Each channel is converted and read in a successive manner, thus introducing a delay equal to the sum of the acquisition period and the readout period between any two samples. Simultaneous sampling as depicted on the right synchronizes the sampling of all channels to within the accuracy offered by the combination of

the sample synchronization pulse and the aperture jitter specification of the ADCs used in the sampling system.

The necessity of implementing simultaneous sampling in the μIRU becomes apparent when considering the sampling instances in reference to the spacecraft attitude angular evolution as sketched at the top of the figures. The concept of the μIRU is to resolve attitude dynamics occurring beyond the bandwidth of the μASC, and to do so by evaluating the measured difference between spatially separated linear accelerometers. As such, any temporal disparity in the sampling of the accelerometer outputs, as would be the case for successive operation, allow fast dynamics to distort the difference signal, thus degrading performance in the high frequency domain. Also, having the temporal disparity to contend with makes relating the μIRU data to the μASC COI much more complicated, as each accelerometer measurement would synchronize differently. From these considerations it is clear that the μIRU sampling system must implement simultaneous sampling of all channels to ensure data consistence.

4.6.3 Sample Synchronization for Multiple Channels

Provided no suitable ADC can be identified which is capable of accommodating all the necessary channels, performing simultaneous sampling of at least eight individual channels might require the application of more than a single A/D converter. In this case, as no asynchronous operations are allowed, the sampling system implementation must support direct hardware synchronization between all employed analog to digital converters.

4.6.4 Environmental tolerance levels

As for all components employed in the μIRU, environmental tolerance levels must be on par with those of the components pertaining to the μASC CHU. Particularly TID irradiation and thermal performance shall be assessed as part of the selection process.

4.6.5 Power Consumption

ADC power consumption constitutes a pertinent issue to the selection process, as power is not only a restricted resource, but its dissipation also a source of thermomechanical instability for the μASC CHU. Low power consumption is thus weighted heavily in the ADC selection.

4.6.6 Feature Integration

Many contemporary A/D converters provide more or less stand-alone operations, featuring both internal reference circuitry, digital communication interfaces and other amenable characteristics. Such devices usually require little more than a few external passives, decouplants and diligent board layout to achieve optimal performance. For the envelope constricted μIRU augmentation, a high degree of feature integration is highly desirable, particularly when considering the need to accommodate at least 8 individual channels for A/D conversion. However, in lieu of the particulars of the μIRU operating environment, a high degree of feature integration might become a liability when considering susceptibility to irradiation or thermally induced performance deterioration, hence the ADC selection for the μIRU augmentation seeks to implement the physically smallest solution possible including only essential features.

4.6.7 Survey and Selection

When the A/D converter part survey and selection was conducted in 2007, relatively few devices where found to provide the unique combination of traits envisioned for the μIRU ADC. To achieve full sample rate conversion of all the AC and DC channels pertaining to the μIRU accelerometers, at least 16 channels would be required (8 AC + 8 DC channels). Or if the DC sample rate requirement was fully relaxed at least 9 (8 AC + 1 DC channels, with DC channels multiplexed 8→1).

Specifically the simultaneous sampling requirement profoundly affected the number of applicable multi-channel ADCs, as most such converters remain highly application specific (eg. RF front ends, multiphase power line monitoring, motor control etc.) often leading to the relaxation of certain performance parameters to advance others. Commonly it was found that simultaneous sampling multi-channel ADCs where optimized towards throughput rates at the expense of power consumption, and consequently a topological decision was forced between using a single converter or multiple synchronized converters. Conceptually both solutions have amenable traits, yet even though applying and synchronizing a single channel ADC per accelerometer channel would be physically possible, the associated form factor and power consumption issues would far overshadow the synchronization problem.

The adopted solution to this conundrum was a hybrid approach where two simultaneous sampling multi-channel ADCs would be operationally synchronized, thereby providing a sufficiently large number of channels to cover both the full AC implementation (8 channels) and a relaxed DC implementation (4 channels, with DC channels multiplexed 8→4) for a total of 12 ADC channels.

With this approach DC channels throughput could be realized at half the AC channel rate.

Device	Supply Range [V]	Consumption [mW@V_{in}]	Resolution [*Bit*]	SINAD [*dB*]	No. of channels	Samplerate [*ksps*]	Internal V_{Ref} [*V*]	Internal Clock [*kHz*]	Interface	Package	Operating Temperature [°C]
MAX1316	4.75↔5.25	230@5.0	14	76.5	8	250	2.5	Ext.	Parallel	LQFP-48	-40↔85
MAX1149[a]	2.7↔3.6	3.6@3.3	14	81	8	116	2.5	2100	SPI	TSSOP-20	-40↔85
LTC1408I	2.7↔3.6	13.2@3.3	14	76	6	600	2.5	Ext.	3-wire	QFN-32	-40↔85

[a] Differential, successive device. Not simultaneous sampling.

Table 4.1. *2007 survey of 14Bit multi-channel ADCs applicable to the μIRU augmentation.*

Table 4.1 provides an overview of the devices identified during the 2007 survey which could be considered applicable to the μIRU augmentation in accordance with the previously outlined critical parameters. Obtaining 4,6 and 8 channel COTS devices with 14Bit resolution proved rather trivial and devices with characteristics along the lines of the MAX1149 was and continue to be abundant. However, the MAX1149 is architecturally simple when compared to the MAX1316 and the LTC1408I, as it does not implement simultaneous sampling, rather just a multiplexer structure which successively connects each input to the SAR converter. Moreover, conversion runs of its internal clock which cannot be halted, hence it would operate in direct violation of the μASC synchronicity requirement, and thus cannot be considered a viable candidate for the μIRU augmentation. The two remaining devices both exhibit most of the desired characteristics and are architecturally quite similar, offering fully differential inputs, sample hold circuits and input aperture skews of less than 200ps. However, the Linear Technology LTC1408I produces some distinct advantages. Most importantly, its power consumption is very low for a simultaneous sampling device, effectively a factor of 14 lower than that of the MAX1316. Secondly its interface is extremely simple, and designed to run of an external clock only, while allowing direct control of the conversion instance by a simple logic signal transition. It is as such, inherently synchronized to the master clock applied. The MAX1316 offers similar features, a main advantage being the full 8 channels available, yet the parallel data interface puts it at a disadvantage due to the sheer number of signals involved. Moreover, it is physically larger than the LTC1408I, and offers only marginally better effective signal to noise ratio.

In the end, the LTC1408I can be considered an enabling device from a μIRU perspective. Providing all of the key features necessary for the μIRU augmentation to be designed in accordance with the μASC imposed requirements whilst delivering the required resolution and signal-to-noise ratio, the device does so with amenable form factor and power consumption levels. Moreover,

synchronizing two devices will be straightforward, and allow both AC and DC signals to be converted with only a marginal relaxation in the DC timing specification. However, being a COTS component, the environmental tolerance level of the LTC1408I is questionable. As such, the last steps of the μIRU ADC selection procedure involved an extensive TID screening test to determine if the LTC1408I architecture would meet the μASC irradiation tolerance requirements. The results of this test is provided in the subsequent sections.

4.6.8 LTC1408I Total Ionizing Dose Screening Test

Considering the criticality of the A/D converters in the μIRU design, a detailed TID test methodology was developed and executed as part of the selection process. The main ambitions of this test where to characterize the LTC1408I ADC device for a number of performance critical parameters, including:

- Internal reference integrity
- Noise levels
- Missing codes
- Response monotonicity
- Sample/hold integrity

To this end the test circuit schematized in Figure 4.9 was developed, which allows the irradiation response of the internal reference and the performance of the sampling system to be assessed. The first parameter is determined by simply monitoring the reference voltage level as well as the device current consumption over radiation using precision $6\frac{1}{2}$ digit multimeters.

The remaining parameters require a substantially more elaborate approach to assess, as it is necessary to assert every possible bit value for all six channels of the ADC. In general, two suitable approaches can be identified to assert the $2^{14} = 16384$ levels between 0V and V_{ref}, namely excitation using a vary slowly varying sinusoid with an amplitude equal to or greater than V_{ref}, or direct excitation using a Digital to Analog Converter (DAC) capable of resolving all levels.
In this context the latter approach was selected, and an input signal to all six channels where generated using the 16Bit MAX5203 DAC from Maxim IC. As the DAC references to 3.0V it provides an LSB of 45.78μV, whereas the the LSB of the LTC1408I operating from its internal 2.5V reference amounts to 152.6μV. As such, each LSB of the ADC should be resolved by three settings of the DAC, thus providing ample design margin to ensure that excitation of all levels is achieved.
The test operations where under the control of the PIC18 microcontroller as depicted in Figure 4.9, and followed a repeating pattern every 20 minutes. The test sequence initiated with the recording of device temperature and DAC reference level and subsequently the DAC is started from 0V output incrementing in 1LSB_{DAC} steps. At each step, all six channels of the LTC1408I are sampled

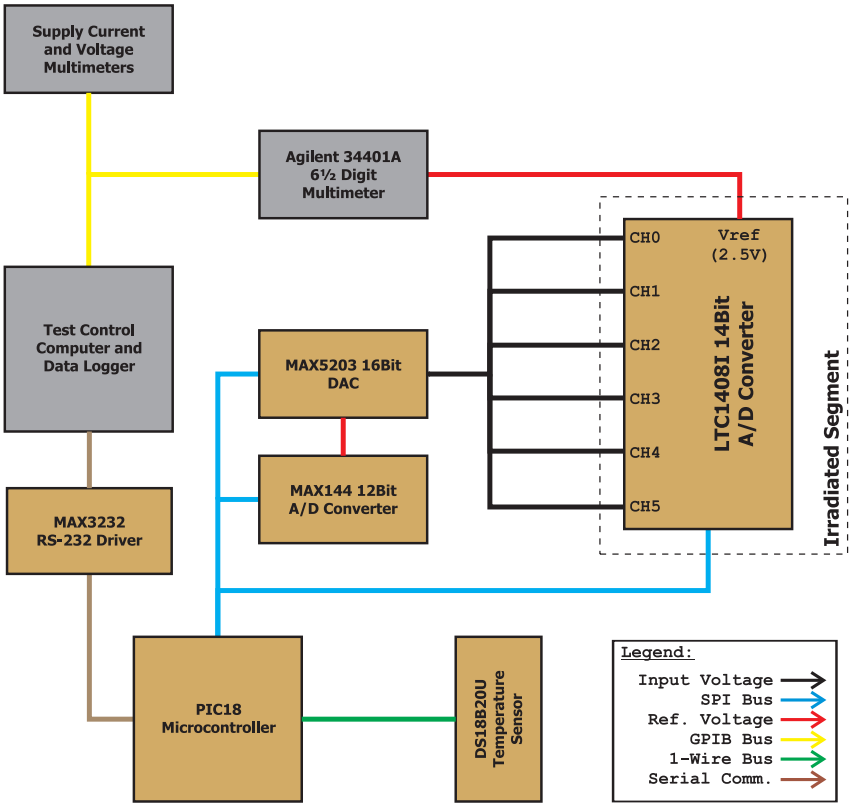

Figure 4.9. *LTC1408I irradiation test setup overview.*

simultaneously, converted, the data read by the PIC18 and finally delivered to the test computer. For a total of 65536 DAC increments and 6 channels converted in 14Bit resolution, the total amount of data produced every 20 minutes exceeds 5.2Mbyte. It should also be noted that the GPIB bus data and the PIC18 data are sampled asynchronously but with similar 20 minute intervals. From a data treatment perspective, analyzing the amount of data produced requires substantial computing power which has been graciously provided by the DTU G-Bar. Missing codes and ADC monotonicity is easily verified by ensuring that all possible bit values are present and that every bit value is either equal to or larger than the preceding value. Quantifying the integrity of the six channel sample/hold circuitry and the SAR is however more difficult as is separating their influence. In this context the adopted method looks at two main parameters, namely interchannel mean μ and interchannel variance σ^2, for the sample number s each defined as:

$$\mu(s) = \frac{\sum_{i=1}^{6} CH_i(s)}{6} \tag{4.5}$$

$$\sigma^2(s) = \frac{\sum_{i=1}^{6} \left(CH_i(s) - \mu(s)\right)^2}{6} \tag{4.6}$$

Here the fact that all six channels are subject to identical excitation and supposedly sampled with an aperture skew of less than 200ps [Linear-2006] is utilized. The expectation would as such be for the instantaneous sample mean of the channels to produce a value equal to the excitation level, and to do so with a variance between them in accordance with the device noise specification.

Results

Having conducted TID screening on the LTC1408I in accordance with the outlined methodology has resulted in the specific data included as Figure 4.10

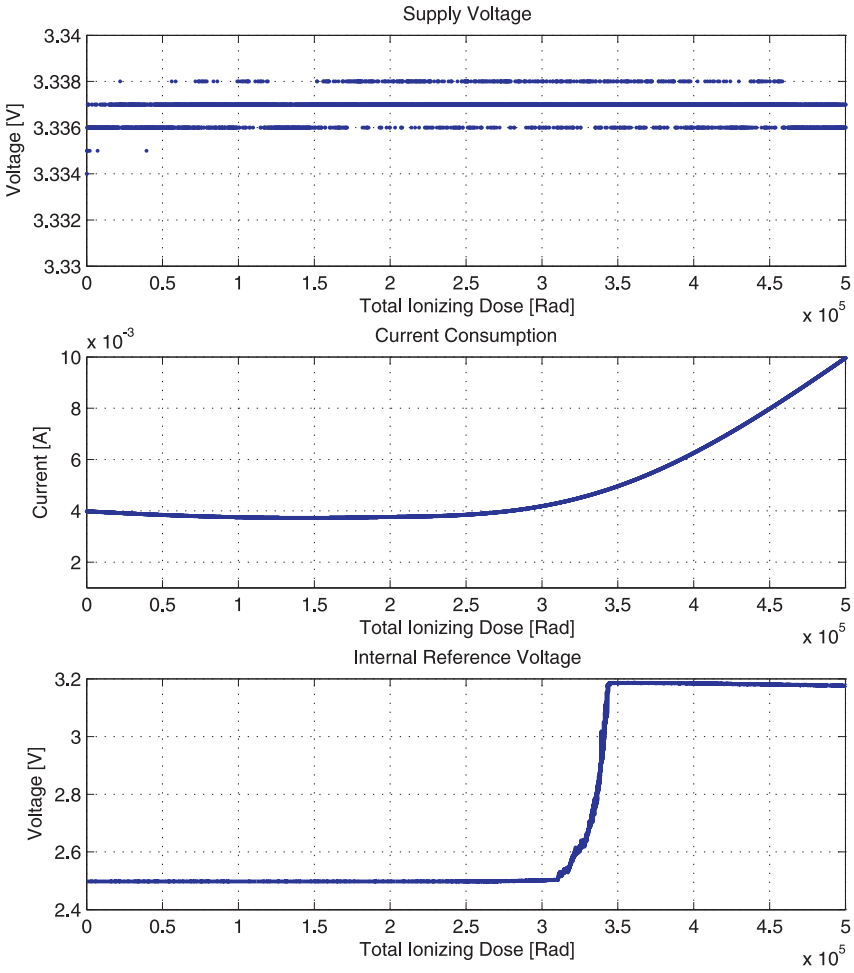

Figure 4.10. *LTC1408I irradiation test data set 1.*

Of these results, the performance of the internal voltage reference is of particular interest. As the μIRU design strategy calls for utilizing a unified reference for both A/D converters in the instrument, the internal reference the ADCs must be disabled. The LTC1408I does, however, provide no control option for directly disabling the internal reference, rather it must be overdriven by

an external reference voltage which exceeds the internal reference voltage by a minimum of 50mV. For nominal operations that would entail a minimum external reference voltage of 2.55V, yet as the irradiation response shows, the internal reference voltage increases over TID exposure.

Correctly overdriving the internal reference thus becomes a significant factor in designing the unified external reference circuitry for the two μIRU ADCs, with the necessary voltage level being the main concern. As the LSB size is dictated by the reference voltage level, extending the reference far beyond the nominally required 2.55V would serve to unnecessarily dilute the resolution of the instrument. As such, the straightforward solution of using a heavily filtered +3.3V ratiometric rail derived from the +5V supply as the external reference remains undesirable from the perspective that the LSB size would increase from the nominal $152.59\mu V/Bit$ to $201.42\mu V/Bit$[2] To ameliorate the LSB dilution incurred by adopting an external reference, a compromise solution has been chosen which implements a single 3.0V dedicated external reference for the two μIRU ADCs. This solution will be elaborated upon in Section 4.9.

Figure 4.11 provides the DAC reference data and the temperature data as measured during the test, with the temperature maintaining a near constant level. Note that the apparent noise pertaining to the DAC reference voltage is partly an artifact of it having been sampled with a 12Bit ADC only. Also, the exact value of the reference is of limited criticality provided it remains above 1.5V, corresponding to a full range output of the DAC of 3.0V which will ensure correct excitation of the LTC1408I.

Under the aforementioned conditions the interchannel mean and interchannel variance levels have been subjected to evaluation. As Figure 4.13 illustrates, the mean of all six channels produces a linear relationship with the excitation voltage as would be expected for proper conversion. This behavior remains constant up to a TID of roughly 34krad where irregular responses are first visible, and at around 40krad a distinct drop in mean value occurs particularly for higher excitation values.

This behavior seems somewhat consistent with that of the internal reference, even though direct correlation is not entirely verifiable from the mean value alone. The deterioration of the internal reference does as such show its earliest onset at around 31krad as indicated by Figure 4.10. However, looking to the interchannel sample variance $\sigma^2(s)$ versus excitation voltage and TID as depicted in Figure 4.13 indicates the presence of another deteriorating effect, in all probability pertaining to the sample/hold part of the ADC circuitry.

The interchannel sample variance $\sigma^2(s)$ is seen to begin deviating from its

[2]These values should be compared to the nominal accelerometer output noise level of 361mV at $212Hz$ single pole bandwidth as determined by equation 3.15.

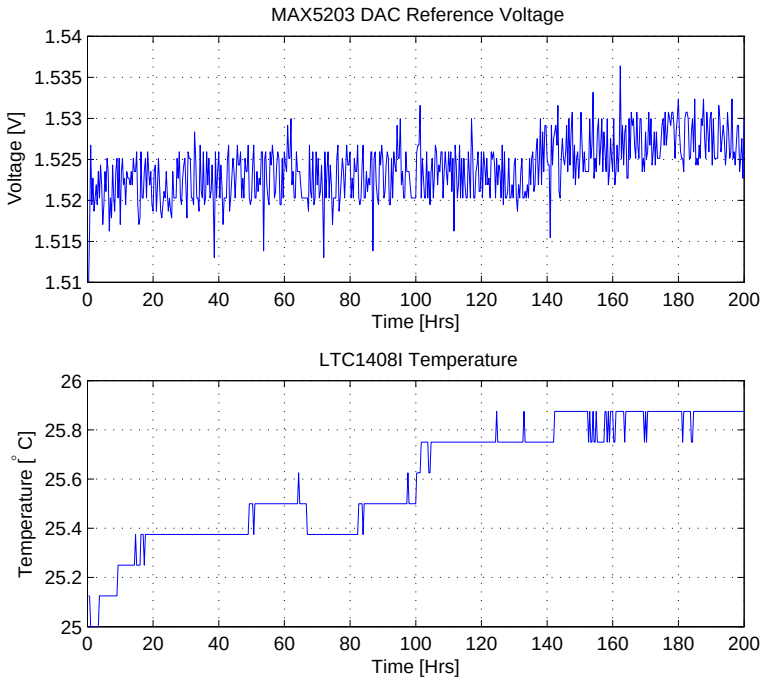

Figure 4.11. *MAX5203 DAC reference voltage and temperature.*

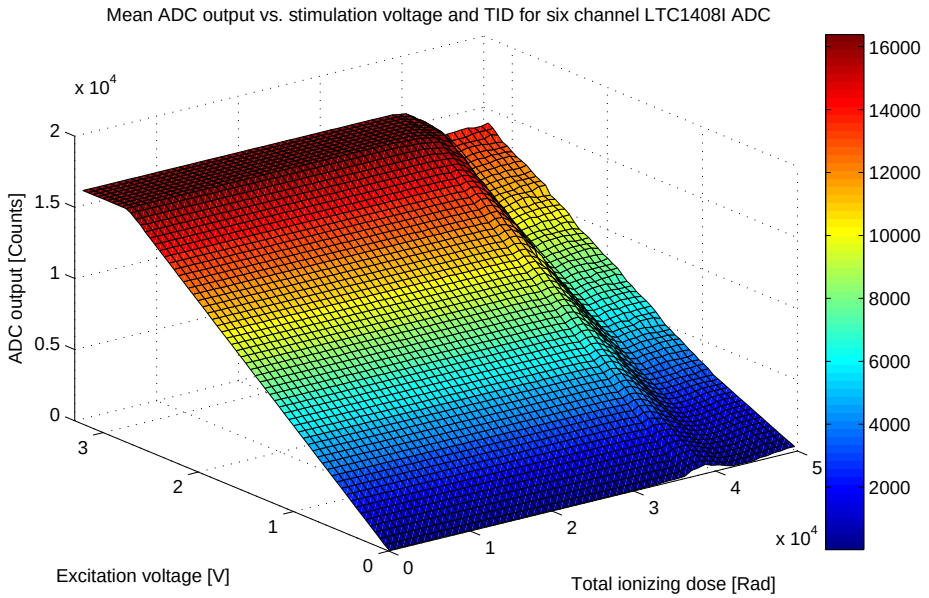

Figure 4.12. *LTC1408I interchannel sample mean $\mu(s)$ vs. TID and excitation voltage.*

nominal value of around 15 when the accumulated dose reaches ∼29krad and rise rapidly as the TID approaches ∼35krad. As the variance magnitude is

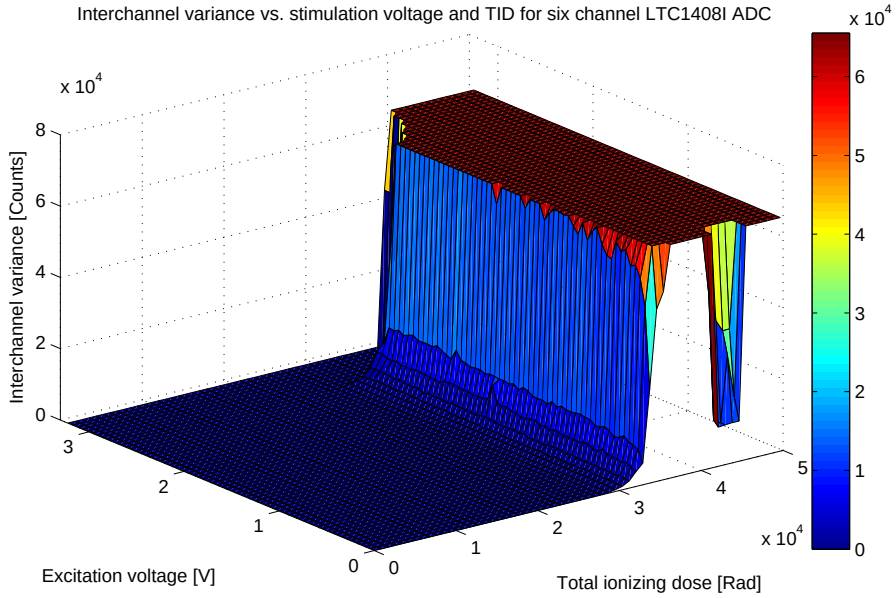

Figure 4.13. *LTC1408I interchannel sample variance $\sigma^2(s)$ vs. TID and excitation voltage. Note that the variance magnitude has been artificially truncated at 16Bit to enhance visibility.*

calculated by subtracting the sample mean, the TID effects on the internal reference are not reflected in the interchannel variance deviations. To assess whether functional impairment of the sample/hold or SAR circuitry is responsible, the raw channel outputs are evaluated at different levels of accumulated dose. The results of this evaluation are depicted in Figure 4.14 and clearly show how specifically the LTC1408I channels 3 and 4 deteriorate before the four remaining channels. Moreover, the slice at 34.4krad show channel 3 and 4 deviating in opposite directions from the nominal response, thus indicating why the interchannel variance method indicates the issue prior to it being detectable in the interchannel mean calculation.

What remains clear from the irradiation screening test of the LTC1408I is that the internal reference has an impairment limit of around 30krad. Beyond this point overdriving it with an external reference voltage becomes difficult. Similarly, the sample/hold or SAR segment of the device is observed to perform nominally up to a TID of ∼29krad, after which graceful degradation of individual channels is observed. It is also clear that an isolation test with an external reference should be conducted next to investigate the latter issue further. Furthermore annealing rates should be subject to investigation in the same context. Pending the outcome of further testing and annealing rate assessment, the employment of the LTC1408I in the μIRU augmentation will ultimately depend upon accepting the ∼29krad TID exposure rating as sufficient or within the range of what can accommodated using spot shielding,

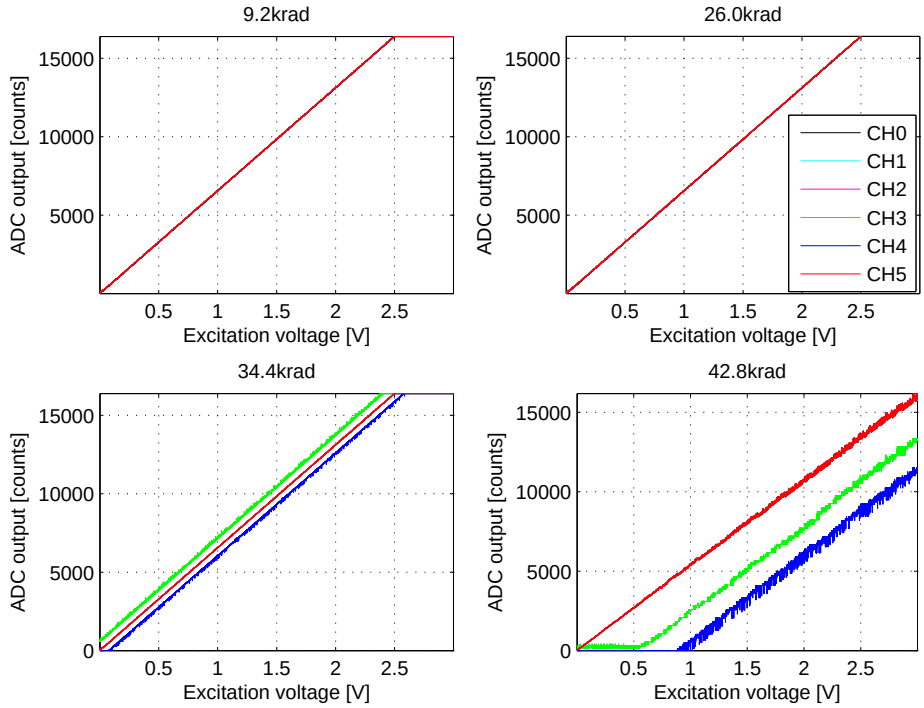

Figure 4.14. *LTC1408I raw channel outputs at discrete TID levels vs. excitation voltage.*

or alternatively qualifying another part. Within the framework of the development project, the irradiation performance of the LTC1408I has been deemed sufficient for the Tier One implementation.

4.7 Signal Filtering Strategy

The physical signal path between the accelerometers and the LTC1408I ADC has been designed to achieve three critical objectives:

- Migration from the single-ended nature of the LIS2L02AL output to the fully differential input of the LTC1408I.
- The separation of the LIS2L02AL output signal into DC and AC quantities.
- Anti-alias filtering to delimit the LIS2L02AL bandwidth to the relevant range and to reduce noise.

Single ended vs. differential signaling

The LTC1408I features differential inputs on all six channels, which constitutes a distinct advantage from a signal conditioning perspective, yet cannot be fully harness by the single ended outputs of the LIS2L02AL accelerometers. The hardware filtering stages of the μIRU must as such provides a means of optimally interfacing the accelerometer signal to the LTC1408I inputs.

DC and AC signal separation

As was demonstrated in [Bjarnoe-2007] DC measurements from the μIRU where unnecessary to obtain complementary fused operations with the μASC, rather including the DC response would lead to excessive long term stability issues that could otherwise be avoided. Analysis showed a signal bandwidth extending from ∼1Hz to ∼200Hz would encompass nearly all attitude disturbances known to exist on spacecraft, hence delimiting the accelerometer frequency range accordingly was deemed prudent. However, to facilitate calibration procedures along the lines of those proposed in Chapter 6, the instrument would benefit immensely from making the DC output data available as well. As such, the filtering strategy must accommodate both AC and DC response for all channels, but with emphasis on AC throughput.

AC filtering type selection

When discussing filter types the first step is to assess whether the bandpass requirements to the AC filter branch infer a narrow- or wide-band filter solution. As a wide-band bandpass filter can be realized by cascading low- and highpass stages this configuration offers advantages in terms of implementation modularity and simpler designs, yet offers superior performance for applications with relative wide pass-bands only. The assessment is made using the concept of percentage bandwidth P_B as introduced by [Lancaster-1977], which states that for percentages bandwidths below ∼80% the wide-band filter type will perform sub-optimally. For the application at hand P_B can be determined as:

$$P_B = 100\% \cdot \frac{f_H - f_L}{\sqrt{f_H * f_L}} = 100\% \cdot \frac{200Hz - 1Hz}{\sqrt{200Hz \cdot 1Hz}} \simeq 1407\% \qquad (4.7)$$

where,

- f_H denotes upper 3dB frequency $[Hz]$.
- f_L denotes lower 3dB frequency $[Hz]$.

The obtained result clearly suggests that a wide-band filtering approach should be utilized for optimal performance over the frequency band of interest. Figure 4.15 provides an overview of the proposed signal conditioning chain used

for a single accelerometer axis, and shows how DC and AC components are separated. It should be noted that due the LTC1408I A/D converter only having 6 channels, the DC components are multiplexed in pairs of two, hence the reduced samplerate for DC channels. Also it should be stressed that the DC channels are only intended for calibration and orthogonalization purposes. The AC channels will be used when fusing the μIRU and microASC data to reduce the influence of long term bias variations in the accelerometer outputs.

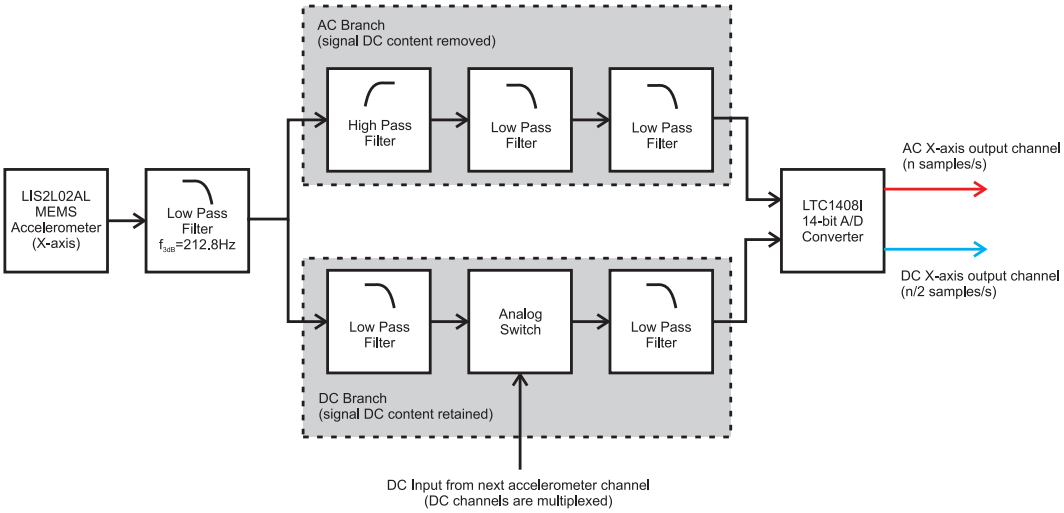

Figure 4.15. *Single channel signal conditioning chain topology.*

With the design values for the delimiting frequencies of the bandpass filter having been previously derived as $f_L = 1Hz$ and $f_H = 200Hz$ [Bjarnoe-2007] as well as the wide-band filter structure and the topology of Figure 4.15 being adopted, the following sections provide details regarding the implementation of individual filter stages.

4.7.1 Common Filter Stage 0

The first stage of the accelerometer signal filter chain is common to all subsequent filter stages and implemented in accordance with the manufacturer recommendations [ST-2006]. The LIS2L02AL accelerometer provides an output voltage proportional to incurred acceleration level with a nominal scale factor of 660mV/g and offset to half its supply voltage or 1.65V for the nominal 3.3V supply.

As illustrated by Figure 4.16, the LIS2L02AL accelerometer provides each output signal with a medium level output impedance set by an on-chip resistor specified in the interval $R_s = 110k\Omega \pm 30k\Omega$. The substantial production tolerances of this on-chip component constitute a natural artifact associated with the manufacturing process, yet despite the lack of precision, it provides the option of implementing a minimalistic single pole RC filter with a 20dB

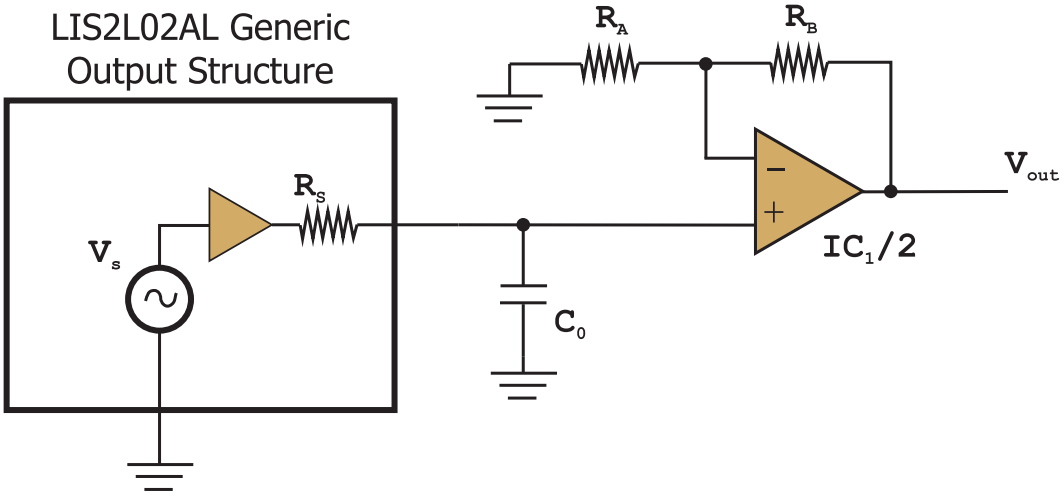

Figure 4.16. *μIRU stage 0 signal conditioning configuration.*

per decade roll off directly at the accelerometer by adding a single external capacitor. This output stage configuration of the accelerometer is particularly advantageous for the range of commercial applications where mainly low frequency content measurements are needed, as the bandwidth and thereby the sensor noise can be suppressed directly while maintaining a signal conditioning interface which requires a minimum of external components. [ST-2006] specifies a minimum load capacitance of $C_0 = 1nF$ to maintain stability and to ensure bandwidth limiting below the 2.0kHz resonating frequency of the LIS2L02AL accelerometer proof mass.

For the μIRU application, stage 0 further incorporates a non-inverting opamp buffer stage. This buffer is intended to provide suitable drive capability to subsequent filter stages and to provide a means of introducing signal gain directly at the sensor level if deemed necessary at some point in the μIRU prototyping process. The nominal configuration will implement a unity gain solution by setting $R_B = 0$ and leaving R_A unmounted in reference to Figure 4.16. IC_1 is a rail-to-rail input/output operational amplifier (opamp) incorporated into the design in a ratiometric configuration with the LIS2L02AL accelerometer. The /2 designation serves to indicate that the opamp used is in fact a dual channel version, with one opamp assigned to either of the two output axes of the LIS2L02AL accelerometer. Again, a number of operational amplifier candidates have been surveyed for use in the filter branches of the μIRU prototype, a subset of which are compared in Table 4.2 with regards to key specifications in relation to the μIRU application. The primary areas of concern pertaining to opamp selection naturally encompass noise and environmental performance, yet considering the total number of devices required for eight identical filter branches, power consumption and physical size also becomes critical parameters influencing device selection, as does the ability to simplify the design by using the same opamp throughout the system.

Device	Supply Range [V]	Consumption [μW@3.3V$_{in}$]	Noise Voltage (0.1Hz-10Hz) [μV_{RMS}]	V. Noise Density ,f=10kHz [$nV/\sqrt{Hz}$]	C. Noise Density [$pA/\sqrt{Hz}$]	Offset Voltage [μV]	Gain Bandwidth Product [kHz]	Package	Operating Temperature [°C]
MAX4092	2.7↔6	430	16	12	1.5	30	500	μMAX	-40↔85
MAX4236	2.4↔5.5	1160	0.2	14	-	20	1700	SC70	-40↔85
MAX4452[a]	2.7↔5.25	1750	-	15	0.5	400	80000	SC70	-40↔85
MAX412[b]	2.4↔5.25	8250	0.1	1.5	1.2	120	28000	SC70	-40↔85
AD8552	2.7↔5.5	3135	1.6	75	0.002	1	1500	μSOP	-40↔125
AD8613	1.8↔5.0	165	2.3	22	0.05	400	350	SC70	-40↔125
LMP2011	2.7↔5.0	3630	0.85	35	-	25	3000	SOT23	-40↔125
LMV358	2.7↔5.5	260	-	36	-	1700	1200	SOT23	-40↔125

[a] Presently on the μASC declared components list (DCL).
[b] Previously on the μASC DCL.

Table 4.2. *COTS rail-to-rail operational amplifiers surveyed for μIRU filtering chain application.*

Of all the opamps surveyed the MAX4092 and the MAX4236 where selected for irradiation screening. The MAX4092 with the intention of it being employed as the generic opamp throughout the μIRU system, as it provides reasonable noise performance with very limited power consumption. Moreover, it is available in a dual opamp version in the 3mm×5mm μMAX packaging, which is suitable for achieving high density PCB layouts. The MAX4236 provides better noise performance near DC and thus it was selected to be used in the common re-biasing/offset generating circuit for the filter branches described in further detail in Section 4.7.4. Both devices passed irradiation screening, with the MAX4092 experiencing no degradation at all over 210krad exposure, and the MAX4236 degrading gracefully beyond 30krad TID. The details of these tests have been included in Appendix C.

It should be noted that the minimalistic approach to the stage 0 design is adopted to retain the possibility of implementing this filter stage directly onto the sensor PCB for optimal performance. As the flight implementations of this board are intended to reach a physical scale of less than 5mm × 10mm × 1mm, only very limited surface area remains available and consequently the PCB area subtended by filter stage 0 must be minimized.

Based upon the schematic designations in Figure 4.16 an idealized, lossless transfer function for Stage 0 $H_{stage0}(s)$ can be formulated as outlined by equation 4.9.

$$H_{stage0}(s) = \frac{V_{out}(s)}{V_s(s)} = \frac{R_A + R_B}{C_0 R_s R_A s + R_A} \tag{4.8}$$

$$A_{stage0} = 1 + \frac{R_B}{R_A} \tag{4.9}$$

where:
A_{stage0}: denotes stage 0 gain $[V/V]$.

For the unity gain implementation with R_A unmounted and $R_B = 0$, equation 4.9 reduces to:

$$H_{stage0}(s) = \frac{V_{out}(s)}{V_s(s)} = \frac{1}{C_0 R_s s + 1} \tag{4.10}$$

Plotting equation 4.10 as a function of frequency for the worst case parametric combinations of circuit component values ($R_s = 110k\Omega \pm 30k\Omega$, $C_0 = 6.8nF \pm 5\%$) results in the response envelope illustrated in Figure 4.17. It is clear that the difficulties associated with implementing accurate large scale resistors in integrated circuitry affects the performance of this filter stage by allowing significant deviations in cutoff frequency to occur for different instances of the same implementation.

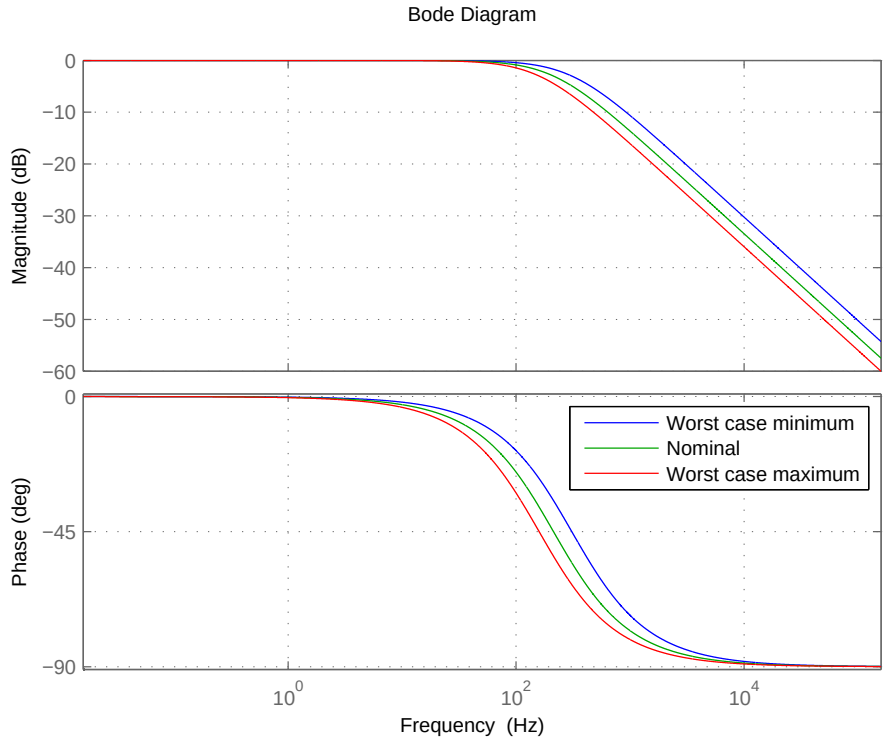

Figure 4.17. *μIRU prototype filter stage 0 bode plot.*

The theoretical noise performance of stage 0 should ideally be governed by the contribution from the accelerometer sensor. To verify that this is indeed the case, a noise analysis for the nominal unity gain case is conducted using the configuration model depicted in Figure 4.18 and the formalization of the Equivalent Noise Bandwidth (ENB) principle as introduced by

[TI-1999, Areny-2001]. Note that the analysis prerequisites include using the Maxim Integrated Products MAX4092AUA dual opamp as IC_1, as well as the assumptions that C_0 constitutes a noiseless entity and the individual noise sources being uncorrelated.

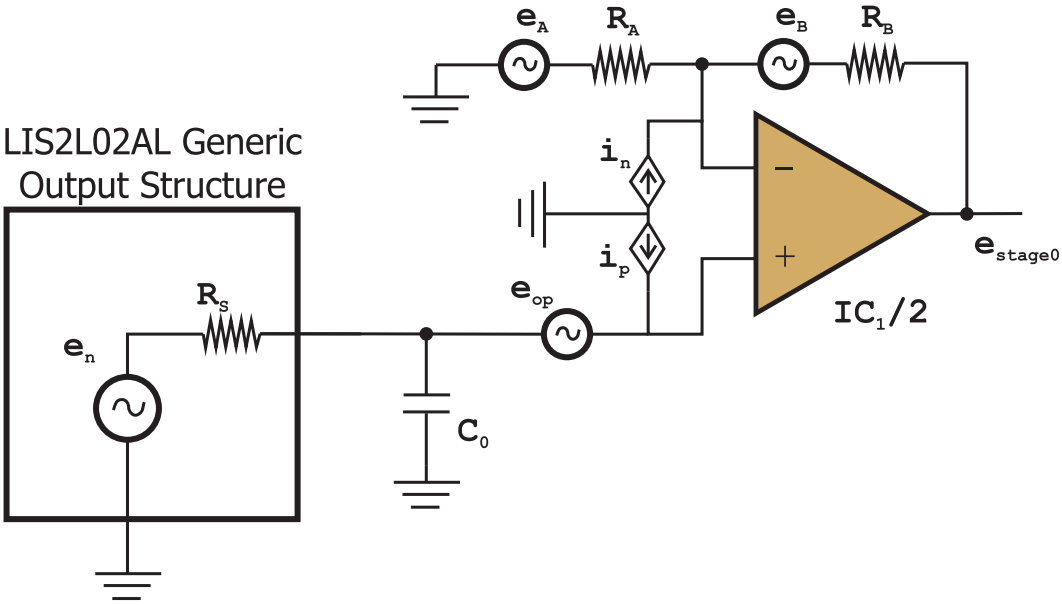

Figure 4.18. *Common filter stage 0 noise analysis model.*

Quantifying the output noise contributions from the individual sources depicted in Figure 4.18 yields equation 4.11 through 4.18, where k signifies the Boltzmann constant, T the absolute temperature, and B, f_H, f_L delimit filter bandwidth, upper and lower frequency bound, respectively:

Accelerometer Contribution:

$$\begin{aligned} \overline{E}^2_{acc} &= \int_0^\infty |A_n(f)|^2 (s_a n_d)^2 \, df \cdot \left(\frac{R_A + R_B}{R_A} \right)^2 \\ &= (s_a n_d)^2 \left(\frac{R_A + R_B}{R_A} \right)^2 \int_0^\infty \frac{1}{(2\pi f R_s C_s)^2 + 1} \, df \end{aligned} \tag{4.11}$$

where:
$A_n(f)$: signifies the frequency dependent filter gain.
s_a: denotes the accelerometer scale factor $[mV/g]$.
n_d: denotes the accelerometer output noise density $[g/\sqrt[Hz]{}]$.

Resistor Thermal Noise Contributions:

$$\overline{E}_{tA}^2 = 4kBTR_A \left(\frac{R_B}{R_A}\right)^2 \tag{4.12}$$

$$\overline{E}_{tB}^2 = 4kBTR_B \tag{4.13}$$

Resistor Excess Noise Contributions:

$$\overline{E}_{eA}^2 = 0.66NI \cdot V_{DC}\sqrt{\ln\frac{f_H}{f_L}}\left(\frac{R_B}{R_A}\right)^2 \tag{4.14}$$

$$\overline{E}_{eB}^2 = 0.66NI \cdot V_{DC}\sqrt{\ln\frac{f_H}{f_L}} \tag{4.15}$$

Operational Amplifier Noise Contributions:

$$\overline{E}_{op}^2 = \int_{f_L}^{f_H}\left(e_{op}\left(\frac{R_A+R_B}{R_A}\right)\right)^2 df \tag{4.16}$$

$$\overline{E}_{in}^2 = \int_{f_L}^{f_H}\left(i_n R_B\right)^2 df \tag{4.17}$$

$$\overline{E}_{ip}^2 = \int_{f_L}^{f_H}\left(i_p R_s\left(\frac{R_A+R_B}{R_A}\right)\right)^2 df \tag{4.18}$$

Compounding equation 4.11 through 4.18 and adding the $1/f$ input referred voltage noise specification of the MAX4092AUA of $\overline{E}_{op,f} = 16\mu V_{RMS}$ allows the total stage RMS output noise to be assessed as:

$$\overline{E}_{RMS} = \sqrt{\overline{E}_{acc}^2 + \overline{E}_{tA}^2 + \overline{E}_{tB}^2 + \overline{E}_{eA}^2 + \overline{E}_{eB}^2 + \overline{E}_{op}^2 + \overline{E}_{in}^2 + \overline{E}_{ip}^2 + \overline{E}_{op,f}^2} \tag{4.19}$$

Applying these equations to the physical combination of the LIS2L02AL MEMS accelerometer and the associated stage 0 filter yields the noise budget given in Table 4.3. The 1σ RMS values provide a clear illustration of how the accelerometer noise density contribution dominates the total output noise as would be expected for a well conditioned stage 0.

Contribution	Min [μV_{RMS}]	Nom [μV_{RMS}]	Max [μV_{RMS}]
$\overline{E}_{acc}$	313	362	435
$\overline{E}_{tA}$	-	-	-
$\overline{E}_{tB}$	0	0	0
$\overline{E}_{eA}$	-	-	-
$\overline{E}_{eB}$	0	0	0
$\overline{E}_{op}$	0.43	0.43	0.43
$\overline{E}_{in}$	0	0	0
$\overline{E}_{ip}$	1.75	2.40	3.05
$\overline{E}_{op,f}$	16	16	16
Totals:	**313.44**	**362.36**	**435.3**

Table 4.3. *LIS2L02AL accelerometer and stage 0 filter noise budget.*

4.7.2 AC Filter Stages 1 Through 3

The AC filter stages serve to connect the output of the accelerometer (as derived from the output of common filter stage 0) to the A/D converter, while realizing an AC coupling of the signal to remove the DC content. Moreover, as the signal requires re-biasing after AC coupling to allow A/D conversion by the LTC1408I, an active stage 1 was adopted to augment the drive capability of the AC coupled signal. Stage 2 is thus added in reference to good engineering practice by band limiting the noise contribution from the amplifier. This single-pole RC band limiter is put at a frequency close to f_H in order to ameliorate anti-aliasing performance of the signaling chain.

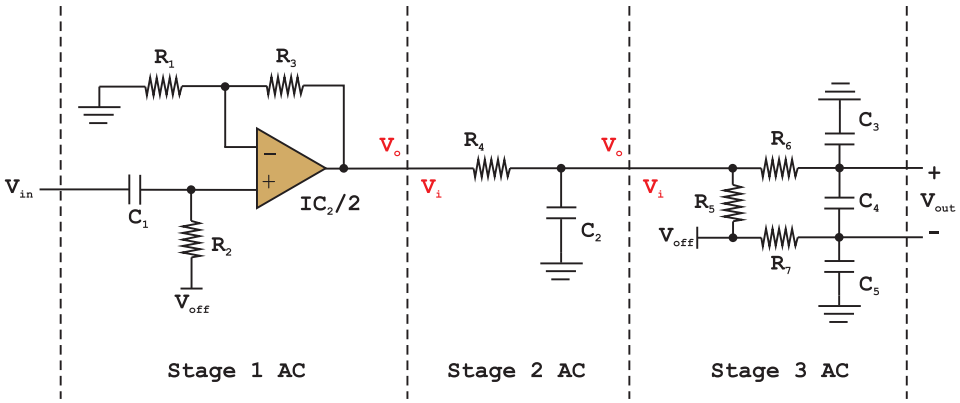

Figure 4.19. *μIRU data conversion module AC filter stages 1 through 3 electronic configuration.*

The purpose of stage 3 is not to incorporate a specific filter response as such, rather the low pass characteristic is a natural artifact of the necessary circuitry to correctly bias the differential ADC inputs. Passive component values in

stage 3 are though exceedingly small (f_{3dB} in the MHz range), effectively voiding its influence in the frequency region of interest. From Figure 4.19 the transfer functions pertaining to the individual AC filter stages can be derived as equations 4.22 through 4.24. The nominal configuration calls for unity gain implementation throughout the signaling chain, yet the prototype incorporates the possibility of introducing hardware gain in the AC filter branch stage 1 if deemed necessary at any point during development.

$$H_{stage1_{AC}}(s) = = \frac{V_o(s)}{V_{in}(s)} = \frac{C_1R_2(R_1+R_3)s}{R_1(C_1R_2s+1)} \tag{4.20}$$

$$A_{stage1_{AC}} = 1 + \frac{R_3}{R_1} \tag{4.21}$$

where:
$A_{stage1_{AC}}$: denotes stage 1 gain $[V/V]$.

For the unity gain implementation with R_1 unmounted and $R_3 = 0$, equation 4.20 reduces to:

$$H_{stage1_{AC}}(s) = \frac{V_o(s)}{V_{in}(s)} = \frac{C_1R_2s}{R_1(C_1R_2s+1)} \tag{4.22}$$

$$H_{stage2_{AC}}(s) = \frac{V_o(s)}{V_i(s)} = \frac{1}{C_2R_4s+1} \tag{4.23}$$

$$H_{stage3_{AC}}(s) = \frac{V_{out}(s)}{V_i(s)} \tag{4.24}$$

$$= \frac{(C_4+C_5)R_7s+1}{(C_3(C_4+C_5)+C_4C_5)R_6R_7s^2+((C_3+C_4)R_6+(C_4+C_5)R_7)s+1}$$

where:
R_5: has been left unmounted.

Calculating the frequency responses of the individual stage transfer functions using the nominal component values yields the Bode plots depicted in Figure 4.20, clearly showing the corner frequencies of the individual stages.

Note that noise analysis calculations similar to those established for stage 0 have also been performed upon the entire AC filter chain, showing the total output referred noise voltage pertaining to the AC filter chain being dominated by accelerometer sensor noise as intended.

Part	Value
R_1	N/A
R_2	330kΩ
R_3	0
R_4	47kΩ
R_5	N/A
R_6	51Ω
R_7	51Ω
C_1	450nF
C_2	12nF
C_3	47pF
C_4	47pF
C_5	47pF

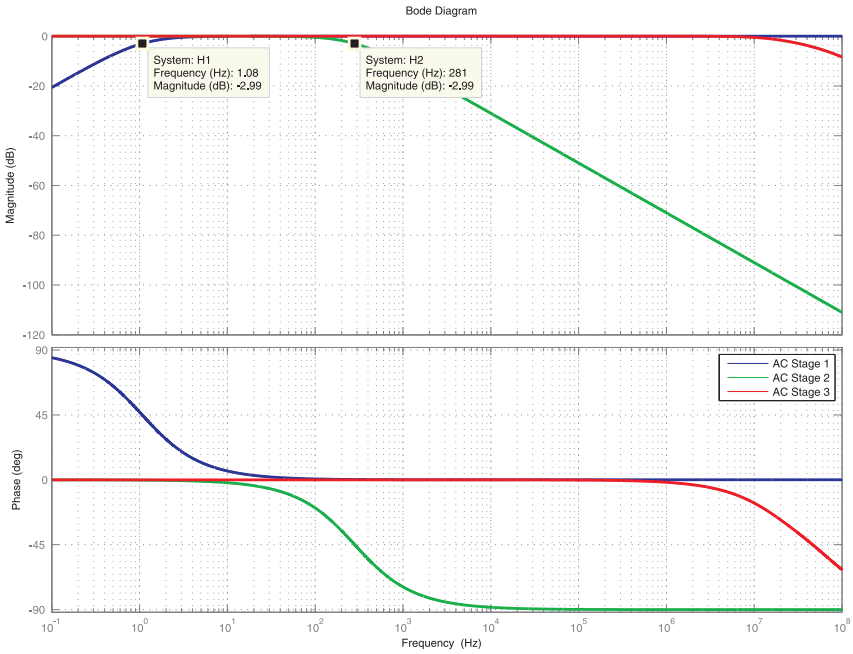

Figure 4.20. *Component values in reference to Figure 4.19 and Bode plots for individual AC filter stages.*

4.7.3 DC Filter Stages 1 and 2

As previously established the μIRU DCM features two six channel ADCs for a total of twelve simultaneously sampled channels. Of these only four can be assigned to the total eight DC channels thus necessitating each ADC to accommodate four DC signals on two input channels using multiplexing. As such, the multiplexing filter structure depicted in Figure 4.21 has been devised as a means of alternately coupling the X-axis signal and the Y-axis signal from a single accelerometer to the same ADC input channel.

The only active part involved in this coupling is the analog switch used as multiplexer. This device has been again been selected based upon an exhaustive survey and subsequent thermal and TID screening, the details of which are elaborated upon in Appendix C. Based upon these evaluations and the ability of the device to sustain >45krad TID without degradation, led to the selection of the Maxim IC MAX4736 dual channel analog switch for this application.

$$H_{stage_{1_{DC}}}(s) = \frac{V_o(s)}{V_{in}(s)} = \frac{1}{C_6 R_8 s + 1} \tag{4.25}$$

$$\begin{aligned} H_{stage_{2_{DC}}}(s) &= \frac{V_{out}(s)}{V_i(s)} \\ &= \frac{(C_8 + C_9)\, R_{12} + 1}{\xi s^2 + ((C_7 + C_8)R_{on} + C_7 R_{11} + C_8(R_{11} + R_{12}) + C_9 R_{12})s + 1} \end{aligned} \tag{4.26}$$

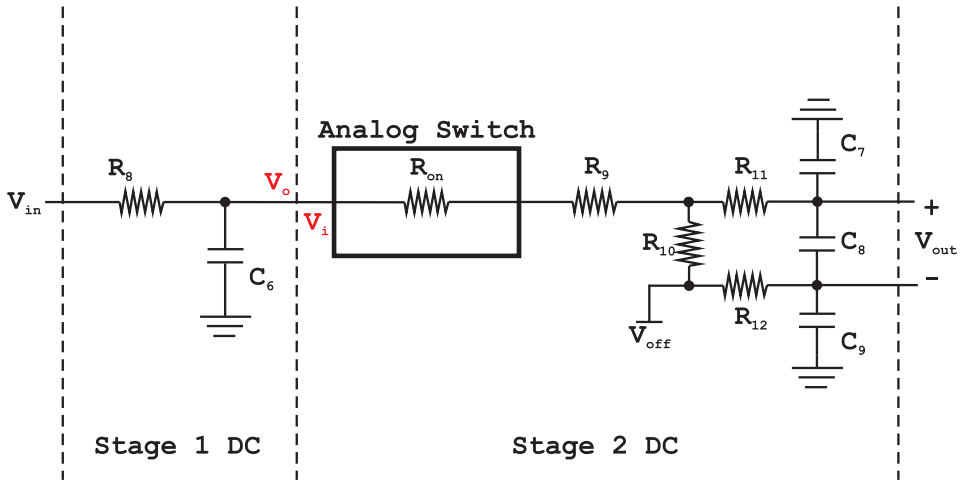

Figure 4.21. *μIRU data conversion module DC filter stages 1 through 2 electronic configuration.*

where:
ξ: signifies $((C_7(C_8 + C_9) + C_8C_9)(R_{on} + R_{11})R_{12})$.
R_{10}: has been left unmounted.

With the stage transfer functions established, the Bode plots are derived for the nominal component selection outlined in Figure 4.22. This configuration positions the -3dB roll-off for the first DC stage at 282Hz to avoid reducing the overall system amplitude response to much below 200Hz when the system is combined with stage 0.

As for the AC filter stages, noise analysis has also been performed upon the DC filter stages. This analysis shows the total output referred noise voltage pertaining to the DC filter chain being governed by the accelerometer sensor noise, as would be the case for a well conditioned filter chain.

Having established the characteristic of the individual stages in the μIRU prototype filter branches, the combined system depicted in Figure 4.23 represents the overall filtering topology of the DCM design for a single accelerometer output channel.

From here a unified transfer function and the associated frequency response for either DC or AC channels can be determined. The Bode plots for both AC and DC channels are compared in Figure 4.24, as are their respective step responses.

The full signal conditioning chain is seen to provide both an AC and a DC coupled version of the accelerometer output, with the lower cutoff frequency in the AC branch at $f_{L,-3dB} = 1Hz$ and the upper cutoff frequency for both AC and DC branches at $f_{H,-3dB} = 156Hz$. The latter specification is arrived at through the convolution of the stage 0 and stage 1 DC/stage 2 AC frequency

Part	Value
R_8	47kΩ
R_9	10Ω
R_{10}	N/A
R_{11}	51Ω
R_{12}	51Ω
R_{on}	0.6Ω
C_6	12nF
C_7	47pF
C_8	47pF
C_9	47pF

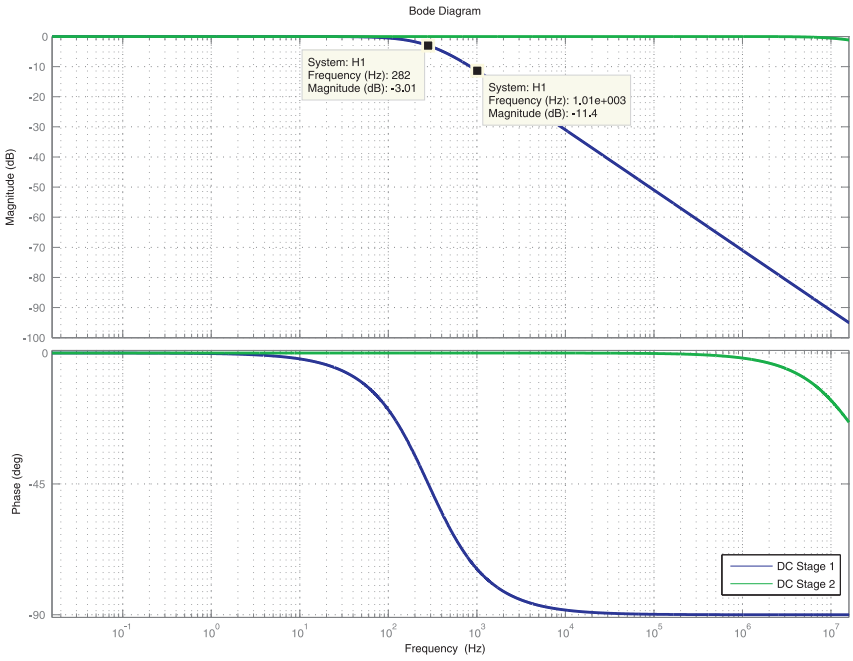

Figure 4.22. *Component values in reference to Figure 4.21 and Bode plots for individual DC filter stages.*

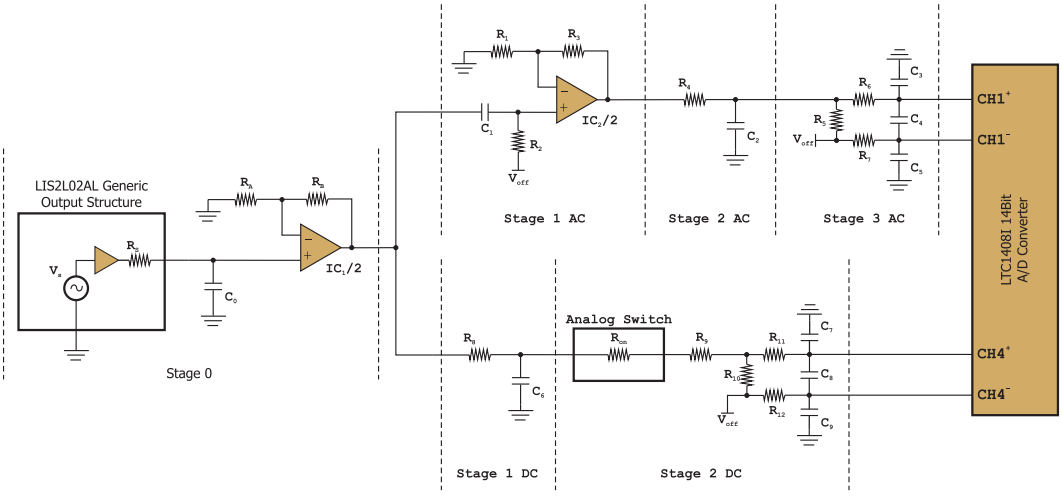

Figure 4.23. *Full signal path of a single accelerometer channel in the μIRU augmentation. The combination of AC stages 1-3 and DC stages 1-2 thus constitutes half a filter branch implementation as illustrated in the Figure 4.6 overview.*

responses. Moreover, a certain a limited phase shift is observed within the passband of the AC filter branch, yet this can be directly compensated in post-processing, by including the applicable AC transfer function model in the μIRU accelerometer state estimation algorithm.

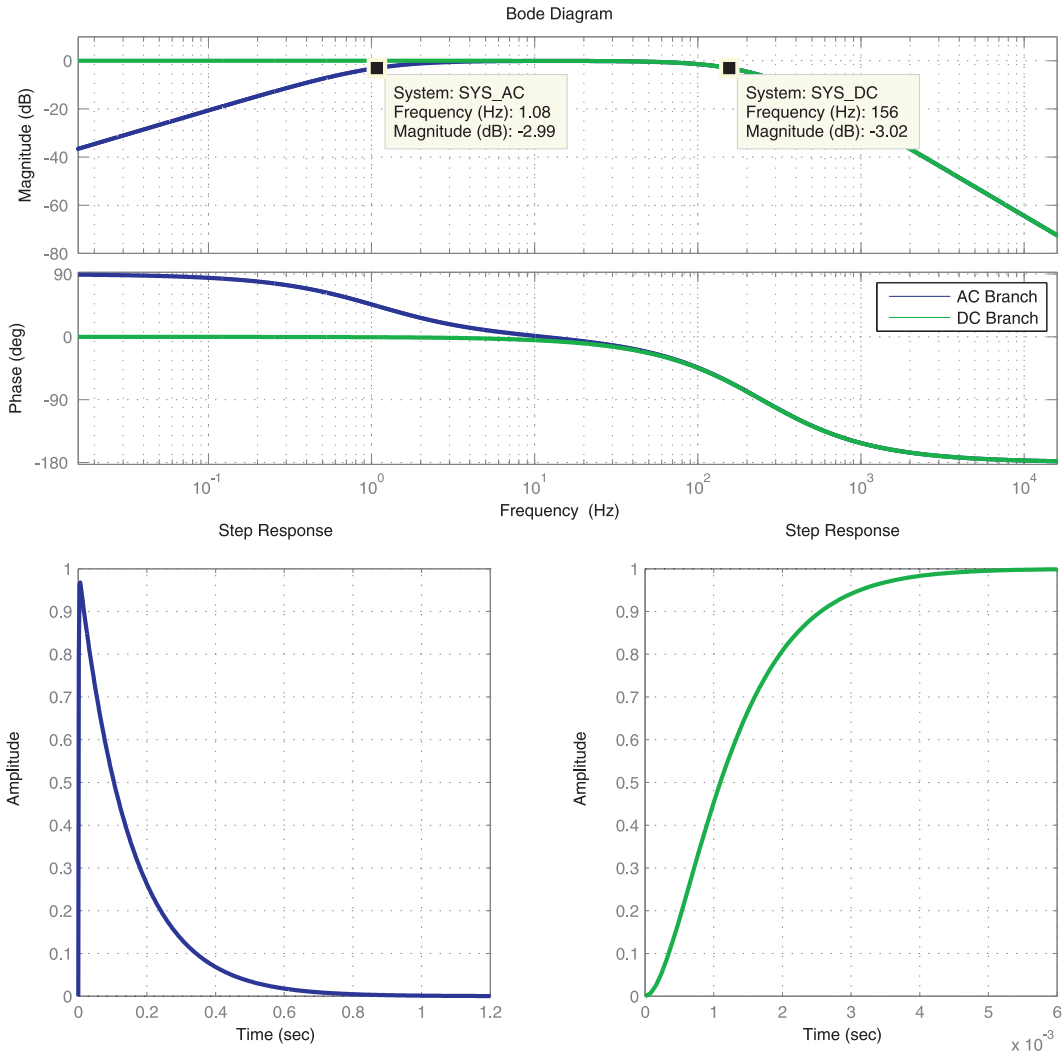

Figure 4.24. *Bode plot and step response of full AC and DC systems including stage 0 contribution.*

4.7.4 DC Re-Biasing and Offset Generation Stage

As observed in Figure 4.23 the accelerometer signal chain is fed an offset voltage at certain points, namely AC stage 1 and 3, as well as DC stage 2. The offset voltage is generated by the circuit shown in Figure 4.25, and locks in ratiometrically with the ADC external reference voltage, as its input is derived hereof.

The circuit employs the low noise MAX4236 opamp previously described, and the offset voltage generated is used in all accelerometer channels for both ADCs. Principally the offset stage allows a pseudodifferential signal to be generated by re-biasing the AC coupled signal with the V_{off} voltage. Subsequently, stage 3 AC facilitates the differencing of the combined signal again with respect to V_{off} in the ADC conversion process. This concept allows the

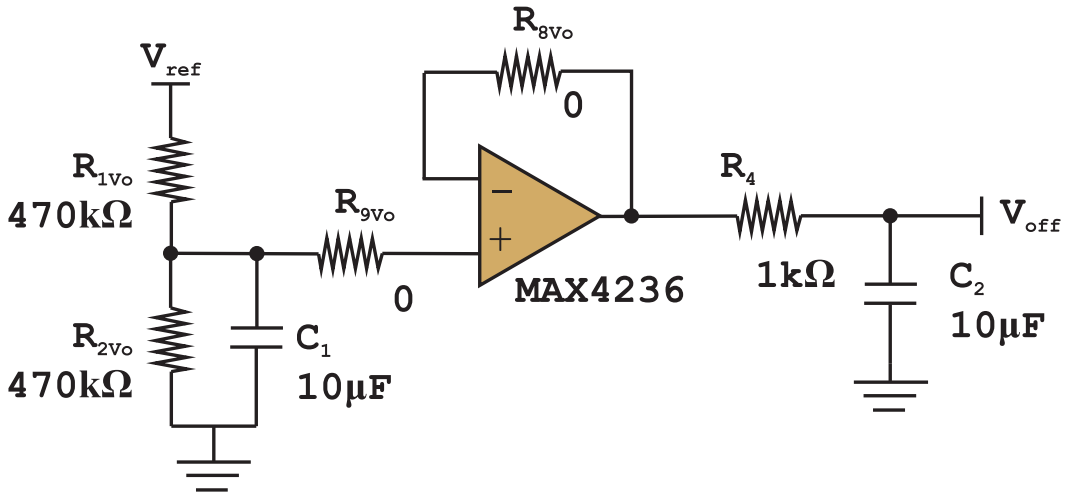

Figure 4.25. *Re-biasing and offset generator stage.*

excellent common mode rejection of the differential ADC input to be fully utilized, even though the signal source is single-ended.

Additionally the circuit performs a necessary function when re-biasing the AC coupled signal to near mid-range with respect to the ADC reference voltage, thus making it possible to operate the ADC in bipolar mode from a single voltage only. From systems perspective this simplifies the implementation of the conversion circuit immensely. Moreover, operating the offset voltage level ratiometrically with the ADC external reference, ensures the AC channel bias exhibit extremely low noise levels and very limited long term drift, which translates directly into enhanced quality of the converted quantities.

The notion of re-biasing all AC coupled accelerometer channels to the same voltage level and subsequently converting the signal with respect to that same offset voltage, introduces an added benefit when considering differential operations between two accelerometer signals (eg. $V_{ACC1,X}$ from ADC1 and $V_{ACC3,X}$ from ADC2). In the voltage domain having identical reference level and offset level for both ADCs essentially removes all common mode signals, thus reducing the simplified differencing expression to the following relation:

$$\begin{aligned} V_{diff,X} &= \left(\frac{(V_{ACC1,X} - V_{off})}{V_{ref}} + \bar{e}_{ADC1}\right) - \left(\frac{(V_{ACC3,X} - V_{off})}{V_{ref}} + \bar{e}_{ADC2}\right) \\ &= \frac{V_{ACC1,X} - V_{ACC2,X}}{V_{ref}} + \sqrt{\bar{e}^2_{ADC1} + \bar{e}^2_{ADC2}} \end{aligned} \tag{4.27}$$

When considering the ADC reference noise contributions $\bar{e}_{ADC1}$ and $\bar{e}_{ADC2}$ as being uncorrelated. Effectively this approach succeeds in making the exact re-biasing and offset level inconsequential for differential operations between the accelerometers.

With regards to the DC channels Figure 4.23 shows these being differenced from the offset level as well during conversion. This conversion strategy is a necessity which arises from the ADC being operated in bipolar mode to best accommodate the AC channels, and hence is only capable of converting signals within $\pm V_{ref}/2$ from 0V. As such, the latent 1.65V bias ($V_{supply}/2$ for the accelerometers) of the DC channels makes direct conversion impossible, wherefore the offset voltage of ∼1.5V is employed in the differencing conversion. Naturally this approach provides a substantial offset in in the DC output data which must be calibrated, yet it ensures that the full ±2g range of the accelerometer output is accommodated for the DC channels as well.

4.8 Power Distribution Topology

Collocated in the μASC CHU, the μIRU augmentation relies entirely upon the existing interface connections between the CHU and DPU. As such, no dedicated power supply line can be assigned to the μIRU, and the required voltage levels must thus be generated from levels already used in the CHU. The CHU features three internally accessible voltage levels namely -9V, +5V and +15V. Of these, +5V and 15V are supplied from the DPU via the harness, whereas -9V is generated internally in the CHU using a push-pull inverting stage coupled between the +5V and +15V rails. This voltage converter stage is locked to the CL clock signal derived from the CHU primary clock to avoid asynchronous noise impacting the camera performance. As the -9V line is only used as a reference rail for the CCD it has been tailored to support only minor loads. As such, external usage of the -9V line will affect its tuned stability, thus adversely affecting the CCD noise levels which would be unacceptable.

With regards to the +5V and +15V lines both are directly subject to SEL detection and mitigation in the DPU power supply, and particularly the former is designed to support higher loads as the bulk of the CHU electronics operate of this rail. The μIRU has been designed to operate at +3.3V for optimal compatibility with the LIS2L02AL accelerometer and the LTC1408I A/D Converter as well as to minimize power dissipation and the associated thermal impact on the CHU. Hence it seems prudent to power the μIRU from the +5V rail to ascertain the minimum span between the CHU and μIRU rails.

The design of the power conditioning circuitry required for deriving the +3.3V supply voltage from the +5V rail has been heavily influenced by the primary requirement to not operate circuitry at asynchronous frequencies with respect to the CHU primary clock within the physical framework of the μASC CHU. Therefore a configuration has been sought which provides adequate conditioning and stability levels in a non-active manner, effectively limiting the solu-

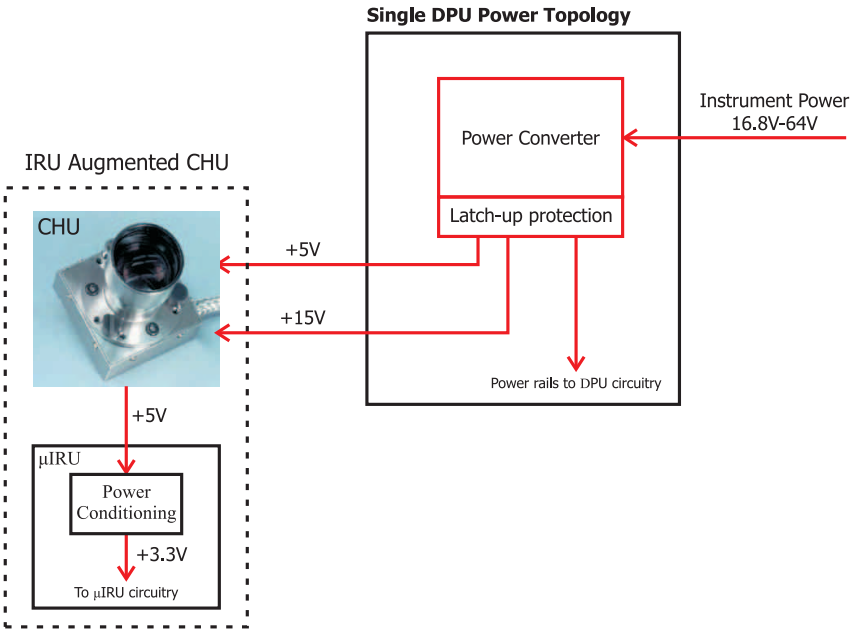

Figure 4.26. *μIRU agumented μASC power system topology [SIG-2006a].*

tion space to resistive division, diode coupling, shunt regulators (Zener and avalanche diodes) or low dropout regulators (LDO). To assess the viability of either solution a preliminary power budget was construed as outlined by Table 4.4. The first thing that should be remarked with regards to the power budget is the clear discrepancy with regards to the μASC derived requirement specification of limiting μIRU consumption to $> 35mW$. As seen that limit is broken by the four accelerometers and two ADCs alone, thus giving a clear indication that meeting this requirement will be near impossible for the current electronics configuration.

As further illustrated by the preliminary power budget, deriving the 3.3V supply voltage from the +5V CHU rail using resistive division would be highly inefficient. Similarly, dropping the 1.7V over a diode coupling is possible but could potentially introduce an undesirably large temperature dependency of the supply voltage. With regards to the Zener option this is indeed desirable considering the high performance levels associated with these devices with respect to noise, thermal and long term stability, yet its use is rejected due to the high generic sensitivity to high energy particle exposure as reported by [Merayo-1999]. The remaining option of utilizing a LDO for power conditioning is highly desirable in terms of design compactness, component count and supply voltage quality levels.

A number of suitable COTS LDOs for 5V→3.3V migration has been surveyed (as listed in Table 4.5), and a few evaluated for this particular application. Particularly fixed output parts have been sought to minimize the number of additional parts required. In the end, the primary candidate LP2985A from

μIRU Augmentation Preliminary Power Budget			
Part	**Function**	**Number used**	**Consumption** [mW]
LIS2L02AL	Accelerometer	4	11.2
LTC1408I	A/D Converter	2	26.4
ATmega168	Microprocessor	1	9.9(@8MHz)
REF5030I	ADC Reference	1	4.0
MAX4092	Filter opamp	16	6.9
MAX4236	Precision opamp	1	1.1
MAX4736	Analog switch	2	0.0066
DS18B20U	Temp. sensor	1	5.0
Misc.	Res loads, etc.	-	10
		Total:	**74.5**
		Total with 20% margin:	**89.4**

Table 4.4. *μIRU Augmentation Preliminary Power Budget derived from part specifications.*

Device	**Manufacturer**	**Technology**	**Supply Range [V]**	**Consumption [μW@5V$_{in}$]**	**Nom. Dropout Voltage [mV]**	**Output Voltage/Current [V]/[mA]**	**Tolerance [%]**	**Output Voltage Noise [μV_{RMS}]**	**Package**	**Operating Temperature [°C]**
MAX8840	Maxim IC	PMOS	2↔6	200	120	3.3/150	±2	13	μDFN-6	-40↔85
MAX8891	Maxim IC	PMOS	2↔6	200	120	3.3/150	±3	230	SC70-5	-40↔85
LP2985A	Natnl. Semi.	PNP	2.5↔16	1100	110	3.3/150	±1	30	SOT23-5	-40↔125
TPS71433	Texas Instr.	PMOS	2.5↔10	24	310	3.3/80	±5	575	SC70-5	-40↔125
TPS71733	Texas Instr.	PMOS	2.5↔6.5	500	300	3.3/325	±3	38	SC70-5	-40↔125
FAN2500	Fairchild	PMOS	2.7↔6.5	125	100	3.3/100	±5	225	SOT23-5	-40↔125

Table 4.5. *Survey of commercially available 3.3V fixed output low dropout regulators.*

National Semiconductor was selected over the MAX8840 from Maxim IC for TID screening and subsequent μIRU Tier One prototyping. The selection was made based on several features in the LP2985A design including the tight 1% output tolerance, low ground current and PNP based bipolar architecture. The latter distinguishes itself from the majority of competing devices which utilize MOS-based topologies, but does in turn represent an interesting perspective from an irradiation tolerance perspective.

4.8.0.1 LP2985A Irradiation Screening

When subjecting the LP2985A LDO regulator to irradiation screening, a basic test setup was created which mimics the loading applied to the part when

employed in the μIRU. As such, it was fed a +5V supply voltage and tasked with providing a +3.3V output voltage to a 220Ω resistive load, representing the μIRU minimum load. Also a reverse bias BAT54S Schottky diode was added between the input and the output of the part. The results of this test are included as Figure 4.27.

As the data clearly illustrates, the LP2985A incurs no functional impairment over 50krad exposure. Moreover, the part manages to maintain the output voltage within 0.8% of the starting value throughout the test, and the current consumption tracks this behavior. In terms of irradiated response, common failure modes of the generic LDO design will often pertain to its bandgap reference or the threshold voltage of the PMOS gate, however as the LP2985A uses a bipolar pass element it should theoretically be more prone to the latter, yet no adverse effects can be observed directly. In all the irradiation screening results for the LP2985A LDO are very positive, and pending SEE susceptibility testing no radiation issues have been identified which would preclude its use in the μIRU augmentation.

4.9 μIRU ADC External Reference Design

The μIRU ADC reference contributes a determining factor in establishing the LSB size and thereby the resolving power of the sampling system. The Linear Technology LTC1408I 14Bit six channel A/D Converter selected for the μIRU features an internal 2.5V reference, however, as was shown during the course of the ADC selection process, the long term stability of said reference when exposed to ionizing radiation is limited. Moreover, the baseline electronics design of the μIRU calls for a minimum of two six channel ADCs in the implementation, and to achieve identical thermal and irradiative responses from both, a single dedicated external reference will deliver a common well-conditioned reference voltage to both ADCs. Although it should be noted that using a single external voltage reference for both ADCs will not ameliorate the differences between the resistive ladders in each ADC, even though vast improvements in the matching between converted quantities pertaining to each ADC is obtained.
As specified by the manufacturer, the internal reference of the LTC1408I must be overdriven with a stable external voltage of at least 2550mV (50mV higher than the internal reference voltage), if an external reference is to be used. This drive level requirement together with thermal and irradiative tolerances constitute the preeminent requirements to choosing the external reference generator.

Of the reference technologies considered particularly two separate types provide reasonable over performance over temperature without necessitating ovenized thermal control, those being bandgap (Series) and zener (Shunt) type devices. Although zeners provide excellent long term stability and very low

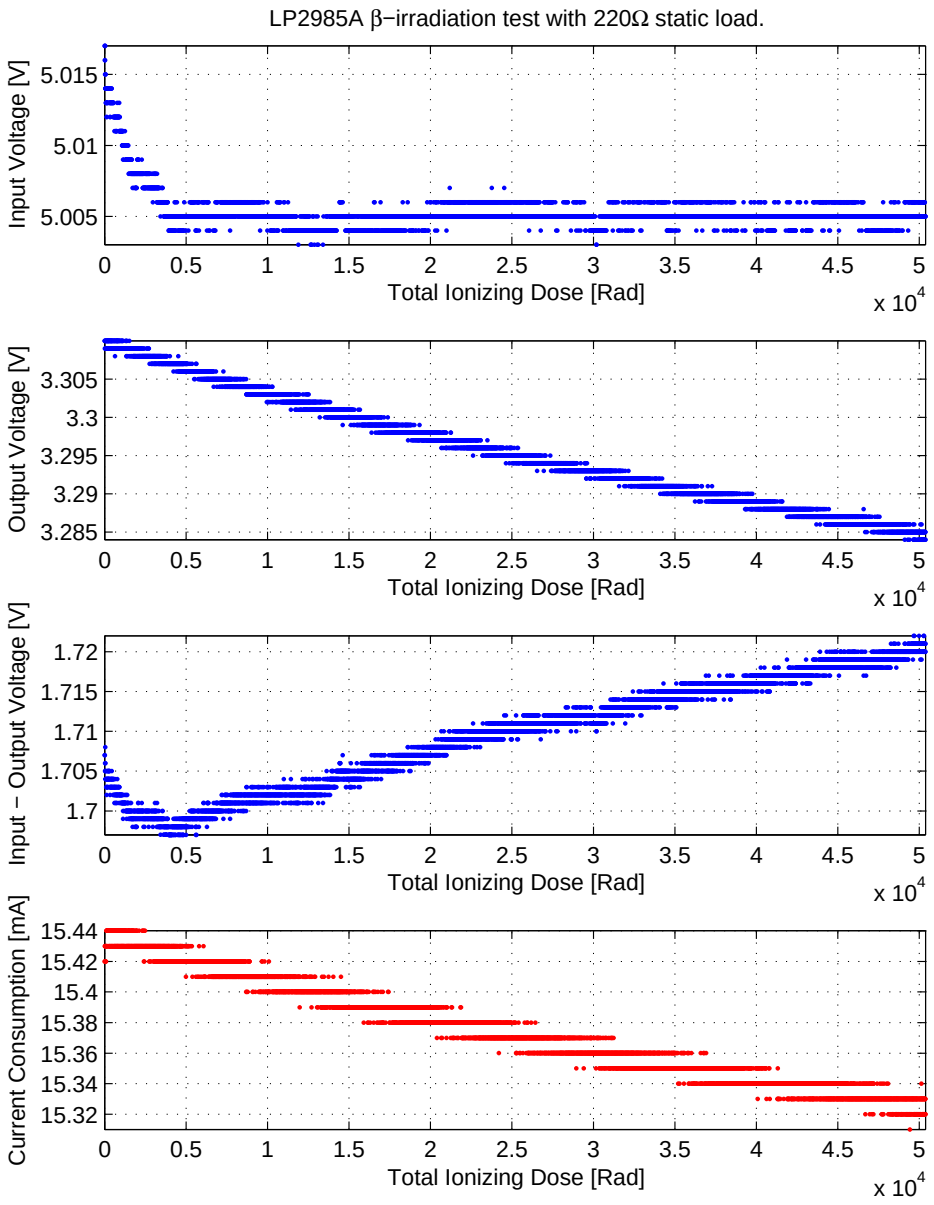

Figure 4.27. *LP2985A Low Dropout Regulator β-irradiation test data. Screening test conducted with a 220Ω static load to mimic μIRU minimum load. Data corrected for attenuating effects pertaining to the component packaging, hence TID is delivered to device die.*

noise output noise voltage these are however disregarded for the μIRU application as generic zener devices are know to exhibit sensitivity to high energy particle exposure [Merayo-1999].

Device	Manufacturer	Technology	Consumption [μW@5V_{in}]	Output Voltage[V]	Tolerance [%]	Output Voltage Noise [μV_{RMS}] (0.1Hz-10Hz)	Long-Term Drift [$ppm/\sqrt{kHr}$]	Temperature Coefficient [$ppm/^{\circ}C$]	Package
REF5030I	TI	Bandgap	4	3.0	±0.05	6.4	2.2	3	MSOP-8
AD780AR	ADI	Bandgap	5	3.0	±0.05	2.8	4.5	3	SO-8
REF193	ADI	Bandgap	0.23	3.0	±0.3	21	12.6	10	SO-8
LTC6652	Linear	Bandgap	2.8	3.0	±0.05	2.1	60	5	MSOP-8
LM4030	Natnl. Semi.	Zener	-	4.096	±0.05	105	40	10	SOT23
LTZ1000A	Linear	Zener	-	7.0	±3.3	1.4	0.3	5	TO-5

Table 4.6. *Survey of commercially available precision voltage reference devices applicable to the μIRU prototype.*

Table 4.6 presents a subset of the voltage reference devices surveyed for use in the μIRU prototype. Of the devices surveyed, particularly those with fixed output voltages in the range 3.0V to 2.6V as well as excellent noise, thermal and power consumption performance specifications have been sought. Two preeminent devices where identified as being directly applicable to the μIRU prototype, namely the Texas Instruments REF5030I and the Analog Devices AD780AR. Both devices can be implemented as 3.0V series reference devices, resulting in a LSB size for the LTC1408I A/D Converter of:

$$LSB_{LTC1408I} = \frac{V_{ref}}{2^{14}Bit} = \frac{3V}{2^{14}Bit} = 183.1\mu V/Bit \tag{4.28}$$

The LTC1408I A/D Converter specifies an intrinsic noise level of 0.7LSB RMS of Gaussian white noise or $e_{ADC,RMS} = 128.2\mu V_{RMS}$ for a 3.0V external reference, hence the noise specification pertaining to the external reference should be substantially smaller than this value to ensure no performance degradation. However, as both the REF5030I and the AD780AR are designed for >16Bit applications, they are capable of producing noise levels of less than $9\mu V_{RMS}$ and $4\mu V_{RMS}$ when properly bandwidth limited (eg. f_{-3dB} <10Hz). At such noise levels, the total RMS noise of the ADC system will be dominated by the LTC1408I intrinsic noise, as illustrated by equation 4.29 and 4.30.

$$E_{Tot,AD780AR} = \sqrt{e^2_{ADC,RMS} + e^2_{AD780AR,RMS}} \simeq 128.26\mu V_{RMS} \tag{4.29}$$

$$E_{Tot,REF5030I} = \sqrt{e^2_{ADC,RMS} + e^2_{REF5030I,RMS}} \simeq 128.52\mu V_{RMS} \tag{4.30}$$

Evidently, both these reference devices achieve the desired performance level and resource consumption, yet being COTS devices, no detailed specifications regarding irradiation tolerance level and thermal behavior are available. As this constitutes critical issues, screening tests where conducted to aid in the selection of the best candidate.

4.9.1 External Reference Total Ionizing Dose Screening Test

Each of the two external reference devices selected for evaluation have been subjected to TID screening, in order to quantify the effect of irradiation exposure to the output voltage level and noise performance. As depicted in Figure 4.28, the REF5030I performs poorly as it essentially fails to maintain a stable output level after ∼5krad exposure. The device is then seen to degrade gracefully until full functional failure is incurred at roughly 81krad.

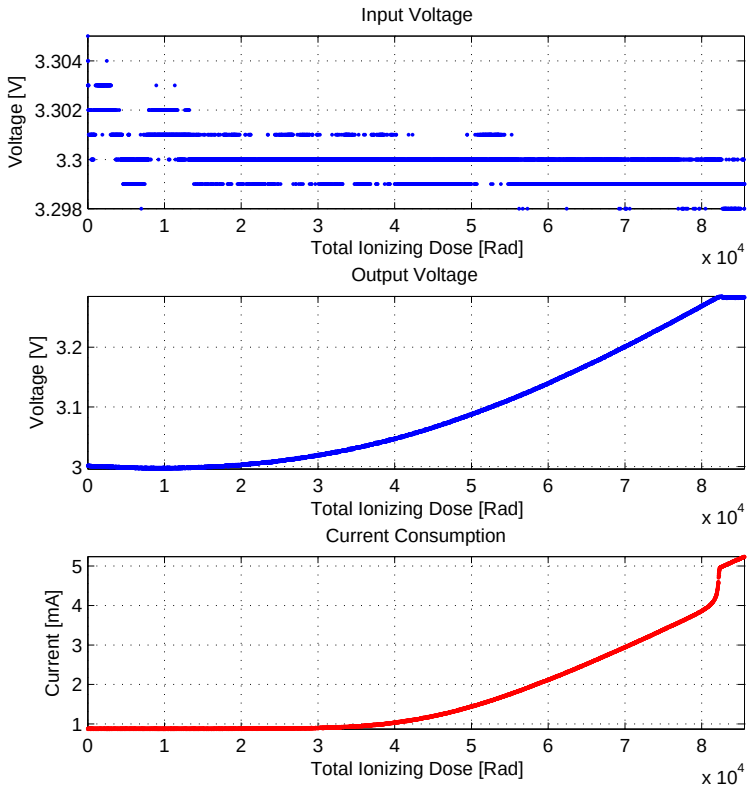

Figure 4.28. *REF5030I irradiation test response.*

A post-irradiation relaxation test was also conducted, but the REF5030I device failed to recover any functionality over a 150 hour period at 21°C.

An identical test was conducted on the AD780AR external reference device with the result depicted in Figure 4.29. Note here that the AD780AR offers a temperature compensation output which is also monitored, yet no definitive conclusions can be drawn from this as the temperature throughout the test was not controlled.

What can be gathered from the test result is however a much more amenable behavior than was shown by the REF5030I. The output voltage is seen to shift

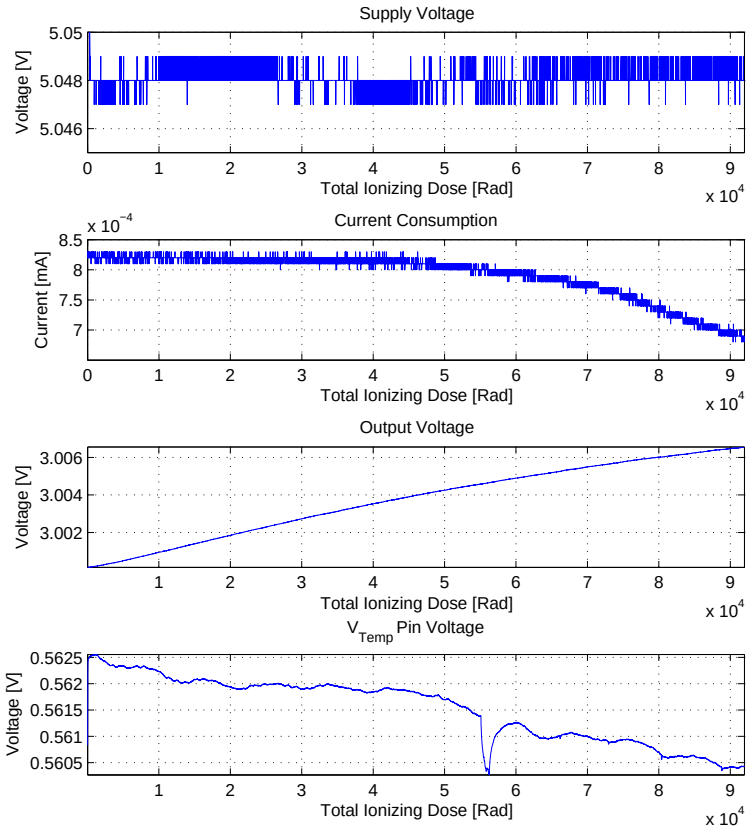

Figure 4.29. *AD780AR irradiation test response.*

roughly 6mV (6000ppm) over a TID of 90krad, yet at no point is functional impairment incurred. Moreover, the device current consumption reaches the 10% baseline limit only after a TID of 75krad. As the test was finalized, the device functionality remained intact, and as for the REF5030I a post-irradiation relaxation test was conducted with the results illustrated in Figure 4.30.

The relaxation is seen to occur within the first ∼10 hours of source removal, after which a much slower annealing process commences with a near linear characteristic. The annealing rate at 21°C is determined to be approximately 0.7ppm/hour.

4.9.2 External Reference Thermal Response Test

In addition to the irradiation screening a thermal response test of the external reference candidates was also conducted. This test serves not only to establish

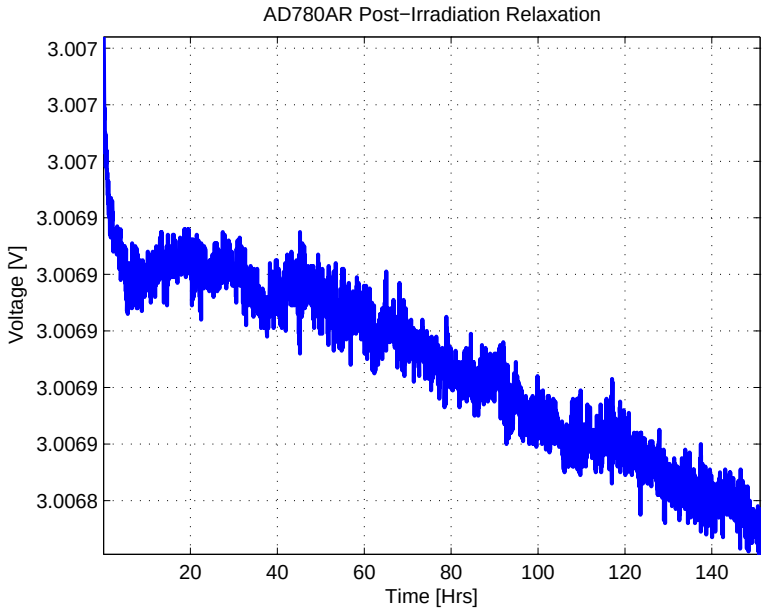

Figure 4.30. *AD780AR post-irradiation test relaxation.*

a temperature compensation model for the reference voltage, but also to ensure that the external references maintain sufficient voltage margin to correctly overdrive the internal reference of the LTC1408I A/D converter, as necessary to ensure its proper operation. To this end, the first characterization test is performed on the LTC1408I, to determine the thermal response of its internal reference.

The result hereof is included as Figure 4.31, and clearly show a significant temperature dependency of the LTC1408I power consumption. Moreover, a total drift of 14mV is observed over a 95°C temperature span, ascertaining a maximum value of 2.506V. The manufacturer specification specifies an overdrive voltage of minimum +50mV to disable the LTC1408I internal voltage reference, hence an external reference should not drop below 2.556V over temperature, if nominal operations are to be retained.

From the data in Figures 4.32 and 4.33, both external reference candidates are seen to exhibit output voltage characteristics over temperature which are compliant with the LTC1408I overdrive requirement. The two devices are seen to provide near identical thermal drift scales (∼2mV over 140°C), with the REF5030I thermal compensation model fit being slightly better with a 3^{rd} order polynomial as compared to the result ascertained for the AD780AR with a 4^{th} order polynomial.

From these screening tests and performing well under irradiation, the AD780AR emerges as the primary external reference candidate. Moreover, the AD780AR is available in a Mil. Spec. 883B version, which may be considered for the

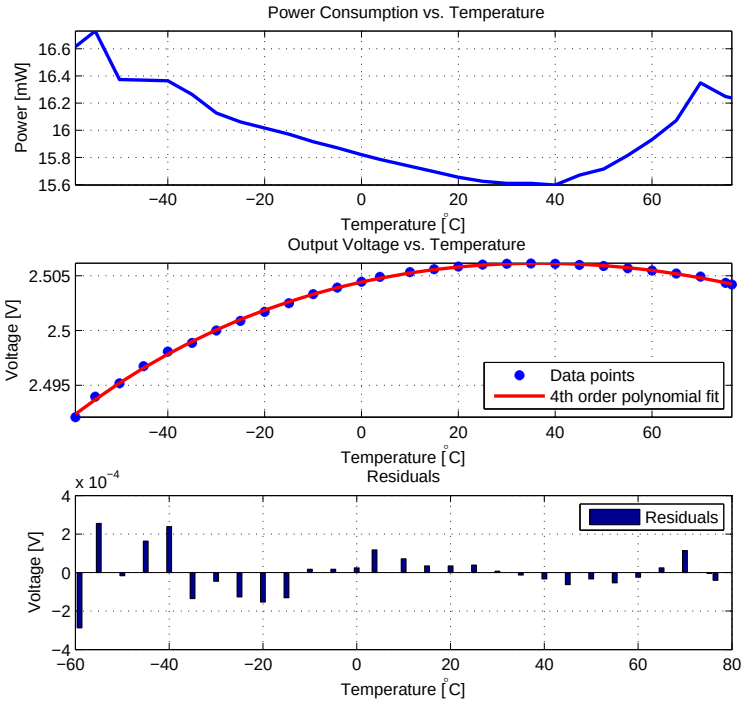

Figure 4.31. *LTC1408I thermal test response. Polynomial Fit:* $V_{out}(T) = -2.13 \cdot 10^{-11}T^4 + 4.16 \cdot 10^{-9}T^3 - 1.49 \cdot 10^{-6}T^2 + 9.68 \cdot 10^{-5}T + 2.5044[V]$

flight version of the μIRU.

4.10 Passive Parts Selection

The selection of passive parts for the μIRU prototype design has been done in accordance with the recommendations of ECSS-Q-ST-60C and under strict adherence to the ESA derating standard as defined by the ECSS-Q-ST-30-11C. The applied derating analysis exhibits no non-conformances in the design.

4.11 Magnetic Cleanliness

Magnetic cleanliness remains an issue of the utmost importance for the μASC stellar reference sensor, as one of its primary areas of application is as an absolute attitude reference for space-based magnetometry. When employed for such purposes, it is necessary for the CHUs of the μASC to maintain an invariant physical orientation with respect to the magnetometer reference frame. This will often be achieved by colocating the stellar reference sensor and the

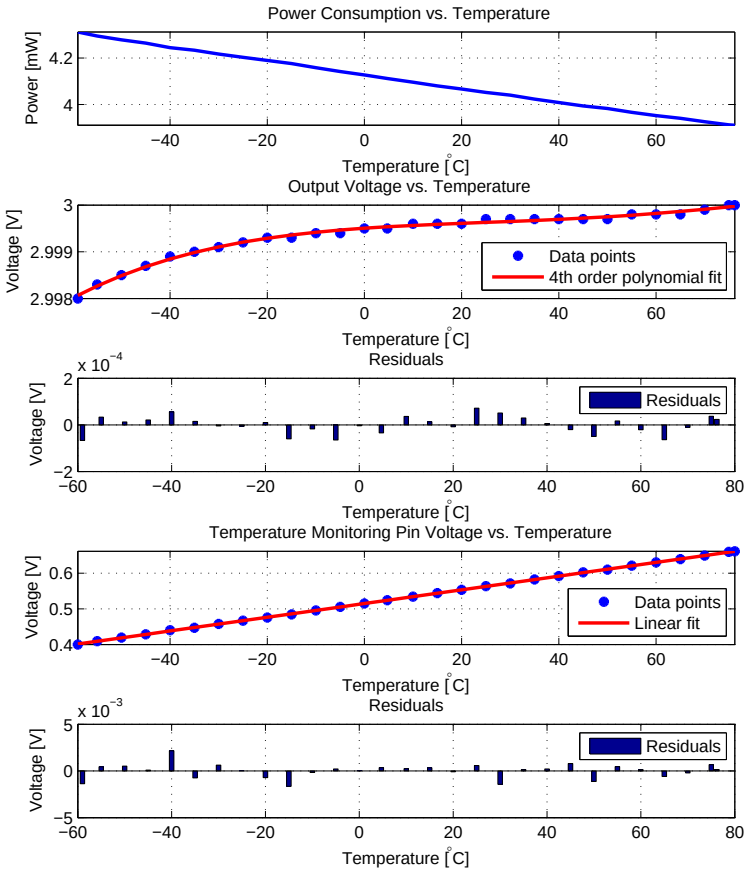

Figure 4.32. *AD780AR thermal test response. Polynomial Fits:* $V_{out}(T) = -7.99 \cdot 10^{-12}T^4 + 2.22 \cdot 10^{-9}T^3 - 1.34 \cdot 10^{-7}T^2 + 7.07 \cdot 10^{-6}T + 2.9995[V]$ $V_{temp}(T) = 0.0019T + 0.5149[V]$

magnetometer on a dedicated and thermally invariant fixture, which commonly provides an instrument separation on the order of decimeters. As such, maintaining dynamic and static magnetic fields associated with the operation of the stellar reference sensor at a minimum constitutes a design criteria of paramount importance, and this naturally extends to any μIRU augmenting implementation as well.
So as to ensure that components used in the μIRU augmentation does not adversely impact the residual magnetic moment specification presently associated with the CHU, all parts considered during the selection process have been subjected to magnetic screening to assess their static moments.

The assessment is performed empirically on a part-by-part basis using the institute astatic magnetometer setup with the worst case moment m_{wc} calculated using equation 4.31 as provided by [Primdahl-1990]. The results of this

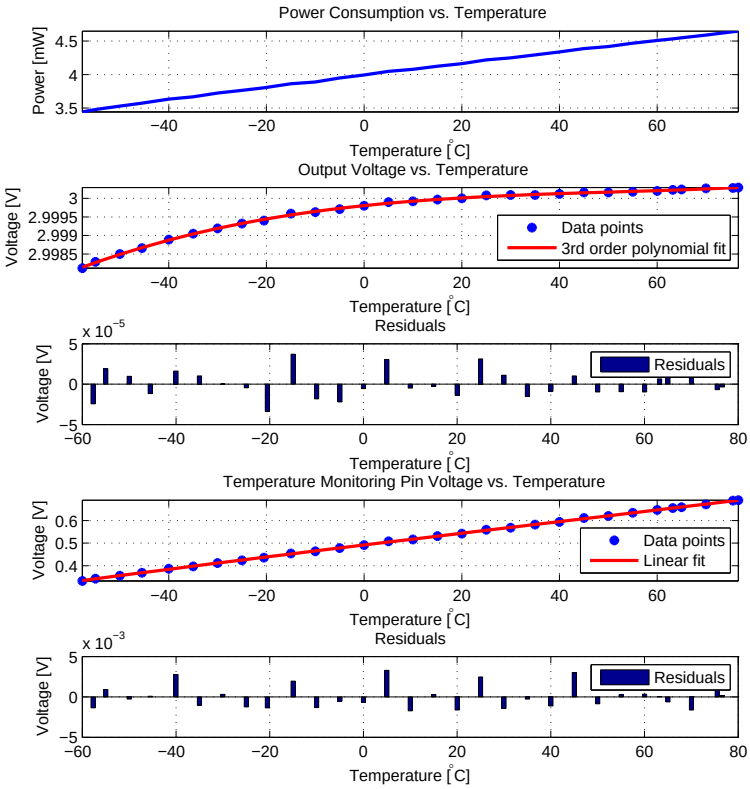

Figure 4.33. *REF5030I thermal test response. Polynomial fits:* $V_{out}(T) = 1.23 \cdot 10^{-9}T^3 - 1.90 \cdot 10^{-7}T^2 + 1.37 \cdot 10^{-5}T + 2.9998[V]$
$V_{temp}(T) = 0.0026T + 0.4898[V]$

evaluation are tabulated in Table 4.7.

$$m_{wc} = 2mAm^2 \cdot R_r \left(\frac{R_x}{R_S}\right)^4 \tag{4.31}$$

where:
R_r: denotes the readout scale $[mm]$.
R_x: denotes the spacing between the part under test and the astatic magnetometer $[mm]$.
R_S: denotes the standard moment separation which is an instrumentation constant defined as $R_S = 290mm$.

In addition to the static residual moments, the μIRU electronics may contribute dynamic moments due to the time varying electrical current associated with the operations of the instrument. Over the course of the project a methodology has been developed which allows the influence of dynamic moments to

Part	Type	Distance R_x $[mm]$	Readout R_r $[mm]$	Moment $[Am^2]$
LIS2L02AL	Accelerometer	20	< 2.5	$< 110 \cdot 10^{-9}$
LTC1408I	A/D converter	20	0	0
Atmega168	μ-processor	20	0	0
REF5030I	Volt. reference	20	40	$1.8 \cdot 10^{-6}$
AD780AR	Volt. reference	20	0	0
MAX4736	Analog switch	20	0	0
MAX4236	Opamp	20	0	0
MAX4092	Dual opamp	20	0	0
LP2985	LDO regulator	20	0	0
DS18B20U	Temp. sensor	20	0	0
BAT54S	Schottky diode	20	5	$230 \cdot 10^{-9}$

Table 4.7. *Static residual moments of μIRU electrical components prior to degaussing.*

be minimized at the PCB level by using a combination of design techniques, including:

- Migration to twisted pair cabling only, and matching of wire twisting groups.
- Solid Ground and power plane pairing in the PCB stackup.
- High density PCB stackup to minimize both vertical and lateral current loops.
- Component level back wiring on part-by-part basis.
- Component power and return through planes and vertical connections only.
- Track level back wiring for both power and signal lines.

The very successful application of these principles to the μASC CHU PCB in support of the Swarm and Juno mission efforts gives credence to the method, and the improved design demonstrates a magnetic distortion signature of <20pT at 10cm distance as compared to the previous design signature of 0.5nT at 10cm distance [Joergensen-2009]. The intention is to apply the same principles to the Tier three μIRU augmentation design, so as to maintain the excellent performance of the combined instrument in this regard.

4.12 Summary

This chapter has sought to convey the main considerations that have gone into the design of the μIRU prototype as well as perspectives for the physical implementation of the instrument design, as will be discussed in Chapter 5. Using the physical and functional envelope presented by the μASC to derive a

design baseline, the developed design adheres strictly to the minimum impact requirement, and will in its current configuration be directly integrable with the μASC CHU whilst imposing minimal loading to the configuration of that instrument. Additionally the chapter at hand has succeeded in identifying key electronic components that will allow the baseline μIRU design to be realized, and eventually iterated into a physically compatible augmentation for the μASC.

4.13 Bibliography

[Areny-2001] John G. Webster Ramon Pallàs-Areny. *Sensors and Signal Conditioning*. John Wiley and Sons Inc., second edition, 2001.

[Babkin-2004] E.V. Babkin, M. Yu. Belyaev, N.I. Efimov, V.V. Sazonov, and V.M. Stazhkov. Determination of the microacceleration quasisteady component onboard the international space station. *Cosmic Research*, Vol. 42, No. 2:162–171, 2004.

[Bjarnoe-2007] Jonas Bjarnoe. *Inertial Sensor Augmentation of Stellar Reference Units in the High Frequency Domain*. DTU Space, 2007.

[Bushnell-1999] Glenn S. Bushnell and Marc D. Becraft. Flight test of an international space station active rack isolation prototype system. *Smart Material Structures*, Vol.8:791–797, 1999.

[Butterfield-1996] Ansel J. Butterfield and Stanley E. Woodard. Measured spacecraft instrument and structural interactions. *Journal of Spacecraft and Rockets*, Vol.33, No.4, 1996.

[Chubb-1975] W.B. Chubb, H.F. Kennel, C.C. Rupp, and S.M. Seltzer. Flight performance of skylab attitude and pointing control system. *Journal of Spacecraft and Rockets*, Vol.12, No.4:220–227, 1975.

[Dyne-1993] S.J.C. Dyne, D.E.L. Tunbridge, and P.P. Collins. The vibration environment on a satellite in orbit. IEE Colloquium, 1993.

[Fabula-2005] Austin Lesea Joseph J. Fabula. The continuing impact of design and process hardning on the nseu sensitivity of advanced cmos pld technologies. In *MAPLD Internation Conference*, 2005.

[Ingham-1998] Michel D. Ingham. Microdynamics and thermal snap response of deployable space structures. Master's thesis, Massachusetts Institute of Technology, 1998.

[Joergensen-2009] John L. Jørgensen. Juno mag critical design review - 19.0 design and implementation chu, 2009.

[Jono-2002] Takashi Jono, Morio Toyoshima, Nobuhiro Takahashi, Toshihiko Yamawaki, Keizo Nakagawa, and Akio Yamamoto. Laser tracking test under satellite microvibrational disturbances by oicets atp system. *SPIE*, Vol.4717:97–104, 2002.

[Kester-2004] Walt Kester. *Analog-Digital Conversion*. Analog Devices, 204.

[Lancaster-1977] D. Lancaster. *Active-Filter Cookbook*. Howard W. Sams and Co. Inc., first edition edition, 1977.

[Lee-2000] Shinak Lee, James W. Alexander, and Muthu Jeganathan. Pointing and tracking subsystem design for optical communications link between the international space station and ground. *Free-Space Laser Communication Technologies XII, SPIE Proceedings*, 3932, 2000.

[Linear-2006] Linear Technology. *LTC1408I Datasheet*. Linear Technology, 2006.

[Merayo-1999] José María García Merayo. *Magnetic Gradiometry*. PhD thesis, Technical University of Denmark, 1999.

[Ortiz-2003] Gerry G. Ortiz, Shinhak Lee, and Bill. Laboratory demonstration of the sub-microradian atp subsystem for deep space optical communications. *Free-Space Laser Communication Technologies XV, SPIE Proceedings*, 2003.

[Parvez-1990] S.A. Parvez. Gstar satellite disturbance from plume impingement. *Journal of Spacecraft and Rockets*, Vol. 27, No. 3:275–278, 1990.

[Primdahl-1990] Primdahl. A pedestrian's approach to magnetic cleanliness. Technical report, Danish Space Research Institute, 1990.

[Rice-1999] James E. Rice, James C. Fox, William G. Lange, Robert W. Dietrich, and William O. Wagar. Microgravity acceleration measurement system for the international space station. In *IEEE 0-7803-5276-9*, 1999.

[Rogers-1993] M.J.B Rogers, C.R. Baugher, R.C. Blanchard, R. DeLombard, W.W. Durgin, D.H. Matthiesen, W. Neupert, and P. Roussel. A comparison of low-gravity measurements on-board columbia during sts-40. *Microgravity - Science and Technology*, 1993.

[SIG-2006a] Space Instrumentation Group. microadvanced stellar compass electrical interface control document. Technical report, DTU Space, 2006.

[SIG-2006b] Space Instrumentation Group. micro advanced stellar compass general information, asc-dtu-prp-3000. Technical report, DTU Space, 2006.

[ST-2006] ST Microelectronics. *LIS2L02AL Datasheet*. ST Microelectronics, 2006.

[Storey-2004] James C. Storey and Michael J. Choate. Landsat-5 bumper-mode geometric correction. *IEEE Transactions on Geoscience and Remote Sensing*, Vol.42, No.12:2695–2703, 2004.

[Sutliff-1999] T.J. Sutliff. Space acceleration measurement system-ii: Microgravity instrumentation for the international space station. *Instrumentation and Measurement Technology Conference*, 1999.

[TI-1999] Texas Instruments Incorporated. Noise analysis in operational amplifier circuits - slva043a. Technical report, TI, 1999.

[Toyoshima-2001] Morio Toyoshima and Kenichi Araki. In-orbit measurements of short term attitude and vibrational environment on the engineering test satellite vi using laser communication equipment. *Society of Photo-Optical Instrumentation Engineers*, Vol.40, No.5:827–832, 2001.

[Tryggvason-2001] B.V. Tryggvason, R.F. Redden, and R.A. Herring. The vibration environment on the international space station: Its significante to fuild-based experiments. *Acta Astronautica*, Vol.48, No.2-3:59–70, 2001.

[Tunbridge-1990] D. Tunbridge. The "pax" instrument on olympus. *ESA Bulletin*, No.64:84–91, 1990.

[Whorton-2000] Mark S. Whorton. Microgravity vibration isolation for the international space station. In *Space Technology and Applications Internation Forum-2000*, 2000.

Chapter 5

μIRU Sensor Prototyping

The chapter at hand seeks to convey the details of the baseline physical implementation of the system level design previously described. The development philosophy and the different hardware elements developed for the μIRU prototype are presented and the implementation specifics discussed.

5.1 Prototype Development Philosophy

Establishing a fully functional prototype of the μIRU instrument has been an ongoing effort throughout the project. The goal has been to realize a prototype which emulates all aspects of the envisioned instrument, while maintaining both a level of functionality and a form factor that also provides for stand-alone experimentation independently of the μASC. Moreover, the prototype instrument must support adaptations of signal filtering and gain constants to allow different philosophies to be evaluated.

As sought illustrated by Figure 5.1, the development philosophy segments the process into three steps of increasing complexity. The main goals and requirements pertaining to each step or tier are outlined below:

Tier One

The Tier One main target is to establish a development platform which functionally and performance-wise mimics the envisioned μIRU augmentation for the μASC CHU. It is the intention to emulate performance with regards to noise levels and resolution, hence environmental performance will not be directly targeted in this phase. Moreover, the physical form factors associated with the Tier One implementation only attempts to mimic correct sensor placement with respect to the GEO 3 configuration, not the scale of miniaturization

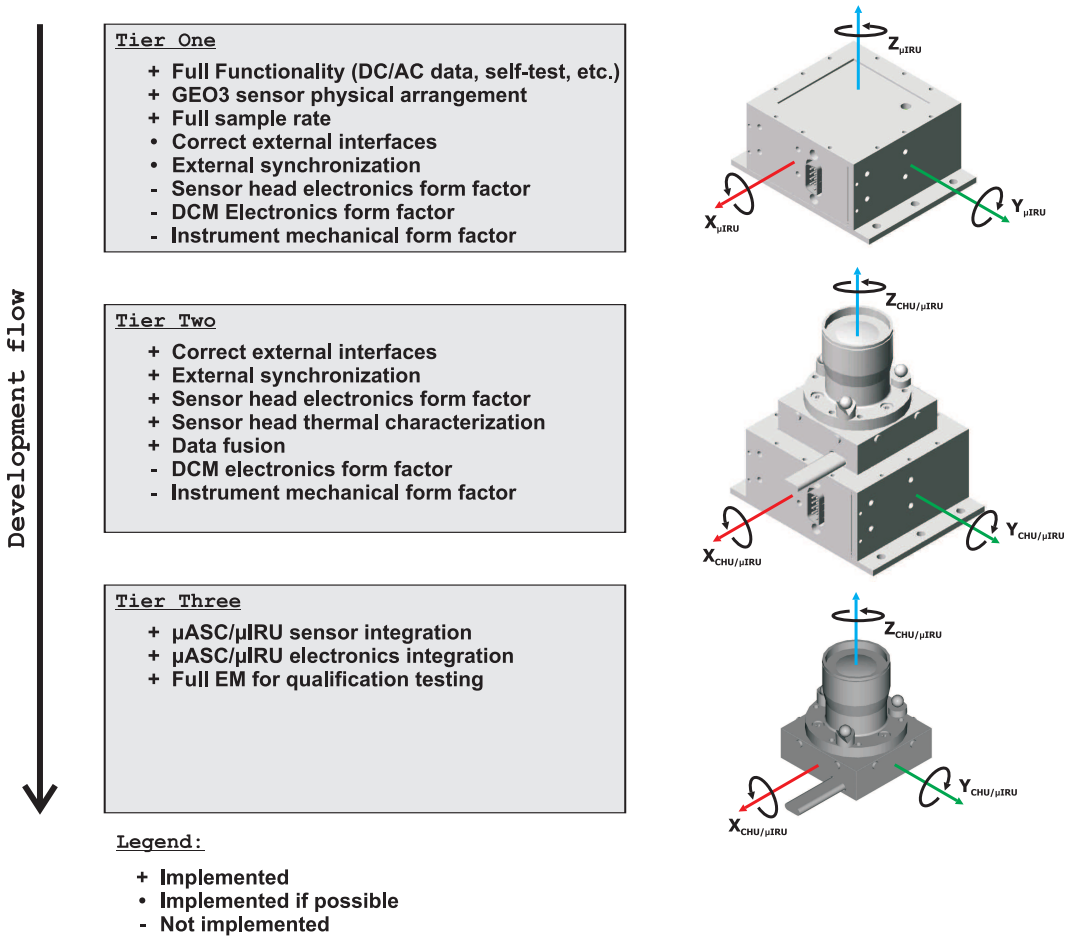

Figure 5.1. *µIRU prototype development philosophy.*

required for co-integrating the μIRU into the CHU envelope.
The Tier One effort concludes with a fully functional μIRU implementation for which a set of calibration procedures have been developed successfully tested. At this point a finished μIRU prototype capable of delivering calibrated three axis differential accelerometer data should be at hand.

Tier Two

The tier two implementation builds upon Tier One, by augmenting the previously established prototype platform with an EM CHU. This will happen in two stages, whereof the first will demonstrate only the ability to operate the existing Tier One electronics implementation through the CHU/DPU interface. As such, this also entails developing the required software and firmware

entities for the μASC DPU to acquire and process the μIRU attitude data. The second stage of the process migrates the placement of the accelerometer sensor complement from the Tier One prototype structure into the CHU back shell in accordance with specifications of the GEO 3 configuration. This is done whilst retaining the μIRU Data Conversion Module (DCM) electronics within the Tier One structure. As such, a hybrid system is established which allows full intercalibration experimentation between the μASC and its μIRU augmentation, albeit with the consequence of a potential non-representative level of performance due to the DCM filter and conversion electronics pertaining to the accelerometer sensors not being collocated in the CHU.

Tier Three

Tier three represents the final step towards establishing a fully representative EM of the μIRU augmented stellar reference sensor. To achieve this the DCM implementation of the μIRU prototype must be migrated into an EM design, which is physically compatible with the CHU envelope. Moreover, this also entails the final parts selection for the μIRU sensor and DCM, which must be completed in accordance with the micro Advanced Stellar Compass Product Assurance Plan [SIG-2007] as well as all applicable ECSS standards.

The work presented within the current chapter focuses mainly on the efforts associated with establishing Tier One of the μIRU implementation.

5.2 Tier One Mechanical Configuration

For the μIRU prototype implementation a mechanical design has been developed which will allow both Tier One and tier two systems to be realized. By adopting modular panelized approach, a six panel structure has been devised which allows four LIS2L02AL accelerometers to be retained in the GEO3 physical constellation as envisioned for the μIRU augmentation of the μASC CHUs.

Moreover, the mechanical configuration allows a standard configuration CHU to be attached directly to the top of the μIRU prototype, thus facilitating direct interfacing with the CHU control signals as required by the tier two implementation. Each of the six panels have been CNC machined directly from AL6061 aluminum stock and their interconnects are established using M2 and M3 brass screws, in keeping with the desire to utilize only nonmagnetic structural elements.

Table 5.1 provides an overview of the mass budget pertaining to the structural elements of the μIRU prototype. Mass elements and CoM are tracked for the

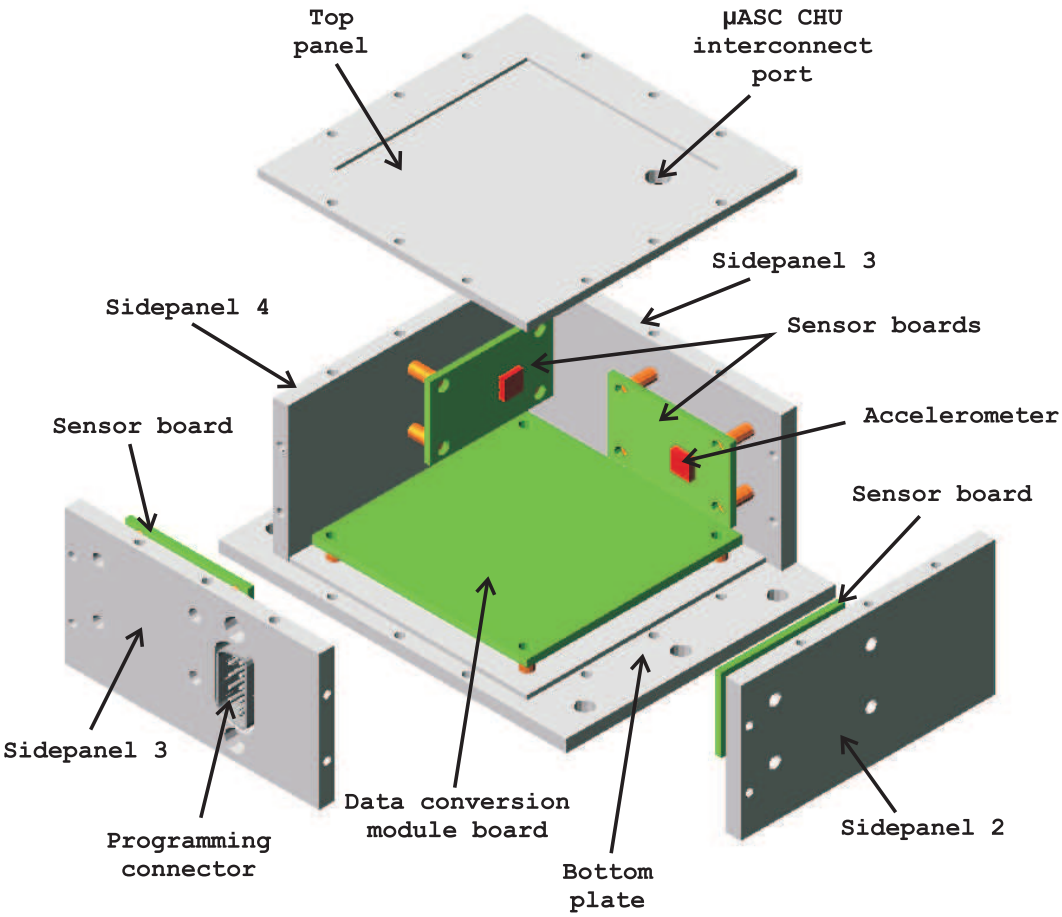

Figure 5.2. *Rendered exploded view of the µIRU prototype structure.*

prototype unit to allow for correct balancing of the dynamic calibration rig as elaborated upon in Chapter 6.

Part	Calculated Mass [g]	Measured Mass [g]
Topplate	40.3	40.6±0.1
Bottomplate	60.4	60.6±0.1
Sideplate 1	21.9	21.8±0.1
Sideplate 2	24.3	24.5±0.1
Sideplate 3	24.3	24.4±0.1
Sideplate 4	24.3	24.4±0.1
Screws	15	12.2±0.1
Total:	210.5	208.5± 0.7

Table 5.1. *µIRU prototype structural mass budget.*

Detailed mechanical drawings of all structural elements of the µIRU prototype are included in Appendix E.

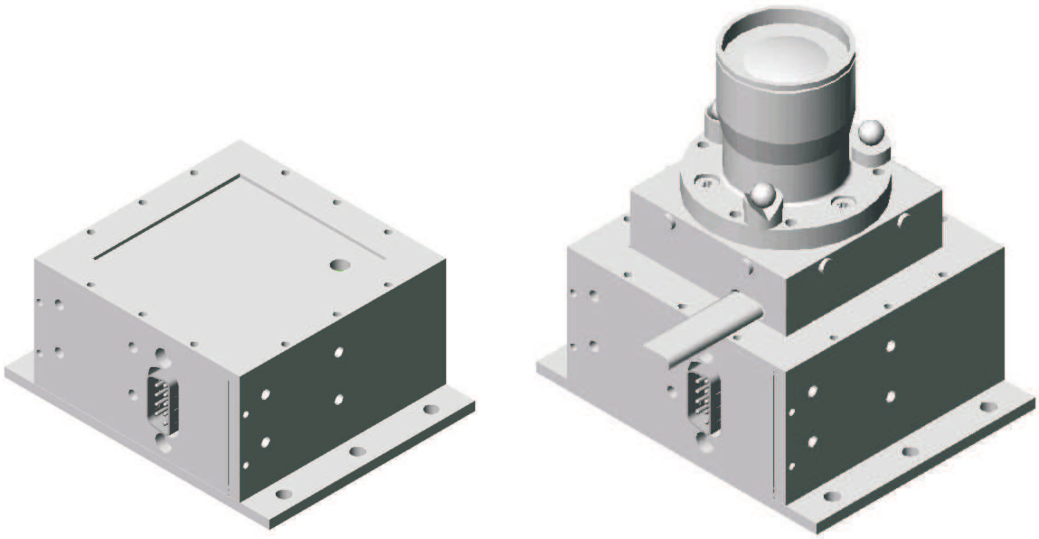

Figure 5.3. *Rendered assembled views of μIRU prototype structure with and without CHU attached.*

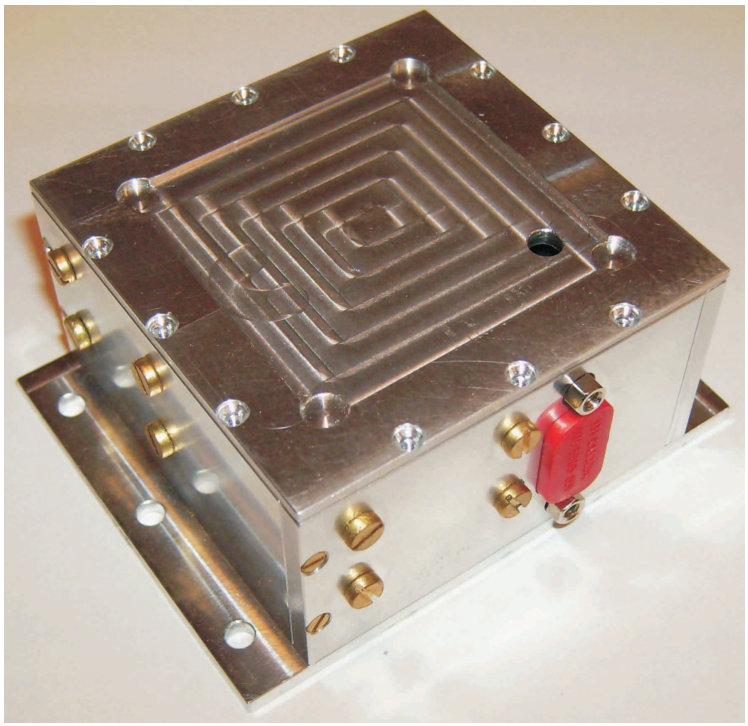

Figure 5.4. *Assembled μIRU prototype.*

5.3 Tier One Sensor Head Mechanization

The accelerometer sensor head has been configured within the prototype mechanical structure so as to emulate the GEO3 sensor arrangement as accurately

as possible. The most significant difference between the envisioned flight configuration and the prototype configuration is the way in which the accelerometers have been mounted. In the flight configuration, the accelerometers will be glued into position within CHU titanium back housing. The mechanical interface will be between the top of the accelerometer package and the inside of the CHU back housing, which entails the mechanical stability of the accelerometer positioning being conditioned by the excellent thermomechanical stability of the CHU structure. In the prototype configuration as depicted in Figure 5.5, the mounting scenario is somewhat different. Here the individual accelerometers will be carried by dedicated sensor PCBs of a substantially larger form factor than those planned for the flight configuration. Each of the accelerometer sensor boards are then bolted to the side panels of the structure using Ø3mm brass screws torqued to 80Nm.

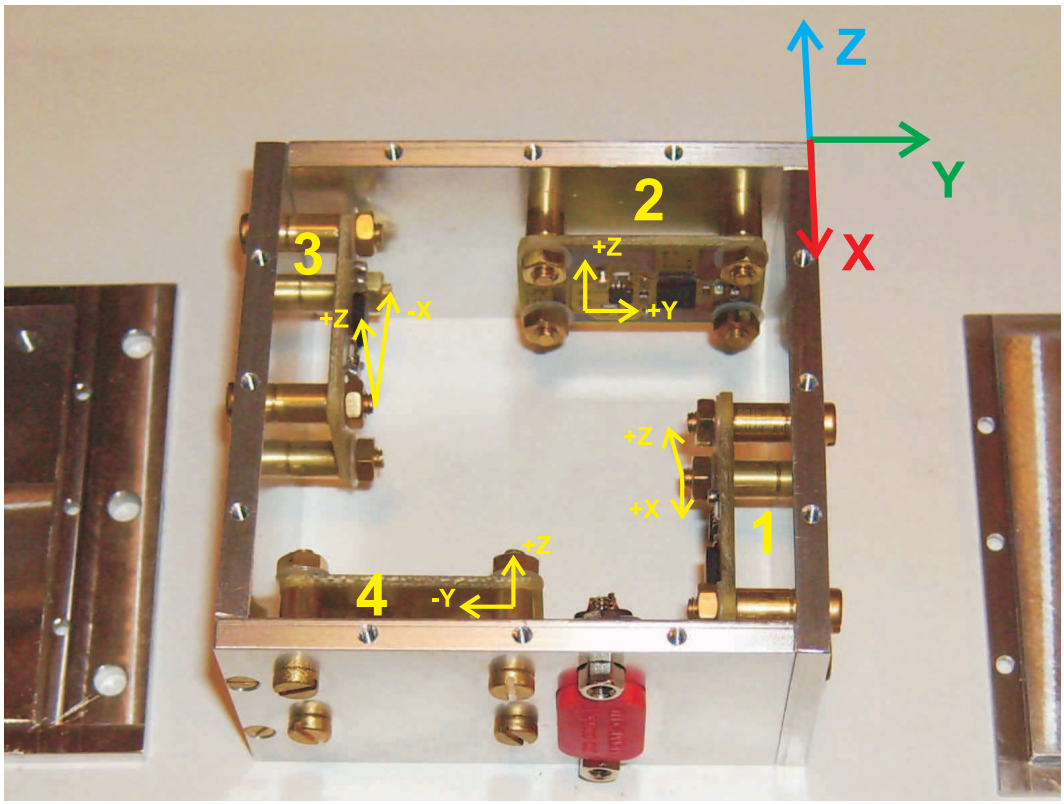

Figure 5.5. *µIRU prototype sensor mounting and intrinsic coordinate system. Sensor head depicted with first iteration sensor boards.*

The board mount approach has been adopted to facilitate hardware debugging for ease of development, yet it also infers the mechanical stability of the accelerometer positioning being conditioned by the thermomechanical stability of the carrier PCBs and their attachment to the µIRU prototype structure. As such, the µIRU Tier One prototype configuration is only to be calibrated and experimented with at room temperature, to ensure minimum performance im-

pact being incurred by thermomechanical instability of the sensor orientation and positioning. With regards to the coordinate frame conventions and sensor numbering introduced by Figure 5.5, it must be emphasized that these are employed consistently throughout this dissertation, and referenced directly to the coordinate convention employed by the μASC CHU. The prototype sensor head mechanization matrices describing the orientation $\mathbf{D}_{\mu\mathbf{IRU}}$ and relative positioning $\mathbf{R}_{\mu\mathbf{IRU}}$ of the sensors have thus been refined based upon precision measurements made on the as-built assembly. These matrices are provided below, with the position vectors given in $[mm]$ and referenced relatively to the accelerometer sensor 1 origo.

$$\begin{aligned}\mathbf{D}_{\mu\mathbf{IRU}} &= \left[d_{A1_x}, d_{A1_z}, d_{A2_y}, d_{A2_z}, d_{A3_x}, d_{A3_z}, d_{A4_y}, d_{A4_z}\right] \\ &= \begin{bmatrix} 1 & 0 & 0 & 0 & -1 & 0 & 0 & 0 \\ 0 & 0 & 1 & 0 & 0 & 0 & -1 & 0 \\ 0 & 1 & 0 & 1 & 0 & 1 & 0 & 1 \end{bmatrix}\end{aligned} \tag{5.1}$$

$$\begin{aligned}\mathbf{R}_{\mu\mathbf{IRU}} &= \left[r_{A1_x}, r_{A1_z}, r_{A2_y}, r_{A2_z}, r_{A3_x}, r_{A3_z}, r_{A4_y}, r_{A4_z}\right] \\ &= \begin{bmatrix} 0 & 0 & -40.3 & -40.3 & -36.2 & -36.2 & 4.1 & 4.1 \\ 0 & 0 & -4.1 & -4.1 & -44.4 & -44.4 & -40.3 & -40.3 \\ 0 & 0 & 0.1 & 0.1 & 0 & 0 & 0.1 & 0.1 \end{bmatrix}\end{aligned} \tag{5.2}$$

5.4 Tier One Electronics Prototyping

The two separate electronic segments of the μIRU prototype, namely the sensor boards and the DCM board have both undergone two development iterations. The first iteration consisted of an in-house board production run on two layer PCB, to facilitate rapid prototyping and functional evaluation. The second iteration implemented the lessons learned from the first iteration in establishing not only functionally representative behavior, but also the representative performance and noise levels. For the latter iterations, detailed schematic drawings and PCB layout have been included in Appendix F.

5.4.1 μIRU Prototype Sensor Boards

The μIRU prototype sensor boards have been implemented fully in accordance with the design outlined in Chapter 4. Constructed as a two layer 32×18×1.6mm FR-4 PCB, the board allows the accelerometer sensor to be physically positioned in the GEO3 configuration within the Tier One mechanical prototype.

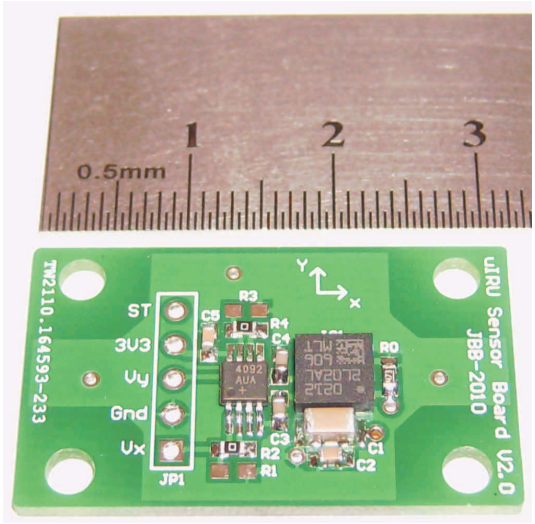

Figure 5.6. *µIRU Tier One prototype sensor boards.*

The sensor board electronics configuration uses the common stage 0 implementation with unity gain and a nominal single-pole roll-off at $f_{3dB} = 212Hz$, obtained with a high precision 6.8nF ceramic capacitor on the LIS2L02AL output pins.

5.4.2 µIRU Prototype Data Conversion Module

The µIRU prototype DCM is implemented on a 60×60×1.6mm four layer FR-4 PCB. Also implemented in accordance with Chapter 4 design specifications, it features two synchronized LTC1408I A/D converters, thus providing eight direct conversion AC channels and four multiplexed conversion DC channels, with the latter being sampled at half the effective rate of the AC channels.

A full overview diagram of the Tier One DCM implementation and the associated accelerometer signal paths has been included as Appendix D. The Tier One implementation pairs the ADC and ACC channels in accordance with Table 5.2, where the accelerometer designation convention has been directly derived from Figure 5.5.

The DCM features the correct electrical interfaces to the CHU, namely +5V, Ground, clock, VR synchronization and the IDAT data output line, thus rendering it ready for tier two experimentation. For standalone operations, the DCM is capable of generating its own internal clock signal at either 1MHz or 8MHz, or be driven from an externally generated clock source in a free-running manner (without necessitating the VR synchronization signal). Output data is delivered in UART/TTL compatible formats on the IDAT line for direct PC interfacing through a RS-232 level converter.

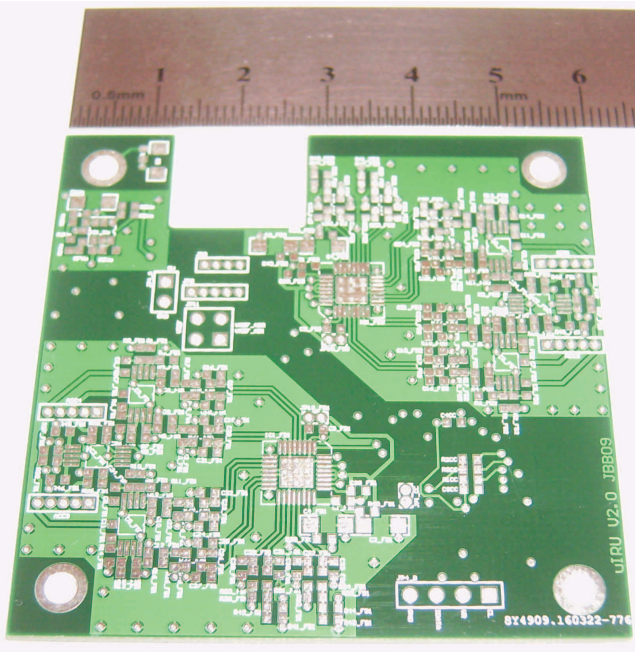

Figure 5.7. *μIRU Tier One prototype DCM board.*

ADC #	ADC Channel	Switch= 0 (Even)	Switch= 1 (Odd)
1	0	ACC1 $+Z_{AC}$	$-\|\|-$
1	1	ACC1 $+X_{AC}$	$-\|\|-$
1	2	ACC2 $+Y_{AC}$	$-\|\|-$
1	3	ACC2 $+Z_{AC}$	$-\|\|-$
1	4	ACC1 $+X_{DC}$	ACC1 $+Z_{DC}$
1	5	ACC2 $+Y_{DC}$	ACC2 $+Z_{DC}$
2	0	ACC3 $+Z_{AC}$	$-\|\|-$
2	1	ACC3 $-X_{AC}$	$-\|\|-$
2	2	ACC4 $-Y_{AC}$	$-\|\|-$
2	3	ACC4 $+Z_{AC}$	$-\|\|-$
2	4	ACC3 $-X_{DC}$	ACC3 $+Z_{DC}$
2	5	ACC4 $-Y_{DC}$	ACC4 $+Z_{DC}$

Table 5.2. *μIRU prototype ADC and accelerometer channel pairing.*

5.5 μIRU Prototype Software

The Atmel ATmega168 microprocessor used as the main functional control unit of the μIRU prototype DCM runs a custom software implementation denoted as "IRUapp". Written in *C*, "IRUapp" provides full control of all the functionalities of the μIRU prototype and implements a continuous mode of operations which has been optimized for the largest possible sample rate. When the μIRU operates in stand-alone configuration (without a source of

external synchronization) the "IRUapp" program execution flow follows the sequence outlined in Figure 5.8. A similar flow chart for VR synchronized operations has been included in Appendix B.

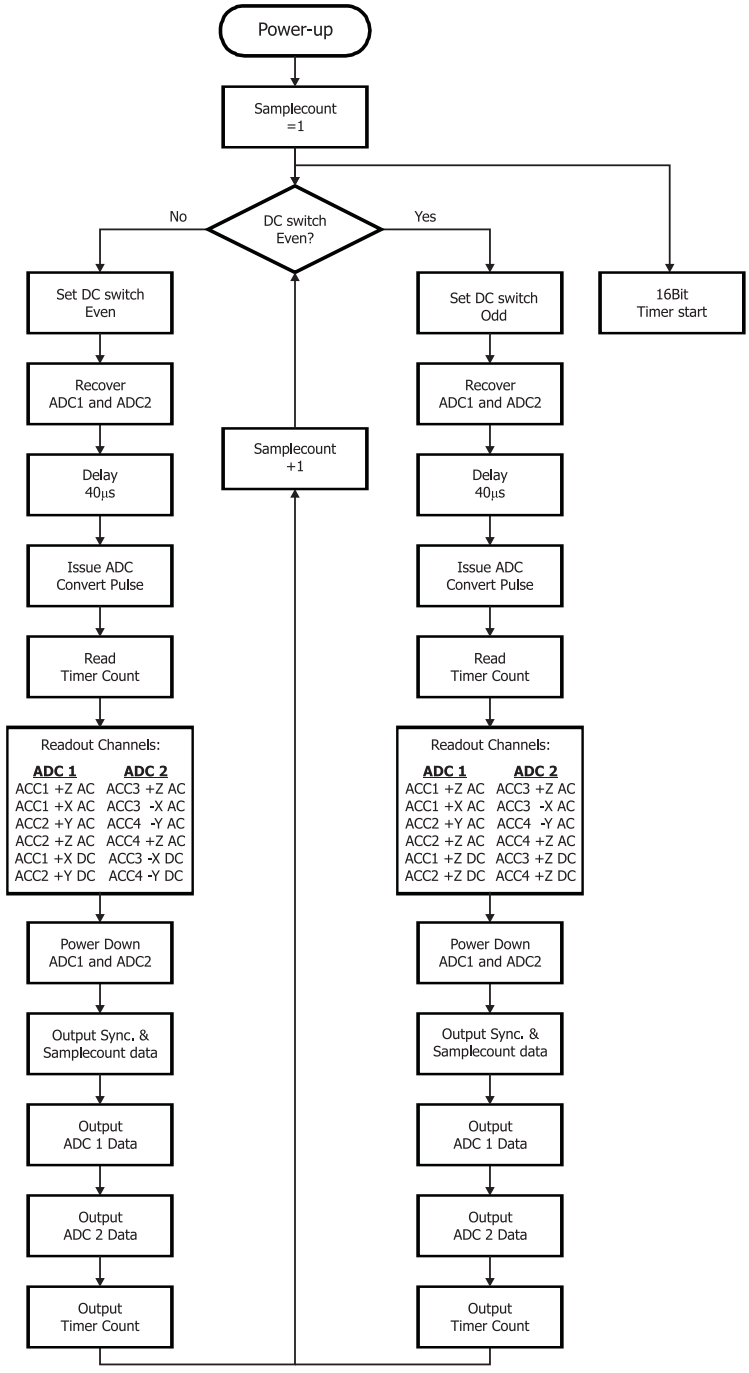

Figure 5.8. *IRUapp program flow for the μIRU stand-alone operating mode.*

Execution time for each of the two main program flow branches illustrated in Figure 5.8 have been balanced so as to ensure identical latency. In its present implementation the "IRUapp" stand alone configuration thus provides exactly

3650 clock periods between two assertions of the ADC convert pulse, which synchronously initiates A/D conversion for both ADCs of the μIRU DCM. Following completion of the A/D conversion procedure, the raw data is output from the μIRU without any additional treatment or filtering. The output data pertaining to a single sample consists of a synchronization byte, a sample counter, the accelerometer data, and a timer counter, in all maintaining a constant length for the sample package regardless of its content. The detailed data budget for a single sample is constructed as described in Table 5.3:

Byte #	Content	Length [Bit]
1	Sync. flag (0xAA)	8
2-3	Sample counter	2×8
4-15	ADC1 data	12×8
16-27	ADC2 data	12×8
28-29	Sample timer count	2×8
	Total:	**232**

Table 5.3. *μIRU prototype single sample data budget.*

With each sample totaling 232 bits and the acquisition and delivery of each sample taking exactly 3650 clock cycles, the sample rate n_s of the μIRU prototype ultimately depends upon the applied master clock frequency f_{clk} and the output data baud rate B_d in accordance with equations 5.3 and 5.4.

$$n_s(f_{clk}) = \frac{f_{clk}}{3650\,\text{clks}} \quad [\text{samples/s}] \tag{5.3}$$

$$n_s(B_d) = \frac{B_d}{232\,\text{Bit}} \quad [\text{samples/s}] \tag{5.4}$$

As illustrated by Figure 5.9 the linear relationships between μIRU sample rate and the applied master clock frequency/baud rate yield two characteristic delimiting curves.

From these curves the limiting sample rate can be derived for a given master clock frequency and/or baud rate setting. Similarly, the maximum sample rate can be ascertained for a given practical combination of settings. In relation to these settings it is worth noting that the μIRU datarate is directly linked to the μASC stellar reference sensor frame rate by the clock synchronization that exists between the instruments. As the duration of the μIRU sample acquisition and delivery procedure is fixed, clock synchronization ensures a fixed number of samples per μASC frame regardless of the μASC frame rate setting, yet the total number of μIRU samples per second still scales proportionally with the master clock frequency. This relationship has been analyzed in detail with the results tabulated in Table 5.4.

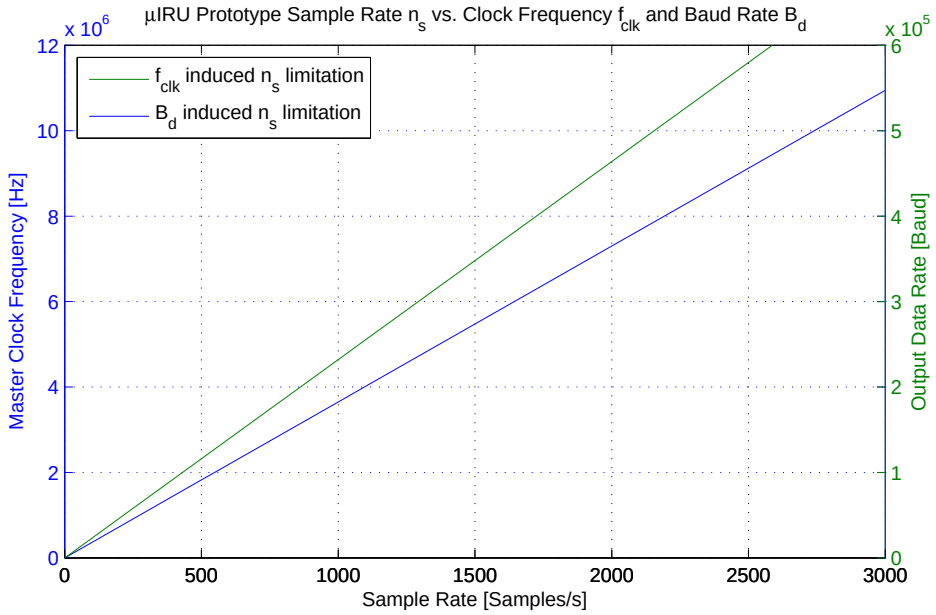

Figure 5.9. *μIRU sample rate versus applied master clock frequency and baud rate setting. Note that the baud rate settings reflect operations with the double data rate feature of the ATmega168 microprocessor enabled.*

	μASC		μIRU	
Clock Source	**f_{clk} [MHz]**	**frame rate [ms/frame]**	**n [samples/s]**	**Datarate [samples/frame]**
μASC	9.216	123.16	2610	321
μIRU standalone (@1Mbaud)	8.000	-	2191	-
CHU emulator[a]	5.000	227.00	1416	321
μASC	4.608	246.31	1305	321
μASC	2.304	492.62	652	321
μASC	1.152	985.24	326	321
μIRU standalone (@57.6kbaud)[b]	8.000	-	248	-

[a] A full description of the CHU emulator is provided in Section 5.6.
[b] μIRU baudrate limited for this frequency/baud combination. Reference Figure 5.9 for details.

Table 5.4. *μIRU datarates for applicable clock sources and clock frequencies. Clockstops for PPS synchronized operations are disregarded in this analysis.*

5.6 The μASC CHU Emulator

During the μIRU design and development phase it has on numerous occasions been necessary to apply realistic control signals to μIRU prototype hardware. So as to avoid jeopardizing EM μASC hardware and to maintain full con-

figuration control over the μASC-μIRU interfaces, a stand-alone solution has been sought. To this end, a CHU emulator has been developed using a Xilinx Spartan-3 FPGA unit, which - from an electrical standpoint - provides fully representative interfaces between the two systems with regards to signal levels and content.

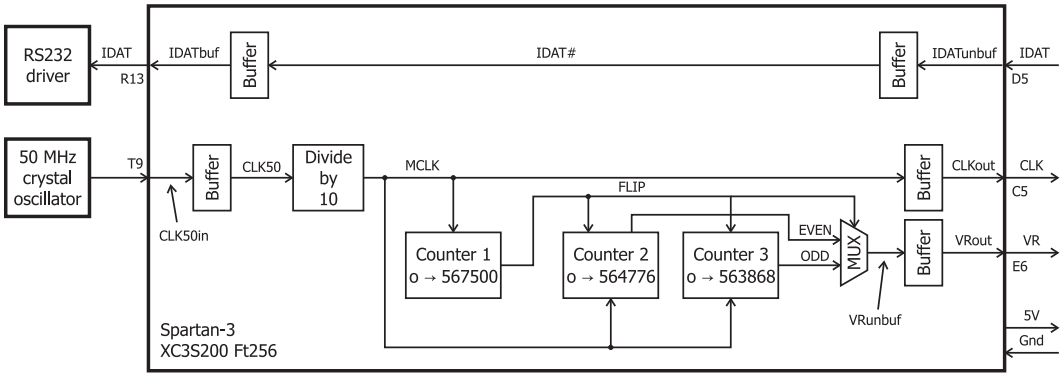

Figure 5.10. *μASC CHU emulator block diagram.*

As illustrated by the block diagram in Figure 5.10, the emulator is constructed in modular fashion using structural VHDL. The CLK clock signal for the μIRU is generated from a 50MHz 10ppm external crystal oscillator signal divided down to 5MHz and buffered prior to being output. The 5MHz MCLK signal is also used to drive three individual counters responsible for implementing emulation of the vertical reset (VR) signal normally used in the CHU. As the falling edge of this signal maintains a fixed temporal correlation with the image centre of integration (COI) of the μASC images it is included in the CHU-μIRU electronic interface to allow time synchronization between the μIRU accelerometer sample data and the stellar reference sensor image data.

In the context of the emulator, the 5MHz drive frequency for the μIRU has been chosen over the 4.608MHz clock nominally provided by the μASC for 4Hz operation. This specific frequency has been adopted to meet the ATMEGA168 timing requirements for 500k baud operation, thus ensuring sufficient data throughput to emulate full μIRU sample rate. Do note that the sample rate discrepancy between operating with the CHU emulator versus the real μASC CHU, only manifests itself as a performance offset rather than a functional limitation, hence constituting a fully acceptable simplification for development purposes.

5.7 Tier One μIRU Prototype GSE

To facilitate development, test and calibration efforts involving the Tier One μIRU Prototype, a number of ground support equipment (GSE) entities have been developed. Each of these are briefly described in the subsequent sections.

5.7.1 The μIRUlab Tool

The μIRUlab interface tool has been specifically developed to support μIRU Tier One development. Implemented in LabView 8.0, it provides basic raw data processing and real-time visualization of both AC and DC signals simultaneously, as well as online estimation of sample mean and variance for the last 5000 samples collected. Moreover, the architecture of the implementation is such that the full range of instrument data rates are supported, as is data logging for all channels at all rates.

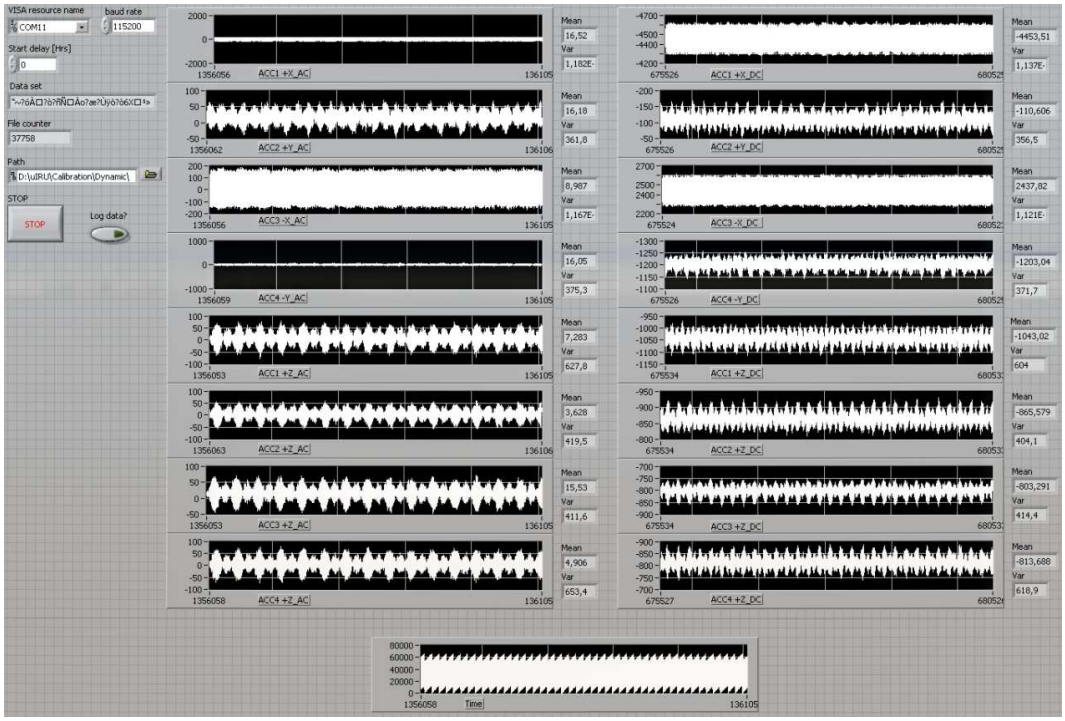

Figure 5.11. *Screenshot of the μIRUlab GUI.*

5.7.2 Wireless Power and Communication Interfaces

Dynamic experimentation and in particular calibration efforts does for the μIRU prototype necessitate physical separation of the external interfaces. As such, a compact GSE package has been developed which provides the instrument with a tightly regulated +5V supply generated from a Lithium-Polymer cell, as well as a high speed wireless communication link based upon a Roving Networks RN-41 Bluetooth module. As the Bluetooth module requires a well regulated 3.3V supply for operations, that specific voltage level is also derived from the Lithium-Polymer cell using a combination of step-up converters and linear regulators. An overview of the GSE package is provided in Figure 5.12.

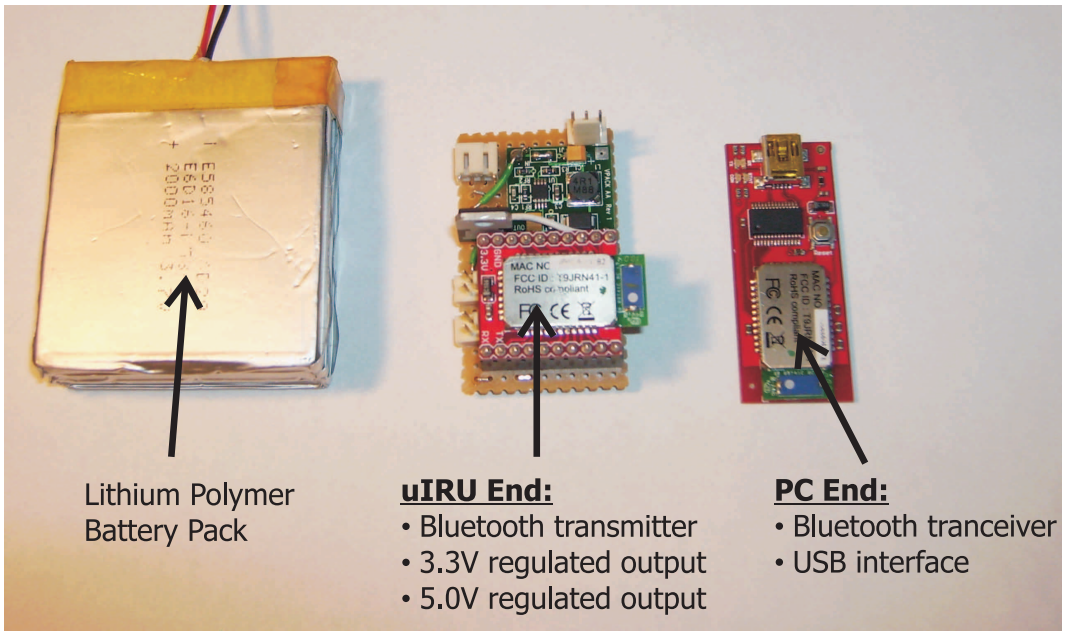

Figure 5.12. *μIRU GSE hardware.*

The counterpart of the GSE package wireless link is a USB-powered RN-41 module attached to the test computer. This computer then operates the μIRUlab interface tool to facilitate data capture for subsequent analysis. With a total mass of only 15 gram (excluding battery), the GSE package is sufficiently compact to be included as part of the dynamic segment under test without affecting the measurements.

5.8 Summary

This chapter has introduced the μIRU Tier One prototype developed as a baseline instrument for evaluating the design principles evolved from Chapter 4, and the specific choices made in establishing its physical implementation. In addition to the instrument itself, associated GSE hardware and software entities developed to support operations have been introduced.

5.9 Bibliography

[SIG-2007] Space Instrumentation Group. Micro advanced stellar compass product assurance plan. Technical report, DTU Space, 2007.

Chapter 6

Sensor Calibration

The process of calibration serves to accurately establish the relationship between the μIRU sensed quantities and the true physical units. The chapter at hand conveys the considerations that have gone into developing a suitable calibration strategy for this type of inertial attitude instrumentation, as well as the realization of the calibration platforms. Subsequently the application of the calibration routines on the Tier One version of μIRU prototype and the associated results are discussed.

6.1 Calibration Philosophy

Relating the engineering units produced by the μIRU instrument to true physical values necessitates the determination of the time invariant quantities pertaining to the sensor equation 2.3, namely the physical position of the accelerometers, their orthogonalization coefficients and their offsets. The μIRU prototype is designed to primarily utilize its AC channels when conducting attitude determination and fused operations with the μASC, yet the prudent inclusion of DC channels in the design still allows static acceleration measurements to be conducted, albeit at half the bandwidth of the AC measurements. For the calibration procedures, however, bandwidth remains of little consequence in establishing the time-invariant design parameters. The envisioned μIRU calibration procedure has been divided into four separate steps, which when combined covers time-invariant parameters of both DC and AC channels for all accelerometer axes. The details and sequencing of these steps are as follows:

Step 1: Static calibration to establish sensor orientations, DC channel scale factors and DC channel offsets.

Step 2: Static calibration to establish AC channel offsets.

Step 3: Dynamic calibration to determine accelerometer positions using DC channels.

Step 4: Dynamic calibration to determine scale factors of AC channels.

Principally step 1 and 3 could be combined by the introduction of calibrated force, yet experiments conducted with combined calibrations of a linear accelerometer array as reported on by [Cappa-2008] have proven to yield poor metrological performance and an increase in RMS errors on measured translation and angular acceleration for a 12 accelerometer cluster of 60% and 100%, respectively. Similarly, step 1 and step 2 may be conducted simultaneously provided both AC and DC channel data are recorded during the procedure.

To clarify terminologies, the proposed static calibration utilizes the gravitational field as a calibrated source of acceleration, thus allowing individual sensors to be exposed to different discrete levels of acceleration by simply changing their orientation in the field. With measurements only taken at sensor static positions, AC channels will be precluded from seeing any acceleration beyond their offset levels, whereas DC channels on the other hand, will see an angle dependent fraction of the gravity vector.

Dynamic calibration implies subjecting the μIRU sensor assembly to controlled force. By applying a constant rotational motion free from mechanical disturbances to the instrument, it is possible to isolate the centripetal contribution in the sensor equation 2.3. For the statically calibrated accelerometers, the measured acceleration along one of the principal axes will as such depend upon their physical separation along that axis. Hence the relative positions of the accelerometers within the μIRU assembly can be assessed. Further details regarding the physical test setups and operating procedures are provided in subsequent relevant sections.

6.2 Step 1: Static Calibration - The Thin Shell Method

The procedure developed for statically calibrating the μIRU has two primary objectives. Firstly, to establish the exact orientation and scale factor of all the individual accelerometer axes, and secondly to determine the signal level offset pertaining to each accelerometer channel. Several viable procedures exist for accomplishing this part of the calibration. For a single sensor triad, most commonly a high precision 3-axis turn table will be used to work through a series of perfectly orthogonal orientations, thus exposing each sensor axis to exactly $\pm 1g$ and 0g, thereby allowing the parameters to be extracted directly

[Chatfield-1997]. However, even though this procedure is formally correct, it fails to capture most (if any) sensor idiosyncratic behavior beyond the basic calibration parameters, thus making it difficult to accurately asses the quality of the calibration.

A more rigorous method which also does away with the need for the high precision turn table is the thin shell approach, which is also a method of preference for accurately calibrating high performance magnetometers [Merayo-1999]. For the purpose of absolutely calibrating accelerometers, the method is adapted to harness the distinct advantage of the ever present gravitational field. Being a conservative force field, the vector sum of any ideal triad of orthogonal accelerometers exposed to the gravitational field will always be 1g (with reference to the local magnitude of the gravitational acceleration), or expressed formally:

$$G_o = \sqrt{G_x^2 + G_y^2 + G_z^2} = 1g \simeq 9.8157 \frac{m}{s^2} \tag{6.1}$$

As this relation holds true for any orientation of the accelerometer triad, it can be utilized in establishing the calibration parameters. The first step in applying this knowledge is adopting a suitable model to describe the relationship between the measured acceleration quantities in engineering units EU to the reference acceleration level G. The model adopted for the μIRU accelerometers is expressed as equation 6.2.

$$\vec{G} = [\mathbf{T}^{-1}]^T \cdot \mathbf{S} \cdot \left(\vec{EU} - \vec{b} \right) \tag{6.2}$$

where:
G: expresses the gravity vector.
$\mathbf{T}$: expresses the alignment matrix, transforming the non-orthogonal accelerometer axes to an orthogonal body frame.
$\mathbf{S}$: expresses the scale factor matrix.
EU: denotes the measured acceleration vector in engineering units.
b: expresses bias or offset vector.

Expounding the representation of equation 6.2 yields the following detailed expression:

$$\begin{bmatrix} G_x \\ G_y \\ G_z \end{bmatrix} = \begin{bmatrix} T_{11} & T_{12} & T_{13} \\ 0 & T_{22} & T_{23} \\ 0 & 0 & T_{33} \end{bmatrix} \cdot \begin{bmatrix} s_x & 0 & 0 \\ 0 & s_y & 0 \\ 0 & 0 & s_z \end{bmatrix} \begin{bmatrix} EU_1 - b_x \\ EU_2 - b_y \\ EU_3 - b_z \end{bmatrix} \tag{6.3}$$

The particular formulation of the alignment matrix $\mathbf{T}$ stems from the method used to transform the non-orthogonal physical arrangement of the triad accelerometers into an orthogonal representation. Assuming that the physical

non-orthogonal axes (x_p, y_p, z_p) of the accelerometer triad have achieved close alignment to an arbitrary orthogonal body frame (x_b, y_b, z_b) during assembly, the situation depicted in Figure 6.1 manifests itself.

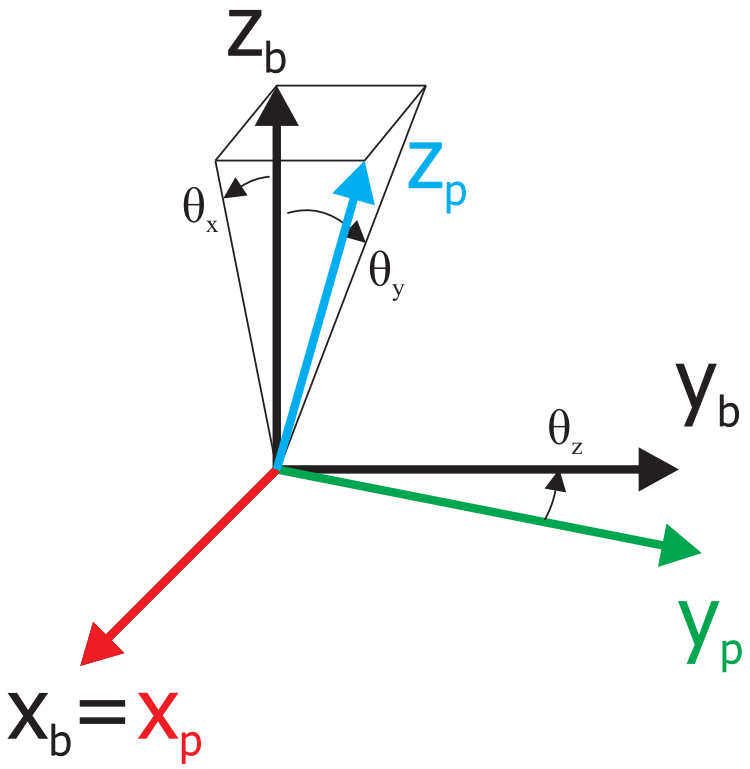

Figure 6.1. *Orthogonalization of non-orthogonal physical frame.*

As described by [Merayo-1999, Angrisano-2009] orthogonalization of the physical accelerometer triad frame may be achieved by a minimalist set of operations by making the simplifying assumption that the x_p-axis from the physical frame is fully aligned with the x_b-axis of orthogonal reference frame.

$$\begin{bmatrix} x_b \\ y_b \\ z_b \end{bmatrix} \equiv \mathbf{T} \begin{bmatrix} x_p \\ y_p \\ z_p \end{bmatrix} \equiv \begin{bmatrix} 1 & 0 & 0 \\ \alpha_1 & \alpha_2 & 0 \\ \beta_1 & \beta_2 & \beta_3 \end{bmatrix} \cdot \begin{bmatrix} x_p \\ y_p \\ z_p \end{bmatrix} \tag{6.4}$$

This assumption leads to the representation of equation 6.4, whereby the physical frame can be orthogonalized by defining the second orthonormal axis y_b, to lie in a plane defined by x_p and y_p, and is only misaligned with respect to y_p by a small angle θ_z. The third orthonormal axis is thus completely defined from the cross product of the first and second axes resulting in a full dextrogiro frame representation. Formally, this proviso may be expressed as:

$$x_b \equiv x_p \tag{6.5}$$
$$y_b \equiv z_b \times x_p = \alpha_1 x_p + \alpha_2 y_p \tag{6.6}$$
$$z_b \equiv \frac{x_p \times y_p}{|x_p \times y_p|} = \beta_1 x_p + \beta_2 y_p + \beta_3 z_p \tag{6.7}$$
$$\tag{6.8}$$

Where the misalignment coefficients α_1, β_1 and β_2 will trend towards 0 for an orthonormal representation and α_2, β_3 towards 1, resulting in the transformation matrix equating to the identity matrix for a fully orthogonal physical frame. The transformation matrix $\mathbf{T}$ of equation 6.3 therefore relates the measured quantities in the physical frame to the orthogonal frame by its inverse transposed i.e. $[\mathbf{T}^{-1}]^T$, thus:

$$\begin{bmatrix} G_x \\ G_y \\ G_z \end{bmatrix} = \left[\mathbf{T}^{-1}\right]^T \cdot \begin{bmatrix} s_x & 0 & 0 \\ 0 & s_y & 0 \\ 0 & 0 & s_z \end{bmatrix} \begin{bmatrix} EU_1 - b_x \\ EU_2 - b_y \\ EU_3 - b_z \end{bmatrix} \tag{6.9}$$
$$= \begin{bmatrix} 1 & -\frac{\alpha_1}{\alpha_2} & \frac{\alpha_1\beta_2 - \alpha_2\beta_1}{\alpha_2\beta_3} \\ 0 & \frac{1}{\alpha_2} & -\frac{\beta_2}{\alpha_2\beta_3} \\ 0 & 0 & \frac{1}{\beta_3} \end{bmatrix} \cdot \begin{bmatrix} s_x & 0 & 0 \\ 0 & s_y & 0 \\ 0 & 0 & s_z \end{bmatrix} \begin{bmatrix} EU_1 - b_x \\ EU_2 - b_y \\ EU_3 - b_z \end{bmatrix} \tag{6.10}$$
$$= \mathbf{K} \begin{bmatrix} EU_1 - b_x \\ EU_2 - b_y \\ EU_3 - b_z \end{bmatrix} \tag{6.11}$$

Where $\mathbf{K}$ compounds the transformation and sensitivity matrices into one, thus yielding:

$$\mathbf{K} = \begin{bmatrix} k_{11} & k_{12} & k_{13} \\ 0 & k_{22} & k_{23} \\ 0 & 0 & k_{33} \end{bmatrix} = \begin{bmatrix} s_x & -\frac{\alpha_1}{\alpha_2} s_y & \frac{\alpha_1\beta_2 - \alpha_2\beta_1}{\alpha_2\beta_3} s_z \\ 0 & \frac{1}{\alpha_2} s_y & -\frac{\beta_2}{\alpha_2\beta_3} s_z \\ 0 & 0 & \frac{1}{\beta_3} s_z \end{bmatrix} \tag{6.12}$$

Applying the reasonable assumption that the misalignment angles of the physical axes with respect to the orthogonal frame can be considered small, allows the coefficient matrix $\mathbf{K}$ to be simplified further:

$$\mathbf{K} \cong \begin{bmatrix} s_x & -\alpha_1 s_y & -\beta_1 s_z \\ 0 & s_y & -\beta_2 s_z \\ 0 & 0 & s_z \end{bmatrix} \tag{6.13}$$

The combination of equations 6.11 and 6.13 provides a linear system which is capable of generating a calibrated orthogonal representation of the raw output

signal from a non-orthogonal accelerometer triad. To achieve orthogonalization and correct signal magnitude from the triad it is however necessary to determine no less than nine calibration parameters, namely the scale factors s_x, s_y and s_z, the misalignment coefficients α_1, β_1 and β_2 and finally the bias vector components b_x, b_y and b_z. To estimate these parameters an overdetermined system will be constructed and solved using a linear least-squares approach. To this end the gravity field will be used as the reference signal, and compared with the sum of squares of the physical signal components as outlined by equation 6.11. Calculating the sum of squares of the physical signal components is done by equating the dot product of equation 6.3 with itself, yielding the factorized result in equation 6.15.

$$\begin{aligned}
\vec{G}\cdot\vec{G} &= (k_{11}(EU_1-b_x)+k_{12}(EU_2-b_y)+k_{13}(EU_3-b_z))^2 + \\
&\quad (k_{22}(EU_2-b_y)+k_{23}(EU_3-b_z))^2 + k_{33}^2(EU_3-b_z)^2 \qquad (6.14)\\
&= k_{11}^2EU_1^2+(k_{12}^2+k_{22}^2)EU_2^2+(k_{13}^2+k_{23}^2+k_{33}^2)EU_3^2\\
&\quad +2k_{11}EU_1k_{12}EU_2+2(k_{12}k_{13}+k_{22}k_{23})EU_2EU_3+2k_{11}k_{13}EU_1EU_3\\
&\quad -2(k_{11}k_{12}b_y+k_{11}k_{13}b_z+k_{11}^2b_x)EU_1\\
&\quad -2\left(k_{11}k_{12}b_x+k_{22}^2b_y+k_{12}^2b_y+k_{12}k_{13}b_z+k_{22}k_{23}b_z\right)EU_2\\
&\quad -2\left(k_{11}k_{13}b_x+k_{33}^2b_z+k_{23}^2b_z+k_{13}^2b_z+k_{12}k_{13}b_y+k_{22}k_{23}b_y\right)EU_3\\
&\quad +k_{11}^2b_x^2+k_{12}^2b_y^2+k_{13}^2b_z^2+k_{22}^2b_y^2+k_{23}^2b_z^2+k_{33}^2b_z^2\\
&\quad +2k_{11}k_{12}b_xb_y+2k_{11}k_{13}b_xb_z+2k_{12}k_{13}b_yb_z+2k_{22}k_{23}b_yb_z \qquad (6.15)
\end{aligned}$$

It should be noted that the two last lines of equation 6.15 reflect the square of the residual signal magnitude as caused by the sensor biases. These could otherwise be expressed as:

$$\begin{aligned}
\vec{G}_b\cdot\vec{G}_b &= \mathbf{K}\begin{bmatrix}b_x\\b_y\\b_z\end{bmatrix}\cdot\mathbf{K}\begin{bmatrix}b_x\\b_y\\b_z\end{bmatrix} \qquad (6.16)\\
&= (k_{11}b_x+k_{12}b_y+k_{13}b_z)^2+(k_{22}b_y+k_{23}b_z)^2+k_{33}^2b_z^2 \qquad (6.17)
\end{aligned}$$

It is clear that a computation of the gravity field magnitude ($\sqrt{\vec{G}\cdot\vec{G}}$) based upon the squared expression in equation 6.15 will be influenced by the non-linear EU terms, hence a linear least squares approach is not directly applicable. However, adopting the parameterization introduced by [Merayo-1999] as adapted to the purpose at hand in equation 6.18, allows the square of the gravity field magnitude to be expressed as a linear combination of EU terms, thus representing the problem in a manner applicable to a least squares linear sense solution.

$$G^2-G_b^2=\begin{bmatrix}EU_1^2 & EU_1 & EU_2^2 & EU_2 & EU_3^2 & EU_3 & EU_1EU_2 & EU_2EU_3 & EU_3EU_1\end{bmatrix}\cdot\vec{p} \qquad (6.18)$$

The vector $\vec{p}$ defined in equation 6.19 thus encompasses the terms derived in equation 6.15 pertaining to each of the EU components, and thereby provide a direct representation of the nine calibration parameters of the accelerometer triad.

$$\begin{bmatrix} p_1 \\ p_2 \\ p_3 \\ p_4 \\ p_5 \\ p_6 \\ p_7 \\ p_8 \\ p_9 \end{bmatrix} = \begin{bmatrix} k_{11}^2 \\ -2(k_{11}k_{12}b_y + k_{11}k_{13}b_z + k_{11}^2 b_x) \\ k_{12}^2 + k_{22}^2 \\ -2\left(k_{11}k_{12}b_x + k_{22}^2 b_y + k_{12}^2 b_y + k_{12}k_{13}b_z + k_{22}k_{23}b_z\right) \\ k_{13}^2 + k_{23}^2 + k_{33}^2 \\ -2\left(k_{11}k_{13}b_x + k_{33}^2 b_z + k_{23}^2 b_z + k_{13}^2 b_z + k_{12}k_{13}b_y + k_{22}k_{23}b_y\right) \\ 2k_{11}k_{12} \\ 2(k_{12}k_{13} + k_{22}k_{23}) \\ 2k_{11}k_{13} \end{bmatrix} \tag{6.19}$$

By determining $\vec{p}$, the parameters of the $\mathbf{K}$ matrix can be directly determined by solving for individual components of $\vec{p}$ in the correct order, thereby leading to the direct expressions of equation 6.20. Similarly, equation 6.21 as derived by [Merayo-2000] provides grounds for estimating the bias vector pertaining to the accelerometer sensor triad directly from the $\vec{p}$ vector.

$$\begin{aligned} k_{11} &= \sqrt{p_1} \\ k_{12} &= \frac{p_7}{2\sqrt{p_1}} \\ k_{13} &= \frac{p_9}{2\sqrt{p_1}} \\ k_{22} &= \sqrt{p_3 - \frac{p_7^2}{4p_1}} \\ k_{23} &= \frac{2p_1p_8 - p_7p_9}{2\sqrt{4p_1^2p_3 - p_1p_7^2}} \\ k_{33} &= \pm\sqrt{p_5 - \frac{p_9^2}{4p_1} + \left(\frac{2p_1p_8 - p_7p_9}{2\sqrt{4p_1^2p_3 - p_1p_7^2}}\right)^2} \end{aligned} \tag{6.20}$$

$$\begin{bmatrix} b_x \\ b_y \\ b_z \end{bmatrix} = \begin{bmatrix} -2p_1 & -p_7 & -p_9 \\ -p_7 & -2p_3 & -p_8 \\ -p_9 & -p_8 & -2p_5 \end{bmatrix}^{-1} \begin{bmatrix} p_2 \\ p_4 \\ p_6 \end{bmatrix} \tag{6.21}$$

It should be noted that a potential sign ambiguity exists with respect to k_{33}. Here, the value should be chosen so as to ensure a right-handed coordinate

system for simplicity in the subsequent rotations needed to align all the triads of the μIRU.

To determine the $\vec{p}$ vector components, equation 6.18 is augmented to generate a scoring function for an overdetermined system. By stacking N different measurements that span the entire range of the sensor triad to create equation 6.22, a linear least squares procedure can be applied which minimizes the sum of the square residuals of the scoring function, thus providing an optimal estimate of the $\vec{p}$ vector for a given set of input data.

$$\begin{bmatrix} G_1^2 \\ G_2^2 \\ \vdots \\ \vdots \\ \vdots \\ G_N^2 \end{bmatrix} - \begin{bmatrix} G_{o_1}^2 \\ G_{o_2}^2 \\ \vdots \\ \vdots \\ \vdots \\ G_{o_N}^2 \end{bmatrix} = \begin{bmatrix} EU_{1_1}^2 & EU_{1_1} & EU_{2_1}^2 & EU_{2_1} & EU_{3_1}^2 & EU_{3_1} & EU_1EU_{2_1} & EU_2EU_{3_1} & EU_3EU_{1_1} \\ EU_{1_2}^2 & EU_{1_2} & EU_{2_2}^2 & EU_{2_2} & EU_{3_2}^2 & EU_{3_2} & EU_1EU_{2_2} & EU_2EU_{3_2} & EU_3EU_{1_2} \\ \vdots & \vdots & \vdots & \vdots & \vdots & \vdots & \vdots & \vdots & \vdots \\ \vdots & \vdots & \vdots & \vdots & \vdots & \vdots & \vdots & \vdots & \vdots \\ \vdots & \vdots & \vdots & \vdots & \vdots & \vdots & \vdots & \vdots & \vdots \\ EU_{1_N}^2 & EU_{1_N} & EU_{2_N}^2 & EU_{2_N} & EU_{3_N}^2 & EU_{3_N} & EU_1EU_{2_N} & EU_2EU_{3_N} & EU_3EU_{1_N} \end{bmatrix} \cdot \begin{bmatrix} p_1 \\ p_2 \\ p_3 \\ p_4 \\ p_5 \\ p_6 \\ p_7 \\ p_8 \\ p_9 \end{bmatrix} \quad (6.22)$$

Formulating equation 6.22 in matrix notation yields the expression provided in equation 6.23, where the $\mathbf{D}$ matrix is comprised of the EU terms introduced by the parametrization equation 6.18.

$$\begin{array}{ccccc} G^2 & - & G_o^2 & = & \mathbf{D} \cdot \vec{p} \\ [N \times 1] & - & [N \times 1] & = & [N \times 9][9 \times 1] \end{array} \quad (6.23)$$

From this expression the $\vec{p}$ vector may be determined directly by applying a numeric least squares solver in adherence to the standard formulation:

$$\vec{p} = \left[\mathbf{D}^T\mathbf{D}\right]^{-1}\mathbf{D}^T\mathbf{G} \quad (6.24)$$

When using the gravitational field as input this expression simplifies even further as $G = 1$ when operating units of [g]. Principally the numerical problem can be solved for N>9, yet the quality of the least squares fit does depend heavily on both data quality, data distribution and the number of measurements N applied. With regards to data distribution, obtaining high quality estimates for the $\vec{p}$ vector relies on excersizing the entire range of the triad being calibrated. With a conservative force field as input stimuli this translates directly into ensuring adequate sample coverage over the unity sphere. How this is achieved is the topic of the subsequent section.

6.2.1 Calibration Data Distribution

A key element in obtaining accurate calibration results with the thin shell method and the least squares estimation principle, is to ensure the collection

of data is uniformly distributed over the unit sphere. From a practical perspective this must be accomplished using a finite number of sensor orientations, to allow the data collection to take place within a reasonable time interval, thus limiting offsets incurred by thermal drift (provided temperature data is not collected and used to compensate the measurements). One approach to distributing the measurement orientations as reported by [Brauer-1997] utilizes equal area representation, considering the unity sphere representation in spherical coordinates $ds = \sin\theta d\theta d\phi$ with the definition proviso outlined in Figure 6.2.

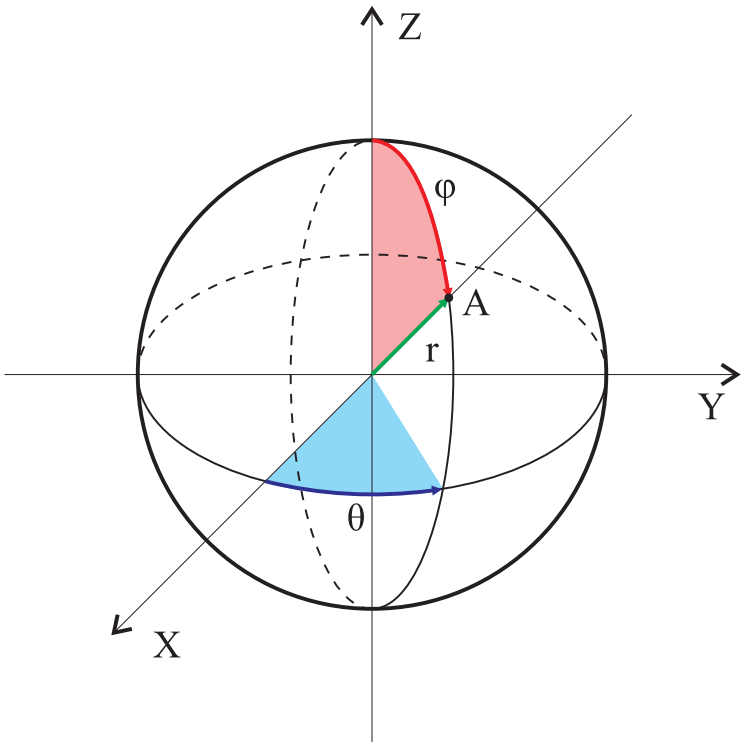

Figure 6.2. *Spherical coordinate convention for the static calibration procedures.*

By dividing the meridians of the sphere into n_θ equal polar angles θ_i in accordance with equation 6.25, the number of azimuth orientations $n_{\phi i}$ needed to obtain equidistant separations between consecutive azimuth angles ϕ_{ij} can be expressed as equation 6.26.

$$\theta_i = \frac{i-1}{n_\theta - 1}\pi \qquad i = 1, 2, \ldots, n_\theta \tag{6.25}$$

$$n_{\phi i} = \text{floor}\left(2\sin\theta_i\left(n_\theta + 1\right) + 1\right) \tag{6.26}$$

where,

$$\phi_{ri} = \begin{cases} \frac{1}{n_{\theta i}} & \text{if } n_{\theta i} \text{ is odd} \\ 0 & \text{otherwise} \end{cases} \tag{6.27}$$

Thus allowing the azimuth angles to be determined from equation 6.28.

$$\phi_{ij} = \frac{j}{n_{\phi i}} 2\pi - \phi_{ri} \qquad j = 1, 2, \ldots, n_{\theta i} \tag{6.28}$$

In this treatise two different measurement distribution sets will be used. One for coarse calibration denoted 33P (containing 33 individual orientations) and one for fine calibration denoted 84P (containing 84 individual orientations). The 33P has been used extensively in the instrument development process, as a reasonably fast means of verifying orthogonalization parameters and offsets to a reasonable degree of accuracy whenever the μIRU prototype was disassembled and reassembled for electronics work. As a visualization aid Figure 6.3 depicts the distribution of measurement orientations for the 33P procedure and their projection onto the unity sphere.

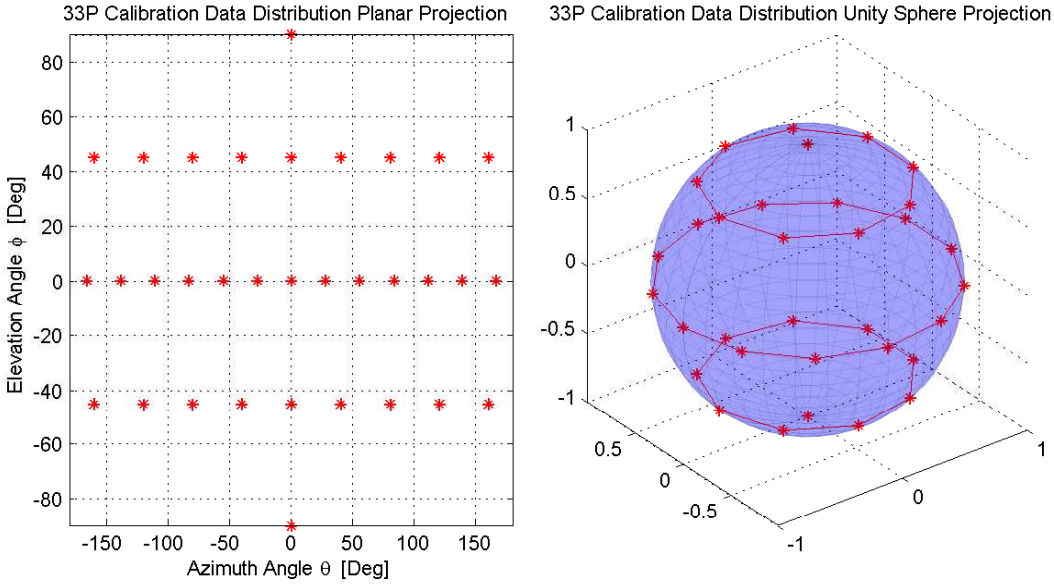

Figure 6.3. *33P ($n_\theta = 5$) calibration data distribution.*

The 84P calibration procedure was devised to produce a much more detailed assessment of the angular orientation dependency of the measurements, and to reveal the influence of the cross-axis sensitivity and hysteresis response of the LIS2L02AL accelerometers as characterized in Chapter 3. Being significantly more laborious to conduct manually than the 33P, the 84P procedure was conducted only twice following final assembly of the μIRU Tier One prototype to fully characterize the instrument.

It should be noted that the correct approach to interpreting the orientation distributions in Figures 6.3 and 6.4, is to envision the +Z-axis of the μIRU aligned with the radius vector pertaining to each point projected onto the unity sphere, while maintaining a fully invariant instrument rotation about the vector.

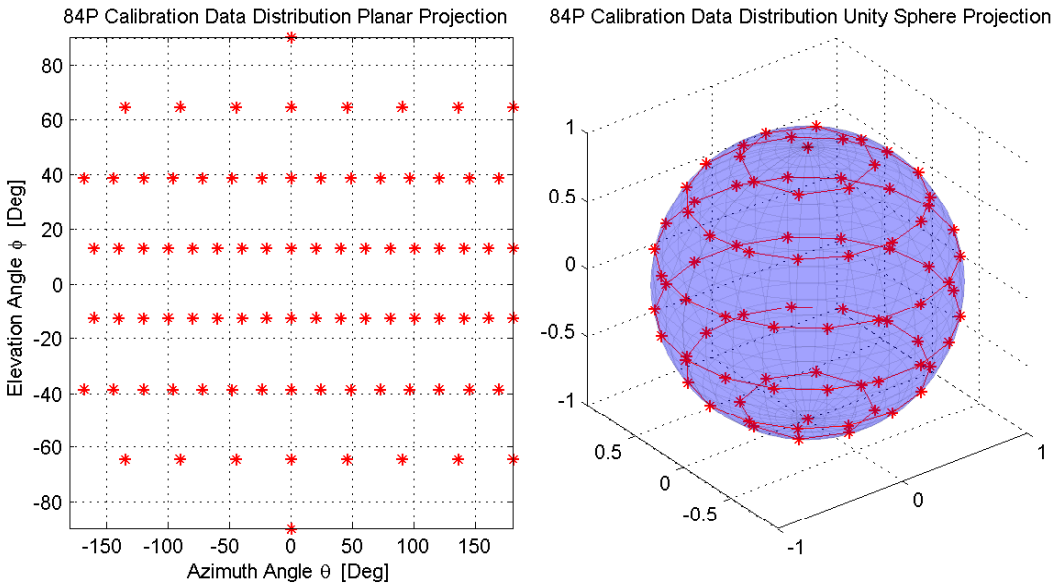

Figure 6.4. *84P ($n_\theta = 8$) calibration data distribution.*

6.2.2 Multiple Triad Static Calibration - Triad Alignment

The methodologies that have presently been outlined for calibrating a triad of linear accelerometers utilize well known metrology principles. Also, they have extensive heritage in their employment for high fidelity scalar calibration of precision vector instrumentation such as aerospace magnetometers [Merayo-2000]. The key difference between such vector instrumentation and the μIRU is the number of individual sensitive axes involved. The basic principle of triad calibration must as such be extended to accommodate the total of eight sensitive axes present in the μIRU instrument.

A full calibration of the μIRU entails determining the biases, scale factors and misalignments for all sensors, however, for that knowledge to be useful it must be available in a unified reference frame. The straightforward solution to problem is to maintain the triad calibration philosophy and subsequently perform a series of rotations to align and scale responses into a unified frame. To this end a suitable reference frame must be established, and for the application at hand the chosen frame is defined by the primary calibrated triad consisting of the ACC1+X, ACC2+Y and ACC1+Z signals as illustrated in Figure 6.5. This triad is hereinafter denoted Triad1. A secondary triad defined by ACC3-X, ACC4-Y and ACC3+Z is also established, hereinafter to be denoted as Triad2.

The two triads combined encompass six of the eight instrument DC channels. The remaining axes not yet addressed are ACC2+Z and ACC4+Z. However, the way in which the triad orthogonalization has been implemented in equa-

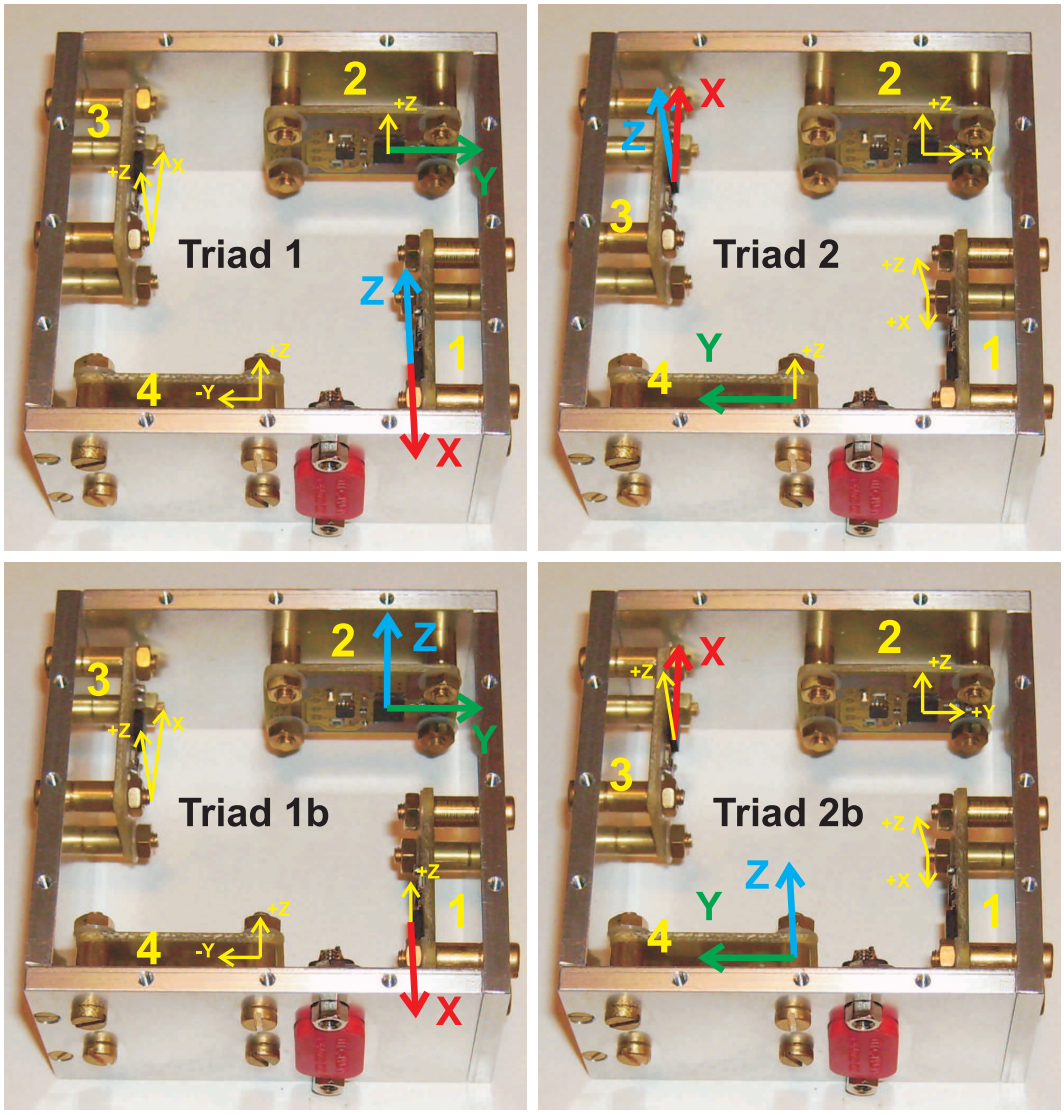

Figure 6.5. *Visualization of μIRU calibration triads. Triad1 (primary) on the top left, Triad2 (secondary) on the top right.*

tion 6.7, lets the Z axis be defined from the cross product of an orthogonal projection of X and Y. Effectively this principle allows both remaining Z-axes to be calibrated with respect to their individual triads without significantly changing the calibration parameters of the remaining axes. As such, two additional triads (Triad1b and Triad2b) are formed which merely substitutes the Z-axes of Triad 1 and 2. In total this definition entails operating with four triads that must all be aligned to the orthogonal reference frame spanned by Triad 1.

From Figure 6.5 its clear that the two primary triads are subject to a large scale misalignment by ∼180° rotation about the Z-axis. This also extends to Triad2b in relation to Triad1. As such, the first step towards fusing the

measurements from the four triads, becomes effectuating a coarse alignment of the four triads by rotating Triad2 and Triad2b 180° about Z by applying the direction cosine rotation matrix $\mathbf{R_Z}$ as defined by:

$$\mathbf{R_Z} = \begin{bmatrix} \cos\pi & \sin\pi & 0 \\ -\sin\pi & \cos\pi & 0 \\ 0 & 0 & 1 \end{bmatrix} \tag{6.29}$$

Through the application of $\mathbf{R_Z}$ all triads can now be considered coarsely aligned, with the misalignments reduced to a fine rotation about the principle axes of Triad1. The present situation can thus be formalized as:

$$\vec{G_{tri1}} \equiv \vec{G_{tri1}} \tag{6.30}$$
$$\vec{G^{1b}_{tri1}} = \vec{G_{tri1b}} \cdot \xi_{\mathbf{1b-1}} \tag{6.31}$$
$$\vec{G^{2}_{tri1}} = \vec{G_{tri2}} \cdot \mathbf{R_Z}\xi_{\mathbf{2-1}} \tag{6.32}$$
$$\vec{G^{2b}_{tri1}} = \vec{G_{tri2b}} \cdot \mathbf{R_Z}\xi_{\mathbf{2b-1}} \tag{6.33}$$

Where $\xi_{\mathbf{1b-1}}$,$\xi_{\mathbf{2-1}}$,$\xi_{\mathbf{2b-1}}$ signify the fine rotation matrices needed to align the secondary triads to the primary triad. It must be stressed that no adaptation of the sensor scale factors or offset will be involved in the procedure, thus the static calibration results for those sensor parameters remain intact. To accurately determine the fine rotation matrices and thereby the representation of Triad1b, Triad2 and Triad2b in the Triad1 reference frame, the static calibration dataset is once again employed. From here, the specific gravity vector $\vec{G_o}$ is known in the individual triads as $\vec{G_{tri}}$ to within the accuracy of the calibration, and as such, moving from Triad2 to Triad1 would entail determining the rotation between the same vector in two different bases. Having this knowledge available for all discrete instrument orientations in the dataset, allows a matrix formulation of the problem to be constructed:

$$\begin{bmatrix} G_o \\ \vdots \\ \vdots \\ G_{o_N} \end{bmatrix}^T = \left(\begin{bmatrix} G_{tri} \\ \vdots \\ \vdots \\ G_{tri_N} \end{bmatrix}^T \mathbf{R} \right) \cdot \begin{bmatrix} \xi_{11} & \xi_{12} & \xi_{13} \\ \xi_{21} & \xi_{22} & \xi_{23} \\ \xi_{31} & \xi_{32} & \xi_{33} \end{bmatrix} \tag{6.34}$$
$$[N \times 1] = ([N \times 1][3 \times 3]) \cdot \quad [3 \times 3]$$

Where $\mathbf{R}$ expresses the $\mathbf{R} = \mathbf{R_Z}$ coarse rotation matrix for Triad2/Triad2b, and the identity matrix $\mathbf{R} = \mathbf{I}$ for Triad1b. The ξ_{ij} coefficients of the fine rotation matrix ξ may be optimally estimated in the least squares sense when solving equation 6.34 for ξ by applying a numeric least squares solver in adherence to the standard formulation:

$$\xi = \left[[\mathbf{G_{tri}R}]^T[\mathbf{G_{tri}R}]\right]^{-1}[\mathbf{G_{tri}R}]^T\mathbf{G_o} \tag{6.35}$$

6.2.3 Static Calibration Procedure Results

The previously outlined static calibration procedure has been applied to the μIRU Tier One prototype, using the physical setup depicted in Figure 6.6. The μIRU and its wireless GSE where attached to the rotation fixture and allowed six hours of powered thermalization prior to commencement of the calibration procedure.

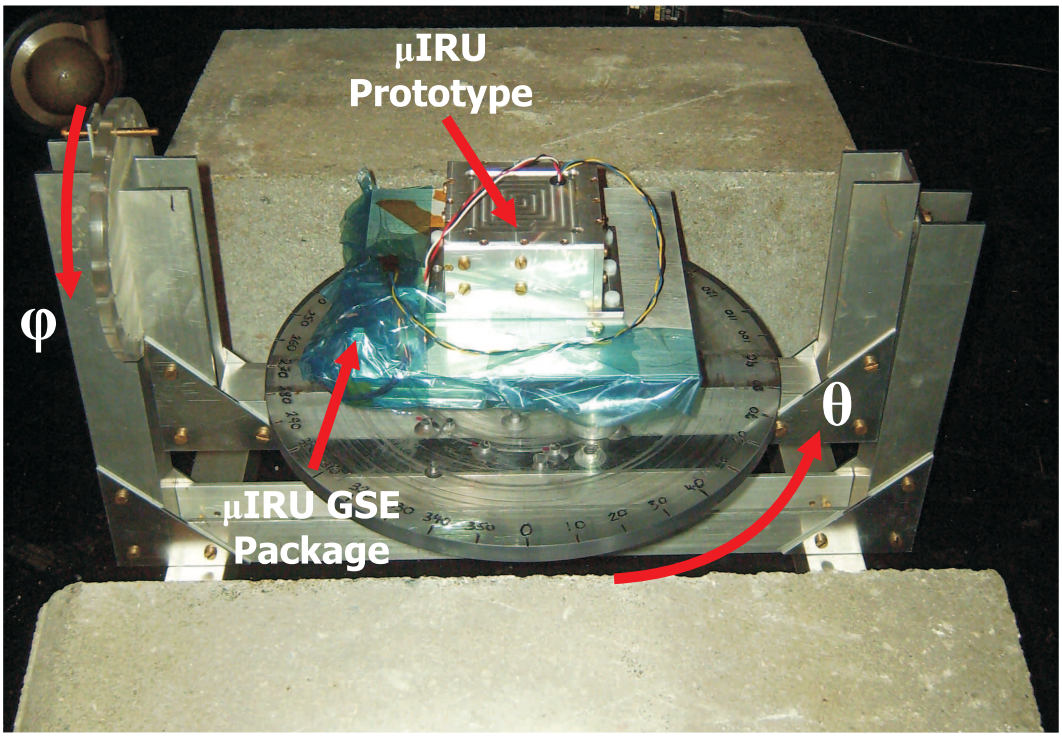

Figure 6.6. *μIRU static calibration setup.*

The calibration was originally planned as a single run of the 84P routine as outlined in Section 6.2.1, yet in lieu of the results of the first 84P run (designated 84P1) being somewhat degraded by external vibrations, a second run (designated 84P2) was conducted moving through the orientations in the opposite order as compared to 84P1. As such, the 84P2 dataset is considered the prime basis for calibrating the μIRU. Looking first at the results pertaining to the primary triad (Triad1) in Figure 6.7, the least square fit residuals over all 84 positions of the dataset reveal a peak-to-peak magnitude error on the order of $\pm$1.5mg, which should be seen in comparison to the nominal $\sim 400\mu g_{rms}$ noise floor of the LIS2L02AL sensor for the design bandwidth. Moreover, the

expectation for an ideal linear sensor with white noise characteristics would be for the residuals to take on a fully random distribution, which is clearly not the case for the residuals pertaining to Triad1 in Figure 6.7.

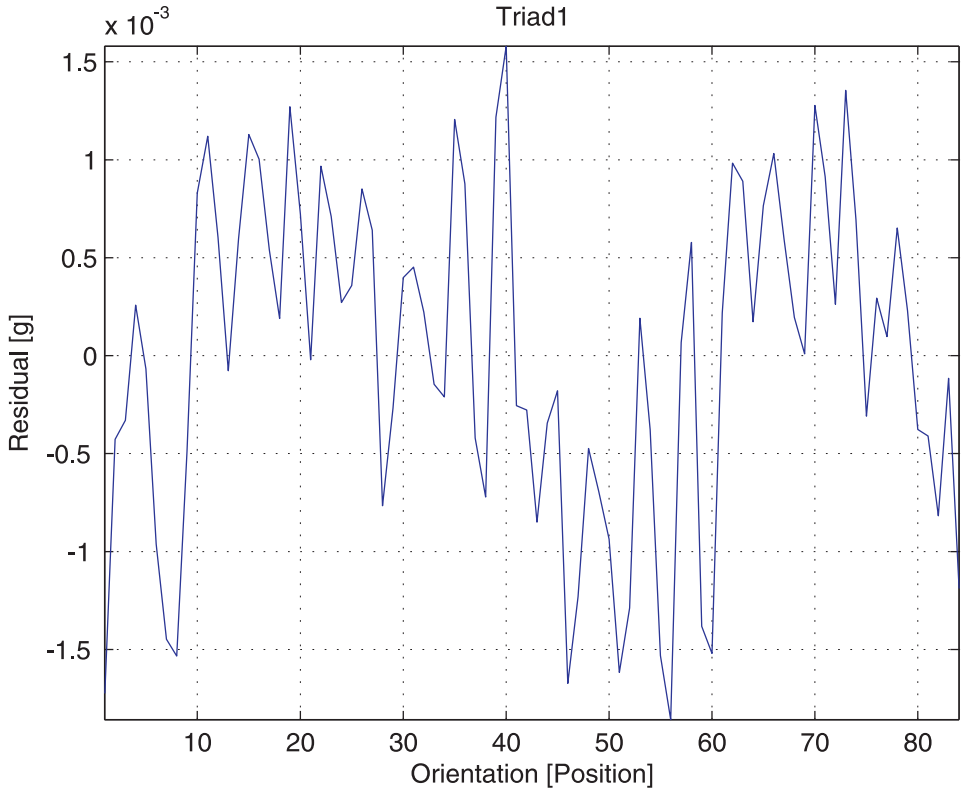

Figure 6.7. *Static calibration residuals for Triad1.*

To study any potential correlation between residual magnitude and instrument orientation, the gravity vector magnitude estimate together with the discrete orientations have been interpolated and projected onto the unity sphere. The results hereof are depicted in Figure 6.8 for Triad1 and clearly show a 90° phase correlation. All indications are that the observed systematic behavior of the residuals can be attributed to the output hysteresis of the LIS2L02AL accelerometer as was identified in Chapter 3. Moreover, this hypothesis is corroborated by the results of the 84P1 run, whereas calibration runs using the 33P routine fail to resolve these sensor idiosyncrasies.

Although undesirable, the hysteretic nature of the sensor outputs does not preclude operating the μIRU instrument, yet it introduces undesirable errors which could otherwise be compensated by using phenomenological modeling of the individual sensors [Ang-2003]. For the treatise at hand however, such a non-physical extension will not be applied, rather the calibration procedure and achievable instrument performance using the linear sensor model will be evaluated. The application of LIS2L02AL phenomenological modeling is as

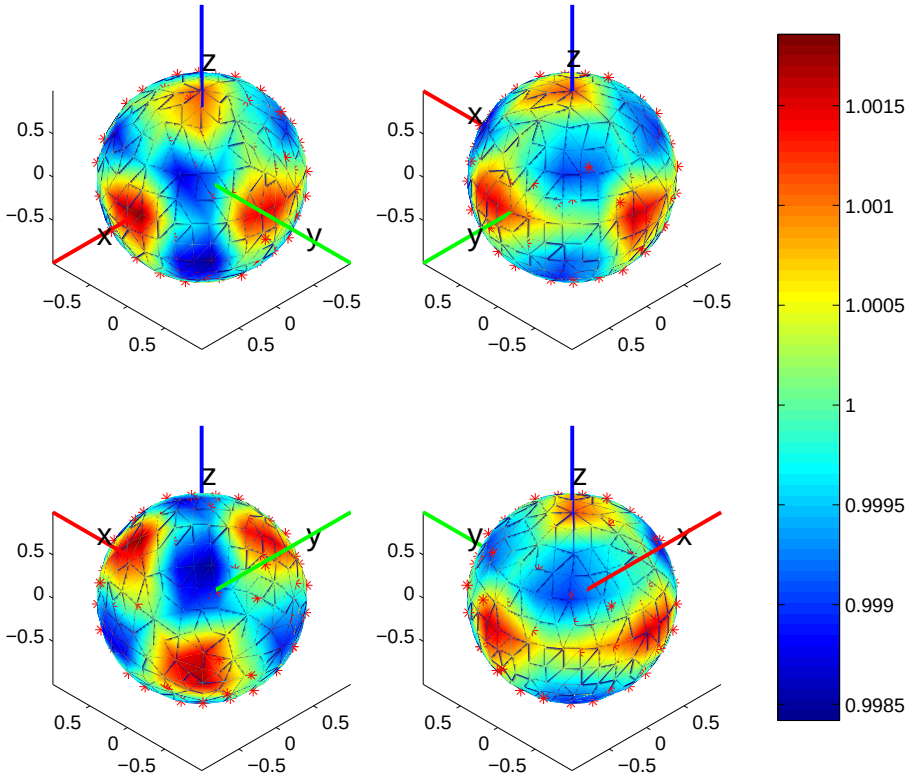

Figure 6.8. *Unity sphere projection of Triad1 gravity vector magnitude estimate and positions.*

such deferred to future project work. By looking at the results for Triad1 it has been established that the static calibration does indeed produce the expected high quality solutions for the high resolution 84P routine. Extending the calculations to the remaining three triads thus generates four individual calibrations with the residuals depicted in Figure 6.9.

As for Triad1 the other three triads produce similar residual magnitudes, and projecting the gravity vector magnitude estimate and instrument orientation vectors onto the unity sphere reveal the same correlation pattern between residuals and orientations. The final remaining step of the static calibration procedure is applied at this point to align the four calibrated triads with the Triad1 reference frame, in accordance with the methodology developed in Section 6.2.2. The three rotation matrices are derived by applying a numerical least squares solver, with the results tabulated in equation 6.36:

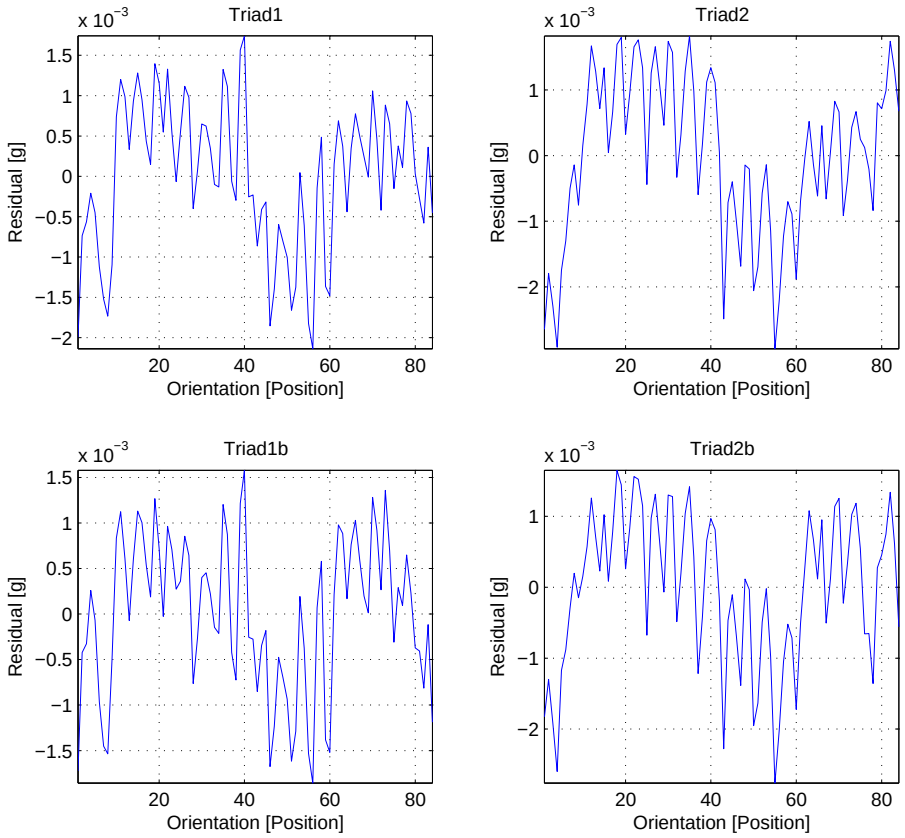

Figure 6.9. *Static calibration residuals for all μIRU triads.*

$$\xi_{\mathbf{1b-1}} = \begin{bmatrix} 0.9994 & 0 & 0.0005 \\ 0.00013 & 0.9994 & -0.0314 \\ -0.0337 & 0.0315 & 0.9992 \end{bmatrix}, \quad |\xi_{\mathbf{1b-1}}| = 1.0001 \qquad (6.36)$$

$$\mathbf{R_Z} \cdot \xi_{\mathbf{2-1}} = \begin{bmatrix} -0.9982 & 0.0073 & -0.0585 \\ -0.0076 & -0.9997 & 0.0051 \\ -0.0585 & 0.0054 & 0.9985 \end{bmatrix}, \quad |\mathbf{R_Z} \cdot \xi_{\mathbf{2-1}}| = 0.9999$$

$$\mathbf{R_Z} \cdot \xi_{\mathbf{2b-1}} = \begin{bmatrix} -0.9993 & 0.0082 & -0.0335 \\ -0.0081 & -0.9997 & -0.0040 \\ -0.0335 & -0.0038 & 0.9998 \end{bmatrix}, \quad |\mathbf{R_Z} \cdot \xi_{\mathbf{2b-1}}| = 1.0000$$

Where the proximity of the matrix determinants to unity indicate that the matrices are indeed true rotation matrices to the working precision of the numerical solver. To assess the quality of the least squares estimate of the individual rotation matrices the residuals of the computation are again evaluated as depicted in Figure 6.11.

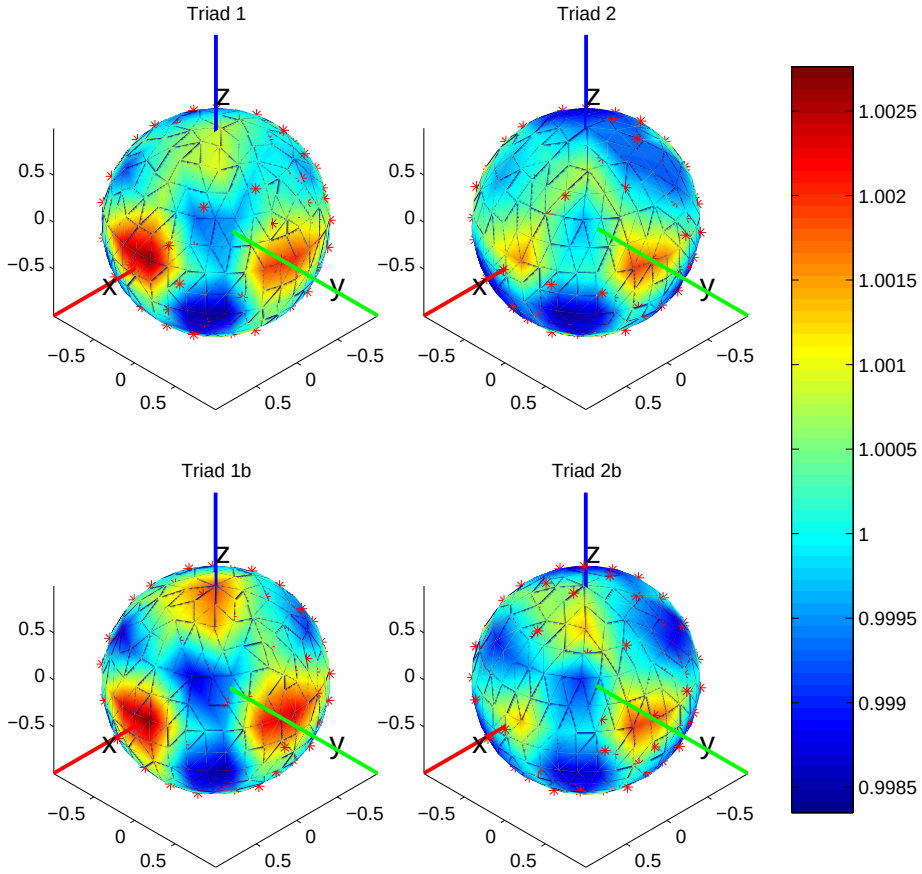

Figure 6.10. *Unity sphere projection of all triad gravity vector magnitude estimate and positions.*

It is evident that the magnitude of the residuals are on the order of those obtained for the orthogonalization of each triads, as would be expected. Moreover, the residuals also show a strong correlation between Triad2 and Triad2b, which is entirely in accordance with the relatively high degree of orthogonality intrinsically present between the two frames. A visualization of exactly what is achieved by the final alignment calibration of the triads is provided in Figure 6.12, which depicts a comparison of the four +Z-axes of μIRU over the 84P2 dataset pre- and post-alignment. Similar results are naturally available for X- and Y-axis components, yet they are less visually appealing as the subtleties are lost to the coarse alignment applied prior to the fine alignment.

In the end, the results of the combined static calibration efforts on the μIRU DC channels can be used to derive unified expressions for accelerations along the axes of the basis $\{G_X, G_Y, G_Z\}$ which are coincident with the orthogonalized principle axes pertaining to Triad1 as governed by the sensitive axes $\{A1_X, A2_Y, A1_Z\}$ from μIRU accelerometers 1 and 2. In reference to the lin-

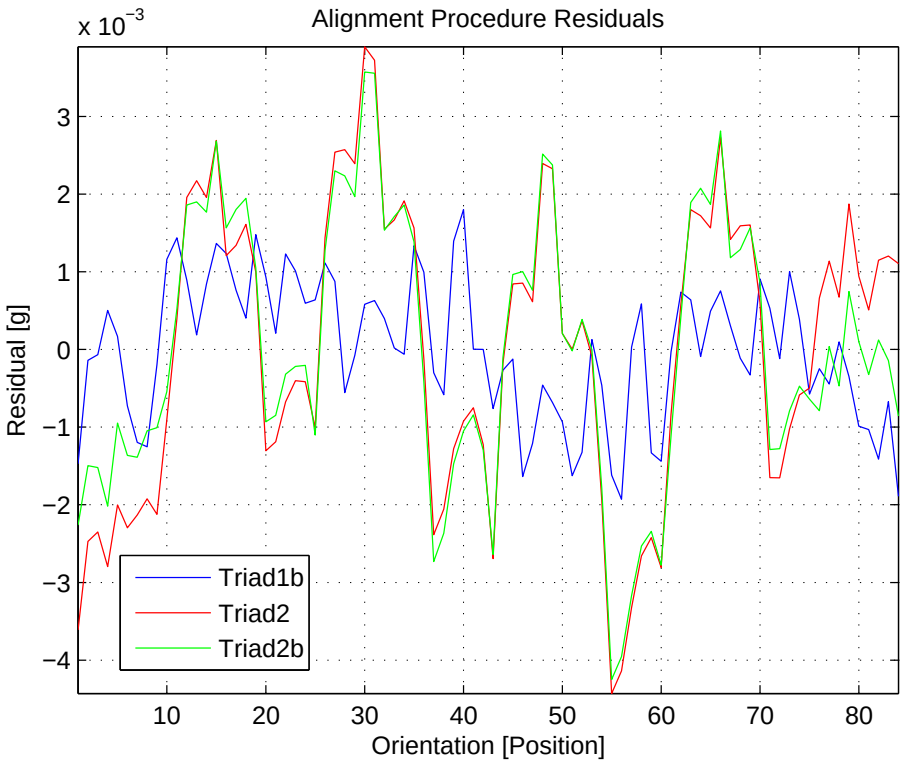

Figure 6.11. *Least squares estimate residuals of triad alignment procedure.*

ear sensing equation 6.3 whilst including the triad alignment rotations, the outputs of the μIRU DC channels in engineering units relate to true physical measurements along $\{G_X, G_Y, G_Z\}$ in units of [g] by the following expressions:

$$\begin{bmatrix} G_X \\ G_Y \\ G_Z \end{bmatrix} = \begin{bmatrix} 1 & 0 & 0 \\ 0 & 1 & 0 \\ 0 & 0 & 1 \end{bmatrix} \begin{bmatrix} 2.8634{\cdot}10^{-4} & -1.8026{\cdot}10^{-7} & -1.1046{\cdot}10^{-5} \\ 0 & 2.7920{\cdot}10^{-4} & -2.1640{\cdot}10^{-6} \\ 0 & 0 & 2.7994{\cdot}10^{-4} \end{bmatrix} \begin{bmatrix} EU_{A1_X} + 934.7285 \\ EU_{A2_Y} + 662.5276 \\ EU_{A1_Z} + 818.3897 \end{bmatrix} \tag{6.37}$$

$$\begin{bmatrix} - \\ - \\ G_Z \end{bmatrix} = \begin{bmatrix} 0.9994 & 0 & 0.0005 \\ 0.00013 & 0.9994 & -0.0314 \\ -0.0337 & 0.0315 & 0.9992 \end{bmatrix} \begin{bmatrix} 2.8614{\cdot}10^{-4} & -2.0197{\cdot}10^{-7} & -1.5973{\cdot}10^{-6} \\ 0 & 2.7943{\cdot}10^{-4} & -1.1020{\cdot}10^{-5} \\ 0 & 0 & 2.8101{\cdot}10^{-4} \end{bmatrix} \begin{bmatrix} EU_{A1_X} + 924.7285 \\ EU_{A2_Y} + 662.5276 \\ EU_{A2_Z} + 784.7031 \end{bmatrix}$$

$$\begin{bmatrix} G_X \\ G_Y \\ G_Z \end{bmatrix} = \begin{bmatrix} -0.9982 & 0.0073 & -0.0585 \\ -0.0076 & -0.9997 & 0.0051 \\ -0.0585 & 0.0054 & 0.9985 \end{bmatrix} \begin{bmatrix} 2.8019{\cdot}10^{-4} & -3.6609{\cdot}10^{-6} & -1.0716{\cdot}10^{-5} \\ 0 & 2.9071{\cdot}10^{-4} & -8.4464{\cdot}10^{-6} \\ 0 & 0 & 2.9331{\cdot}10^{-4} \end{bmatrix} \begin{bmatrix} EU_{A3_X} + 1130.077 \\ EU_{A4_Y} + 901.2124 \\ EU_{A3_Z} + 808.1338 \end{bmatrix}$$

$$\begin{bmatrix} - \\ - \\ G_Z \end{bmatrix} = \begin{bmatrix} -0.9993 & 0.0082 & -0.0335 \\ -0.0081 & -0.9997 & -0.0040 \\ -0.0335 & -0.0038 & 0.9998 \end{bmatrix} \begin{bmatrix} 2.8003{\cdot}10^{-4} & -3.8357{\cdot}10^{-6} & -3.2750{\cdot}10^{-6} \\ 0 & 2.9079{\cdot}10^{-4} & -1.0872{\cdot}10^{-5} \\ 0 & 0 & 2.8736{\cdot}10^{-4} \end{bmatrix} \begin{bmatrix} EU_{A3_X} + 1129.750 \\ EU_{A4_Y} + 901.1960 \\ EU_{A4_Z} + 714.9486 \end{bmatrix}$$

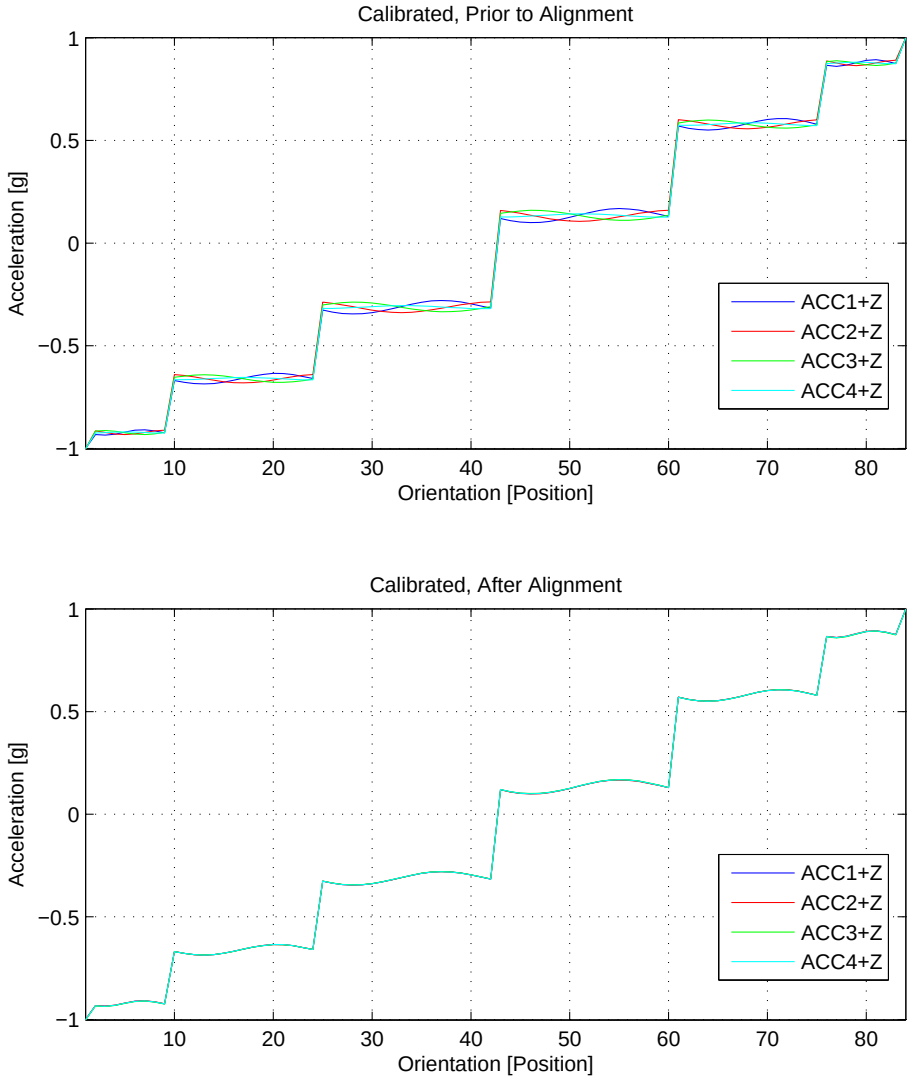

Figure 6.12. *Triad alignment influence on Z-axis responses.*

6.3 Step 2: Static Calibration of AC Channel Bias

The determination of the offsets pertaining to the μIRU AC channels is essentially a question of conducting a direct measurement and verifying its invariance regardless of the instrument static orientation. As such, the AC channel bias parameters are derived from the same dataset as the one applied to the DC channel static calibration previously described.

Channel	Bias [EU]	Std. Dev. [EU]
ACC1 $+Z_{AC}$	7.026	1.439
ACC1 $+X_{AC}$	16.563	1.496
ACC2 $+Y_{AC}$	15.662	1.470
ACC2 $+Z_{AC}$	3.399	1.395
ACC3 $+Z_{AC}$	15.516	1.3708
ACC3 $-X_{AC}$	9.210	1.422
ACC4 $-Y_{AC}$	16.004	1.427
ACC4 $+Z_{AC}$	4.999	1.272

Table 6.1. *μIRU AC output channel bias calibration results.*

Compiling the static calibration data for the AC channels, reveal no correlation between μIRU instrument orientation and AC offset values. Calculating the bias mean and standard deviation values pertaining to the dataset yield the results of Table 6.1. It should be noted that appropriately compensating any thermally induced deviations in AC bias values would be prudent, even though the error introduced hereby would enter the system as a common mode effect. However, the characterization and compensation of such effects are beyond the scope of this treatise and thus deferred to future project work.

6.4 Step 3: Dynamic Calibration of Accelerometer Positions

The dynamic calibration of the μIRU serves to accurately establish the individual relative positions of the accelerometers in the μIRU sensor configuration. For each of the four accelerometers that entails applying a calibration procedure which will allow isolation of the r terms in the linear accelerometer sensor equation. Having established the relative sensing directionality terms d through the static calibration procedures, positions may thus be obtained as the final remaining invariant terms in equation 2.3. The justification for applying the dynamic calibration will be to hone positional knowledge beyond the accuracy with which positions can be directly measured from the mechanical design. The physical measurements performed on the μIRU Tier One prototype and provided in equation 5.3, does as such constitute the design baseline prior to the application of the dynamic calibration procedure, yet having been acquired manually, an estimated measurement error on the order of $\pm$1mm is attributed to these values.

The envisioned dynamic calibration procedure attempts to relax the requirements to the mechanical setup as much as possible, as neither a precision turntable or mechanical exciter will be readily available for these characteri-

zations. As such, a calibration platform based upon a defunct 1970ies Bang & Olufsen turntable has been developed.

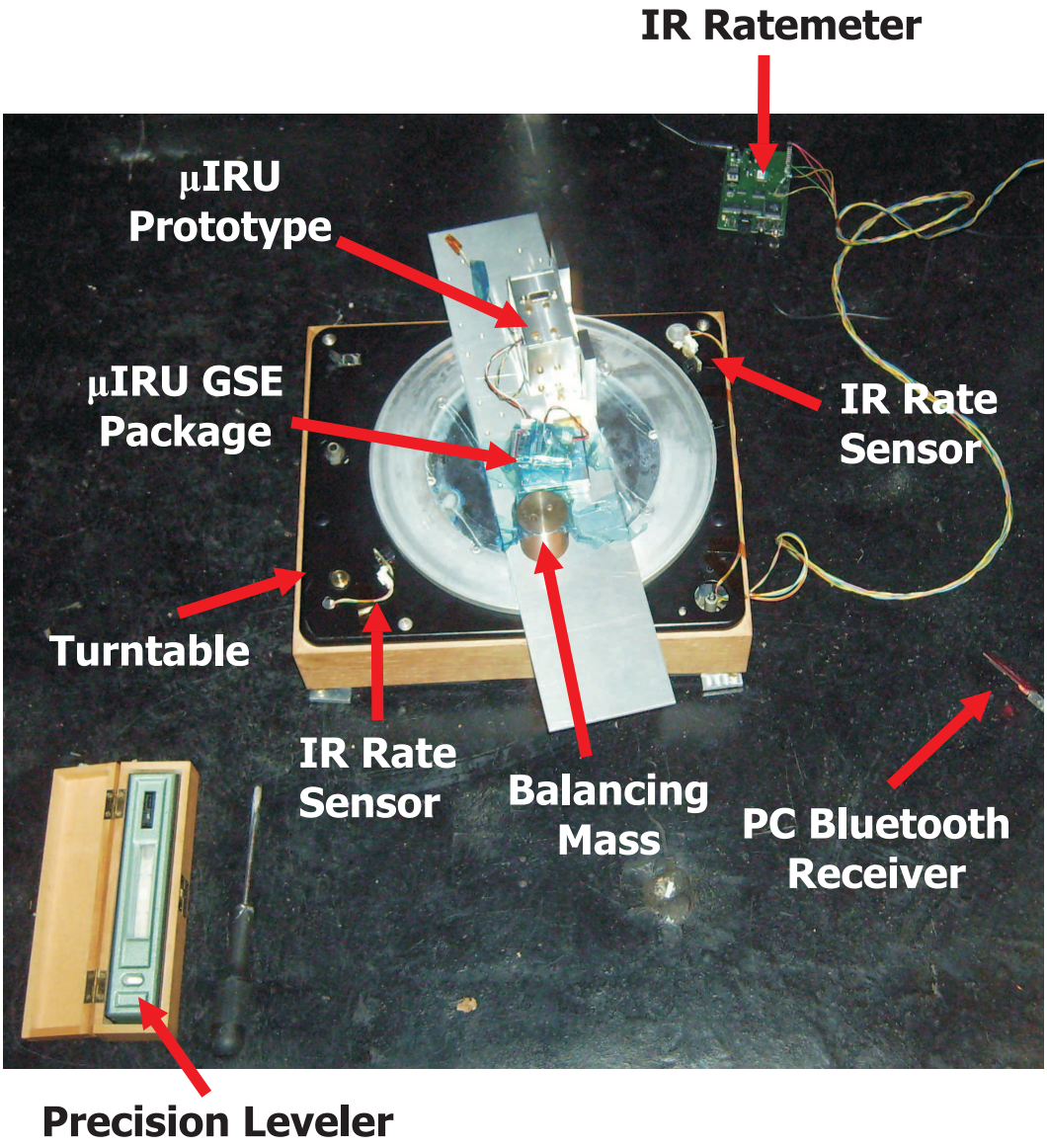

Figure 6.13. *µIRU dynamic calibration setup.*

Depicted in Figure 6.13, the turntable was originally built as a high quality record playing device but clearly had not seen use for a number of years. Even so, the turntable bearings proved intact and of good quality. The drive mechanism was changed to a 12V Maxon DC motor using constant voltage drive, and the means of transferring torque to the spindle adapted to support an elastic belt drive to minimize mechanical noise. The table plate was augmented by an aluminum arm providing mechanical attachment for the μIRU bracket. Also, two infrared (IR) rate sensors where mounted at the perimeter of table plate to provide accurate rotation rate estimates for the spinning plate. The IR sensors

are monitored by a dedicated microprocessor and capable of determining the table rotation rate with sub-millisecond accuracy.

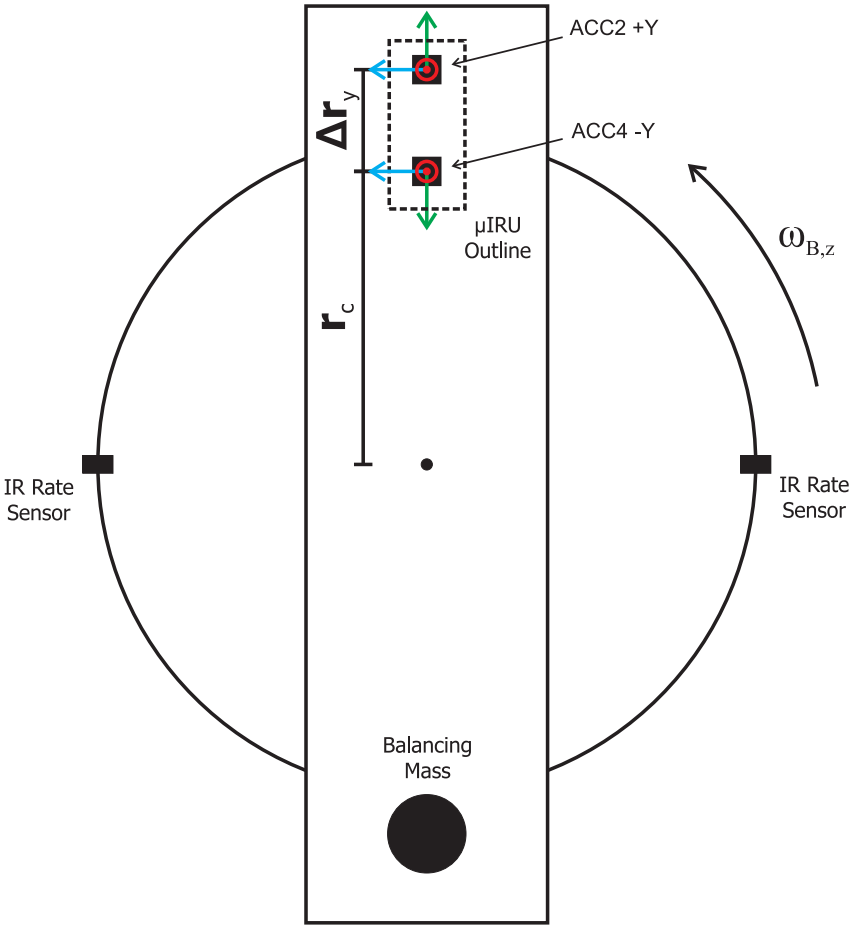

Figure 6.14. *μIRU turntable calibration concept. Shown for μIRU ACC2 and ACC4 Δr_y relative position.*

The calibration principle that the platform in Figure 6.13 seeks to invoke is to determine relative positioning of the accelerometers by isolating the centripetal term in equation 6.38. Successfully doing so provides a direct means of extracting the accelerometer positions, as the centripetal force is equatable from equation 6.38 for simple planar motion:

$$A_S = \left(\ddot{\vec{R}}_1 + (\dot{\vec{\omega}} \times \vec{r}) + [\vec{\omega} \times (\vec{\omega} \times \vec{r})]\right) \cdot \vec{d} \tag{6.38}$$

By adopting the turntable calibration concept depicted in Figure 6.14, the applied motion is limited to $\omega_{B,z}$, thus setting $\omega_{B,x} = 0$, $\omega_{B,y} = 0$. Moreover, the spin rate is kept constant $\dot{\omega}_{B,z} = 0$, which in turn allows equation 6.38 to be reduced to:

$$A_S = d_x \left(-\omega_{B,z}\omega_{B,z}r_x\right) + d_y \left(-\omega_{B,z}\omega_{B,z}r_y\right) \tag{6.39}$$

when expanded into its principle components. If the sensitive axis of the accelerometer aligns with the Y-axis equation 6.39 further reduces to the basic relation:

$$A_{Sy} = -\left(\omega_{B,z}\omega_{B,z}r_y\right) \tag{6.40}$$

As such, by introducing calibrated force along each of the calibrated μIRU principle axes separately, the relative spacing of the differential accelerometer pairs along that axis may be determined. From equation 6.38 and the angular velocity dependencies of that expression, it is though apparent that the motion should be controlled so as to excite only the centripetal term. The other applicable dynamic term, namely the tangential acceleration, depends upon $\dot{\omega}_{B,z}$ not ω. As such, it can be eliminated provided the rotational motion is imposed at a constant angular rate and about a single axis only. The first requirement is addressed by balancing the load on the spindle of the calibration platform and by ensuring no mechanical disturbance is incurred during the test. As work on the platform progressed a series of stability tests where conducted to verify rate performance. Using the infrared sensors, the unloaded turntable spin rate stability was assessed over a period of 2.5 hours at a given fixed motor drive voltage. The resultant rate measurements are depicted in Figure 6.15, and illustrates how the rotation period evolves over time. When the data is tabulated in histogram form, a near Gaussian distribution emerges, clearly giving a mean rotational period of $1855.1ms$ and a standard deviation of $2.0ms$.

The second requirement in isolating the centripetal term is somewhat ameliorated by having achieved a high degree of alignment accuracy of the μIRU on the platform with precision machined mechanical brackets. Moreover, significant performance improvement have been ascertained by ensuring the platform is perfectly leveled during test. Leveling has proven extremely critical to the quality of the measurements, as periodic out of plane motion will excite the tangential terms and significantly degrade performance. Even so bearing noise from the turntable constitutes a significant noise in the measurements.

6.5 Results

Having completed the previous steps in the μIRU calibration procedure, the application of the spin test was executed on the statically calibrated μIRU, for the instrument orientation schematized in Figure 6.14, specifically targeting determination of the Δr_y spacing between accelerometers 2 and 4. The test

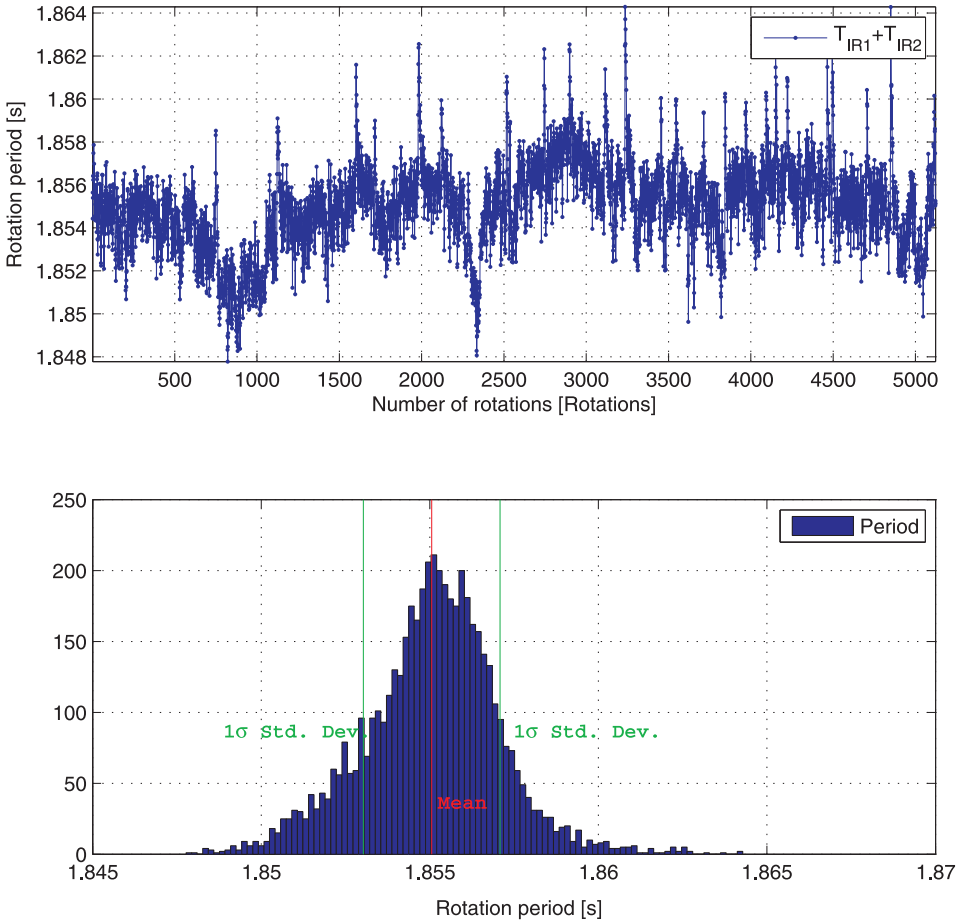

Figure 6.15. *μIRU turntable spin rate stability test.*

was conducted at 5 different spin rates with DC channel data collected for ∼100-420 seconds at each rate.

As shown by the evaluated results in Figure 6.16, the platform succeeds in achieving a near constant spin rate for all tests. The derived Δr_y estimates do however show substantial uncertainties associated with the determined parameter, with the best estimate exhibiting a standard deviation of 1.25mm, which is inherently worse than what could be achieved by manual metrology. Moreover, a correlation between spin rate and sample mean is observed. Observing the test did however also indicate an increase in mechanical noise at higher spin rates, which could account for this behavior. Nevertheless, the parameter estimates derived by this method do converge on the correct interval, yet the mechanical noise associated with the test platform has been found to be prohibitively large. Presently, efforts are being made to further improve the mechanical platform setup and arrive at excitation noise levels comparable to the resolution of the μIRU. If this is achieved, the principles of this method will indeed be applicable to dynamic calibration, yet lacking better data, the

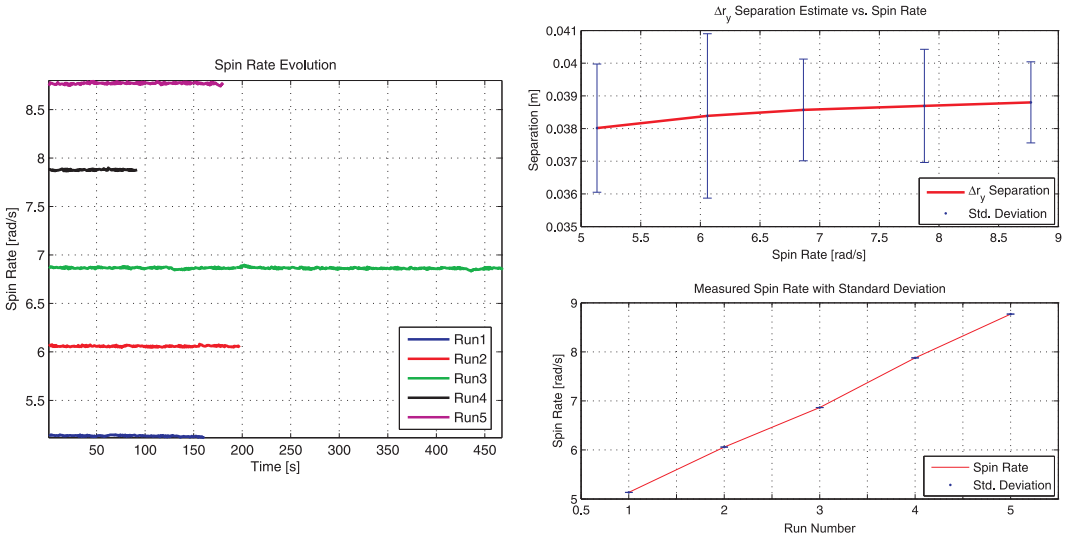

Figure 6.16. *Dynamic calibration results and input spin rates.*

manually acquired relative metrology of equation 6.42 will be used as μIRU sensor positional data for the remainder of this treatise.

$$\mathbf{R}_{\mu\mathbf{IRU}} = \left[r_{A1_x}, r_{A1_z}, r_{A2_y}, r_{A2_z}, r_{A3_x}, r_{A3_z}, r_{A4_y}, r_{A4_z}\right] \tag{6.41}$$

$$= \begin{bmatrix} 0 & 0 & -40.3 & -40.3 & -36.2 & -36.2 & 4.1 & 4.1 \\ 0 & 0 & -4.1 & -4.1 & -44.4 & -44.4 & -40.3 & -40.3 \\ 0 & 0 & 0.1 & 0.1 & 0 & 0 & 0.1 & 0.1 \end{bmatrix}$$

6.6 Step 4: Dynamic Calibration of AC Channels

From a calibration perspective the AC channels of the μIRU benefit immensely from the presence of the DC channels. As both AC and DC signals derive from the same physical sensors, the orthogonalization parameters and alignment rotation matrices determined by the static calibrations in Section 6.2, readily extend to the AC segment. However, the one set of AC calibration parameters which cannot be determined by static measures is the output scale factors, which must be found by other means. A further complication is though incurred by the particulars of the frequency response pertaining to the AC filter branches. Having implemented a wide-band cascaded bandpass filter structure in the AC channels, essentially ensures non-unity gain at the edges of the pass-band which must be properly compensated in the measurement equations. Principally, the μIRU electronics design incorporates a feature which

could aid in this determination, namely the accelerometer self-test, however only limited frequency excitation coverage can be generated by applying this method. Presently, a calibration platform based upon a miniature mechanical exciter is thus being devised for this specific application. By mechanically exciting the entire μIRU assembly with a continuous sinusoid while recording both AC and DC response, an exact transfer function can be established for the AC branch by utilizing the DC response as calibration input. Test and implementation of this method constitutes one of the near term goals for future activities within the project.

6.7 Summary

The conclusion to the chapter, is the fact that a viable methodology has been established for calibrating a multi-axis acceleration sensor such as the μIRU. This has been achieved by utilizing a number of well known calibration principles and extending their reach to encompass what is in principle a 16 channel acceleration sensor. Interestingly the orthogonalization and misalignment correction procedure applied in step 1 to an octet of linear sensors, could in principle be directly extended to much larger sensor complements. Moreover, the fact that it relies only on adopting a number of prudently chosen spatial orientations, makes it a highly cost-effective alternative to applying precision rotation devices to achieve specific gravitational alignment. Also among the lessons learned by establishing and testing these procedures is the impact of accelerometer output hysteresis on the calibration accuracy as well as the necessity of obtaining access to a high fidelity spin platform for dynamic calibrations.

6.8 Bibliography

[Ang-2003] Cameron N. Riviere Wei T. Ang, Pradeep K. Khosla. Design of all-accelerometer inertial measurement unit for tremor sensing. *Proc. International Conference on Robotics and Automation*, 2003.

[Angrisano-2009] S. Troisi G. D. Core A. Angrisano, E. Nocerino. Imu low cost calibration method. Technical report, University of Naples, 2009.

[Brauer-1997] Peter Brauer. *The Ringcore Fluxgate Sensor*. PhD thesis, DTU, 1997.

[Cappa-2008] S. Rossi P. Cappa, E. Patanè. Two calibration procedures for a gyroscope-free inertial measurement system based on a double-pendulum apparatus. *Measurement Science and Technology*, 2008.

[Chatfield-1997] A.B. Chatfield. *Fundamentals of High Accuracy Inertial Navigation*. Progress in Astronautics and Aeronatutics, 1997.

[Merayo-1999] José María García Merayo. *Magnetic Gradiometry*. PhD thesis, Technical University of Denmark, 1999.

[Merayo-2000] F. Primdahl J. R. Petersen O.V. Nielsen J. M. G. Merayo, P. Brauer. Scalar calibration of vector magnetometers. *Measurement Science and Technology*, 2000.

Chapter 7

μIRU Prototype Performance Characterization

The data presented in this chapter aims to characterize the baseline performance of the as-built μIRU tier one prototype. Specifically noise performance of the individual accelerometer channels pertaining to the prototype are assessed and compared to the performance baseline established for the LIS2L02AL accelerometer as established in Chapter 3. Lastly, an angular error accumulation experiment is conducted and the results compared to the model performance.

7.1 Power Budget

Critical to the performance of the μIRU augmented CHU, the augmentation power dissipation has profound implications for the thermomechanical stability of the stellar reference sensor. The original design target was a total augmentation power consumption not exceeding the CHU 10% inferred baseline equivalent to $\simeq$35mW, yet as Figure 7.1 indicates, the prototype fails to meet this specification even at the lowest throughput rates.

As the measurements in Figure 7.1 indicate, achieving such a reduction in power consumption levels for the μIRU prototype baseline design would be close to impossible with the current component selection. However, it is clear that when operating from an external clock source, a substantial power reduction is incurred, as the internal oscillator circuitry of the ATmega168 microprocessor is disabled. As the scenario with the CHU emulator as clock source is close to envisioned nominal operations, consumption levels in the order of 65-70mW for full μIRU throughput are expected. This does though remain roughly a factor of two above the target range.

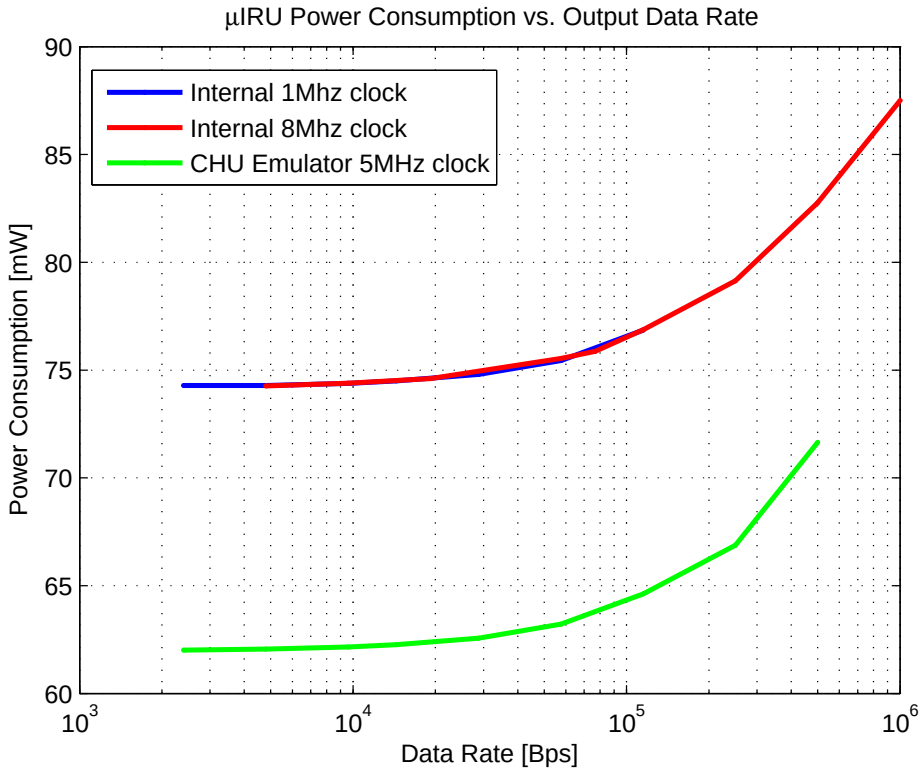

Figure 7.1. *µIRU prototype power consumption.*

7.2 Long Term Stability

To assess the long term stability of the μIRU tier one prototype sensor outputs, a stand-alone test has been conducted with full data rate capture of all AC and DC channels over the course of ∼7.5 hours. The output data representation provided in Figures 7.2 and 7.3 has been divided in accordance with the source ADCs as described by Table 5.2.

During the test, the μIRU prototype has been suspended in a fully static setup at stable room temperature with the Z-axis and gravity vector aligned. Moreover, the derived calibration parameters from Chapter 6 have been applied to orthogonalize and scale the accelerometer measurements. It should also be noted that the DC data has had the mean value subtracted to facilitate direct comparison with the AC data. The measured AC values clearly show the intended stability and, as can be derived from the standard deviation values pertaining to the dataset provided in Table 7.1, also a high degree of consistency between the channels. The DC data on the other hand is seen to exhibit more dynamic behavior, and particularly the DC signals emanating from the +X-axis of accelerometer 1 and the +Z-axis of accelerometer 4 show telltale signs of instability issues. This is of course reflected in the standard deviation measurements for the two channels in Table 7.1.

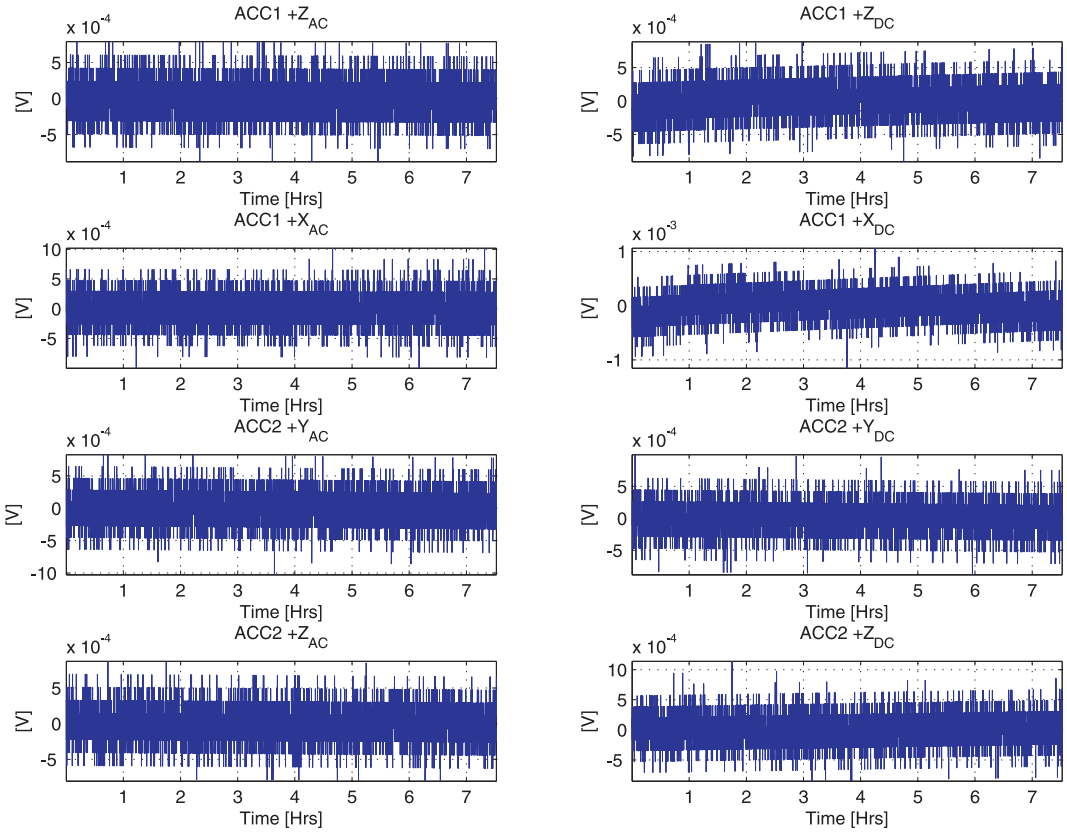

Figure 7.2. *Stability of A/D converter 1 output channels. All channels calibrated, DC data has been detrended for direct comparison.*

ADC #	AC Channel	Std. Dev. [μg]	DC Channel	Std. Dev. [μg]
1	ACC1 $+Z_{AC}$	399.2	ACC1 $+Z_{DC}$	397.5
1	ACC1 $+X_{AC}$	405.8	ACC1 $+X_{DC}$	432.7
1	ACC2 $+Y_{AC}$	396.0	ACC2 $+Y_{DC}$	366.0
1	ACC2 $+Z_{AC}$	380.3	ACC2 $+Z_{DC}$	392.2
2	ACC3 $+Z_{AC}$	383.3	ACC3 $+Z_{DC}$	359.6
2	ACC3 $-X_{AC}$	383.9	ACC3 $-X_{DC}$	377.3
2	ACC4 $-Y_{AC}$	384.5	ACC4 $-Y_{DC}$	383.2
2	ACC4 $+Z_{AC}$	392.5	ACC4 $+Z_{DC}$	465.5

Table 7.1. *μIRU tier one prototype output variance. Measurements pertaining to long term stability dataset.*

7.3 Noise Performance Assessment

Beyond looking at the long term stability of the data produced by the μIRU prototype, a more detailed assessment of the output noise pertaining to in-

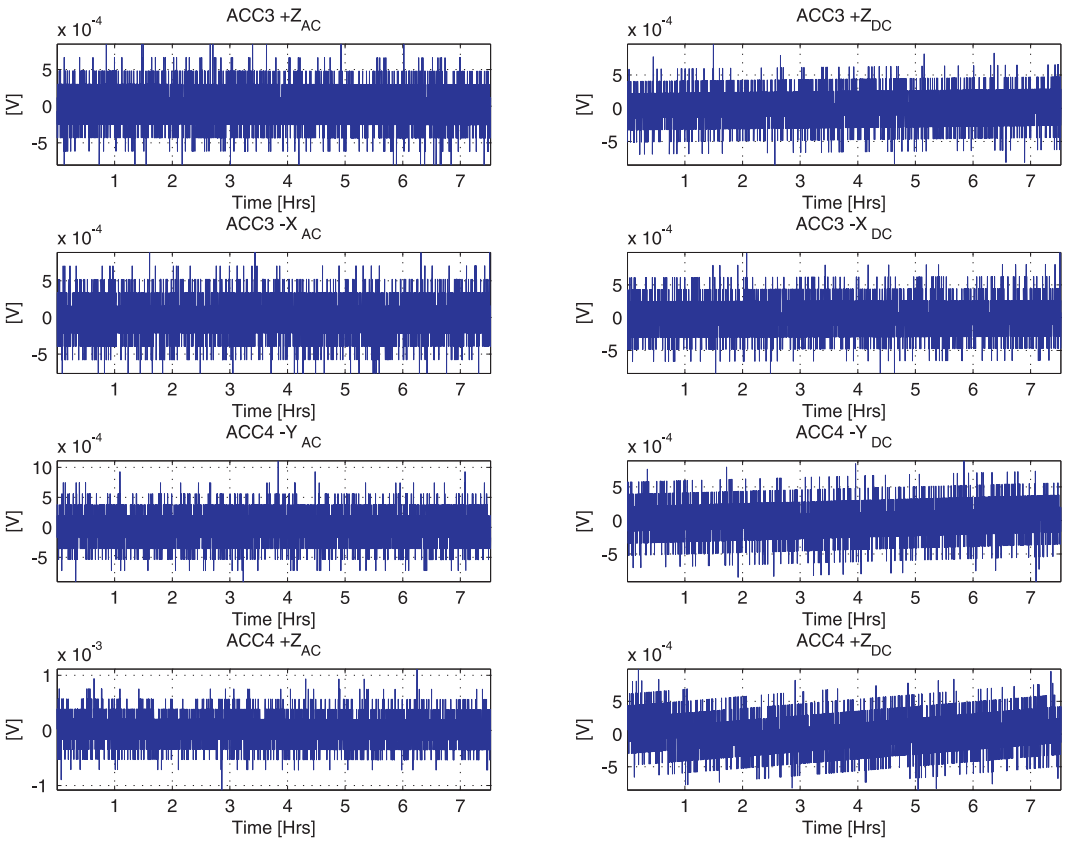

Figure 7.3. *Stability of A/D converter 2 output channels. All channels calibrated, DC data has been detrended for direct comparison.*

dividual channels has been conducted using power spectral density and Allen variance analysis. The power spectral density estimates for AC and DC channels pertaining to ADC1 are depicted in Figure 7.4, and similar measurements for ADC2 in Figure 7.5.

For the ADC1 dataset the AC channels are indeed seen to provide consistent behavior, with white noise characteristics beyond ∼1Hz and band limited noise contributions below the corner frequency. When each AC channel is compared to their respective DC counterpart the consistency is clearly compromised for some signals. As such, the ACC1 $+X_{DC}$ provides a good example of the signal quality being impacted by long term noise contributions not present in the AC data. By calculating the average signal noise power from the PSD data, the values for each channel in Table 7.2 have been tabulated.

As for the ADC1 channels, power spectral density estimates for the ADC2 channels have been derived with the results depicted in Figure 7.5. Here much of the same behavior is seen to manifest itself, with the AC channels providing highly consistent performance also visible in the noise power estimates included in Table 7.3. Several DC channels on the other hand exhibit the same long term instabilities as where identified for certain ADC1 DC channels, yet to

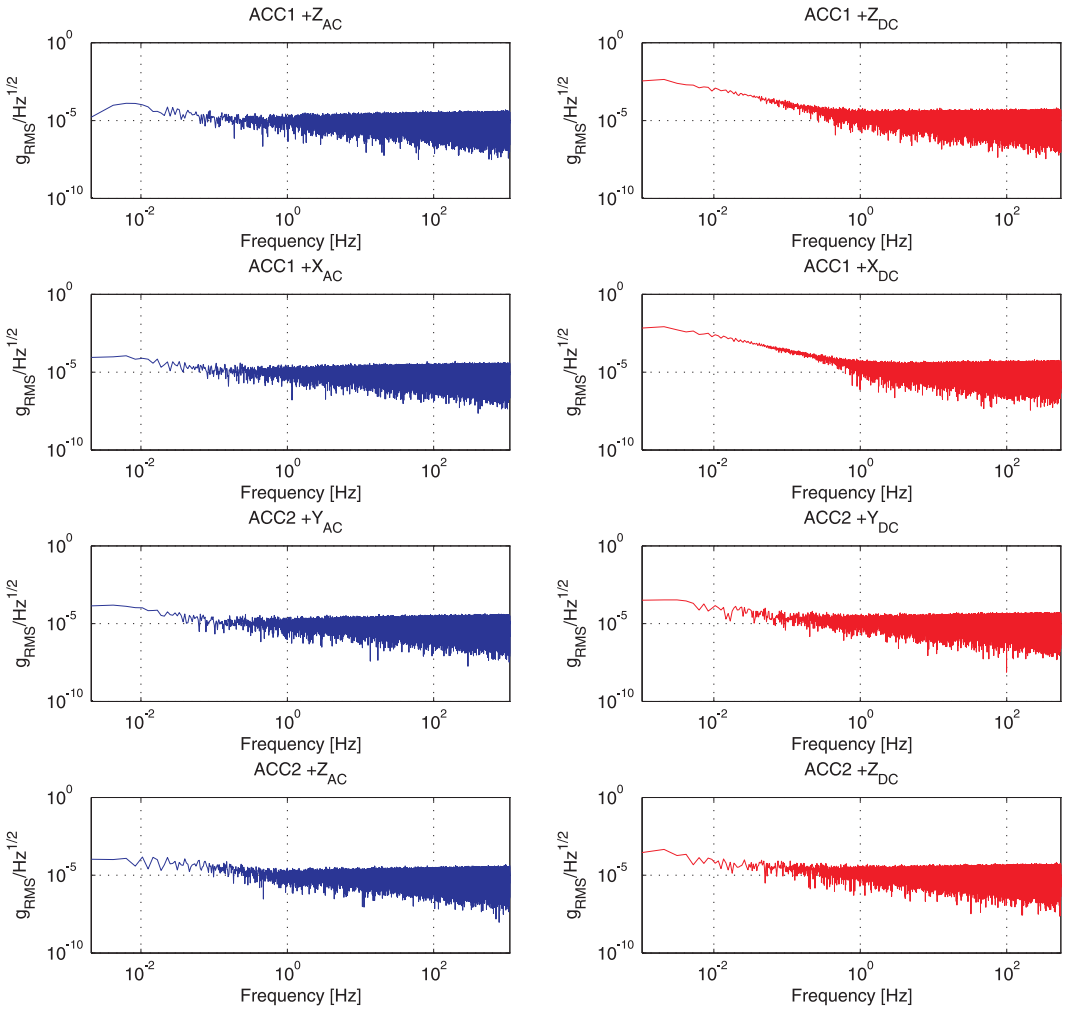

Figure 7.4. *ADC1 DC and AC channel PSD estimates.*

Channel	Noise Power $[\mu g_{RMS}]$	Channel	Noise Power $[\mu g_{RMS}]$
ACC1 $+Z_{AC}$	397.6	ACC1 $+Z_{DC}$	463.6
ACC1 $+X_{AC}$	400.8	ACC1 $+X_{DC}$	652.0
ACC2 $+Y_{AC}$	395.8	ACC2 $+Y_{DC}$	368.5
ACC2 $+Z_{AC}$	384.3	ACC2 $+Z_{DC}$	383.6

Table 7.2. *ADC1 AC and DC channel RMS noise power estimates.*

accurately quantify the nature of the DC channel noise, the concept of Allen variance is once more expounded.

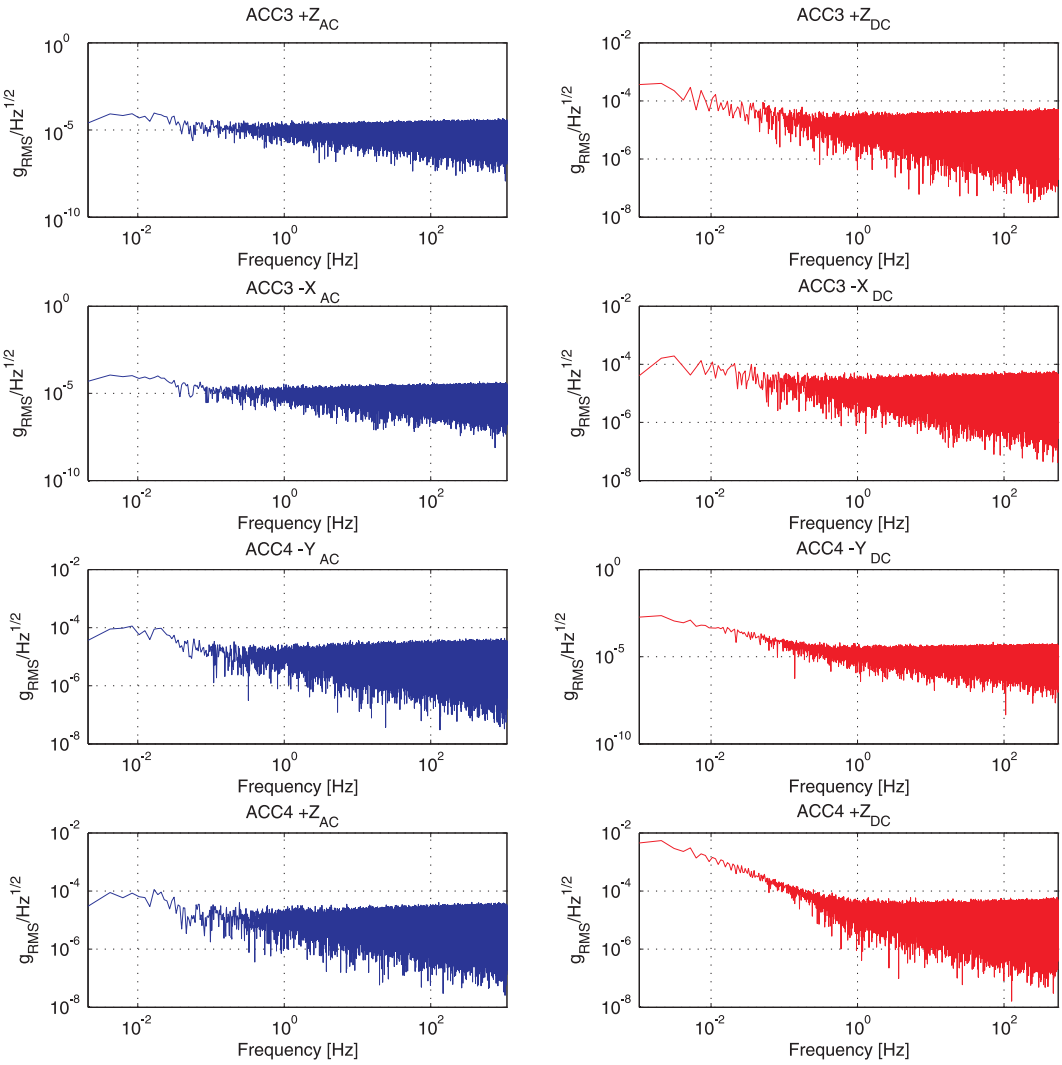

Figure 7.5. *ADC2 DC and AC channel PSD estimates.*

Channel	Noise Power $[\mu g_{RMS}]$	Channel	Noise Power $[\mu g_{RMS}]$
ACC3 $+Z_{AC}$	383.3	ACC3 $+Z_{DC}$	362.5
ACC3 $-X_{AC}$	380.4	ACC3 $-X_{DC}$	376.8
ACC4 $-Y_{AC}$	394.1	ACC4 $-Y_{DC}$	399.0
ACC4 $+Z_{AC}$	380.4	ACC4 $+Z_{DC}$	509.4

Table 7.3. *ADC2 AC and DC channel RMS noise power estimates.*

7.3.1 Allen Variance Analysis

Figure 7.6 and 7.7 provide the Allen deviation plots for the μIRU DC and AC channels, respectively. The data presented in these figures stem from the same dataset used in the long term stability analysis, and provide remarkable

detail regarding the performance of the instrument. As overlapping Allen variance analysis is conducted at the full sample rates on both AC and DC channels, only the first 1 million samples of each channel in the dataset is treated here to limit the computational load. From the DC channel deviation plots in Figure 7.6 it is first and foremost possible to identify two primary noise sources, namely random walk/white noise (-1/2 slope) and rate ramp/trend (+1 slope). The latter is similarly denoted as time varying bias in literature [Tehrani-1983, Barshan-1994, Ang-2004], and seen to correlate with the devices exhibiting the visible degree of long term instability in Figures 7.2 and 7.3, namely accelerometers 1 and 4. The +Z-axis of accelerometer 1 is also seen to differ substantially from the remaining devices with regards to both white noise characteristics and the output noise density which can be identified as nearly $33\mu g/\sqrt{Hz}$, essentially violating the manufacturer typical specification of $30\mu g/\sqrt{Hz}$. As a result, accelerometer 1 must be considered borderline out-of-family with respect to the remaining devices, which also reflects in its bias instability rating on average being a factor of two worse than the other sensors. At higher frequencies however, all devices exhibit behavior in accordance with that detected for the LIS2L02AL accelerometer in the screening testing phase, and at the sample rate a deviation of $\sim 300\mu g$ is observed. Furthermore, it must be stressed that at no point is quantization noise observed, which is testament to the exemplary behavior of the DC channel sampling system

The Allen deviation chart in Figure 7.7 for the AC channels reveal some extremely exciting points about the nature and quality of the developed instrument. Firstly, it is seen that a substantial improvement in overall noise performance is incurred by introducing the lower end band limiting present in the AC channels. As such, having removed the DC content equates to having minimized both wide- and narrow-band noise components pertaining to the LIS2L02AL accelerometer, effectively reducing the wide band white noise component with a factor of 2 as compared to the manufacturer specification. The AC channels do as such on average meet a noise density specification of only $\sim 10\mu g/\sqrt{Hz}$, and at the sampling frequency a deviation of only $\sim 260\mu g$ is observed. It is also evident that the AC branch is equally as well conditioned as the DC branch with no trace of quantization noise present. Looking at the Allen deviation seen beyond 1 second integration time, it should be remembered that the LIS2L02AL signal amplitude rolls off at -20dB/decade. As such, with the accelerometers stationary, the characteristic dual-population behaviour seen does actually not pertain to the accelerometers, rather it is a direct rendition of the performance of the ADC circuitry. This point is emphasized by the two populations being divided by the channel/ADC pairing[1]. As such, the bias instability and random walk ratings observed in the AC channels for >20 second integration times constitute qualitative characterization parameters for the LTC1408I A/D converter rather than the AC coupled

[1] All channels from accelerometers 1 and 2 are converted by ADC1, and all channels from accelerometers 3 and 4 are converted by ADC2.

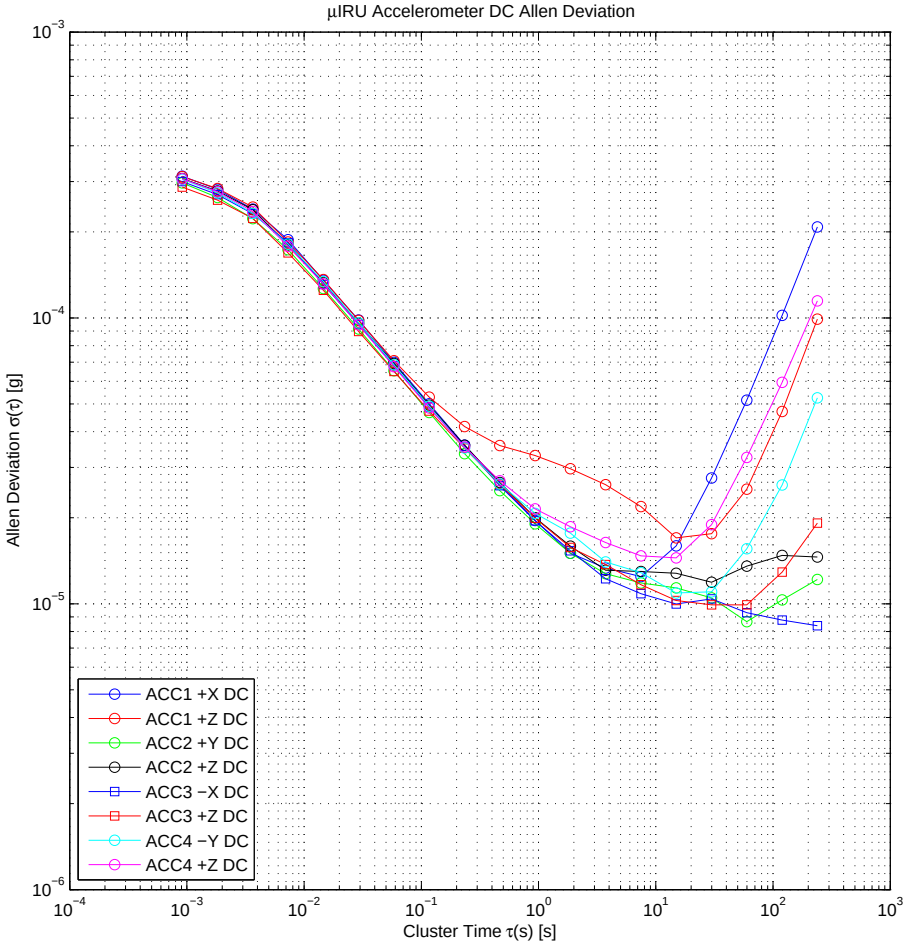

Figure 7.6. *µIRU Allen deviation - DC channels.*

LIS2L02AL accelerometers.

Table 7.4 summarizes the main noise parameters pertaining to the μIRU prototype as derived from the data in Figures 7.6 and 7.7.

What can be derived from this analysis is the fact that the DC channels have succeeded in reaching quality levels on par with those of the stand-alone LIS2L02AL accelerometer sensor. Moreover, the longer term performance of the DC channels is as expected marred by drifting noise contributions, and from an optimality perspective integration times up to $\sim$10 seconds can be utilized. This characteristic should also be taken into account for future static calibration runs. With regards to the instrument AC channels it can be concluded that these are extremely well conditioned and succeed in capturing the full performance of the LIS2L02AL accelerometer over the design bandwidth. For the given combination of accelerometer, bandwidth, filter characteristic

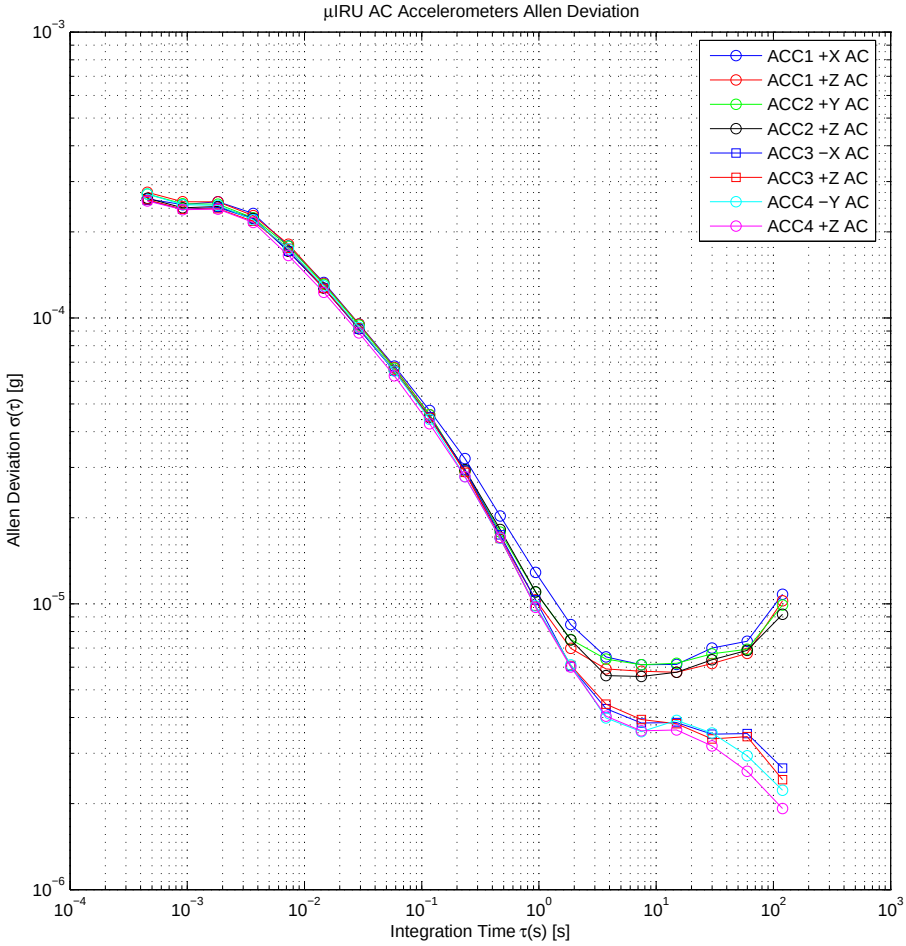

Figure 7.7. *μIRU Allen deviation - AC channels.*

and sample rate, it is as such not possible to obtain better noise performance than what has been realized with the μIRU prototype.

7.4 Error Accumulation Rate Assessment

The final proof of the capability of the μIRU augmentation as an optimized short term attitude sensor that will be provided in this dissertation, is an assessment of the error angle accumulation rate. This assessment is based upon data acquired for the fully stationary and thermalized μIRU over a period of 2 hours. Moreover, it is conducted using the fully calibrated and orthogonalized DC channels sampled at 1kHz, to facilitate direct comparison with the LIS2L02AL manufacturer specification and derived theoretical models for differential operation. The acquired data is analyzed by extracting 1000 sample

Channel	White Noise	Bias Instability		Rnd. Walk	Rate Ramp
$[\mu g/\sqrt{Hz}]$	σ_{WN}	T_{BI}[s]	σ_{BI}	σ_{RW}	R
STM Spec.	30	-	-	-	-
ACC1 $+Z_{AC}$	10.32±0.33	15	3.83±0.49	1.66±0.66	-
ACC1 $+Z_{DC}$	32.99±0.75	15	11.29±1.03	-	11.14±3.89
ACC1 $+X_{AC}$	12.88±0.41	7	4.06±0.37	1.66±0.66	-
ACC1 $+X_{DC}$	19.56±0.44	7	8.26±0.53	-	24.04±8.41
ACC2 $+Y_{AC}$	10.99±0.35	7	4.06±0.37	1.66±0.66	-
ACC2 $+Y_{DC}$	19.04±0.43	60	5.75±1.08	-	-
ACC2 $+Z_{AC}$	11.01±0.35	7	3.70±0.34	1.66±0.66	-
ACC2 $+Z_{DC}$	20.02±0.45	30	7.89±1.03	-	-
ACC3 $+Z_{AC}$	9.80±0.31	15	2.53±0.33	-	-
ACC3 $+Z_{DC}$	19.92±0.45	60	6.58±1.23	1.58±0.52	-
ACC3 $-X_{AC}$	10.32±0.33	15	2.55±0.33	-	-
ACC3 $-X_{DC}$	19.52±0.44	30	6.91±0.89	-	-
ACC4 $-Y_{AC}$	9.84±0.32	7	2.37±0.22	-	-
ACC4 $-Y_{DC}$	20.72±0.47	30	7.31±0.95	-	5.75±2.01
ACC4 $+Z_{AC}$	9.72±0.31	15	2.40±0.31	-	-
ACC4 $+Z_{DC}$	21.46±0.48	15	9.62±0.87	-	14.13±4.95

Table 7.4. *μIRU prototype noise parameters as derived by Allen variance analysis.*

sets randomly distributed throughout the data set, and subjecting the individual acceleration vectors to double trapezoidal integration thus determining sensor displacement. The integration is performed with all initial conditions set to zero ($d_0 = 0$,$v_0 = 0$). Note that the sample sets are detrended prior to integration, so as to remove accumulated displacement due to gravitational acceleration[2]. Applying the basic differential sensing proviso for individual accelerometer pairs in accordance with equation 7.1, results in the time evolution of the differentially sensed angle θ.

$$\theta = \tan^{-1} \frac{d_{A1} - d_{A2}}{L} \simeq \frac{d_{A1} - d_{A2}}{L} \tag{7.1}$$

where:
d_{A1},d_{A2}: signifies the linear displacements calculated by double integration of the accelerometer outputs. L: equals the differential sensing physical baseline equal to $44.4mm$ for the μIRU X-axis used here.

The operational scenario that this procedure attempts to emulate, is essentially the envisioned nominal working environment of the μIRU augmentation when fused with the μASC. Whenever the stellar reference sensor produces an

[2]When subjected to zero-g operation, natural detrending will occur for the μIRU DC channels with the exception of signal long term drift components

absolute attitude update, the extreme fidelity of this measurement establishes a new starting point ($t = 0$) for μIRU attitude integration. As time progresses without any further updates from the μASC, the integration error pertaining to the attitude estimate of the μIRU is bounded only by the noise performance of the sensor, hence the overall quality of the fused instrument attitude knowledge degrades over time. Commonly, the error accumulation specification for an inertial navigation system is provided in terms of the worst case integration error accumulated for the 1σ RMS noise envelope, however having the physical μIRU system available and calibrated allows a direct measurement to be made. As such, Figure 7.8 depicts accumulated angular error from a stationary position over periods of 10 seconds for at total of 1000 vectors. The calculations reflected in the plot utilize only the Y-axis differential data to facilitate direct comparison with the Monte Carlo simulations conducted in Chapter 2, hence the additional error bounding that may be ascertained by compounding measurements from both X-axis and Y-axis differential pairs in establishing Z-axis rotation is not reflected.

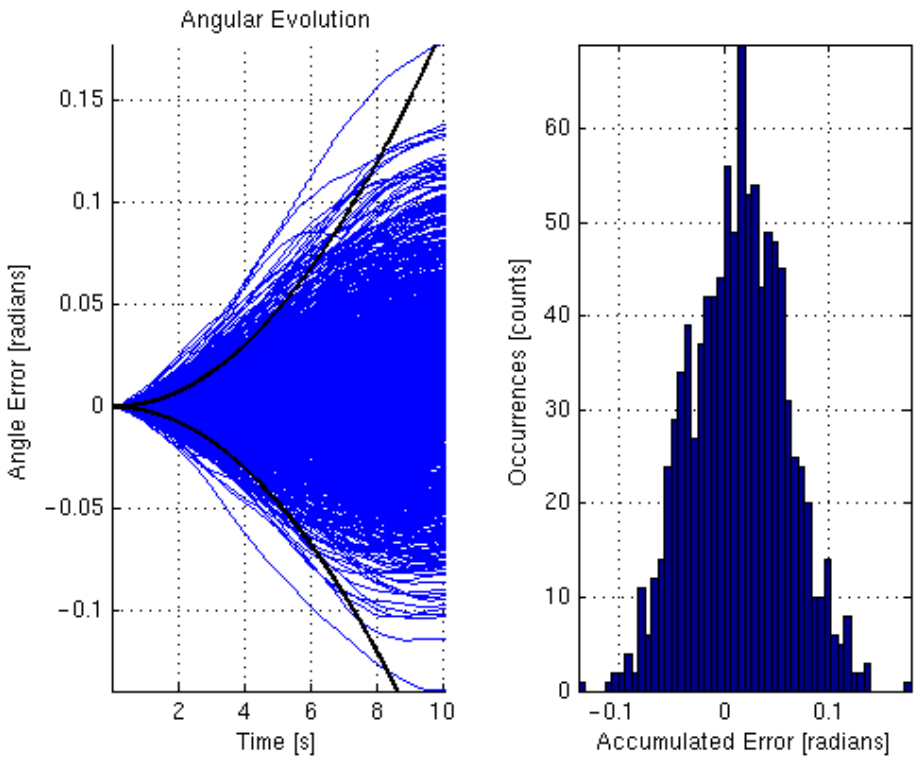

Figure 7.8. *Short term angular error accumulation. Black lines subtend the 1σ worst case accumulated error envelope.*

What can be gathered from Figure 7.8 is key performance characteristics of the μIRU augmentation. The accumulated angular error on the operational time scales envisioned for the cooperatively fused application ($\sim$250ms typically),

is comparable to the performance level of the μASC. Moreover, the angular error is seen to track the theoretical 1σ error growth model of equation 2.7 with reasonable accuracy. From Figure 7.8 the performance at 10 second integration can be tabulated as a mean drift of 0.017 radians(0.974°) with a standard deviation of 0.0143 radians (0.819°). Similar calculations for 250ms integration yield a mean drift of $1.205{\cdot}10^{-4}$ radians (0.0069°) with a standard deviation of $1.19{\cdot}10^{-4}$ radians (0.0068°).

In addition to short term performance, time scales far beyond nominal μASC operations are also of particular interest. In situations where the CHU could be subject to intermittent blinding (eg. the Moon, Sun or Earth limb transversing the field of view), the cooperatively fused instrument could rely entirely on the μIRU measurements to propagate the attitude estimate. As such, repeating the calculations on the same dataset for 100 second periods reveal the long term error accumulation characteristic of Figure 7.9.

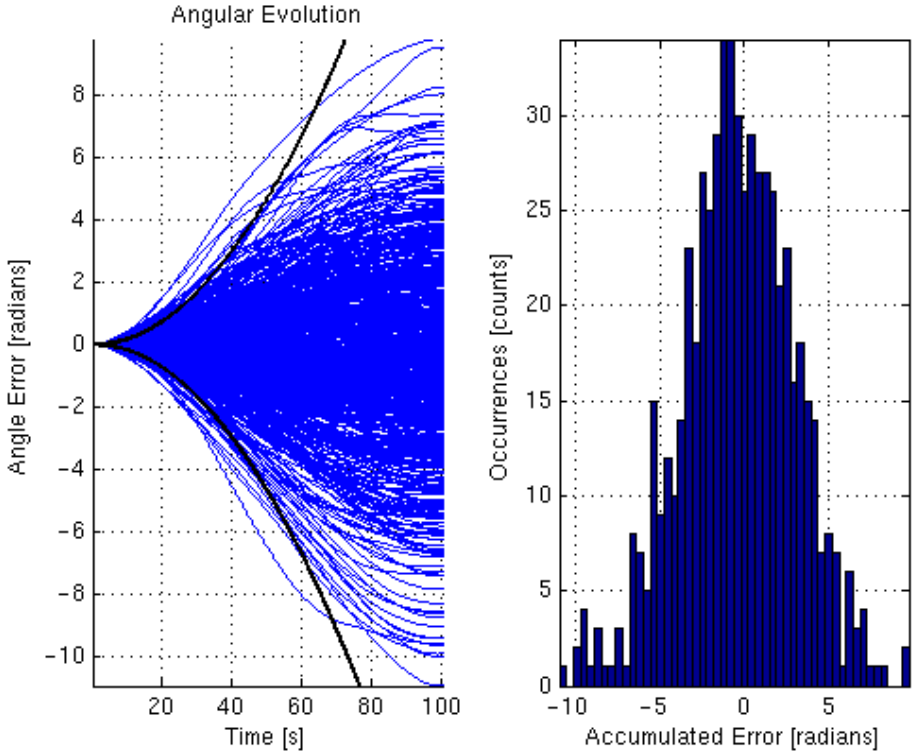

Figure 7.9. *Long term angular error accumulation. Black lines subtend the 1σ worst case accumulated error envelope.*

The long term performance of the instrument is once again seen to trend the 1σ worst case envelope, and a mean drift of 2.176 radians (124.7°) with a standard deviation of 1.511 radians (86.6°) can be identified from Figure 7.9 for a 100 second integration period. Do note that all data in the preceding calculations is acquired using trapezoidal integration applied for absolutely determined initial

conditions. It must also be stressed that the μIRU does not provide a direct measure of its initial velocity to support these integrations, hence this value must be provided by another source such as the μASC (or estimated by an appropriately implemented observer). Even so, these assessments show the μIRU maintaining a 3σ attitude knowledge over a period of 10 seconds of just around 2.5°_{RMS}

7.5 Summary

The power consumption test results reported upon in the beginning of the chapter illustrate a failure to meet the 10% power consumption baseline as imposed by the μASC CHU, rather the instrument will operate nominally at a near 20% baseline. A series of long term stability and noise analysis have been conducted on the calibrated μIRU prototype, and in particular Allen variance analysis has confirmed that the desired properties of the sampling system has indeed been realized with the prototype implementation. Similarly, analysis of the error accumulation characteristics reiterate the the fact that the system is capable of sustaining short term performance levels comparable to those of the μASC, thus furthering the case for fused operations. With the exception of some near out-of-family behavior on part of one DC channel, the results of the chapter at hand unequivocally show the μIRU tier one prototype as a well conditioned instrument.

7.6 Bibliography

[Ang-2004] W. T. Ang. *Active Tremor Compensation in Handheld Instrument for Microsurgery.* PhD thesis, Carnegie Mellon University, 2004.

[Barshan-1994] H.F. Durrant-Whyte B. Barshan. Inertial navigation systems for mobile robots. *IEEE Transactions on Robotics and Automation, Vol. 11*, 1994.

[Tehrani-1983] M. Tehrani. Ring laser gyro data analysis with cluster sampling technique. In *Proceedings of SPIE, vol. 412*, 1983.

Chapter 8

Concluding Comments

This project concludes having succeeded in implementing and characterizing a novel all-accelerometer inertial reference unit optimized towards co-integration with the μASC stellar reference sensor. The μIRU design has been condensed out of a vast open-ended solution space, to accommodate the best possible performance within the physical envelope offered by the μASC framework. Generally, instrument design, development and characterization has been emphasized in establishing a proof-of-concept platform (Tier One) to support future intercalibration and data fusion experimentation activities. To summarize the results of the project, the main findings of each project segment are listed below.

Sensor Head Mechanization and Accelerometer Characterization:
Mechanization expressions for the GEO3 sensor configuration have been established, and a thorough characterization of the LIS2L02AL primary candidate accelerometer has been conducted. The sensor device has proven to be robust and well-conditioned over environmental exposure. Linearity testing confirms the presence of output hysteresis equating to $\sim$1% over $\pm$1g, which is consistent with manufacturer specifications. Further testing implies a quadratic relationship between output voltage, bias and scale factor, which indicates that linearity performance may be improved through phenomenological modeling.

μIRU Design and Prototyping:
By flowing down requirements from the μASC, a baseline design for the μIRU has been developed. Strict adherence to the minimum impact requirement has been maintained, while optimizing sensor performance within applicable constraints. As such, a 12 channel simultaneous sampling system has been designed to operate synchronously with the CHU main clock, thereby negating the influence of asynchronous noise. The sampling system has been optimized towards noise performance and throughput, achieving effective sample rates

of ∼1.3ksps for μASC 4Hz synchronized operations. Moreover, selected parts have been verified to meet environmental tolerance requirements. Adhering to a segmented development profile, the Tier One μIRU prototype has implemented the baseline design and verified its functionalities.

Tier One Calibration and Performance Assessment:
A four step calibration procedure has been developed and applied to fully characterize the time invariant parameters of the μIRU. The static calibration procedure has proven capable of producing high quality parametric estimates, only limited by the non-linear behavior of the sensors. Furthermore, dynamic calibration has been attempted, however, in its present state the calibration platform is incapable of resolving the intended parameters with sufficient accuracy. Subsequent assessments of the performance attributed to the Tier One prototype have confirmed a discrepancy with regards to instrument power consumption. However, performance in terms of sensor channel noise and angular error accumulation rates have proven to meet or exceed theoretical predictions in all cases.

With regards to the four objectives for the project as outlined in Section 1.4 it is clear that 1,2 and 4 have been met directly, whereas the co-integration testing with the μASC as suggested by objective 3 remains pending at this time. However, successful co-integration testing with the CHU Emulator has been achieved.

8.1 Recommendations for Project Continuation

Considering the strenuous advances made during the course of the project, it is evident that significant effort remains prior to achieving a full proof-of-concept test at Tier Three level. However, the μIRU Tier One prototype in its present state would be ready to support basic co-integration testing with the μASC as a means of verifying electrical interface integrity. As such, this would constitute a logical next step.

Subsequently, achieving full AC and DC calibration of the Tier One prototype should be emphasized to demonstrate the viability of the developed procedures. To this end, the AC exciter calibration platform should be finalized, and the turntable platform significantly altered. Recognized as one of the major shortcomings of the calibration procedures, the presently available dynamic platform does not meet requirements. Even though the calibration principle was successfully demonstrated, it is clear that the physical setup needs to be improved. Alternatively, conducting the calibration on a professional low noise rotation stage would be recommended for future development.

With regards to the linear accelerometers, the remaining open issues in characterization will be closed in the immediate future. It is also evident that the

sensor non-linear behavior has significant impact upon the achievable performance of the instrument, and as such efforts should be made towards establishing a non-linear sensor model to ameliorate the adverse effects. Similarly this model should be augmented to incorporate non-linear thermal responses as well.

At the time of writing the first batch of sensor boards for the Tier Two implementation have been finalized and are awaiting integration into the test CHU. As such, pending the establishment of firm calibration procedures, the migration to Tier Two is imminent. However, one significant impediment remains when considering Tier Two experimentation, and that is the software/firmware implementation on the μASC DPU side. For Tier Two operations, the μASC and μIRU operate in full synchronization and the DPU must as such provide data retrieval and basic processing to facilitate experimentation. As work on the necessary DPU software/firmware entities has yet to commence, it is an area that should be prioritized for near term development.

The dissertation hereby concludes the formal summary of the work conducted during the course of the Ph.D project period from March 2007 to August 2010 at Measurement & Instrumentation Systems, DTU Space, developing the μIRU augmentation for the μASC stellar reference sensor.

"AD ASTRA PER ASPERA"
Surmounting adversity - reaching for the stars

August 31^{st}, 2010

Appendices

Appendix A

Allen Variance - A Review

The Allen Variance concept (also known as two-sample variance or AVAR) was a method originally proposed by Dr. David Allen in 1966 as a means of evaluating long term frequency stability of cesium atomic clock oscillators. Since then, the method has seen extensive use in generic time-series stability analysis, and as of late also within the field of inertial sensing, culminating with its selection as the preferred method for IFOG inertial sensor stability analysis [IEEE-1997]. Denoted as σ_y^2 (or $\sigma_y = \sqrt{\sigma_y^2}$ for the Allen deviation), the original Allen variance expression for a finite time-series expresses as equation A.1.

$$\sigma_y^2(\tau) = \frac{1}{2\,(M-1)} \sum_{i=1}^{M-1} \left(\bar{y}_{i+1}(\tau) - \bar{y}_i(\tau)\right)^2 \tag{A.1}$$

Here, y_i indicates the ith of at total of M clusters within the dataset averaged over the sampling interval τ. As the computation progresses the sampling interval increases and the number of clusters decrease, thus signifying that when sampling intervals become comparable to the length of the dataset, the number of possible clusters approach unity and the estimate accuracy degrades accordingly. In practice, the original formulation of the AVAR has been largely superseded by the overlapping method, which when adopting the terminology from [Riley-2008] expresses as equation A.2.

$$\sigma^2(\tau) = \frac{1}{2m^2\,(M-2m+1)} \sum_{j=1}^{M-2m+1} \sum_{i=j}^{j+m-1} \left(\bar{y}_{i+m}(\tau) - \bar{y}_i(\tau)\right)^2 \tag{A.2}$$

An intuitive understanding of the difference between the original AVAR formulation and the non-overlapping formulated can be gained from Figure A.1. The overlapping procedure improves the confidence level of the stability estimate,

yet it is clear that the computational load associated with the overlapping method is substantially larger, especially for longer time-series, as a much larger number of sample combinations must be computed.

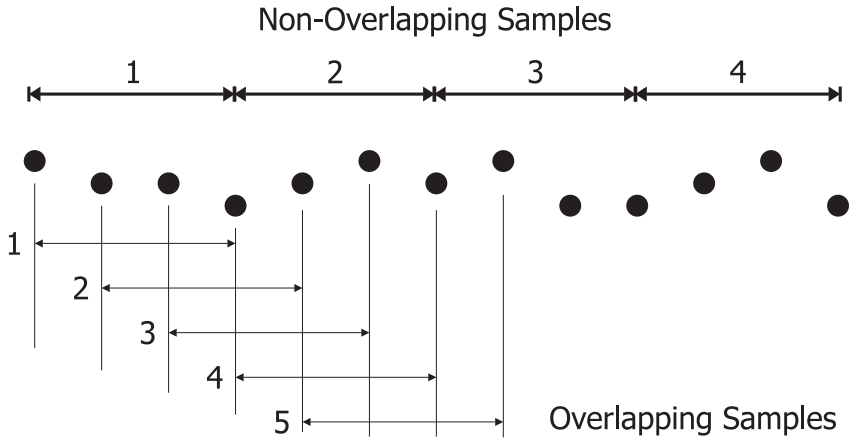

Figure A.1. *Non-overlapping vs. overlapping AVAR for an averaging period of m=3. Figure adapted from [Riley-2008].*

The accuracy of the estimation pertaining to each cluster can be assessed by computing the percentage error as expressed by equation A.3.

$$\delta = \frac{1}{\sqrt{2 \cdot \left(\frac{N}{n} - 1\right)}} \tag{A.3}$$

where:
N: describes the total number of samples in the dataset.
n: describes the total number of samples in a cluster.

For the detailed derivation of the expressions in Table A.1 the interested reader is referred to the in-depth treatment given by [Guerrier-2008].

When plotted log-log, the root Allen variance (Allen deviation) of a time-series has the distinct advantage of different basic random processes as characterized by a specific power spectral density function being identifiable. As such, provided the different noise mechanisms are reasonably separated in the frequency and time domain, at least five basic processes can be identified, namely quantization noise, white noise, bias instability, random walk and rate ramp. Moreover, sinusoidal noise and correlated noise processes also provide a distinctly identifiable character via this method, and it should be noted that in opposition to the other identifiable noise sources, rate ramp does not constitute a random process, rather it is of a deterministic nature [Zhang-2008]. Figure A.2 provides a schematic overview of the different noise processes and the nomenclature of their respective coefficients as seen in an Allen deviation plot.

Noise Source	Coefficient Value	Curve Slope
Quantization Noise	$\sigma_{AV}(\tau) = \sqrt{\frac{3Q_z^2}{T^2}}$	-1
White Noise	$\sigma_{AV}(\tau) = \frac{\sigma_{WN}}{\sqrt{T}}$	-1/2
Bias Instability	$\sigma_{AV}(\tau) = \sigma_{BI}\sqrt{\frac{2\ln 2}{\pi}}$	0
Random Walk	$\sigma_{AV}(\tau) = \sigma_{RW}\sqrt{\frac{T}{3}}$	+1/2
Rate Ramp	$\sigma_{AV}(\tau) = \frac{R \cdot T}{\sqrt{2}}$	+1

Table A.1. *Root allen variance noise terms and coefficients.*

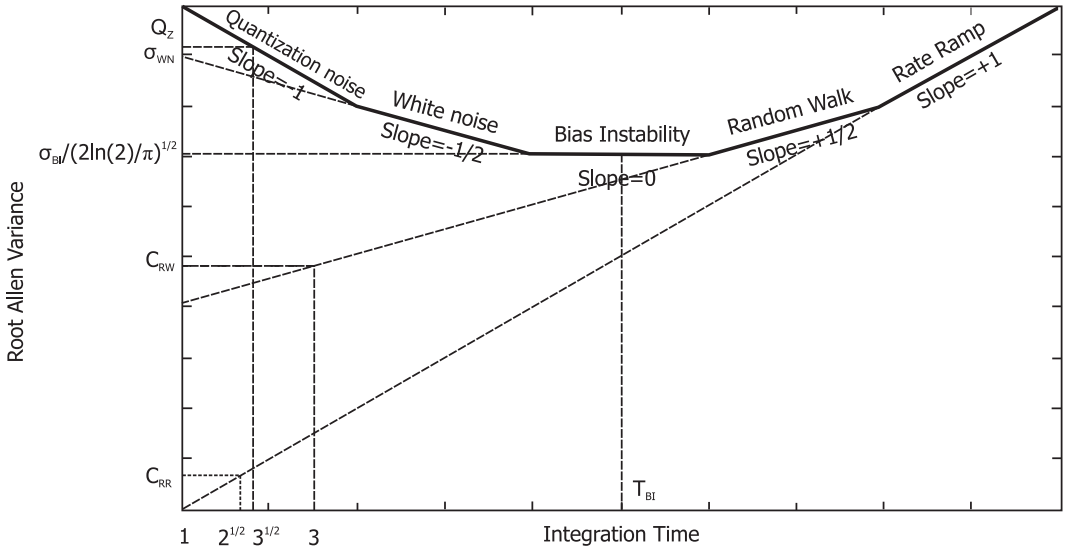

Figure A.2. *Prototype root Allen variance plot and coefficient nomenclature.*

Do note that for physical systems, the transitions between differently sloping regions will not necessarily be well defined and often exhibit noisy characteristics. Moreover, the curve shape depicted in Figure A.2 may change substantially for physical systems, due to the unpredictability of the region length dominated by a noise term. For additional details on the Allen Variance topic, excellent and expounding treatments are provided by [HP-1997, Guerrier-2008].

A.1 Bibliography

[Guerrier-2008] Stéphane Guerrier. *Integration of Skew-Redundant MEMS-IMU with GPS for Improved Navigation Performance.* PhD thesis, Ecole Polytechnique Federale de Lausanne, 2008.

[HP-1997] Hewlett Packard. The science of timekeeping - application note 1289. Technical report, Hewlett Packard, 1997.

[IEEE-1997] IEEE. Ieee standard specification format guide and test procedure for single-axis interferometric fiber optic gyroscopes. Technical report, IEEE Aerospace and Electronic Systems Society, 1997.

[Riley-2008] W.J. Riley. *Handbook of Frequency Stability Analysis - NIST Special Publication 1065*. National Institute of Standards and Technology, 2008.

[Zhang-2008] Peter Mumford Chris Rizos Xin Zhang, Yong Li. Allen variance analysis on error characters of mems inertial sensors for an fpga-based gps/ins system. *Int. Symp. on GPS/GNSS, Yokohama, Japan*, 2008.

Appendix B

μIRU Timing Analysis

B.1 μASC Centre of Integration Positioning

B.2 μIRUapp Program Flow for Synchronized Operations

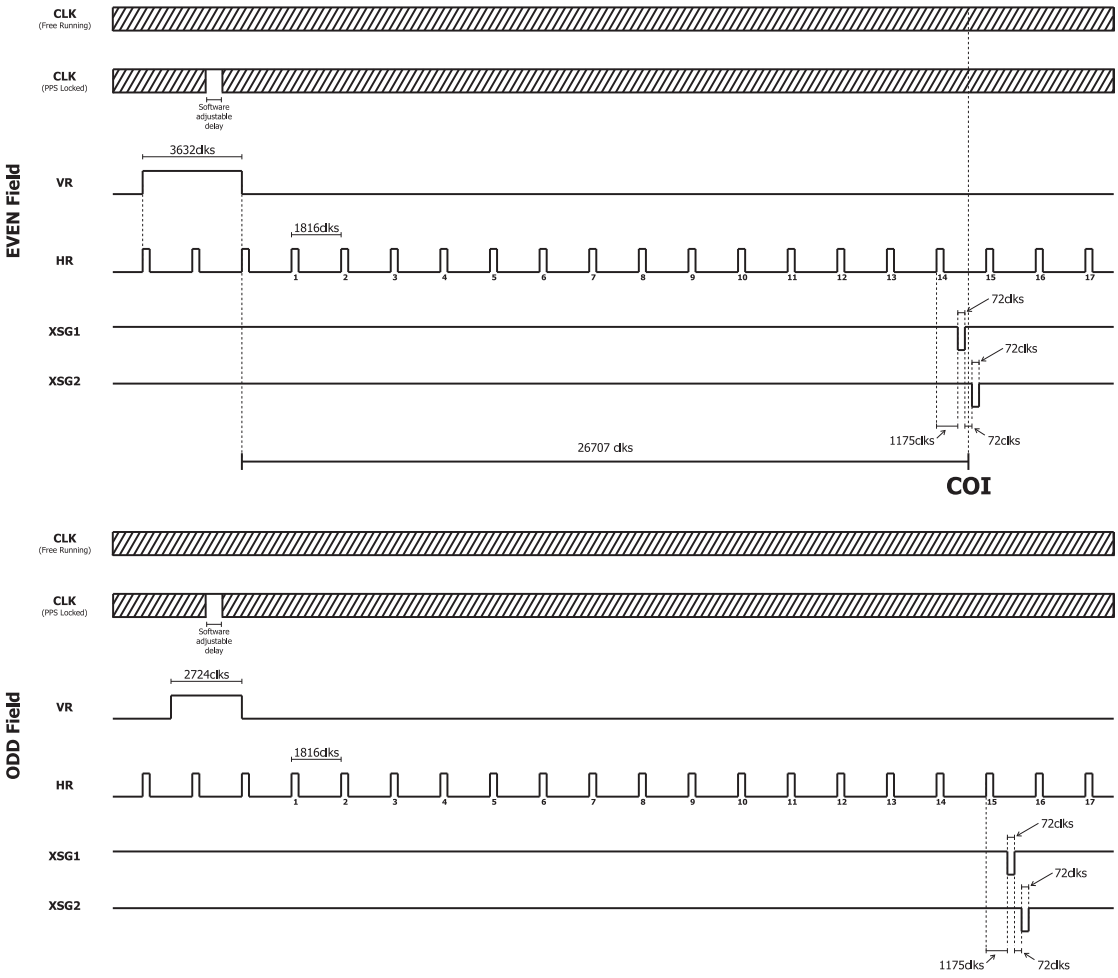

Figure B.1. *μASC Centre of Integration Timing with respect to VR trailing edge.*

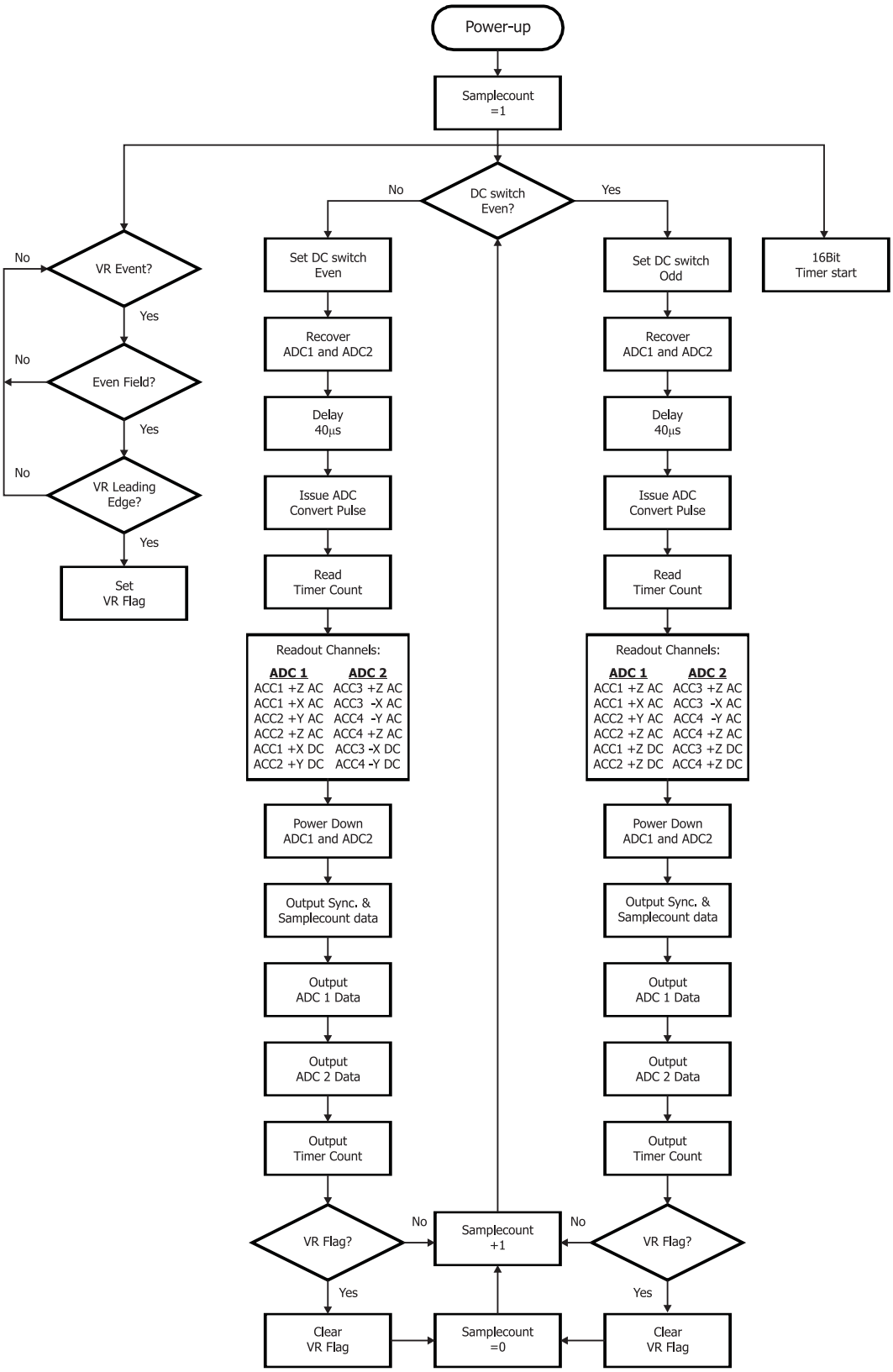

Figure B.2. *μapp synchronized program flow. Applicable conditions are a free-running μASC with VR synchronization (no clock stops).*

Appendix C

μIRU Prototype DCM Parts Irradiation Screening

The subsequent sections provide details regarding the procedures and results of irradiation screening applied to the active components selected for the μIRU prototype filter branches. All data has been corrected for the TID attenuating effects pertaining to the component packaging material density and thickness.

C.1 MAX4092AUA Operational Amplifier

The Maxim Integrated Products Inc. MAX4092AUA is a dual operational amplifier implemented using bipolar technology and used as the primary active component in the μIRU prototype filter branches. The part has been irradiation screened using the radiation facility setup introduced in Section 3.3.5. During the test, both opamps of the component where continuously operating in a unity gain configuration as depicted in Figure C.1. The temperature was kept at a near constant level of $21°C$.

The acquired primary data depicted in Figure C.2 clearly exhibits a very level of TID tolerance as can be expected for certain bipolar component implementations. As such, the combined current consumption of both opamps is seen to drop about 50μA over 230krad exposure, with output voltages remaining within the resolvability of the excitation voltage signal, indicating no noticeable change in offset voltage. Note here that 6 1/2 digit multimeters where applied only to the output signals due to availability issues.

With both opamps exposed to the same excitation signal, their output voltage difference is compared to evaluate overall stability of the device. Initially a 400μV difference is observed, and this is seen to maintain a near constant mean

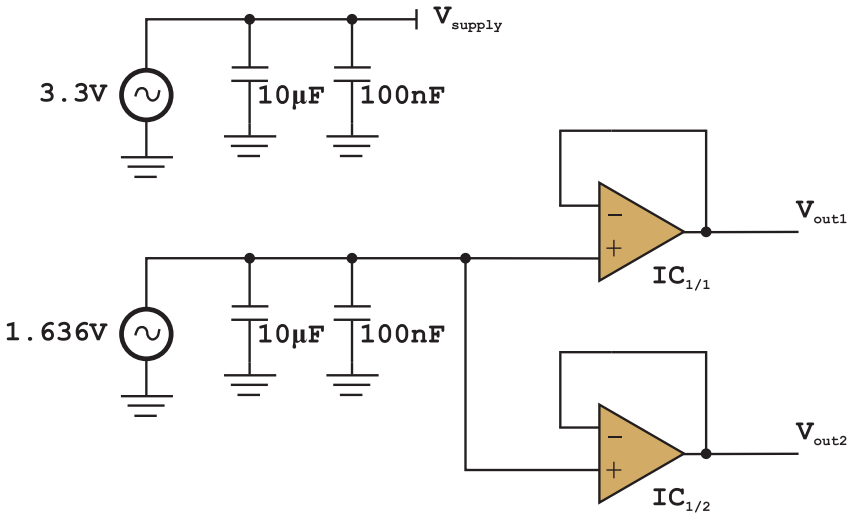

Figure C.1. *MAX4092AUA irradiation test setup.*

and uniform distribution over exposure, albeit with fluctuations on the order of $\pm 200\mu$V observed intermittently at around 210krad.

Moreover, it should be noted that temporal disparity between sampling the output voltages from each opamp combined with power supply noise may at least partly account for the $1\sigma_{RMS}$=$35\mu V$ noise observed in the output difference voltage.

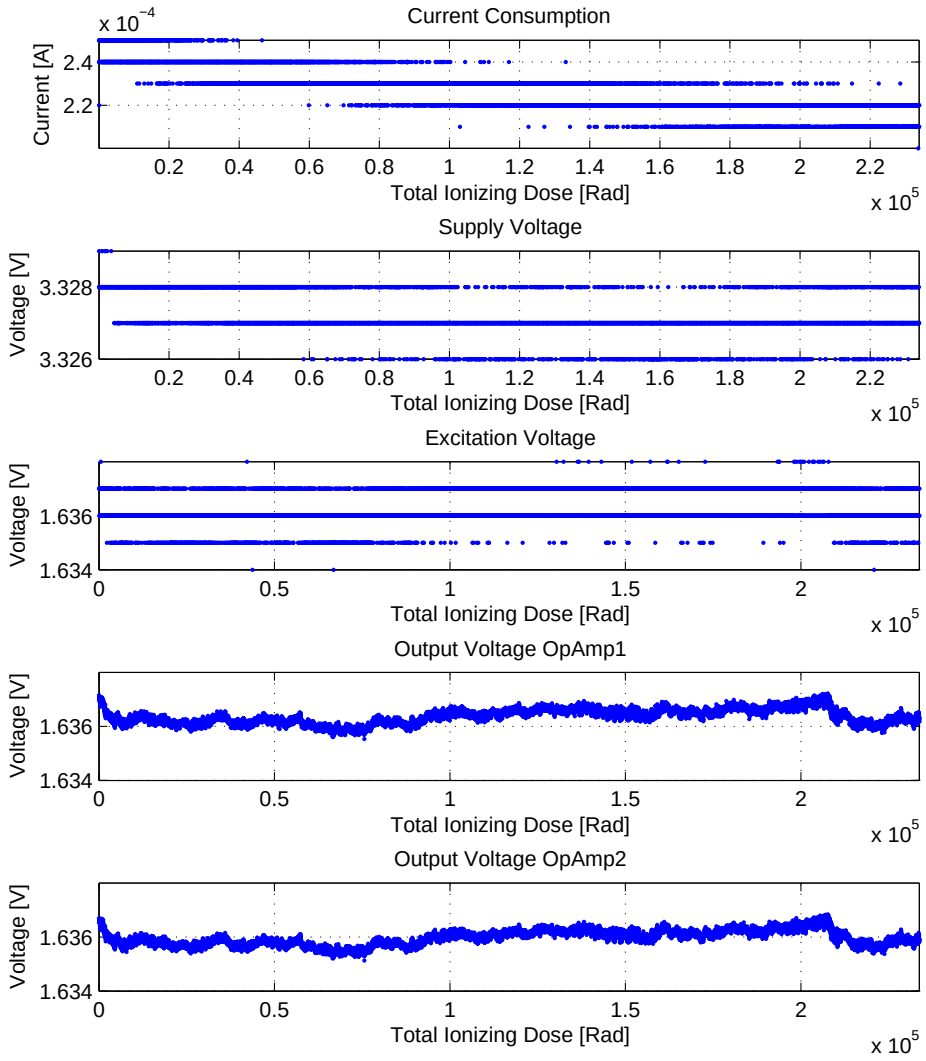

Figure C.2. *MAX4092AUA irradiation screening primary data.*

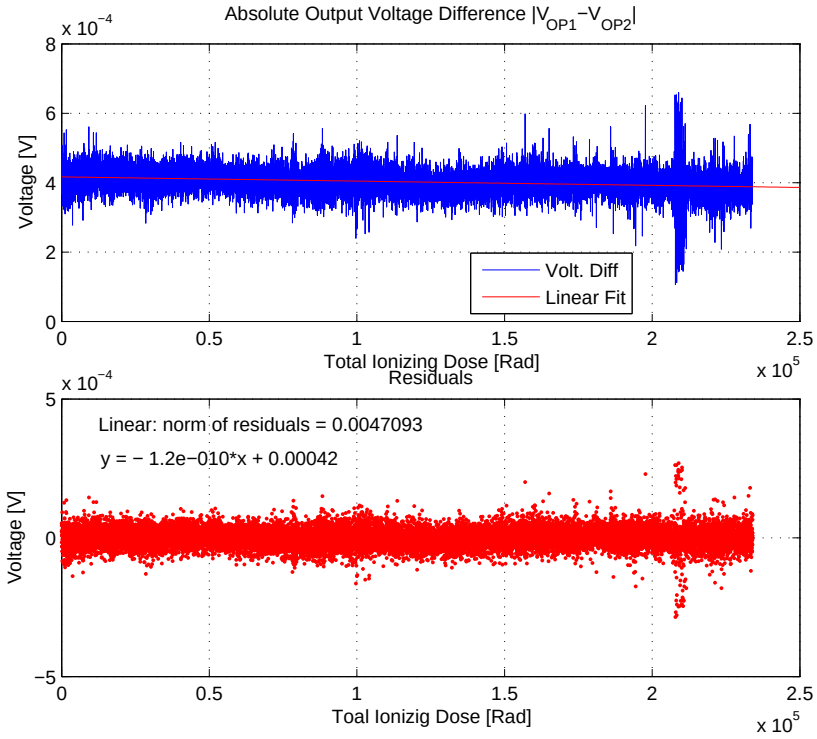

Figure C.3. *MAX4092AUA irradiation screening derived data.*

C.2 MAX4236 Operational Amplifier

The Maxim Integrated Products Inc. MAX4236 is a high precision BiCMOS operational amplifier used in addition to the MAX4092AUA in the DCM filtering branch circuitry of the μIRU prototype. Employed as a buffer amplifier in the offset generating circuit, the opamp has been subjected to TID irradiation screening in that particular configuration as illustrated by Figure C.4.

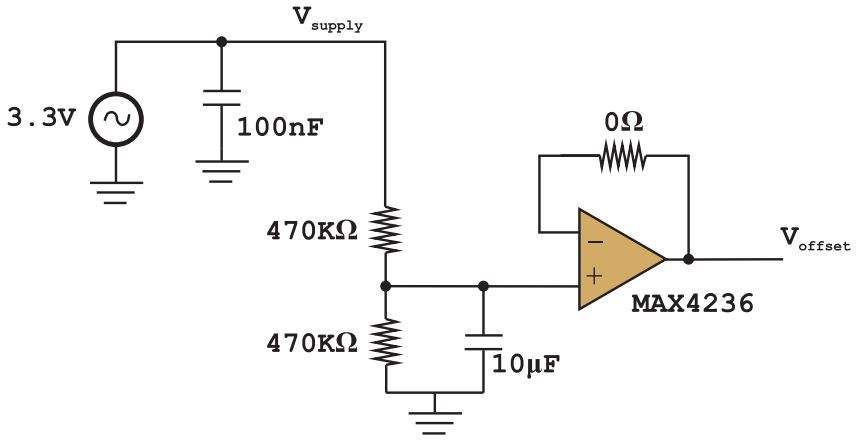

Figure C.4. *MAX4236 irradiation test setup.*

Although resolution limited by the test setup instrumentation, data from the test depicted in Figure C.5 clearly show the MAX4236 opamp experiencing graceful degradation beyond 30krad TID exposure. Below this level device behavior remains nominal and noise performance below the resolving capability of the instrumentation. As this performance is on par with the LTC1408I ADC, the MAX4236 has been selected for usage in the μIRU augmentation prototype.

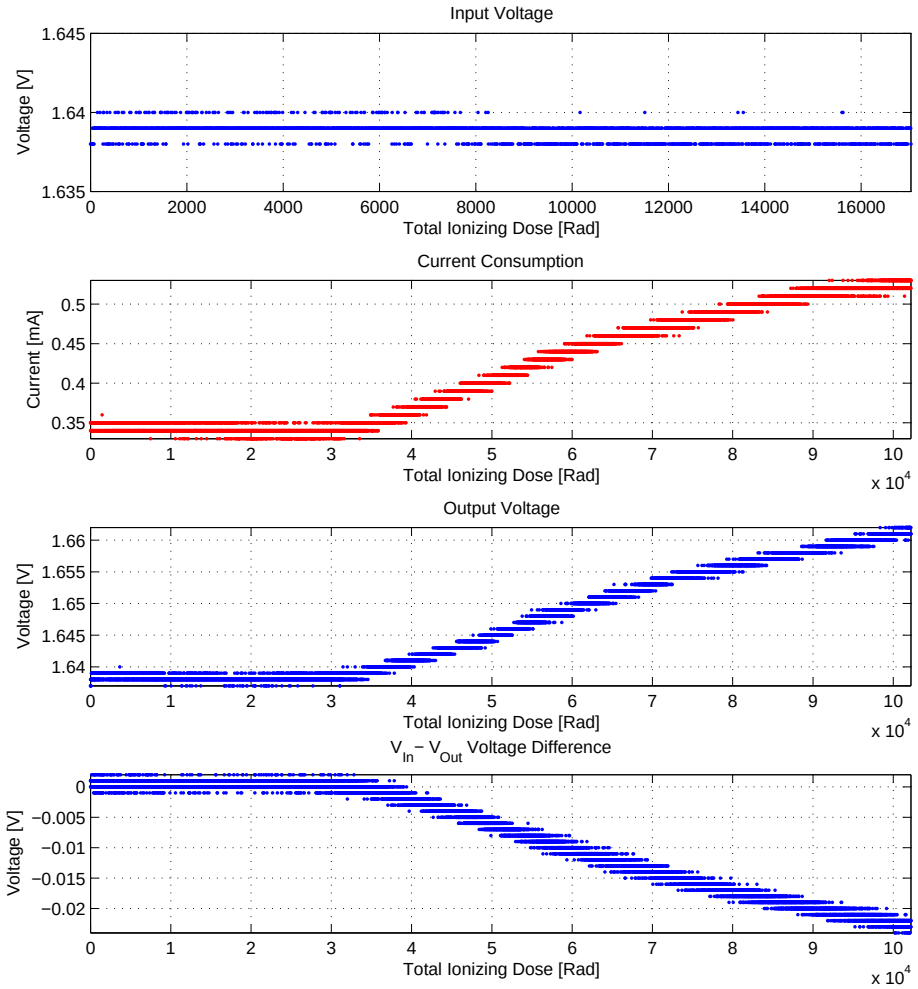

Figure C.5. *MAX4236 irradiation screening data.*

C.3 MAX4736 Dual Analog Switch

The Maxim Integrated Products Inc. MAX4736 CMOS dual analog switch is employed directly in the accelerometer signal chain of the μIRU prototype DCM as a multiplexer between DC channels. As such, the integrity of the DC signal propagated through the analog switch is highly critical and thus the irradiation test setup depicted in Figure C.6 seeks to verify that device critical parameters remain constant under TID exposure. Chief among these parameters is the on resistance of the switches

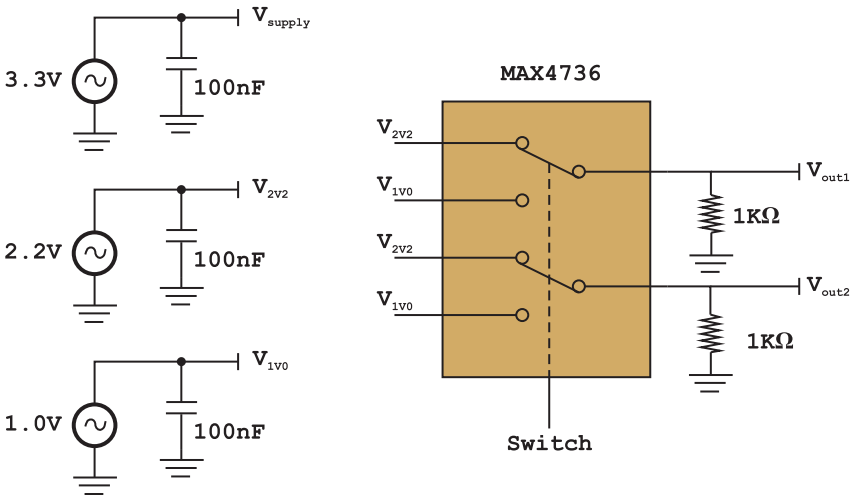

Figure C.6. *MAX4736 irradiation test setup.*

The supply parameters encountered during the test are depicted in Figure C.7 and show the ratiometric operation between the supply voltage and the 16Bit ADC used to record input and output voltage levels pertaining to the switch. Moreover, device current consumption is observed to be constant within the resolving capability of the test instrumentation.

Figure C.8 provides an illustration of the analog switch input/output levels throughout the test. The two topmost plots depict the two input levels between which the switches operate, whereas the two remaining plots depict the difference between the two excitation voltages as observed at the output of the MAX4736 analog switch.

As shown by the data, the mean output voltage levels remain constant to within 20μV over TID exposure, thus indicating a maximum shift in on resistance of $\sim$2%, well within the tolerances requirements imposed by the μIRU application.

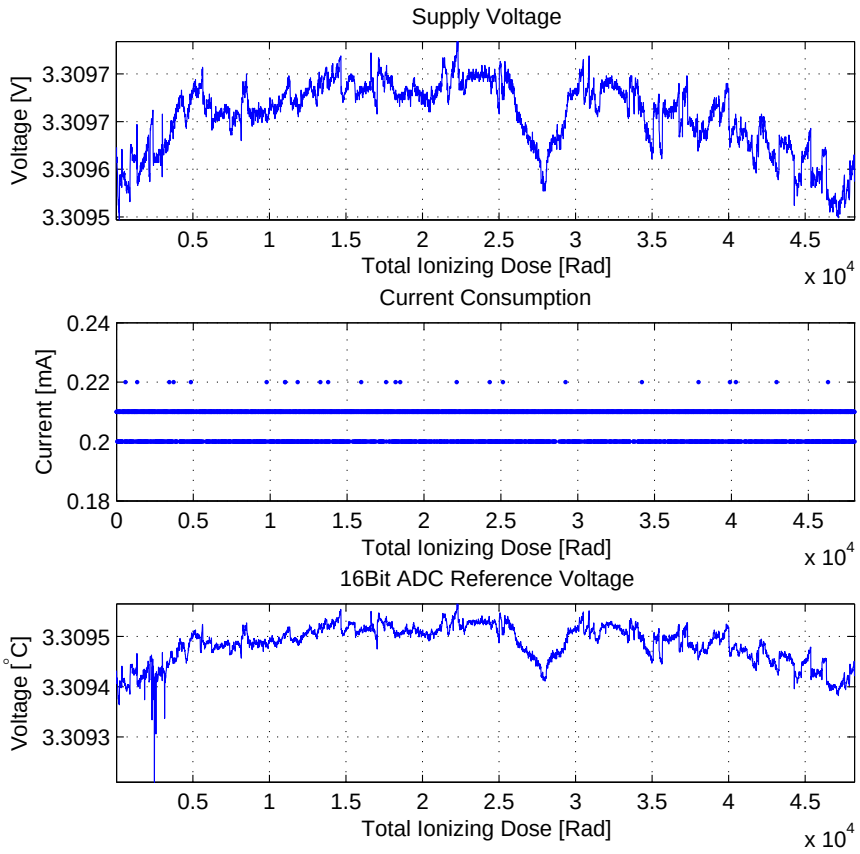

Figure C.7. *MAX4736 irradiation screening test supply parameters.*

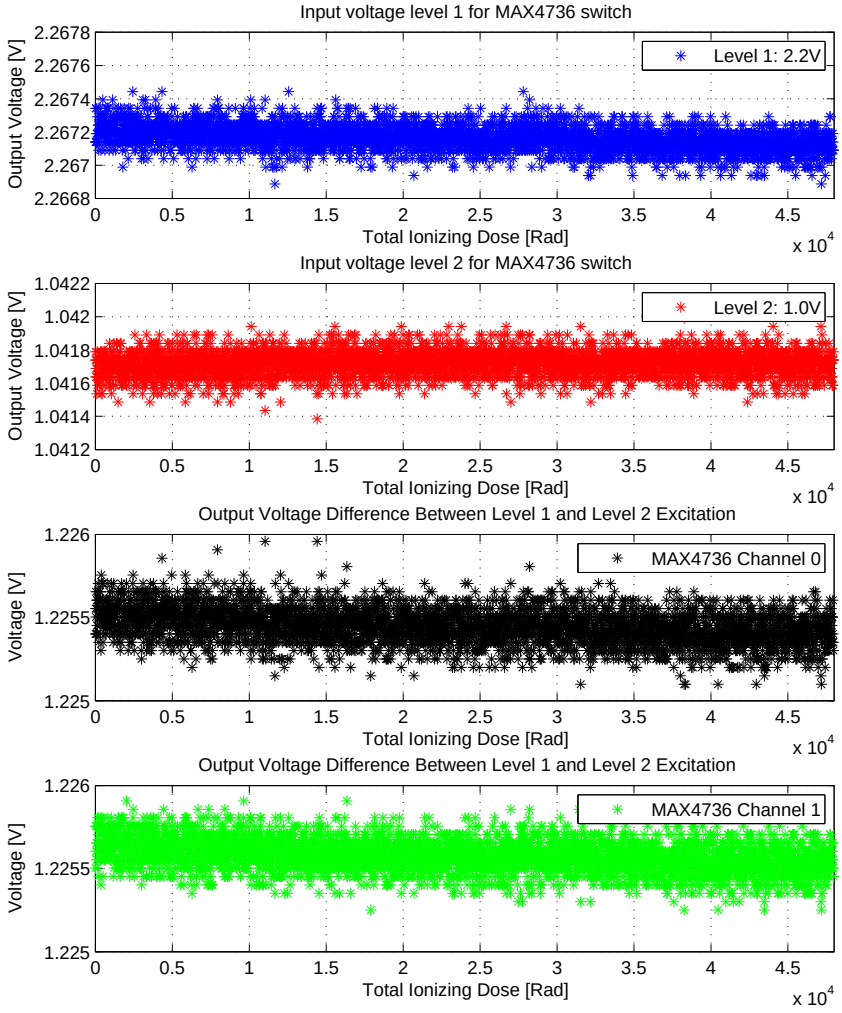

Figure C.8. *MAX4736 irradiation screening test data.*

Appendix D

μIRU Prototype

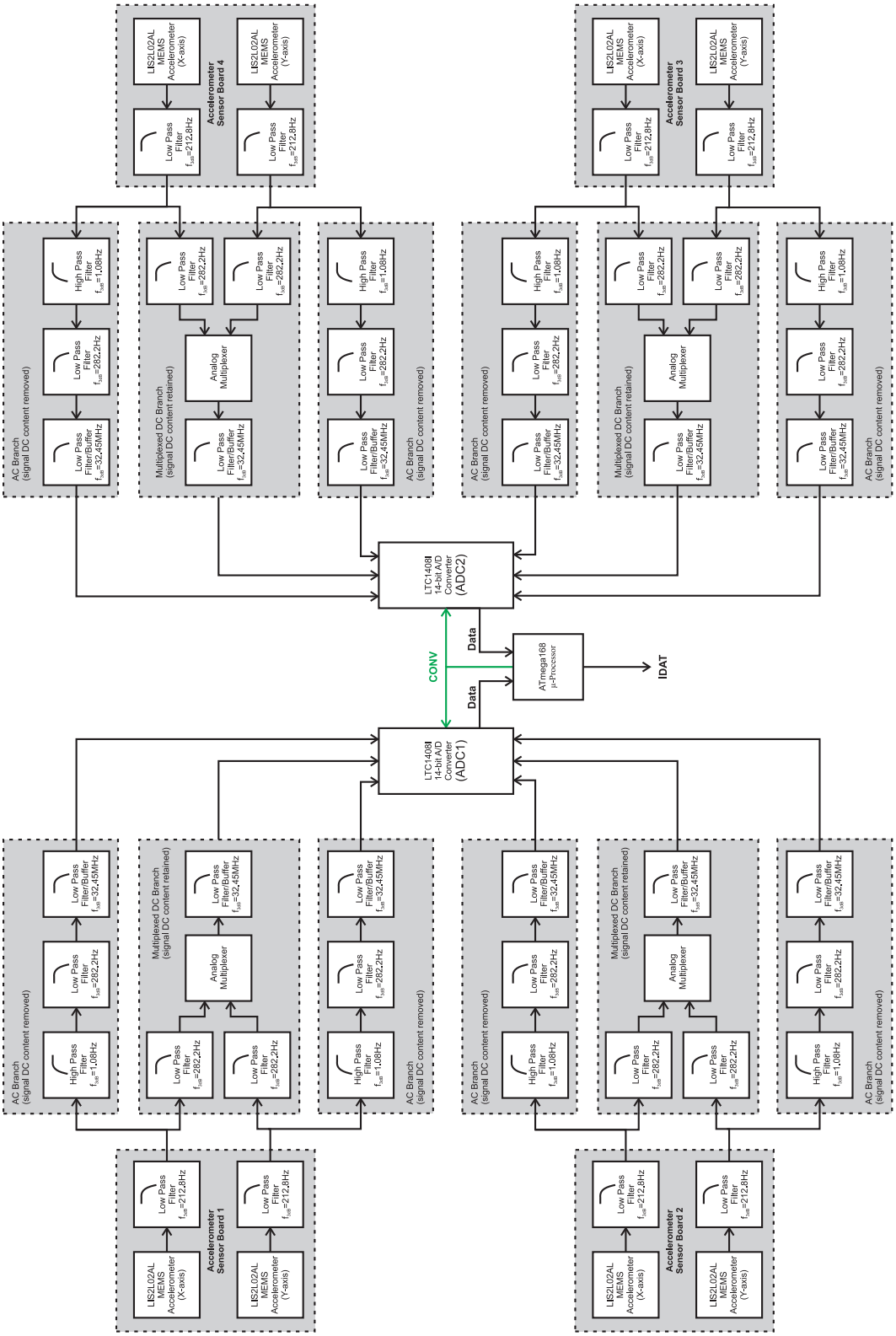

Figure D.1. *Overview of µIRU tier one prototype DCM implementation and signal paths.*

Appendix E

μIRU Prototype Mechanical Design

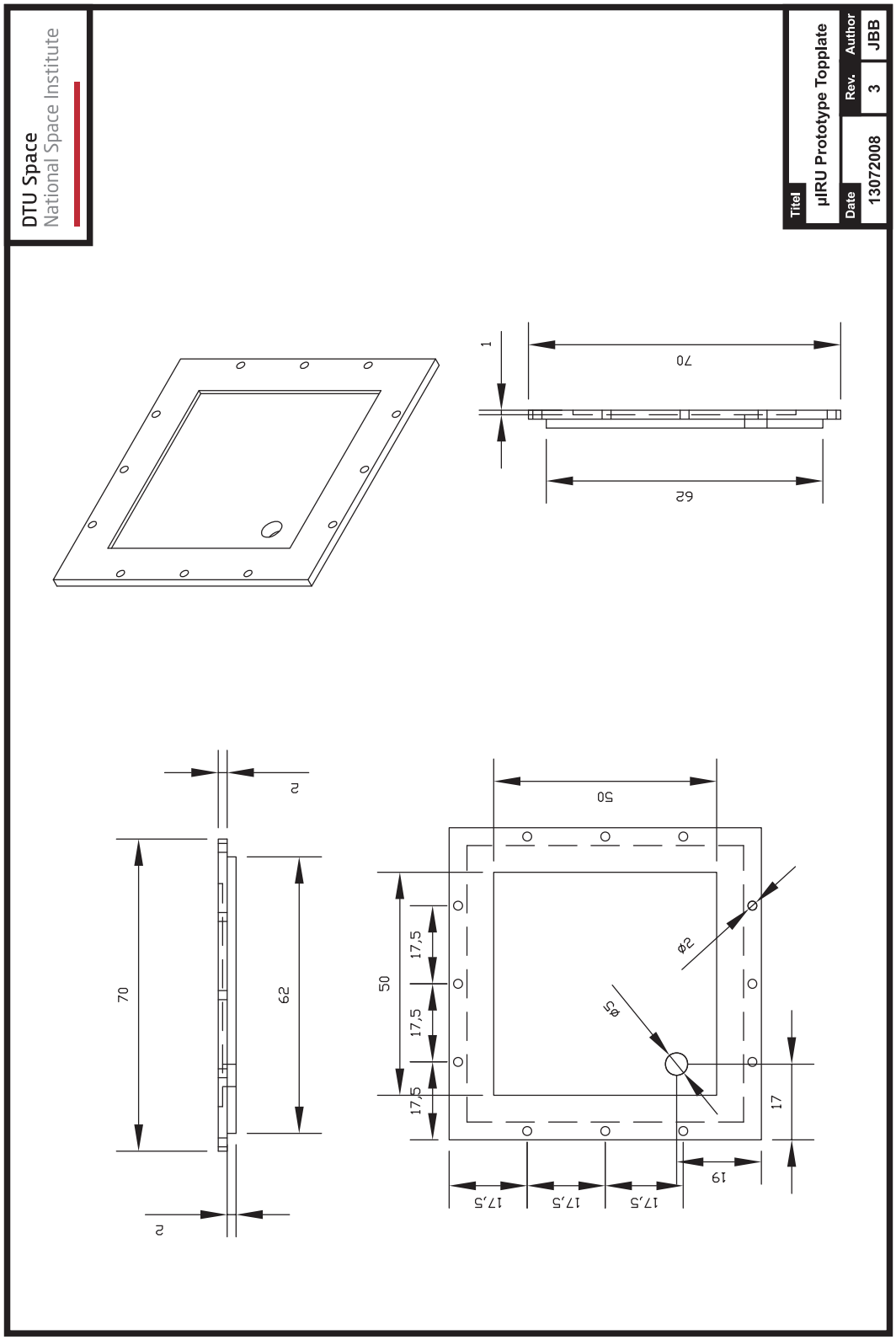

Figure E.1. *µIRU prototype topplate mechanical drawing.*

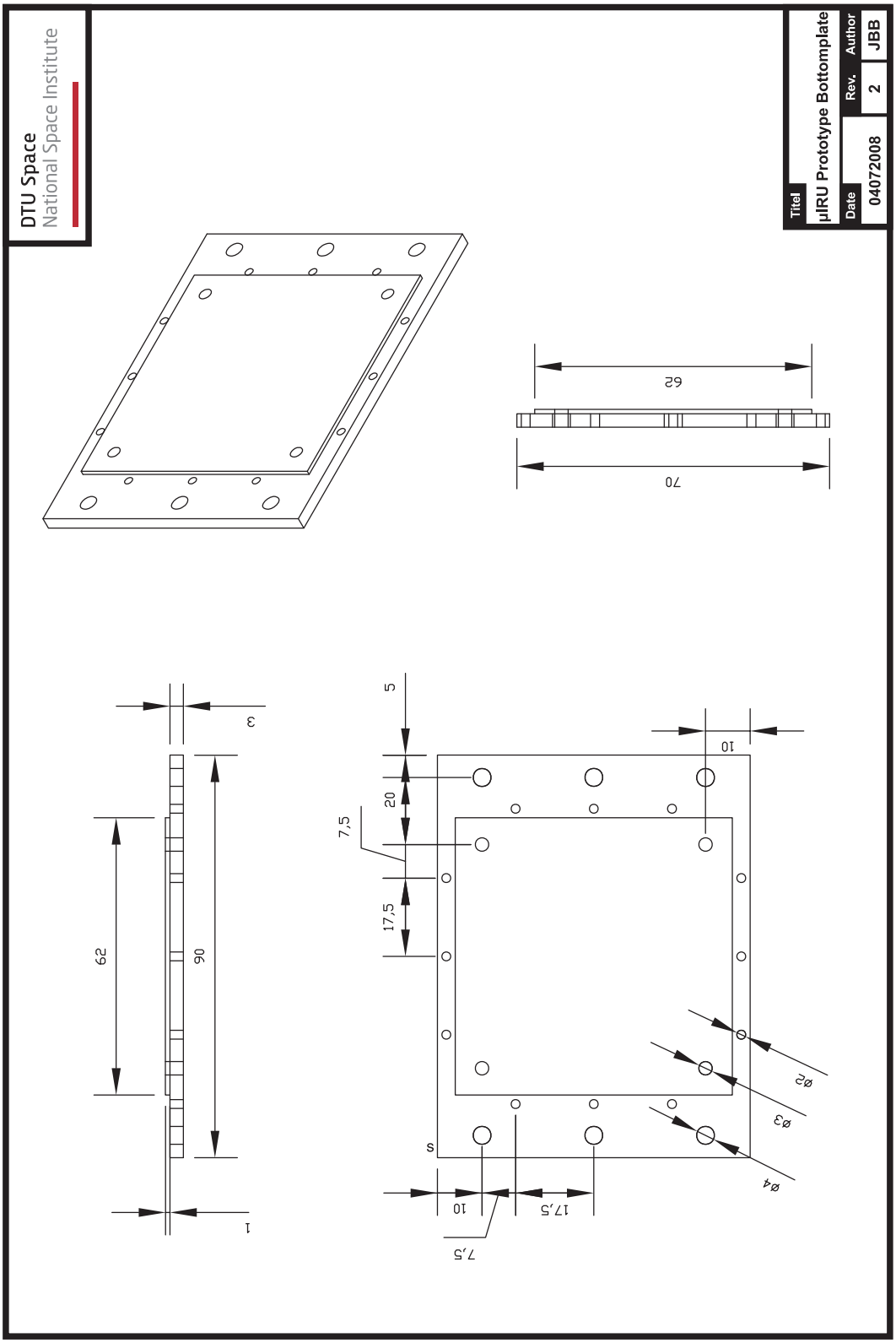

Figure E.2. *μIRU prototype bottomplate mechanical drawing.*

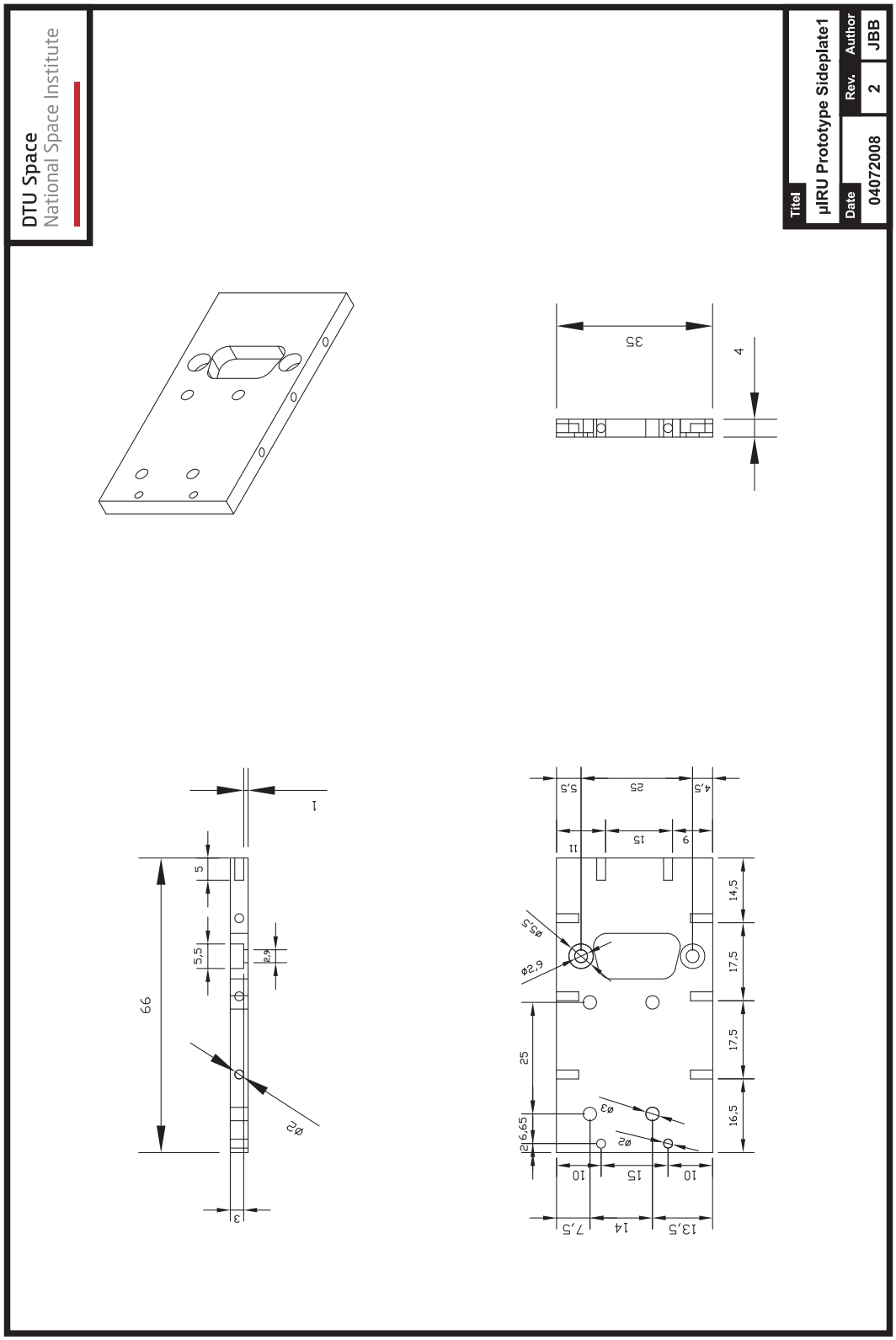

Figure E.3. *µIRU prototype sideplate 1 mechanical drawing.*

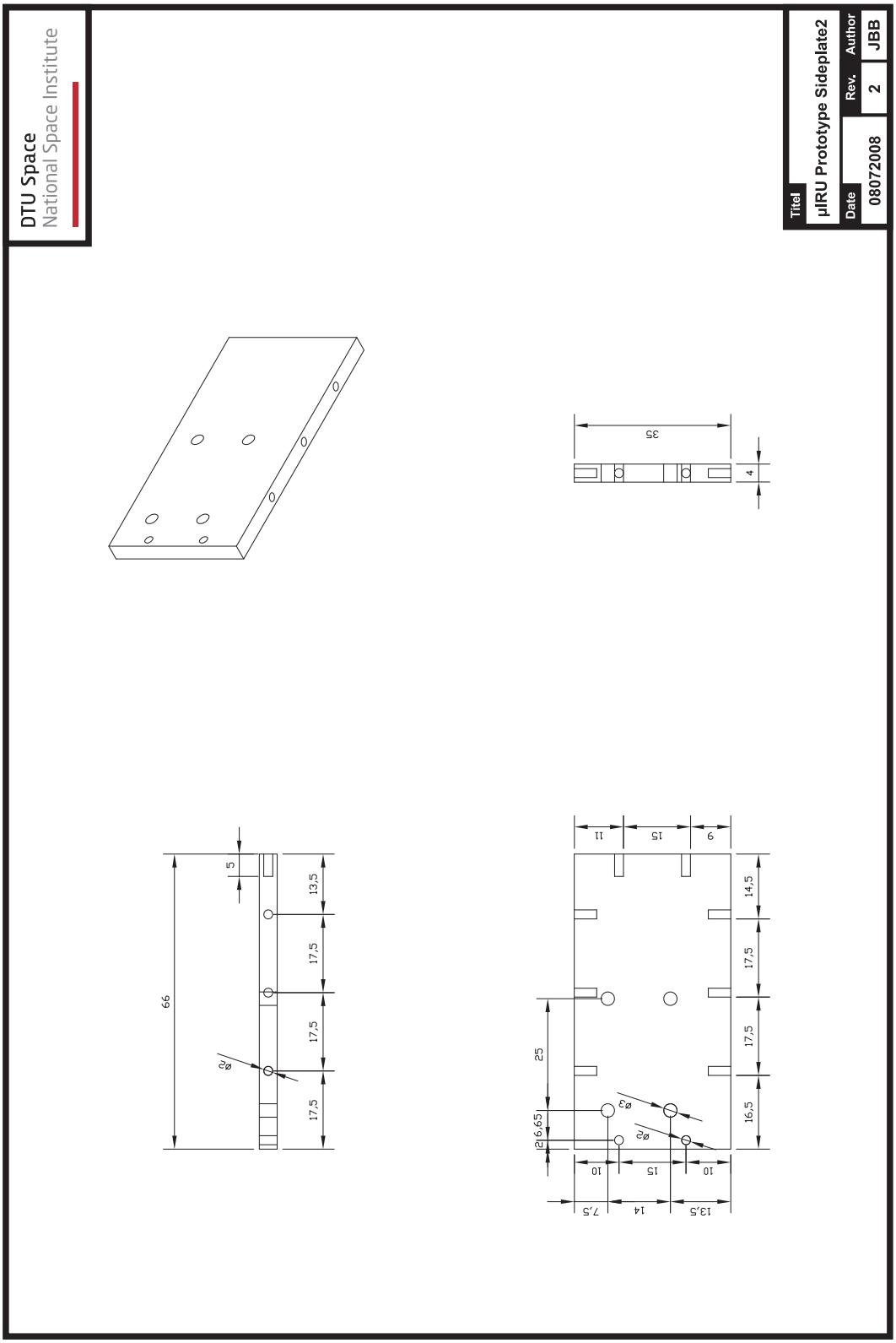

Figure E.4. *μIRU prototype sideplate 2 mechanical drawing.*

Appendix F

μIRU Prototype Schematics and PCB Layouts

F.1 LIS2L02AL Sensor Board Schematics

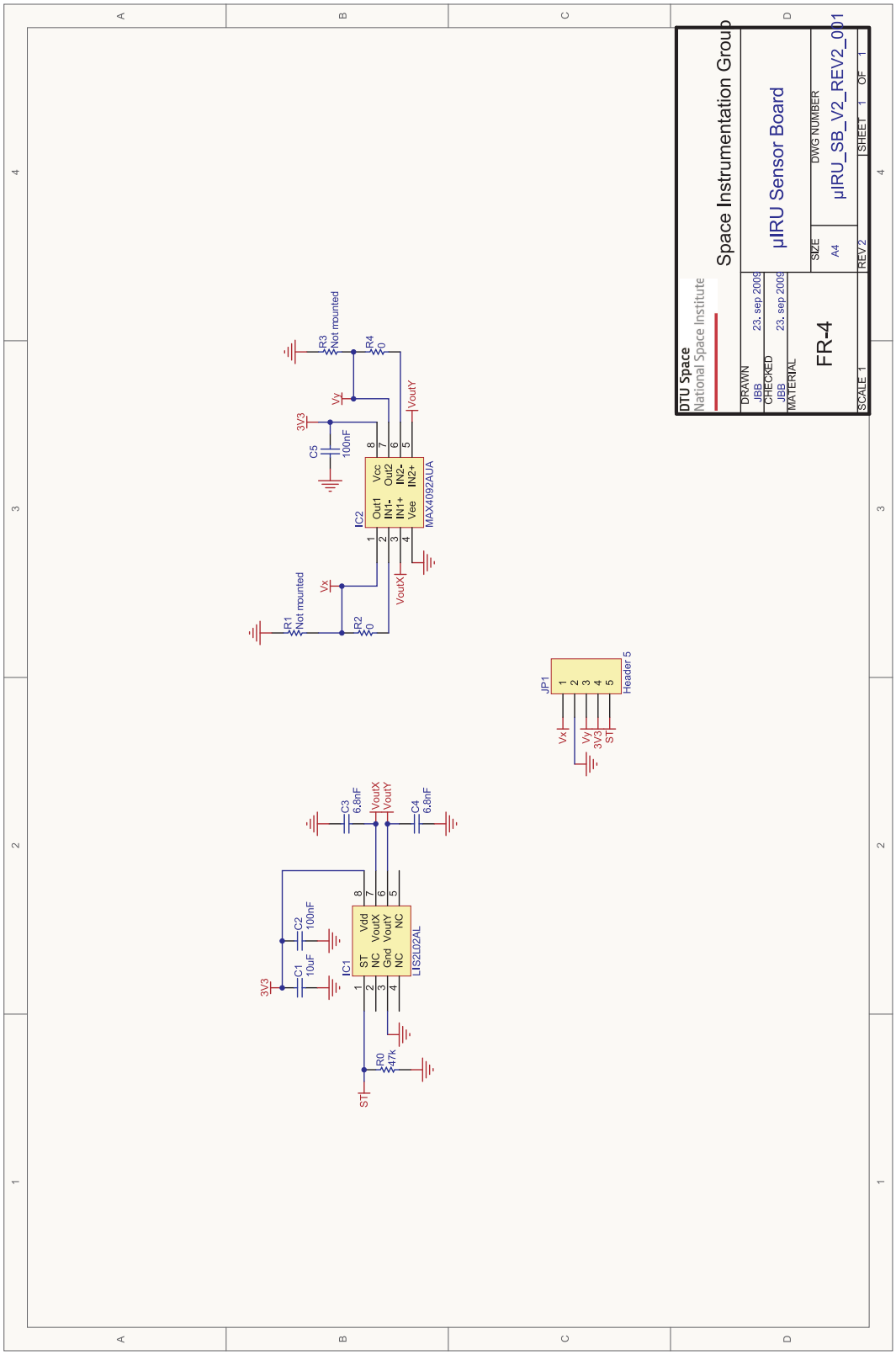

Figure F.1. *LIS2L02AL sensor board schematic.*

F.2 LIS2L02AL Sensor Board PCB Layout

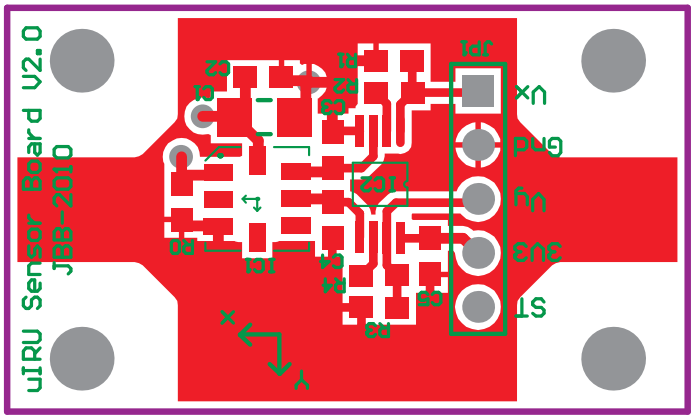

Figure F.2. *LIS2L02AL sensor board top layer.*

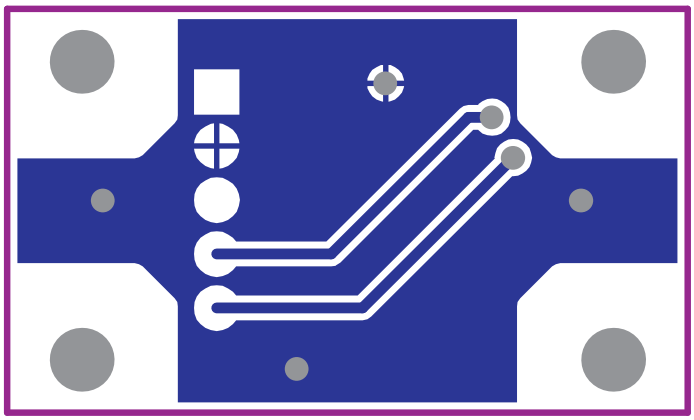

Figure F.3. *LIS2L02AL sensor board bottom layer.*

F.3 Data Conversion Module Schematics

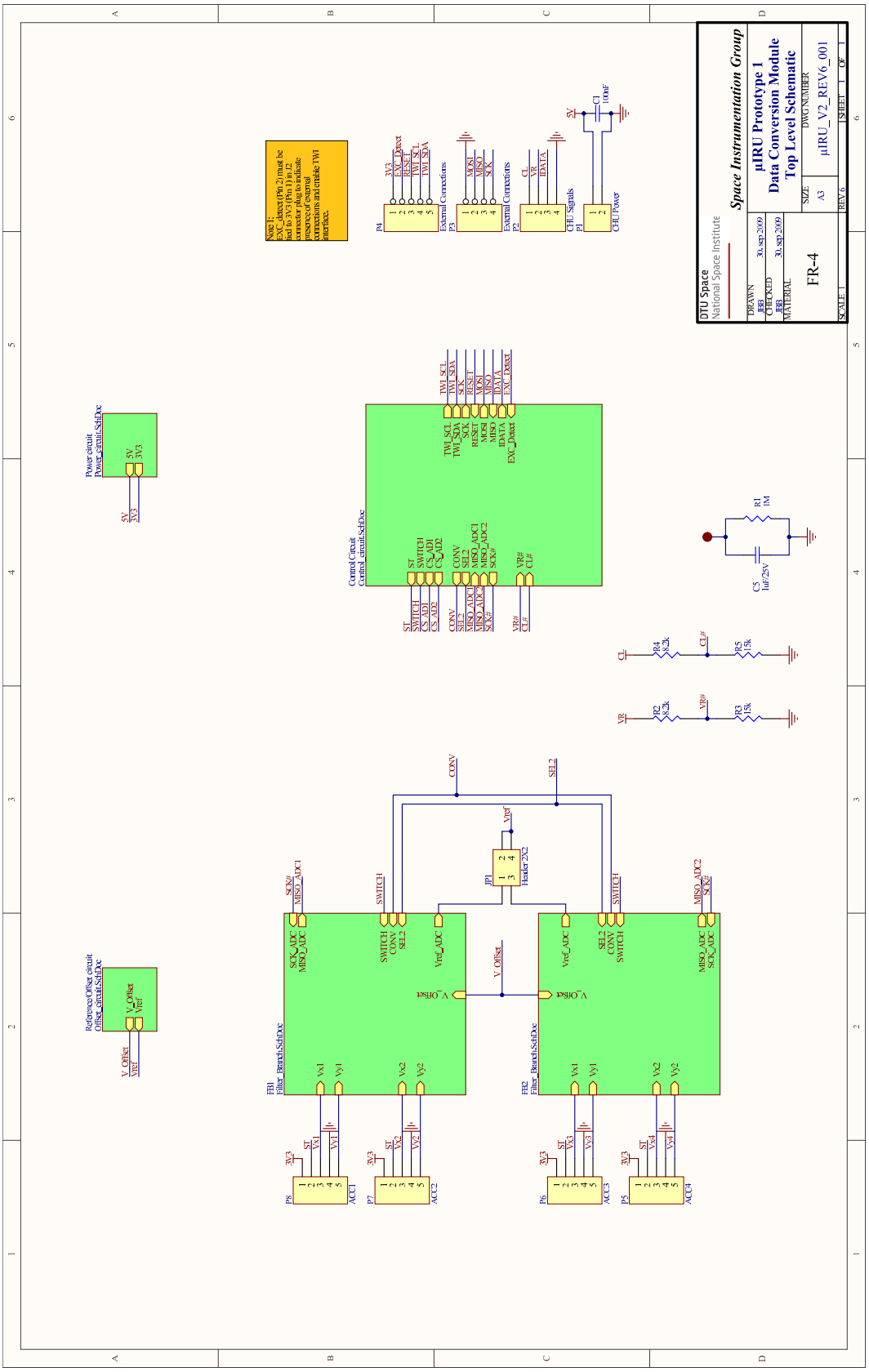

Figure F.4. *Data conversion module top level schematic.*

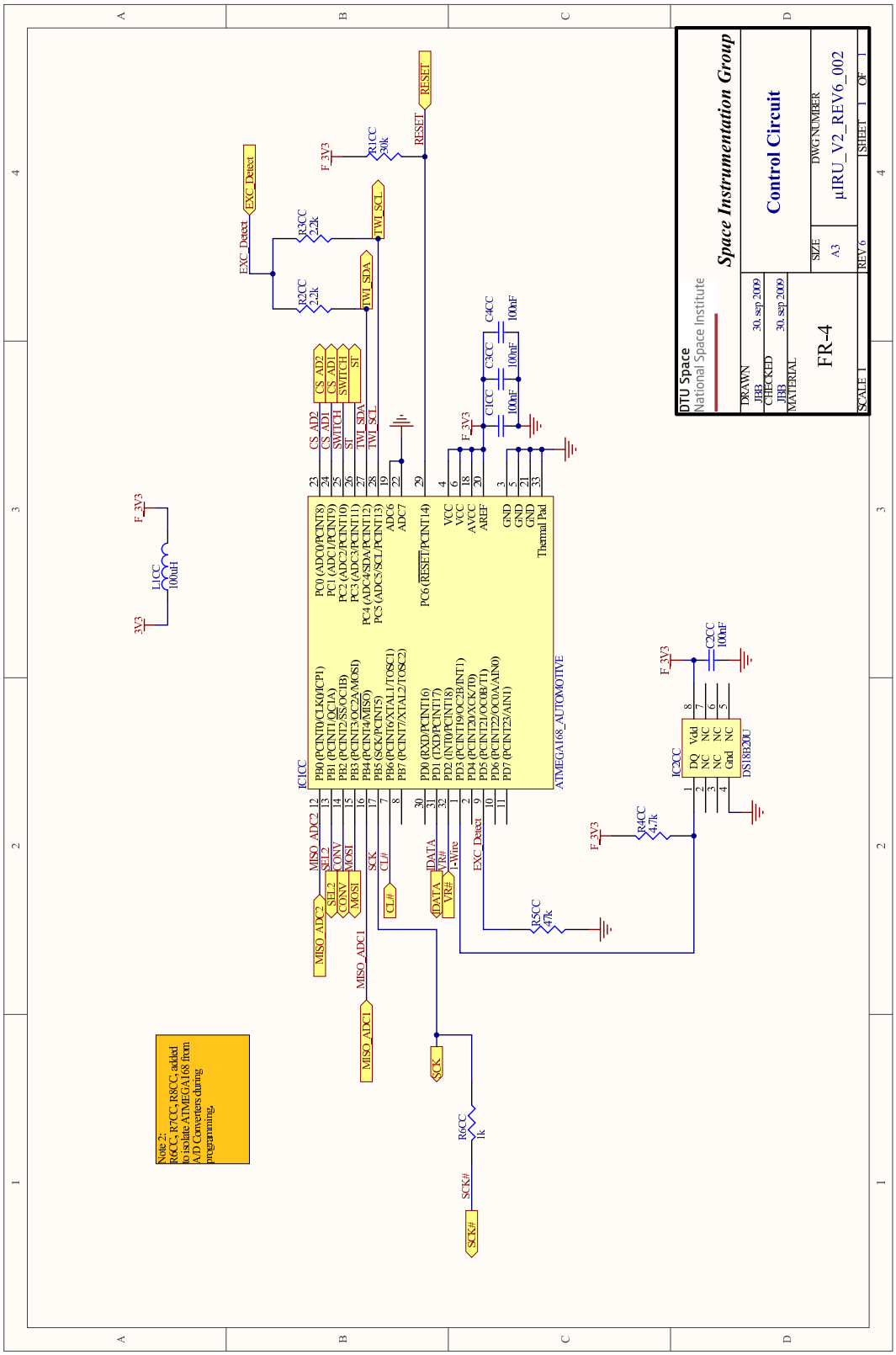

Figure F.5. *Data conversion module control circuit schematic.*

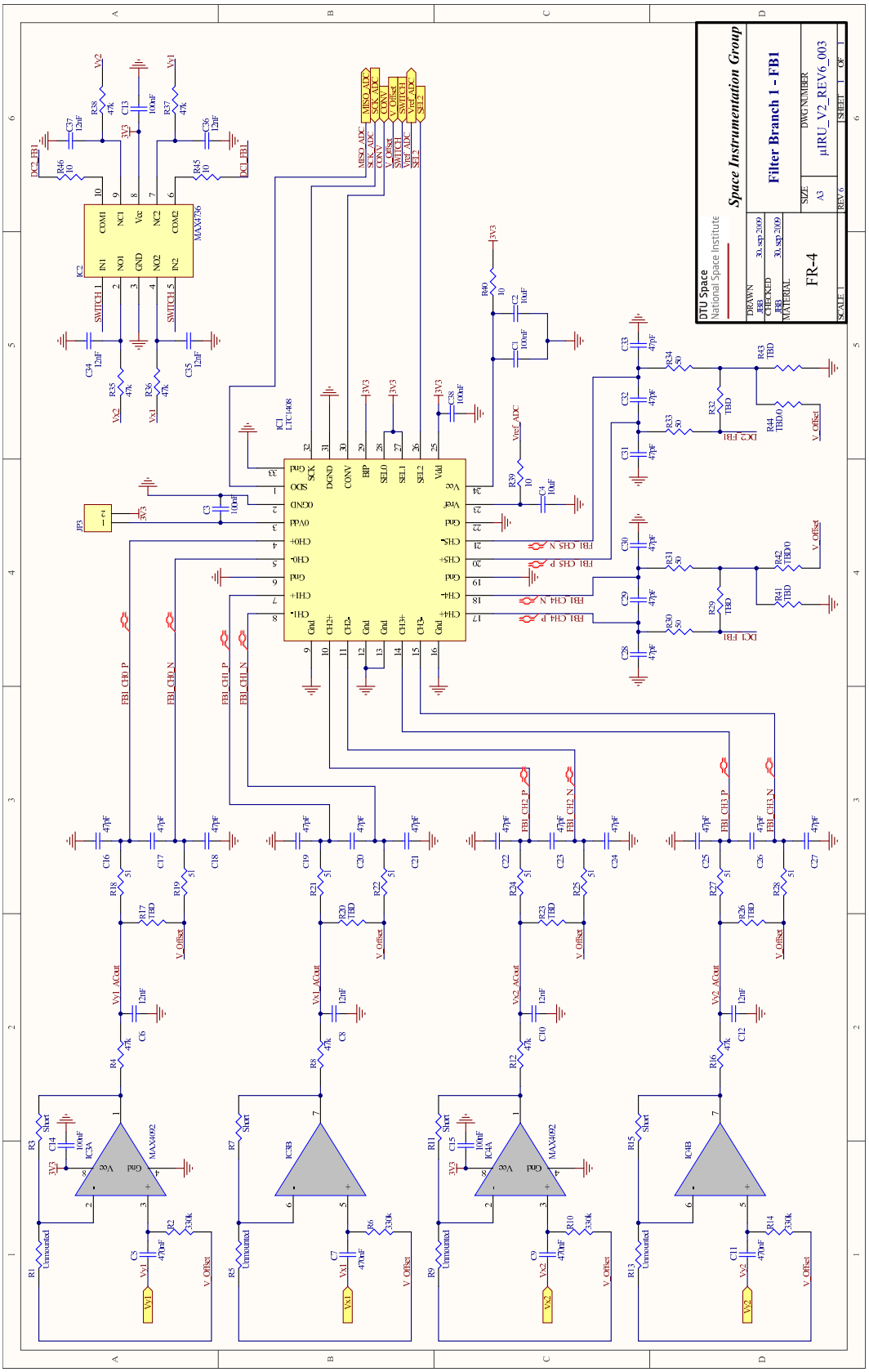

Figure F.6. *Data conversion module filter branch 1 schematic.*

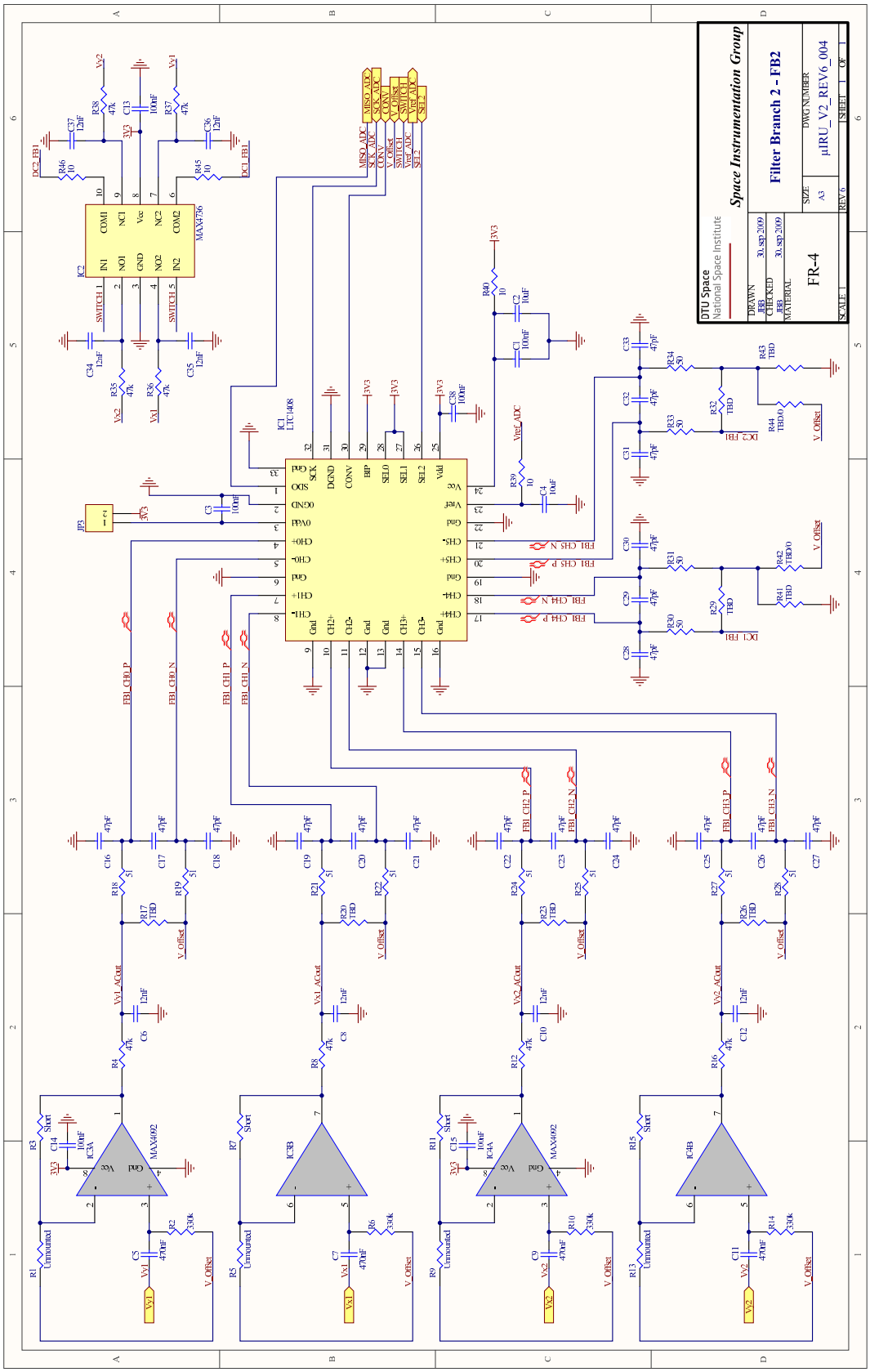

Figure F.7. *Data conversion module filter branch 2 schematic.*

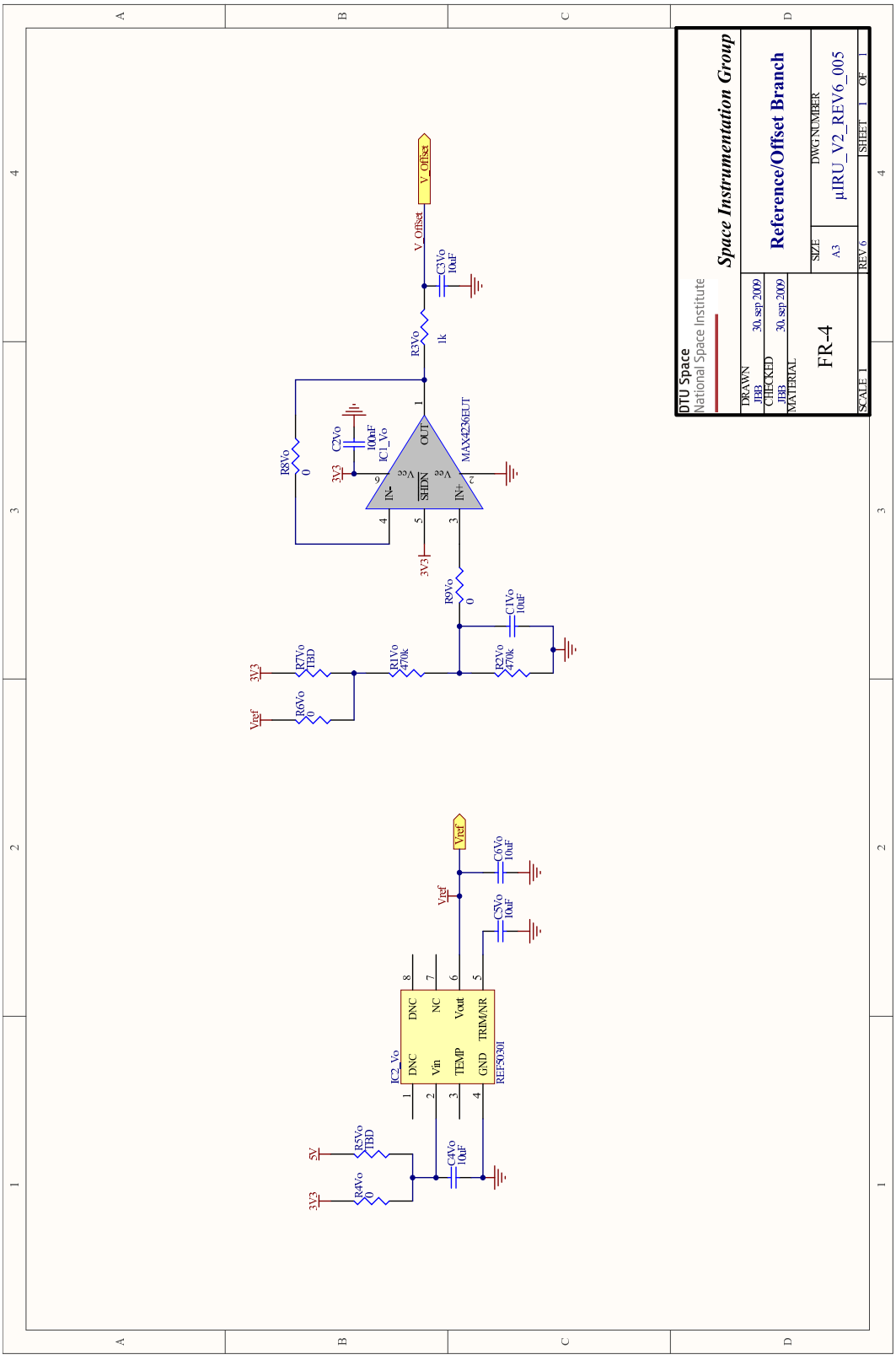

Figure F.8. *Data conversion module reference/offset branch schematic.*

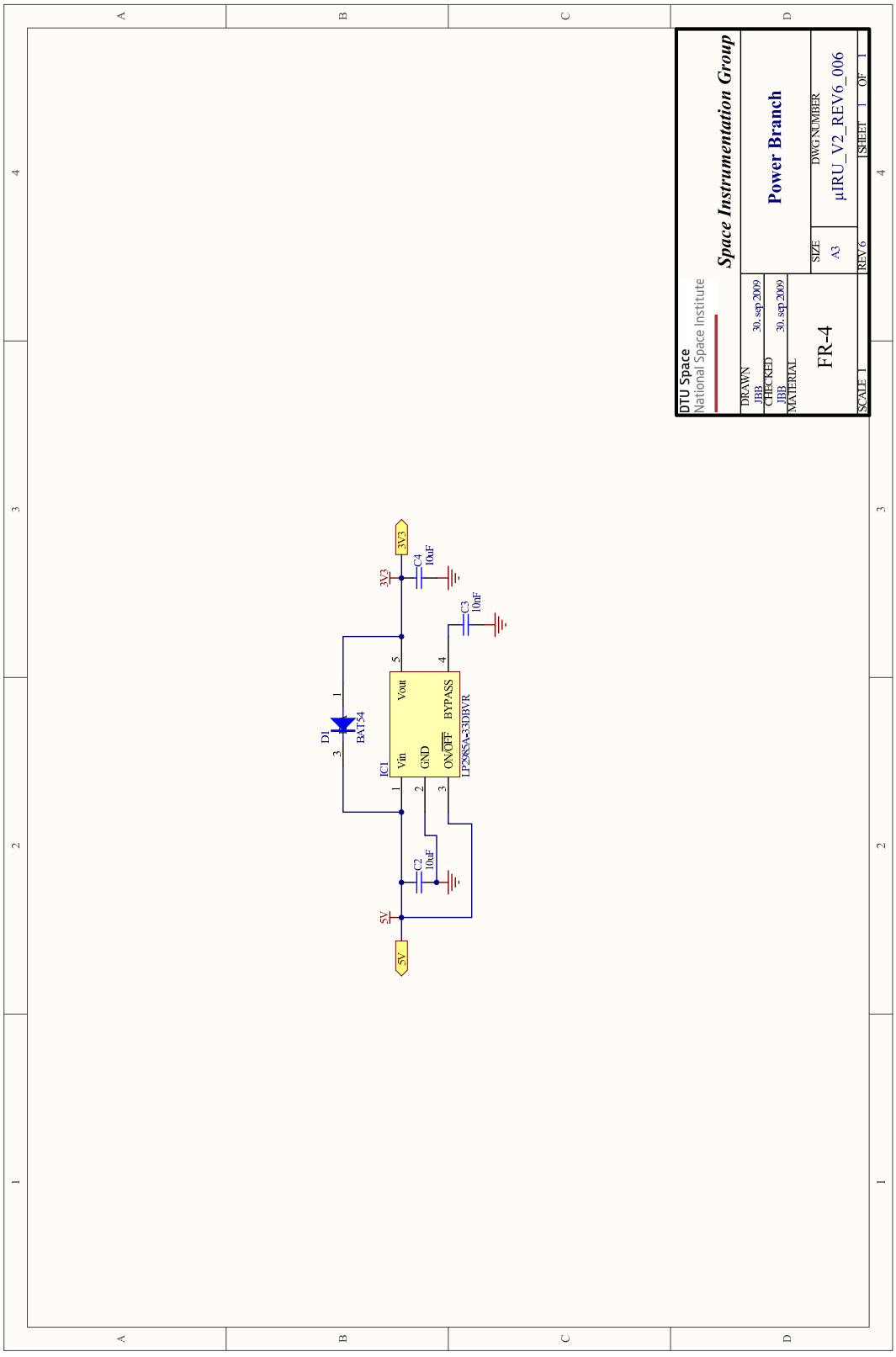

Figure F.9. *Data conversion module power branch schematic.*

F.4 Data Conversion Module PCB Layout

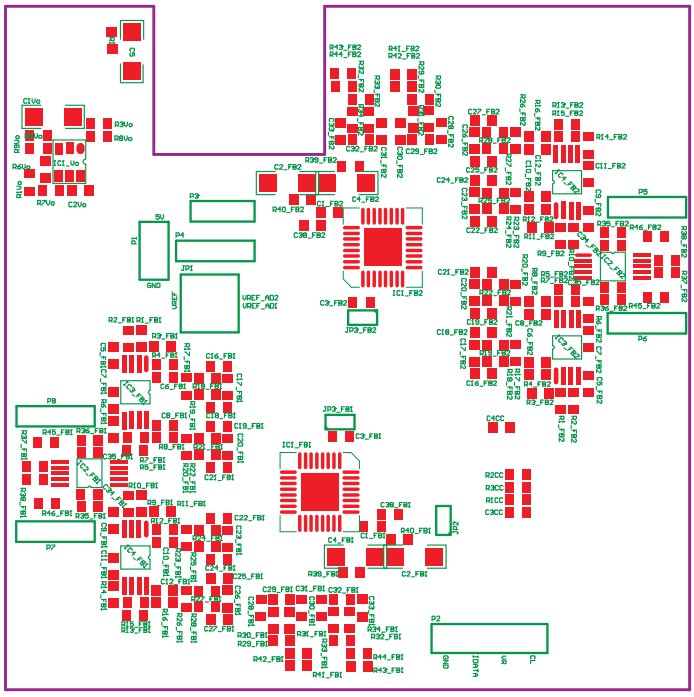

Figure F.10. *μIRU DCM top overlay.*

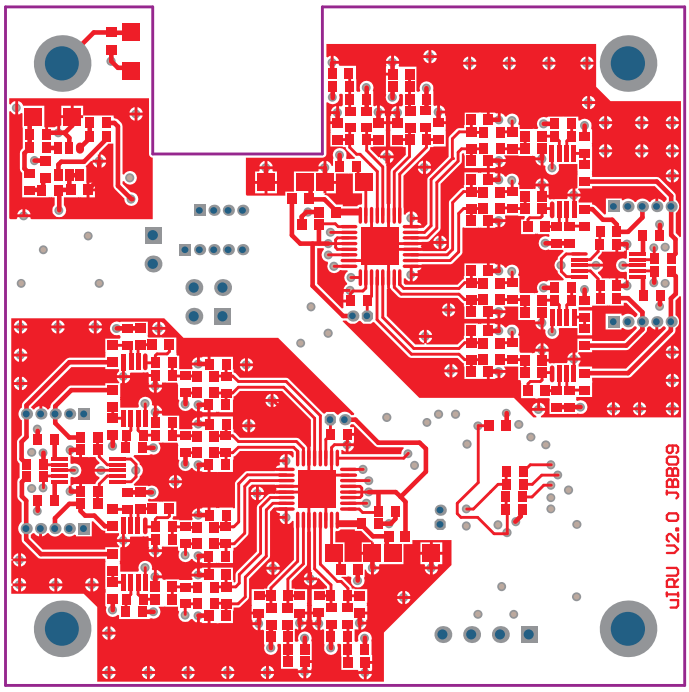

Figure F.11. *μIRU DCM top layer.*

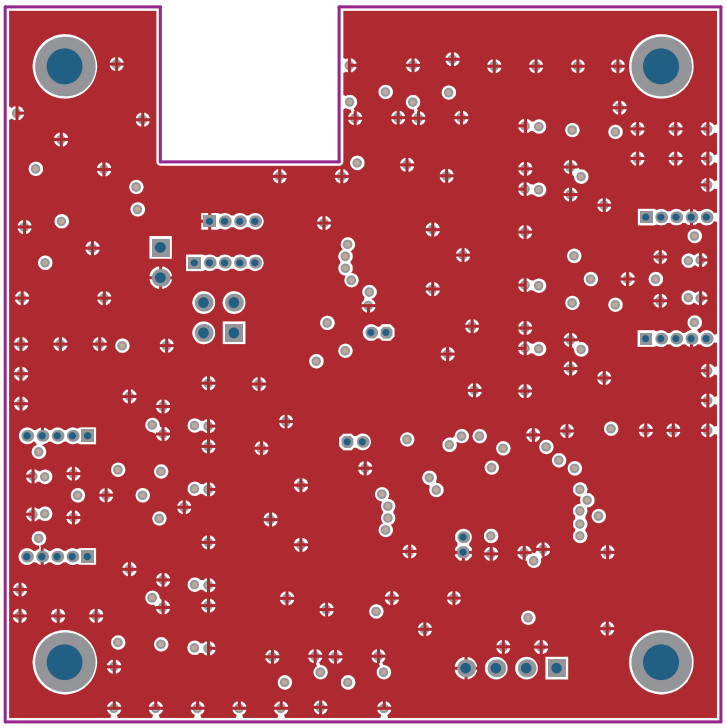

Figure F.12. *µIRU DCM middle layer 1.*

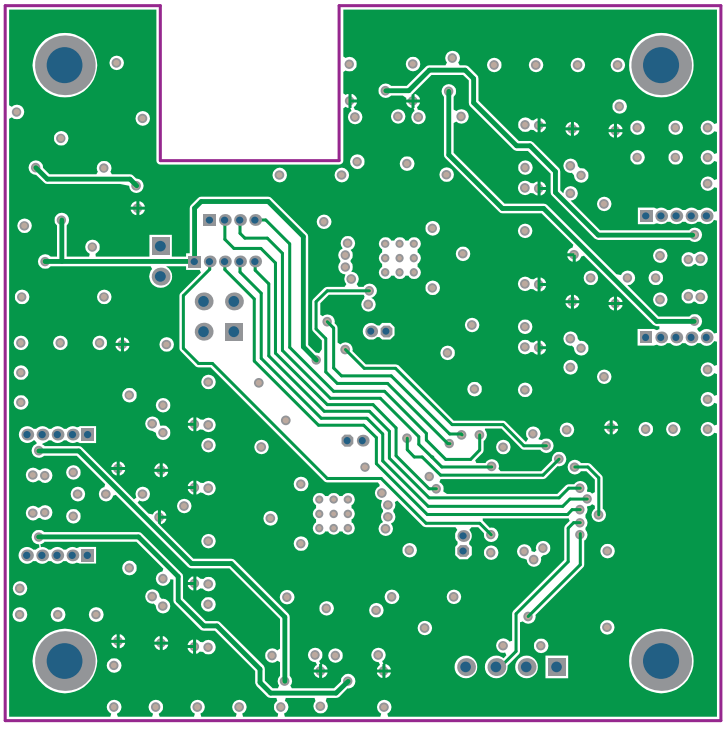

Figure F.13. *µIRU DCM middle layer 2.*

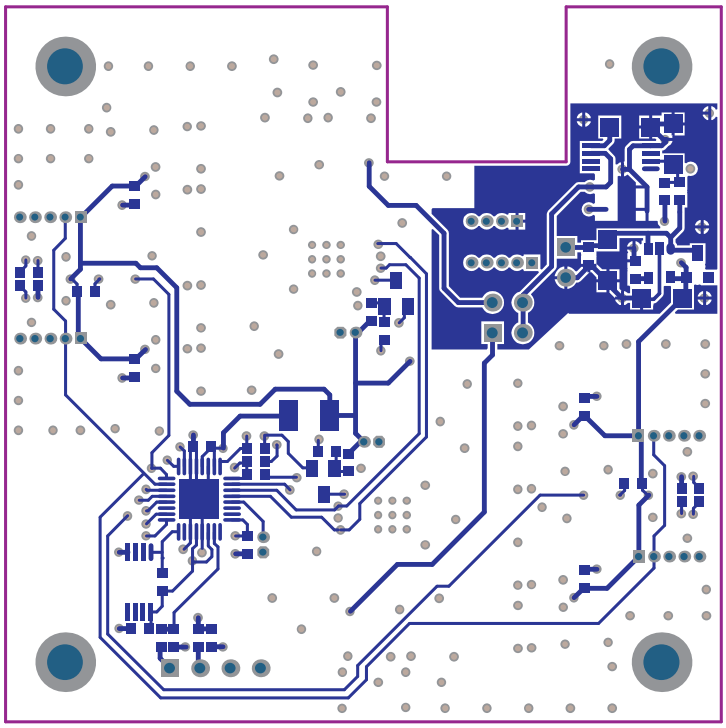

Figure F.14. *μIRU DCM bottom layer.*

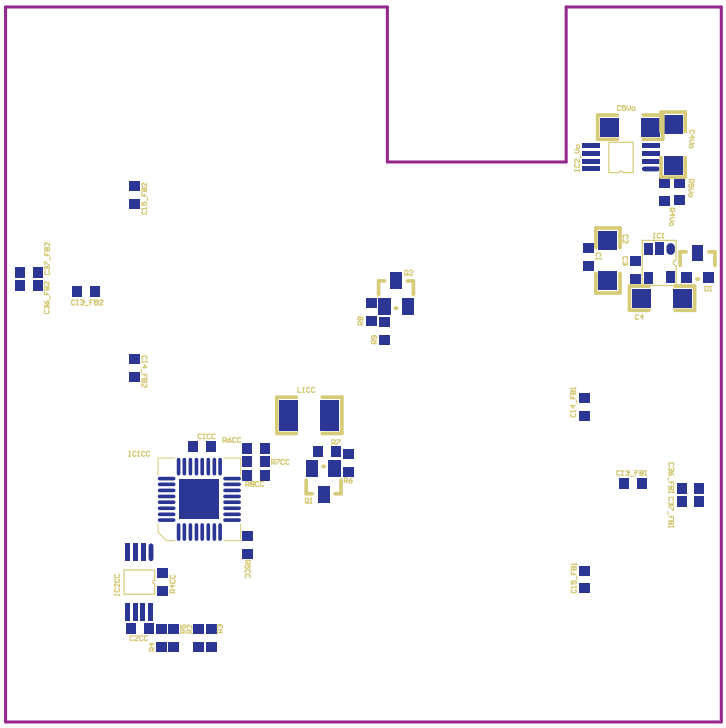

Figure F.15. *μIRU DCM bottom overlay.*